1-1-2018

Mapping with Modern Prosumer Small Unmanned Aircraft Systems: Addressing the Geospatial Accuracy Debate

Madison Palacios Dixon

Mapping with modern prosumer small unmanned aircraft systems: Addressing the geospatial accuracy debate

By

Madison Palacios Dixon

A Thesis
Submitted to the Faculty of
Mississippi State University
in Partial Fulfillment of the Requirements
for the Degree of Master of Science
in Geosciences
in the Department of Geosciences

Mississippi State, Mississippi

August 2018

Mapping with modern prosumer small unmanned aircraft systems: Addressing the geospatial accuracy debate

By

Madison Palacios Dixon

Approved:

_____
John C. Rodgers, III
(Major Professor)

_____
Padmanava Dash
(Committee Member)

_____
William H. Cooke, III
(Committee Member)

_____
Robert J. Moorhead
(Committee Member)

_____
Renee M. Clary
(Graduate Coordinator)

_____
Rick Travis
Dean
College of Arts & Sciences

Name: Madison Palacios Dixon

Date of Degree: August 10, 2018

Institution: Mississippi State University

Major Field: Geosciences

Major Professor: Dr. John Rodgers

Title of Study: Mapping with modern prosumer small unmanned aircraft systems: Addressing the geospatial accuracy debate

Pages in Study 183

Candidate for Degree of Master of Science

Modern prosumer small unmanned aircraft systems (sUAS) have eliminated many historical barriers to aerial remote sensing and photogrammetric survey data generation. The relatively low cost and operational ease of these platforms has driven their adoption for numerous geospatial applications including professional surveying and mapping. However, significant debate exists among geospatial professionals and academics regarding prosumer sUAS ability to achieve "survey-grade" geospatial accuracy ≤ 0.164 ft. in their derivative survey data. To address this debate, a controlled accuracy test experiment was conducted in accordance with federal standards whereby prosumer sUAS geospatial accuracies were reported between 15.367 ft. – 0.09 ft. horizontally and 496.734 ft. – 0.330 ft. vertically at the 95% confidence level. These results suggest prosumer sUAS derived survey data fall short of "survey-grade" accuracy in this experiment. Therefore, traditional surveying instruments and methods should not be relinquished in favor of prosumer sUAS for complex applications requiring "survey-grade" accuracy at this time.

ACKNOWLEDGEMENTS

The research presented herein was made possible through the support of numerous individuals, organizations, and entities which are hereby acknowledged in great gratitude for their respective contributions. Mr. Dallas Brooks, Director of the Raspet Flight Research Laboratory, for the opportunity to serve Mississippi State University as a Graduate Research Assistant while pursuing a graduate degree. Mr. Rodney Lincoln, Director of George M. Bryan Airfield in Starkville, MS, for cooperation in safely coordinating and conducting unmanned aircraft system (UAS) operations on the grounds of George M. Bryan Airfield, and for the use of his personal all-terrain vehicle during research field work. Mr. Mark Mattox, Mrs. Patsy Mattox, Mr. Josh Mattox, Mr. Jake Mattox, and Mr. Bradley Gray, of EMC Surveying & Mapping, for the use of EMC resources including Trimble R-6 real time kinematic (RTK) differential-global positioning system (DGPS), ASUS field laptop, ESRI ArcGIS software, and Trimble Business Center software. Dr. Christoph Strecha, Mr. Andrew McIntyre, and Mr. Paul Sparr, of Pix4D, for academic use licenses of Pix4D Mapper Pro for photogrammetric processing and export of all remotely sensed UAS data. Mr. Ralph Dixon and Mrs. Monica Dixon, for their computational hardware and software contributions. Finally, to Drs. John Rodgers, Padmanava Dash, William Cooke, and Robert Moorhead for their tremendous support and guidance throughout the research process.

TABLE OF CONTENTS

ACKNOWLEDGMENTS ii

LIST OF TABLES vi

LIST OF FIGURES vii

CHAPTER

I. INTRODUCTION 1

Problem statements and research justification 2
Research Objective 3

II. BACKGROUND 5

Overview 5
UAS groups and distinctions 5
Prosumer sUAS 7
Small unmanned aircraft system (sUAS) remote sensing 8
Photogrammetric applications 9
Stereoscopic photogrammety 10
Structure-from-motion (SfM) 12
Professional Surveying 13
Federal Surveying Standards 14
Survey-grade accuracy 16

III. LITERATURE REVIEW 18

Earliest studies 18
Modern developments 19
Applied geospatial studies 21
sUAS + SfM accuracy considerations 22
Observed accuracies in existing research 25
Need for additional research 26

IV. FIELD METHODS 28

Survey areas 28
In situ survey equipment 30

In situ field methodology....30
In situ field methods for survey area #1 (SA-1)....32
In situ field methods for survey area #2 (SA-2)....35
Remote sensing survey equipment....38
Remote sensing field methodology....40
Specific data collection parameters....40
Remote sensing field methods for survey area #1 (SA-1)....42
Remote sensing field methods for survey area #2 (SA-2)....45
Metereological considerations....47

V. DATA PROCESSING METHODS....50

Pix4D mapper pro....50
Specific processing parameters....51
Initial processing....51
Point cloud generation....54
Raster data generation....58
In situ data incorporation....62
Ground control point (GCP) implementation....63
Checkpoint implementation....66
Processing iterations and resulting survey datasets....68

VI. GEOSPATIAL AND STATISTICAL ANALYSIS....70

Geospatial analysis....70
Error calculation....70
Initial tie points....71
Point cloud....73
Digital surface model (DSM)....76
Statistical analysis....80
Root mean square error (RMSE) calculation....80
Accuracy (95% confidence) calculation....82

VII. RESULTS....84

Accuracy results overview....84
Accuracy reporting and classification results....92
Descriptive analysis of resulting accuracies....95
All survey datasets (18 total)....95
0GCP outliers removed, ≥ 5GCP datasets only (14 total)....97
P4P ≥ 5 GCP datasets only (7 total)....99
Frequency distribution for resulting accuracies....100

VIII. DISCUSSION....104

Research objective evaluation....104
Question 1. What geospatial accuracies were observed?....104

Question 2. What accuracy classifications (FGDC) were achieved? 109
Question 3. Is “survey-grade” accuracy achieved, both horizontally and vertically? 111
Additional discussion 121
Error calculation considerations for various survey data types 121
P4P accuracy considerations 122
Revisiting field method considerations 123
Opportunities for additional research 124

IX. SUMMARY AND CONCLUSIONS 127

Summary 127
Conclusions 131
Final thoughts 134

REFERENCES 136

APPENDIX

A. National Geodetic Survey (NGS) Monument DJ1746 Datasheet 141

B. National Weather Service (NWS) Observations for July 26, 2017 146

C. P3A_SA-1_12GCP COMPREHENSIVE ERROR EVALUATION 148

D. P3A_SA-2_21GCP COMPREHENSIVE ERROR EVALUATION 157

E. P4P_SA-1_12GCP COMPREHENSIVE ERROR EVALUATION 166

F. P4P_SA-2_21GCP COMPREHENSIVE ERROR EVALUATION 175

LIST OF TABLES

6.1 Error to GCP Initial Position for P4P_SA-2_21GCP checkpoints 72

6.2 Error values for P4P_SA-2_21GCP point cloud survey data 76

LIST OF FIGURES

2.1 Stereoscopic Fields-of-View and 3-Dimensional Perception 10

4.1 Survey Areas Map (SA-1, SA-2) 29

4.2 NGS Monument DJ1746 and Trimble R6 Base Station 31

4.3 Ground control point (GCP) placement 34

4.4 Survey Area #1 (SA-1) – GCPs and Checkpoints 35

4.5 Checkpoint placement 37

4.6 Survey Area #2 (SA-2) – GCPs and Checkpoints 38

4.7 Pix4D Capture – Remote sensing data collection parameters 41

4.8 Flight Plans – P4P at Survey Area #1 (SA-1) 44

4.9 Flight Plans – P4P at Survey Area #2 (SA-2) 46

4.10 Cloud-obstructed incident lighting - P4P remote sensing data at SA-1 49

5.1 Pix4D “Initial Processing” Parameters 52

5.2 Pix4D “Point Cloud and Mesh” Parameters 56

5.3 Pix4D “DSM, Orthomosaic and Index” Parameters 60

5.4 Ground Control Point (GCP) Implementation 65

5.5 Checkpoint Implementation 67

5.6 Resulting Survey Datasets 69

6.1 Error calculation for initial tie points 71

6.2 3D point selection for point cloud error calculation 73

6.3 Error calculation for point cloud survey data 75

6.4 Raster pixel identification for digital surface model (DSM) error calculation 77

6.5 Vertical error calculation for digital surface model (DSM) survey data 79

6.6 RMSE formulas 81

6.7 Horizontal RMSE ($RMSE_r$) formula 81

6.8 Horizontal Accuracy ($Accuracy_r$) and Vertical Accuracy ($Accuracy_z$) formulas 83

7.1 Accuracy results (ft.) for all sUAS + SfM derived survey data 85

7.2 Horizontal vs. vertical accuracy comparison (0GCP outliers removed) 88

7.3 P3A vs. P4P accuracy comparison (0GCP outliers removed) 89

7.4 Resulting accuracies at SA-1 (0GCP outliers removed) 90

7.5 Resulting accuracies at SA-2 (0GCP outliers removed) 91

7.6 FGDC accuracy classifications 93

7.7 Descriptive statistics for all survey datasets 95

7.8 Descriptive statistics for ≥ 5GCP survey datasets 97

7.9 Descriptive statistics for P4P ≥ 5GCP survey datasets 99

7.10 Frequency distribution of accuracy in ≥ 5GCP and P4P ≥ 5GCP datasets 101

7.11 SA-1 and SA-2 accuracy distributions (0GCP outliers removed) 102

7.12 P3A and P4P accuracy distributions (0GCP outliers removed) 103

8.1 Resulting accuracy by sUAS + SfM dataset 106

8.2 Highest reported accuracies (ft.) by sUAS platform and survey area 112

8.3 Survey-grade accuracy evaluation of sUAS + SfM error values 114

8.4 Horizontal error in relation to survey-grade accuracy at P4P_SA-1_12GCP 119

8.5 Vertical error in relation to survey-grade accuracy at P4P_SA-1_12GCP 120

CHAPTER I

INTRODUCTION

Recent statistics from the United States (U.S.) Federal Aviation Administration (FAA) demonstrate a significant increase in the use of unmanned aircraft systems (UAS) for all variety of educational, commercial, and governmental applications (FAA 2017). Aerial surveying and mapping by UAS, or more commonly small UAS (sUAS < 55 lbs.), has become an increasingly common application as it supports multiple present uses for commercial UAS recognized by the FAA. Recently, the practice of surveying and mapping by sUAS has become increasingly automated with resulting survey data often requiring minimal input on behalf of the sUAS operator. However, the adequacy of sUAS derived survey data for high-accuracy geospatial applications, such as professional surveying, remains in question (Mah & Cryderman 2015, Jaud et al. 2016, Pineux et al. 2017). This holds especially true of survey data derived consumer, or "prosumer", sUAS platforms which account for the vast majority of sUAS registrations in the U.S.

Modern prosumer sUAS platforms manufactured since 2015 represent the latest in a long history of airborne technologies deployed for geospatial studies and applications. However, given the emerging status of modern prosumer sUAS, scientific research on the components, applied capabilities, and derivative scientific data from these specific platforms remains lacking in comparison to traditional airborne technologies such as polar-orbiting satellites, manned aircraft, and even earlier generations of UAS

(Remondino et al. 2011, Colomina & Molina 2014, Nikolakopoulos et al. 2017). While the cumulative body of sUAS research is growing, research which focusses exclusively on modern prosumer sUAS platforms still remains limited. Among these studies, research efforts focusing exclusively on the derivative geospatial accuracy of modern prosumer sUAS survey data remains even further limited (e.g. Hugenholtz et al. 2013, Uysal et al. 2015, Agüera-Vega et al. 2017, Cook 2017). Additionally, the rapid advancement and releasing of new prosumer sUAS generations with improved capabilities often leaves older platforms and their corresponding research efforts inapplicable, if not irrelevant. Therefore, scientific research which specifically examines today's modern prosumer sUAS survey data accuracies is needed to support the many geospatial applications and individuals presently deploying these platforms.

Problem statement and research justification

Uncertainty regarding prosumer sUAS ability to achieve survey-grade data accuracy represents a significant problem. The relative low cost, operational ease, and semi-professional capabilities of these modern prosumer sUAS have increasingly driven their adoption for geospatial tasks, including high-accuracy applications such as professional surveying. These factors have also contributed to a rise in the entrepreneurial pursuit of aerial surveying and mapping by prosumer sUAS operators who often lack the expertise and/or oversight of a professional surveyor. In the worst cases, these operators are completely unaware of the many geospatial considerations involved in their aerial surveying efforts and resulting datasets. Meanwhile, professional surveyors and geospatial experts alike remain in debate over the legitimacy of prosumer sUAS derived survey data for high-accuracy geospatial applications (Clapuyt et al. 2016,

Pineux et al. 2017). Holland et al. 2016 perhaps summarizes this debate best in questioning "whether a UAV and a simple camera can produce data suitable for a mapping agency". Until further research is conducted, the problematic uncertainty surrounding prosumer sUAS survey data and its use for high-accuracy geospatial applications will likely remain.

To address this problem, an accuracy test of sUAS derived survey data by established, documented standards and procedures is needed. The purpose of this thesis research has been to conduct such an accuracy test using the established guidelines of the U.S. Federal Geographic Data Committee (FGDC). In doing so, it is the immediate goal of this thesis to provide scientific insight into the geospatial accuracy debate surrounding prosumer sUAS derived survey data. In a larger context, the broader goal of this research is to contribute to the greater scientific understanding and successful utilization of UAS technologies and derivative geospatial data.

Research objective

In consideration of these specific needs and goals, the objective of this thesis research was to address the geospatial accuracy debate surrounding sUAS and Structure-from-Motion (SfM) derived survey data. To do so, a controlled experiment was designed and conducted per FGDC accuracy testing standards. In this experiment, survey data from an instrument of higher accuracy was used as a ground-truth data to test the accuracy of sUAS + SfM survey data. During the experiment, sUAS data collection and SfM processing were designed to optimize resulting survey data accuracy based on proven practices in current scientific research. For example, sUAS data collection was conducted in (mostly) favorable meteorological conditions (wind < 5 mph, cloud cover <

1/8 opaque clouds) in an attempt to mitigate the influence of these conditions on resulting survey data accuracy.

Ultimately, it was the objective of this thesis research to answer the following questions in regards to sUAS + SfM survey data accuracy. First, what geospatial accuracies are observed in sUAS + SfM derived survey data according to FGDC standards and accuracy testing procedures? Next, what FGDC accuracy classification(s) does the sUAS + SfM survey data achieve? Lastly, is "survey-grade" accuracy at 0.164 ft. (5 cm.) achieved both horizontally and vertically in any sUAS + SfM data?

Research Questions:

1. What geospatial accuracies are observed in survey data derived from modern prosumer sUAS platforms and SfM photogrammetry.
2. Which accuracy classification(s) does resulting survey data achieve according to the FGDC Geospatial Positioning Accuracy Standards, *Part 2: Standards for Geodetic Networks*.
3. Is survey-grade accuracy at 0.164 ft. (5 cm) achieved, both horizontally and vertically, in modern prosumer sUAS derivative survey data.

It is hypothesized that geospatial survey data derived from modern prosumer sUAS and SfM photogrammetry does not currently achieve survey-grade accuracy at 0.164 ft. (5 cm) or greater both horizontally and vertically. To test this hypothesis, research methodologies have followed the established formulas and procedures for accuracy testing and classification as set forth in the FGDC Geospatial Positioning Accuracy Standards (FGDC 1998). Before proceeding, the following chapters provide relevant, detailed background information to establish the fundamental research context, and a thorough review of the existing scientific literature relating to this topic.

CHAPTER II

BACKGROUND

Overview

Modern (post-2015) sUAS, also sometimes referred to as unmanned aerial vehicles (UAV) or simply "drones", represent the culmination of numerous technological advances in the fields of aviation, robotics, and remote sensing. While military use of unmanned aircraft long predates modern sUAS, recent technological advances have resulted in modern platforms which are now easily deployable for numerous civilian operations and applications. For most of these applications, aerial remote sensing represents the fundamental task for which sUAS are most frequently deployed (Remondino et al. 2011, Colomina & Molina 2014). For this thesis research, remote sensing by prosumer sUAS, and all subsequent methodologies, have been conducted in order to perform detailed accuracy testing of sUAS derived survey data. The following sections provide detailed background information to establish the fundamental thesis research context.

UAS groups & distinctions

UAS are most frequently "grouped" according to maximum takeoff weight (MTOW) and operational altitude thresholds established by the United States (U.S.) Department of Defense (DoD). For example, Group 3 UAS, those weighing 55 lbs. – 1,320 lbs., represent the first UAS grouping which are considered "large" as they exceed

the 55 lb. threshold of "small" UAS. Similarly, Group 5 UAS, the largest class of UAS groupings, include all UAS platforms weighing > 1,320 lbs. and operating at altitudes above 18,000 feet (ft.) mean sea level (MSL). All sUAS are grouped according to these DoD group classifications as Group 1 UAS (< 20 lbs.) and Group 2 UAS (20 lbs. – 55 lbs.; Fladeland et al. 2017, Marshall et al. 2016).

Despite these established groupings, civilian distinctions are often used in referring to various sUAS platforms as an alternative to the traditional DoD group classifications. In general, these distinctions are similar to that of civilian electronics and primarily refer to sUAS platform capability, and the associated level of experience or skill on behalf of the sUAS operator. Specifically, these distinctions include "consumer", "prosumer", and "professional" sUAS.

Consumer sUAS, as with consumer electronics, refer to sUAS platforms possessing limited capabilities and requiring minimal sUAS operational experience. Alternatively, professional sUAS refers to highly specialized platforms which require a certain degree of skill or experience on behalf of the sUAS operator in order to perform a specific task. These professional sUAS platforms are typically, and sensibly, found in use by individuals and organizations which are considered established professionals in their respective fields – such as the use of a light detection and ranging (LiDAR) equipped sUAS by a registered professional land surveyor (RPLS). The final distinction, prosumer sUAS, differs from these former distinctions and requires additional discussion as it represents the subject this thesis research.

Prosumer sUAS

Prosumer sUAS share similarities and differences with both consumer and professional sUAS. These platforms, like consumer sUAS, generally require minimal prior experience and remain relatively easy to operate. However, modern prosumer sUAS, again referring to post-2015 platforms, increasingly approach the specialized capabilities generally associated with professional sUAS. These capabilities are made possible by onboard sUAS components including high-resolution sensor payloads, global navigation satellite system (GNSS) receivers, and inertial measurement units (IMU) which were previously reserved only for professional sUAS. Recent technological advances have allowed these components to now become commonplace in modern prosumer sUAS platforms. The advancement of these components is likewise demonstrated in many now-common civilian electronic devices, such as smartphones.

What remains unique to prosumer sUAS, however, is the reduction or outright elimination of tremendous operational cost and expertise barriers which were previously inherent to airborne flight operations. Historically, these cost and experience barriers firmly excluded the participation of individuals or organizations which were not professional aviators, sensor operators, etc. However, the relative ease of use and borderline professional capabilities of modern prosumer sUAS have recently changed this dynamic. Additionally, the inaugural implementation of FAA regulations for commercial sUAS operations in August 2016 tremendously advanced the legitimacy of sUAS, including prosumer platforms, as viable tools for both industry and academia (FAA 2018).

The cumulative impact of these factors has undoubtedly contributed to the proliferation of prosumer sUAS platforms as we know them today. According to FAA statistics, the vast majority of commercial sUAS registrations in the U.S. belong to prosumer platforms (FAA 2017). These statistics firmly demonstrate the increasing acceptance and use of modern prosumer sUAS platforms in numerous professional fields. However, this trend toward legitimacy has not inherently translated into operational or applicational proficiency of prosumer sUAS in every professional field for which they are deployed. For this research, prosumer sUAS proficiency in the practice of high-accuracy surveying, mapping, and modeling applications has been evaluated.

Small unmanned aircraft system (sUAS) remote sensing

Aerial remote sensing represents a longstanding scientific practice in which the use of prosumer sUAS is exceptionally new. Historically, aerial remote sensing has been conducted by large satellites and traditional manned aircraft which were capable of successfully deploying the sensors and components necessary for performing this task. However, modern advances and reduced operational barriers described above have allowed prosumer sUAS to be increasingly deployed for demanding remote sensing applications. Specifically, the advancement of low-cost, user-friendly compact digital cameras and similar sensor technologies have greatly increased the ability of modern prosumer sUAS to achieve high resolution remote sensing data (Colomina & Molina 2014, Franesco & Remondino 2014, Cooper et al. 2015). Likewise, the advancement of compact global positioning systems (GPS) and IMU technologies have facilitated prosumer sUAS capabilities for systematic, autonomous remote sensing data collection (Chao et al. 2010, Vasuki et al. 2014, Cooper et al. 2015). As a result, modern prosumer

sUAS now possess the necessary sensors and components to successfully perform aerial remote sensing.

In general, aerial remote sensing remains an applied practice conducted in support of a larger specified application or purpose. This larger purpose tends to dictate the manner in which remotely sensed data are collected, processed, analyzed, interpreted, and utilized. For this research, high accuracy surveying again serves as the larger specified purpose of the remote sensing practice. While this purpose can be achieved through a variety of both passive and active remote sensing systems, compact digital camera sensors are most common to prosumer sUAS platforms. Therefore, digital image data are generally the most common outcome of prosumer sUAS remote sensing data collection. For these data to be of value in the greater mapping and modeling purpose, additional scientific fields and practices must be explored – most notably, the field of photogrammetry and its related concepts.

Photogrammetric applications

In simplest terms, photogrammetry refers to the practice of making geospatial measurements from photos (Birdseye 1940). Much like remote sensing, photogrammetry has a long-established history of scientific and professional use and acceptance. Also similar to remote sensing, photogrammetry has historically relied upon traditional manned aircraft for airborne data collection. Modern prosumer sUAS have changed this dynamic as aerial photos can now be captured at lower altitudes and higher spatial resolutions than were previously possible. In this sense, modern sUAS have greatly contributed to the concept of "close-range" photogrammetry given their relatively close proximity to photographed subject matter as opposed to manned aircraft (Brunier et al.

2016). Furthermore, technological advances in the field of SfM photogrammetry has further advanced the utilization and acceptance of sUAS surveying applications. For the purposes of this research, it is important to acknowledge the role of SfM technology and its fundamental photogrammetric concepts founded in in stereoscopic photogrammetry as described below.

Stereoscopic photogrammetry

Stereoscopic photogrammetry specifically refers to the use of stereo (i.e. overlapping) photos to achieve a 3D perspective of the photographed subject matter (Birdseye 1940). This overlapping nature and resulting 3D perspective as shown in Figure 2.1 below represents the widely understood science of stereoscopy. In this sense, stereoscopy applies not only to stereo photos, but to stereoscopic fields-of-view (FOV) in general, like that of human eyesight.

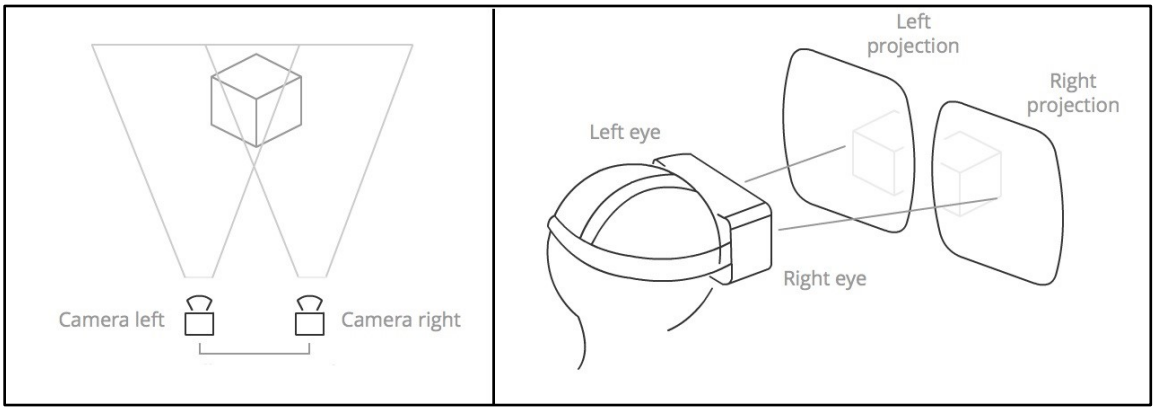

Figure 2.1 Stereoscopic Fields-of-View and 3-Dimensional Perception

Stereoscopic camera positions and resulting stereo image datasets can achieve 3-dimensional perception of subject matter in the same way as human eyesight. In the practice of stereoscopic photogrammetry, this allows for both horizontal and vertical (i.e. 3D) measurements to be made from stereo image subject matter. Image adapted from *The History of VR*. Stereoscopic Vision. 2018.

Given the inherently 3D nature of the geospatial environment which surrounds us, stereoscopic photogrammetry provides the distinct ability for 3D reconstruction, analysis, and measurement of photographic subject matter. Again, this ability is made possible only through the use of stereo photos, as a single photo itself remains implicitly two-dimensional. While the fundamental concepts of stereoscopy remain firmly established, practical methodologies in the field of stereoscopic photogrammetry have continuously evolved through various technological advances (e.g. Whittlesley 1970, Nikolakopoulos et al. 2017).

To begin, proliferation of modern sUAS technology has drastically reduced the geographic scale at which stereoscopic photogrammetry can be practically applied. When captured by manned aircraft, aerial photographs tend to capture subject matter of large geographic extent as a result of the aircraft's operating altitude. In comparison, aerial photographs capture by sUAS, which can only be legally deployed at altitudes up to 400 ft. above ground level (AGL) in most instances, depict subject matter of far less geographic extent. As a result, stereoscopic photogrammetry can now be effectively applied to exceptionally small geographic regions which previously would have required a different methodological approach.

Additionally, early photogrammetric methodologies were conducted manually by a professional photogrammetrist with few or no automated processes. These early methodologies were also applied exclusively to analog, hard-copy photographic data. At present, these methodologies have trended significantly, if not exclusively, toward autonomous digital processes which utilize digital photographic image data (Jensen 2007, Jensen 2015). This trend toward digitization and autonomy comes as the result of

significant advances in computational processing technologies which are increasingly capable of performing photogrammetric operations. For this research, SfM technology and its associated concepts in computer vision and digital scene reconstruction represent an especially important consideration.

Structure-from-motion (SfM)

Modern SfM technologies and practices as we know them today evolved from numerous scientific advances in automated feature matching algorithms and computer vision technologies in the late 1980s and early 1990s (Förstner 1986, Spetsakis & Aloimonos 1991). As a result, SfM photogrammetry has revolutionized the concept and practice of 3D scene reconstruction in stereoscopic photogrammetry.

In traditional stereoscopic photogrammetry, the geospatial position and orientation of an airborne camera and its resulting photographic data must be either inherently known or calculated in order to perform 3D scene reconstruction. This position and orientation information could be inherently known if the airborne camera or aircraft is accompanied by additional components, such as a GNSS receiver. Alternatively, position and orientation information could also be calculated through the use of ground control points (GCPs) representing known positions within the photographed subject matter. Once photographic data position and orientation have been established, traditional stereoscopic photogrammetry still relies upon the experience and intuition of an individual, usually a professionally licensed photogrammetrist, in order to manually perform 3D scene reconstruction.

In the case of SfM photogrammetry, these practices are no longer required to achieve 3D scene reconstruction of photographic data. This is true because SfM

photogrammetry, again relying upon modern computer vision technology and feature matching algorithms, is able to accurately estimate the position and orientation of aerial photographic data through the content of the photos themselves. This task is achieved by SfM's ability to intuitively identify matching features throughout stereo image datasets, and use these features to estimate photographic data position and orientation. In doing so, SfM not only automates the calculation of this position and orientation information (when this information is not already inherently known), but further autonomously performs nearly all of the 3D reconstruction process of stereoscopic photogrammetry.

While varying degrees of autonomy can be practiced in SfM photogrammetry depending on the specific application or individual, it is worth noting SfM's unique ability to successfully, and near fully autonomously, perform 3D scene reconstruction in the absence of specialized airborne positioning components, GCPs, and even the intuition of a seasoned photogrammetrist. However, when applied to a highly demanding professional practice with established geospatial expectations and requirements, the SfM approach requires additional scrutiny in comparison to traditional stereoscopic photogrammetry (Ishiguro et al. 2016, Cook 2017). This is especially true in the case of professional surveying, which represents the intended field and target audience of this thesis research.

Professional surveying

Surveying refers to the long standing professional practice of collecting and accurately communicating the earth's geographic landscape in a variety of 2D and 3D representations. At present, these representations most commonly include maps (2D), point cloud reconstructions (3D), and geospatial models (3D) including Digital Elevation

Models (DEM) and Digital Surface Models (DSM). The practice of surveying generally requires the use of one or more methods of *in situ* and/or remote sensing data collection. In the case of *in situ* data collection, a variety of specialized instruments, such as robotic total stations and real time kinematic (RTK) differential GPS (DGPS), are commonly used to collect points of strategic interest for the geographic area being surveyed.

In the case of remote sensing data collection, a similarly specialized set of instruments, such terrestrial laser scanning systems and robotic total stations, are often utilized, as well as traditional methods of airborne remote sensing. However, recent advances in sUAS remote sensing, as previously described, have spurred significant interest with the professional surveying community. As a result, the utilization of sUAS, including prosumer sUAS platforms, has risen significantly in the application of remote sensing data collection for professional surveying practices (Mah & Cryderman 2015).

Federal surveying standards

Professional surveying and its derivative data are relied upon by many fields and industries which harbor specific geographic and/or geospatial implications and considerations. For example, a professional surveying operation is most often the very first step associated with any form of construction or engineering project. Likewise, a professional survey may also serve as the definitive representation of land ownership boundaries prior to the sale or acquisition of any geographic area and its associated surface or mineral rights. For this reason, professional surveying practices must be formally conducted, and their resulting data confirmed, by a registered professional land surveyor (RPLS) as required by federal law. Furthermore, professional surveying

practices and resulting data are also formally regulated by the U.S. Federal Geographic Data Committee's (FGDC) Geospatial Positioning Accuracy Standards (FGDC 1998).

The earliest form of these modern survey standards came by way of "General Instructions for the Field Work of the U.S. Coast and Geodetic Survey" as published in the early 20th century. While these early instructions successfully established guidelines for consistent surveying field practices, they failed to establish specific thresholds on the basis of geographic data accuracy and precision. This changed around 1921 when the original instructions were amended to include "precise", "primary", and "secondary" accuracy distinctions, and again on May 25th, 1925 with the implementation of "1st", "2nd", and "3rd" Order accuracy classifications by the Board of Surveys and Maps of the Federal Government.

Later, in 1974, the Federal Geodetic Control Committee (FGCC) was formally established and soon published revised documentation as the "Classification, Standards of Accuracy, and General Specifications of Geodetic Control Surveys". This documentation was again revised and re-released in 1984 as the "Standards and Specifications of Geodetic Control Networks". More recently, with increasing interest and use of GPS technology, additional surveying documentation was issued in 1989 as the "Geometric Geodetic Accuracy Standards for using GPS relative positioning techniques" to account for the latest practices and considerations of GPS technology at the time. Eventually, in 1990, the original FGCC was restructured as a sub-committee to the newly formed FGDC which took a wholistic approach to regulating the larger field of professional surveying, as opposed to strictly focusing federal geodetic survey operations. The FGDC Geospatial Positioning Standards in place today, and their corresponding

accuracy requirements and classifications, were finally implemented in 1998 and have remained, for the most part, without significant revision since that time (FGDC 1998).

Survey-grade accuracy

Ever since the first addition of formal accuracy distinctions in the 1920's, all subsequent surveying literature described above have revised and retained some form of numerical accuracy orders, designations, and/or classifications. The reason for these formal accuracy designations is to provide a consistent means of communicating both the horizontal and vertical accuracies of all professionally surveyed geospatial data. Additionally, these accuracy designations can be used to establish the required accuracy of a geospatial data prior to collection, thereby allowing professional surveyors to proactively utilize data collection methodologies which are accepted to meet the required accuracy of the survey. As a result of the latter, specific "grades" of survey instrumentation equipment were established on the basis of their ability to achieve certain degrees of geospatial accuracy in their resulting data. In terms of GNSS/GPS equipment, the United States Geological Survey (USGS) recognizes these grades as mapping-grade, differential-grade, and survey-grade (USGS 2017).

While mapping-grade and differential-grade survey instrumentation are accepted to result in geospatial accuracies of 9.84 ft. (3 meters) and 3.28 ft. (1 meter) respectively, survey-grade instrumentation is general accepted to achieve geospatial accuracies between 0.065 ft. (2 centimeters) and 0.164 ft. (5 centimeters). For this reason, mapping-grade and differential-grade instrumentations and resulting data are considered adequate for surveying efforts requiring lesser degrees of geospatial accuracy than that of survey-grade efforts. Although these data are still significantly valuable for numerous purposes

and applications, survey-grade data remains required for those applications, such as engineering, in which high geospatial accuracy is inherently required for reasons of geographic and/or structural safety and integrity (FGDC 1998, USGS 2017). As a result, survey-grade data are generally subject to a much higher degree of scrutiny among professional surveyors and survey data recipients. It is this scrutiny which has spurred a heated, ongoing debate as to whether modern prosumer sUAS and their derivative geospatial data are truly capably of achieving survey-grade accuracy.

CHAPTER III

LITERATURE REVIEW

Earliest studies

The first unmanned aircraft, known as the "Kettering Bug", was developed by Orville Wright and Charles Kettering in 1918 for experimental use by the U.S. military in the final year of World War I. Post-war research into unmanned aircraft continued briefly but was later halted in the 1920's due to opposing research priorities and tremendous funding deficiencies. Further research into unmanned aircraft operations and applications did not resume in significant capacity until the onset World War II. While the Kettering Bug and other early generations of unmanned aircraft have little in common with the modern sUAS platforms of today, these first platforms demonstrate the earliest historical use of unmanned aircraft – a consideration which often pre-dates typical expectations and perceptions. Furthermore, the development and experimental deployment of early unmanned aircraft like the Kettering Bug undoubtedly laid the foundation on which today's sUAS technologies have been built (Marshall et al. 2016).

Civilian scientific research on unmanned aircraft platforms and applications gained traction in the latter half of the 20th century (Remondino 2011, Marshall et al. 2016). Unmanned aircraft from this time, similar to their military predecessors, were generally not as complex or developed as today's modern sUAS. For example, Whittlesley 1970 utilizes perhaps the simplest form of sUAS, a camera-equipped tethered

balloon, to capture aerial photographs of an archaeological site from a non-traditional perspective. Alternatively, Wester-Ebbinghaus 1980 explores the practice (and perceived scientific value) of UAS aerial photography by using a radio-controlled model helicopter – a platform which more closely resembles modern sUAS. This study in particular remains relevant today as similar radio-controlled single-rotor sUAS (such as the model helicopter in Wester-Ebbinghaus 1980) and multi-rotor sUAS (such as those used in this thesis research) represent the most popular and prevalent form of prosumer sUAS by far. More importantly, these early civilian studies, among few others, represent the pivotal introduction of UAS and sUAS into the field of aerial photogrammetry and photogrammetric surveying.

Modern developments

In consideration of these early research efforts, sUAS photogrammetric surveying remains a relatively new concept and practice. Traditionally, photogrammetric surveying was conducted near exclusively through the use of sensor-equipped manned aircraft for data collection, and hard-copy, analog processing for data interpretation. This traditional methodology has been the subject of its extensive scientific research for many decades, much of which remains fundamentally relevant and applicable to photogrammetric surveying today (e.g. Hirai 1962, Oshima & Usami 1964). However, modern developments in both sUAS platforms and photogrammetric surveying practices have recently altered the landscape of photogrammetric surveying (Tonkin et al. 2014).

As early sUAS began to provide an alternate method of aerial photographic data collection, recent scientific research and resulting technological developments have continuously improved the ability of modern sUAS platforms to capture high resolution

remote sensing data (Remondino et al. 2011, Colomina & Molina 2014, Tonkin et al. 2014). Specifically, scientific research in this area includes studies on modernized, compact digital cameras (McCaffrey et al. 2005), sensor stabilization systems (e.g. Sushchenko & Goncharenko 2016), navigation and orientation components (e.g. Chao et al. 2010, Cooper et al. 2015), and autonomous flight operations (e.g. Vasuki et al. 2014, Cooper et al. 2015). Furthermore, the enactment of U.S. federal regulations for commercial sUAS operations beginning in 2014 further contributed to modern sUAS developments by establishing and legitimizing the use of sUAS for professional applications (FAA 2017).

For photogrammetric surveying practices, the most pivotal modern developments, as previously mentioned, have resulted from scientific research and corresponding developments in the fields of automated feature matching and computer vision technologies (Westoby et al. 2012). In the case of automated feature matching, the development and implementation of complex feature-based algorithms in the late 1980's allowed for autonomous scaling and matching of digital image data and corresponding subject matter – thereby establishing the first concepts of a digital photogrammetric methodology (e.g. Förstner 1986, Harris & Stephens 1988). Additionally, in the case of computer vision technology, scientific research from the early 1990's greatly improved computational motion perception and digital image data subject matter triangulation (e.g. Spetsakis & Aloimonos 1991). The contributions of these research efforts and similar studies eventually resulted in the development of SfM, a modern photogrammetric practice which has since been the subject of much additional research (e.g. Westoby et al. 2012, Tonkin et al. 2014, Clapuyt et al. 2016, Ishiguro et al. 2016).

For the most part, these modern developments in sUAS technology and SfM photogrammetry have resulted in a new, novel, and relatively capable method of photogrammetric surveying, assuming the presence of adequate sUAS components and SfM computational processing hardware and software (Tonkin et al. 2014). However, existing research has also frequently questioned the ability of this new method to achieve the required accuracy of inherently demanding geospatial applications, such as professional surveying (Hugenholtz et al. 2013, Siebert & Teizer 2014, Mah & Cryderman 2015, Pineux et al. 2017).

Applied geospatial studies

In most geospatial applications there exists a longstanding, fundamental need to accurately map or model the geographic topology and/or surface features of a given survey area. Recently, modern sUAS platforms, SfM photogrammetry, and the combination of these technologies in performing photogrammetric surveying, has been found increasing useful in meeting this need – often with greater ease and lower costs than traditional surveying methods (Remondino et al. 2011, Colomina & Molina 2014). This development is clearly demonstrated by the increasing number of recent scientific studies which either utilize, or directly examine, these technologies for a number of geospatial fields and applications (e.g. Westoby et al. 2012, Hugenholtz et al. 2013, Cryderman et al. 2014, Sibert & Teizer 2014).

Despite this recent increase in sUAS utilization, the geospatial accuracy of sUAS + SfM derived survey data remains questionable for geospatial applications demanding consistent, high-accuracy survey data. (e.g. Pineux et al. 2017). This is due, in part, to a number of a pivotal considerations which research has found to influence geospatial

accuracy in sUAS + SfM survey data. The most important and commonly recognized of these considerations (in regards to derivative survey data accuracy) include topology and surface characteristics, meteorological conditions, and survey methodology (Tonkin & Midgley 2016, James et al. 2017).

sUAS + SfM accuracy considerations

To begin, certain land cover characteristics are currently unbecoming of the sUAS + SfM methodology's ability to achieve accurate survey data. For example, dense vegetation is widely known to inhibit SfM's ability to return accurate ground positions and elevation measurements (Wallace et al. 2016, Watanabe & Kawahara 2016). This is true as sUAS data collection is limited to the field-of-view (FOV) of the onboard sensor payload. In the absence of a specialized sensor, dense vegetation obstructs this FOV from collecting data at ground level for accurate topological mapping and modeling.

Surfaces exhibiting steep elevation change (both natural and man-made) are also difficult to accurately map/model using the sUAS + SfM survey method (Bemis et al. 2014, Jaud et al. 2016). First, steep elevation changes may obstruct the FOV of nearby terrain during sUAS data collection in just the same way as vegetation. Furthermore, additional challenges arise if sUAS data collection altitude does not account for and adjust to follow steep topological elevation changes. Properly adjusting sUAS data collection altitude in these areas allows photographic data to maintain a consistent ground sample distance (GSD) across the remote sensing dataset (Udin & Ahmad 2014, James et al. 2017). However, the ability to autonomously perform this adjustment is not yet common in most prosumer sUAS platforms – hence, it is often unconsidered or

overlooked in favor of a fully autonomous workflow (Vasuki et al. 2014, Cooper et al. 2015).

Elevation changes resulting from large, man-made surface features extending into the airspace above a survey area may further complicate and inhibit the sUAS + SfM methodology. These features may impede sUAS ability to safely perform remote sensing data collection at low altitudes. Furthermore, these features often represent the steepest elevation changes in a given survey area and are known to obstruct sensor FOV of surrounding areas, usually more so than naturally occurring surface features. Lastly, these man-made features nearly always possess distinct linear edge features which SfM photogrammetry generally struggles to reconstruct (Ruzgiene et al 2015, Ishiguro et al. 2016, Jaud et al. 2016).

Meteorological conditions are likewise known to influence sUAS + SfM derivative survey data, as well as the data collection process itself (Remondino et al. 2011, Colomina & Molina 2014). High winds (or any wind speed which affects the flight path of the sUAS) are especially troublesome as sUAS platforms must battle these winds while performing remote sensing data collection. As a result, photographic data may be offset or disoriented from its intended position and lead to errors during SfM processing (Cooper et al. 2015, Sushchenko & Goncharenko 2016). Sporadic cloud cover also presents a challenge in the form of incident energy/lighting variations across a survey area. These variations are known to challenge the feature matching algorithms utilized by SfM as topological and surface features are more difficult to match and reconstruct in inconsistent lighting. Similarly, in the absence of sporadic cloud clover, the incident angle of solar energy remains a primary consideration as surface features may cast

shadows within the survey area – again resulting in troublesome lighting variations (Clapuyt et al. 2016, Ishiguro et al. 2016).

Lastly, survey methodology presents the most pivotal of considerations in terms of derivative survey data accuracy. Methodological error is a well-documented source of error in remote sensing data collection practices (Jenson 2007). This holds true in the case of sUAS + SfM photogrammetric surveying and its associated methodologies (Mesas-Carrascosa et al. 2016, Tonkin & Midgley 2016, James et al. 2017). SfM generally requires a quantitatively larger set of images than traditional photogrammetry to perform 3D scene reconstruction. Additionally, SfM also requires an exceptionally higher degree of overlap in stereo images than traditional photogrammetry (Konstantinos et al. 2016, Nikolakopoulos et al. 2017). For this reason, the sUAS + SfM survey methodology is fully dependent on thorough, comprehensive data collection of the entire survey area(s) with appropriate degrees of image overlap. Existing research has demonstrated that failure to perform sUAS remote sensing data collection in this manner will result in incomplete and/or erroneous derivative survey data (Mah & Cryderman 2015, Jaud et al. 2016, Cook 2017).

Furthermore, the georeferencing of sUAS + SfM survey data into geographic or projected coordinate systems requires additional steps in the survey methodology. The use of GCPs, though not required for SfM 3D reconstruction in relative "image space" coordinates, are now inherently required for accurate georeferencing of survey data (e.g. Tonkin & Midgley 2016, James et al. 2017, Molina et al. 2017). Additionally, the use of sampled checkpoints is also required to assess survey accuracy relative to the geographic or projected coordinate system (FGDC 1998). The placement, *in situ* collection, and

integration of these points in the survey methodology workflow presents another source of potential error in sUAS + SfM derivative survey data.

Observed accuracies in existing research

Observed accuracies have varied in applied geospatial studies using the sUAS + SfM method. This is due, in part, to numerous variations in the accuracy considerations above and the rapid release of new and more capable sUAS platforms and components. In the most recent studies, some sUAS +SfM derived survey data appear on the verge of achieving survey-grade accuracy at 0.164 ft. (5 cm.). For example, Agüera-Vega et al. 2017 found geospatial accuracy values of 0.190 ft. (5.8 cm.) – 0.147 (4.5 cm.) in derivative survey data when optimized by 15-20 GCPs during SfM processing. However, in this study the 0.164 ft. (5 cm.) survey grade accuracy threshold was not met at the 95% confidence level – a requirement of accuracy classification by FGDC standards (FGDC 1998). A similar study, Clapuyt et al. 2015, found the geospatial accuracy of sUAS + SfM derived survey data to be approximately 0.196 ft. (6 cm). This study also added that resulting accuracy "can easily be improved" through the use of higher accuracy GCPs. The accuracy results of both studies border on survey-grade distinction and demonstrate significant improvement over similar studies as little as 3-4 years prior (e.g. Hugenholtz et al. 2013, Mancini et al. 2013, Franesco & Remondino 2014).

In most studies, including those mentioned above, observed accuracies are reported in the form of root mean square error (RMSE) values representing error/deviation from benchmark checkpoints or established data within a survey area. For example, Niethammer et al. 2012 reports the accuracy of sUAS + SfM survey data by calculating the RMSE deviations from benchmark terrestrial laser scanning data in

studying the geological impacts of a recent landslide event. In this study accuracy was reported at ~ 0.5 meters based on the calculated RMSE values. Similarly, Siebert & Teizer 2014 also reports sUAS + SfM survey data accuracy in the form of RMSE deviations, this time based on benchmark survey data of higher accuracy from a robotic surveying total station. In this study, accuracy is reported as 0.042 meters - a higher observed accuracy than the previous Neithammer et al. study of 2012 and consistent with similar accuracy improvements over the same time period cited above.

Need for additional research

Variations in the accuracies reported above, while scientifically insightful, have certainly contributed to the debate surrounding sUAS ability to achieve survey-grade accuracy. Again, since most accuracy results are presented in the form of RMSE, these values can sometimes give the impression of survey-grade accuracy. FGDC standards recognize RMSE as an "accepted estimate of geospatial accuracy", however, RMSE values must be subject to further statistical analysis to achieve an FGDC accuracy classification at the 95% confidence level (FGDC 1998, e.g. Agüera-Vega et al. 2017).

Since accuracy is not always the explicit focus of these studies, discussion of accuracy is often surpassed by more extensive discussion of concepts which are specific to the geospatial field of the research effort (e.g. Hugenholtz et al. 2013, Bemis et al. 2014). For this reason, additional research focusing on geospatial accuracy testing and quantification of modern prosumer sUAS + SfM survey data remains continuously needed as sUAS and SfM technologies advance. This is clearly demonstrated by both the increasing number of studies utilizing sUAS, and the documented improvements in sUAS + SfM derived geospatial accuracies in recent research (Clapuyt et al. 2016, Agüera-Vega

et al. 2017). Furthermore, the need for this continued research is regularly acknowledged in existing scientific literature (Remondino et al. 2011, Colomina & Molina 2014, Tonkin et al. 2014, James et al. 2017). Therefore, the thesis research methodologies, results, and conclusions described in the following sections have been designed and conducted to contribute to this scientific research need as best as possible.

CHAPTER IV

FIELD METHODS

For accuracy testing and evaluation, FGDC Geospatial Positioning Accuracy Standards dictate "accuracy testing by an independent source of higher accuracy is the preferred test for positional accuracy" (FGDC Geospatial Positioning Accuracy Standards 1998, Part 3, Section 3.2.2). This method of accuracy testing is likewise endorsed by the U.S. Spatial Data Transfer Standard (SDTS) (ANSI-NCITS, 1998) as referenced in FDGC standards (FGDC 1998). Therefore, in compliance with established standards, two survey area test sites were selected and utilized for accuracy testing of sUAS + SfM derived survey data by an independent source of higher accuracy. Specific survey area details and corresponding *in situ* and remote sensing methodologies are discussed in the following sections.

Survey areas

For this research, two survey area test sites on the grounds of George M. Bryan Field in Starkville, MS were used for accuracy testing and evaluation of sUAS + SfM derived survey data. The selected survey areas represent two fundamentally differing survey environments, each with its own topological and surface characteristics, to allow for a more comprehensive evaluation of sUAS + SfM derived survey data. These survey areas have been hereafter referred to as Survey Area #1 (SA-1) and Survey Area #2 (SA-2) as shown in Figure 4.1 below.

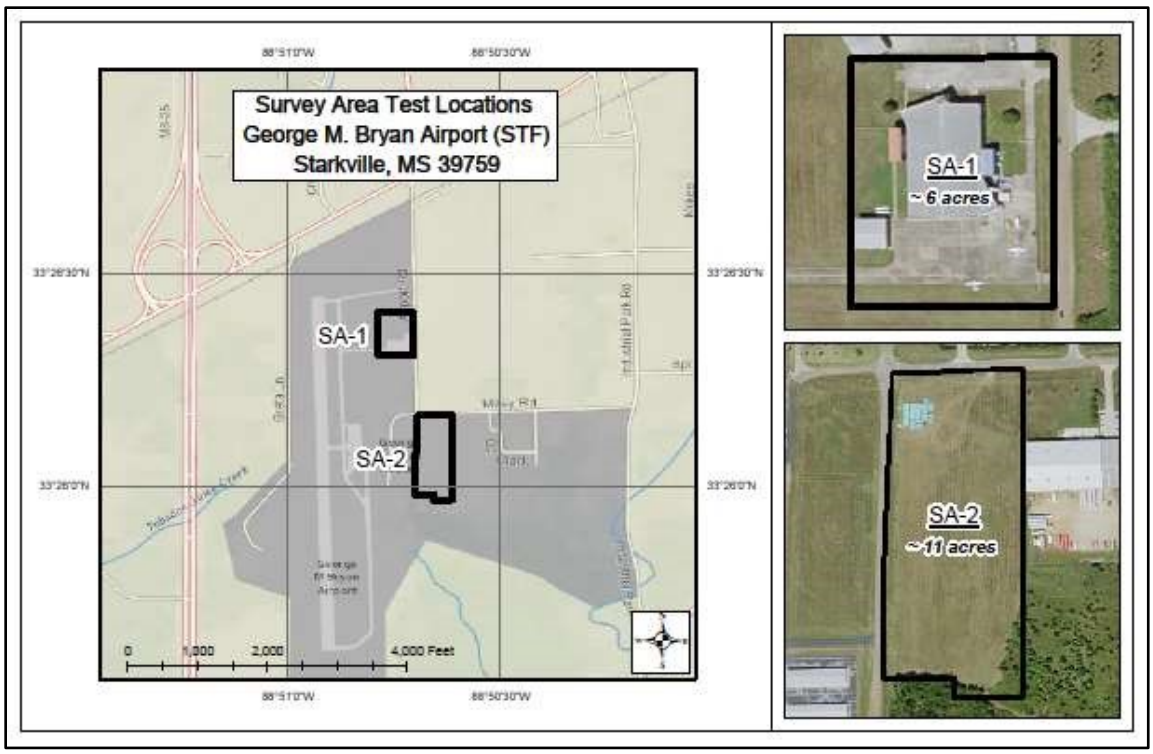

Figure 4.1 Survey Areas Map (SA-1, SA-2)

Survey Area #1 (SA-1) and Survey Area #2 (SA-2) located on the grounds of George M. Bryan Field in Starkville, MS.

SA-1 represents approximately six acres of urban, industrial survey environment with built-up land use features dominating the geographic landscape. Alternatively, SA-2 represents approximately 11 acres of rural, undeveloped survey environment with mostly rangeland land use characteristics. Each survey area provides recognized challenges for the sUAS + SfM survey method. Specifically, SA-1 possess many steep elevation changes and sharp linear features resulting from the built-up landscape. SA-2, on the other hand, is covered in its entirety by short, grassy vegetation. Again, these survey environments were intentionally utilized to allow for accuracy testing of sUAS + SfM derived data across differing landscapes.

In situ survey equipment

For accuracy testing, a Trimble R6 GNSS differential RTK GPS (hereafter Trimble R6) served as the independent means of higher accuracy by which sUAS + SfM survey data were evaluated. Trimble R6 manufacturer specifications show that horizontal and vertical accuracies up to 0.026 ft. (0.008 m.) and 0.049 ft. (0.015 m.), respectively, are achievable using RTK surveying techniques. Therefore, according to FGDC standards, the Trimble R6 system can adequately serve as the independent source of higher accuracy for testing of sUAS + SfM derived survey data in the research experiment. Furthermore, based on manufacturer specifications, the Trimble R6 is clearly capable of achieve geospatial accuracies within the 0.164 ft. "survey-grade" accuracy threshold. This is representative of most professional RTK GPS surveying equipment and provides some context on professional expectations of "survey-grade" instrumentation and corresponding geospatial accuracy.

In situ field methodology

In situ field methods began by establishing the base position of the Trimble R6 in order to collect RTK differential GPS measurements of GCPs and checkpoint locations within both survey areas. National Geodetic Survey (NGS) monument #DJ1746, located nearby on the grounds of George M. Bryan Field, was held as the base position for all RTK differential GPS measurements at both SA-1 and SA-2. This monument serves as the current GPS and vertical control monument for George M. Bryan Field with third-order geodetic control accuracy and FGDC observed network accuracies of 0.0357 ft. (0.0109 m.) horizontally and 0.1266 ft. (0.0386 m.) vertically. The accuracies of NGS monument #DJ1746 shown in entirety in Appendix A, remain in compliance with FGDC

standards for accuracy testing by independent source of higher accuracy. Figure 4.2 below shows the Trimble R6 base station positioned on NGS monument #DJ1746 prior to RTK *in situ* measurement collections at SA-1 and SA-2.

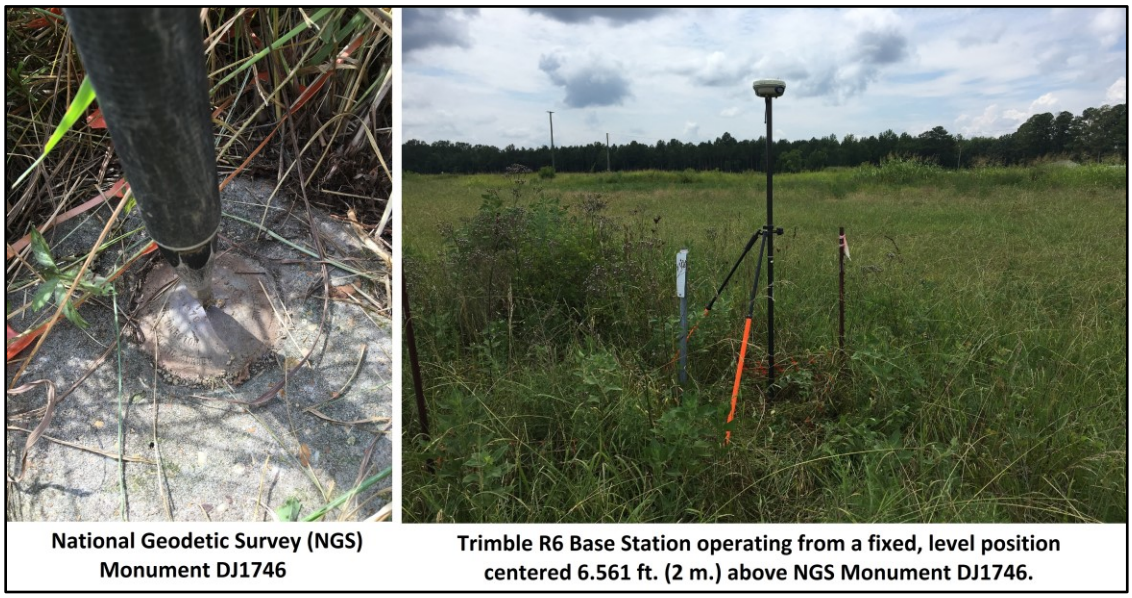

Figure 4.2 NGS Monument DJ1746 and Trimble R6 Base Station

Trimble R6 base station operating from National Geodetic Survey (NGS) Monument DJ1746 as located in the field. Field methodology intended to allow for highest accuracy in real time kinematic (RTK) GPS *in situ* data collection.

With an active base station in place, *in situ* field work continued with the placement and collection of GCPs and checkpoints within SA-1 and SA-2. GCPs were needed to promote accurate georectification of sUAS derived survey data. However, these GCPs could not be used for accuracy assessment purposes as survey data accuracy is biased in GCP locations after georectification. Alternatively, checkpoints were exclusively needed for accuracy assessment purposes. Since checkpoints are not used for

survey data georectification, these points provide unbiased ground-truth positions for use in accuracy assessment of sUAS derived survey data.

Geospatial location measurements for all points were recorded via Trimble R6 as x, y, and z coordinate values in the Geoid 12B earth model, North American Datum of 1983 (NAD83), State Plane – Mississippi East coordinate system (SP – MS East), in U.S. Survey Feet units (ft.). This specific geoid, datum, and coordinate system has been used intentionally as this geospatial framework is accepted in traditional surveying practices to yield the highest local accuracy in the geographic region of this research. Furthermore, the use of U.S. Survey Feet measurement units has also been done intentionally as this is the most common unit of measure for U.S. surveying applications and is often required for geospatial data use by many private and governmental entities.

***In situ* field methods for survey area #1 (SA-1)**

For SA-1, a total of 12 GCPs and 20 checkpoints were placed and collected using the Trimble R6. GCPs were placed systematically across SA-1 with one of the GCPs being intentionally placed on the roof of a built-up structure to promote accurate SfM reconstruction of the survey area. The total number and placement of GCPs for SA-1 represents a frequency distribution of approximately 1 GCP per 0.5 acres of survey area. Checkpoints were placed according to FGDC standards which require that "A minimum of 20 checkpoints shall be tested", and that the checkpoints be "distributed to reflect the geographic area of interest and the distribution of error in the dataset" (FGDC 1998). Since no established distribution of error was available for SA-1 at the time of research, half of the checkpoints (10) were placed on, or adjacent to, built-up surface features which were expected to exhibit higher error based on known SfM photogrammetric

challenges (Ruzgiene et al 2015, Ishiguro et al. 2016, Jaud et al. 2016). The remaining checkpoints (10) were distributed to account for the cumulative reaches of SA-1 per FGDC standards (FGDC 1998).

It is worth noting the quantity of GCPs used here is rather extensive and not necessarily representative of traditional surveying and photogrammetric methods. In traditional practice, as few GCPs as possible are placed during *in situ* fields methods to achieve the desired georectification accuracy. This is because *in situ* GCP placement and collection often requires significant time and effort, sometimes in very hazardous geographic environments. Since these considerations were not a factor in this research, GCPs were placed in an intentionally high frequency in order to provide optimal parameters for accurate georectification (James et al. 2017, Agüera-Vega et al. 2017). Additionally, the use of 20 checkpoints, while minimal by FDGC standards, remains in compliance with required accuracy testing standards. Furthermore, this number of checkpoints was expected to be sufficient given the relatively limited geographic scope of SA-1. Figure 4.3 below demonstrates GCP placement and *in situ* collection via Trimble R6 GNSS Rover in the field at SA-1. Additionally, Figure 4.4 below represents all GCP and checkpoint locations as collected for SA-1.

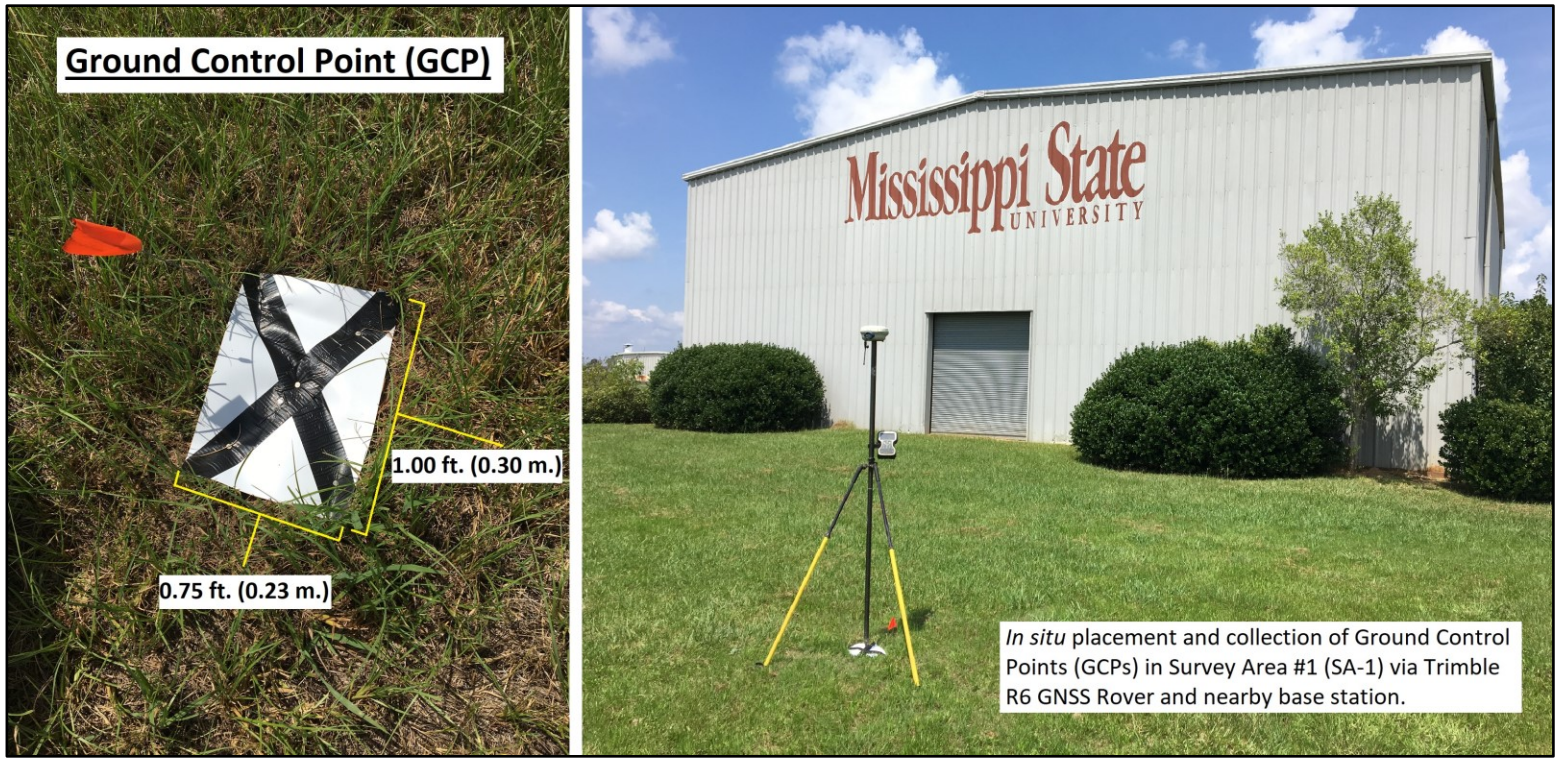

Figure 4.3 Ground control point (GCP) placement

All ground control points (GCPs) placed in SA-1 and SA-2 measure 0.75 ft. x 1.00 ft., with 0.16 ft.-thickness "X" contrast marking. *In situ* GPS measurement with Trimble R6 Rover made at the nail center-point of each GCP.

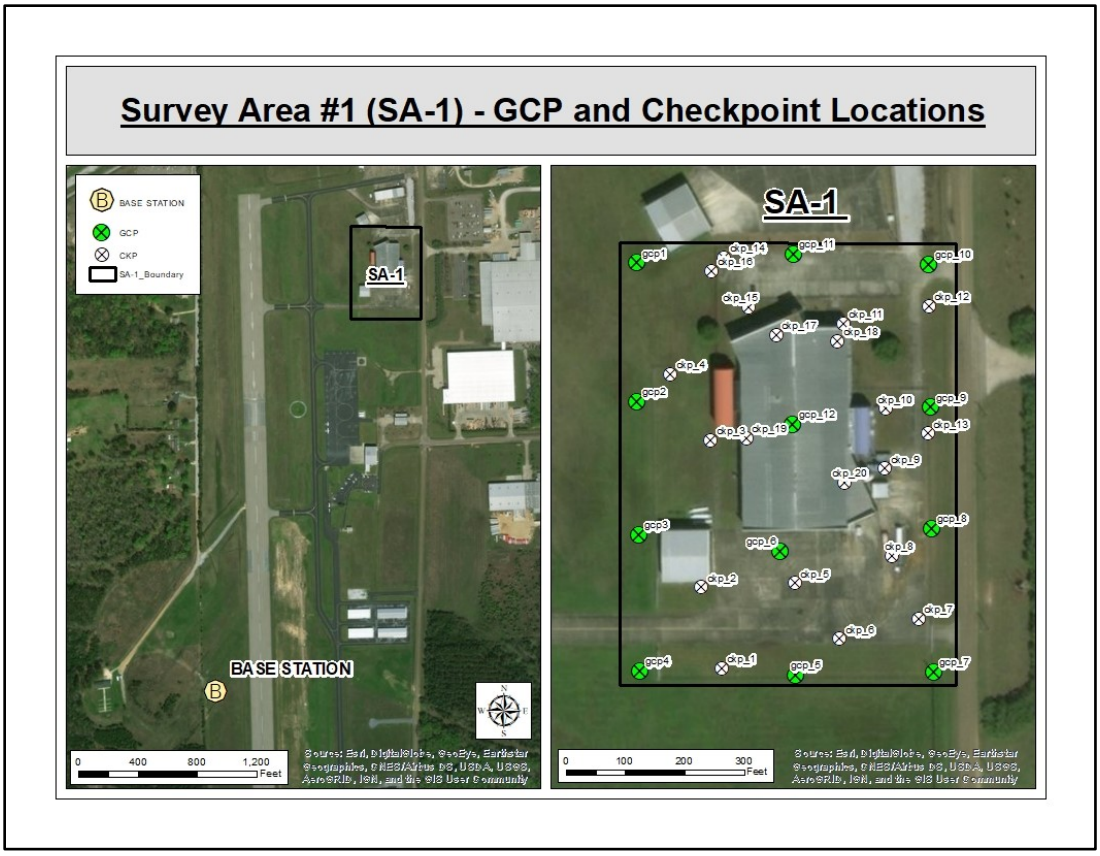

Figure 4.4 Survey Area #1 (SA-1) – GCPs and Checkpoints

SA-1 Ground Control Points (GCP) for georectification, checkpoints (ckp) for accuracy testing, and Trimble R6 Base Station relative to SA-1 for *in situ* data collection.

In situ field methods for survey area #2 (SA-2)

For SA-2, a total of 21 GCPs and 20 checkpoints were placed and collected using the Trimble R6. GCPs were again placed systematically across the entire survey area at an approximate frequency distribution of 1 GCP per 0.5 acres. The additional GCPs used here, in comparison to SA-1, are the result of maintaining this same frequency distribution across the larger geographic acreage of SA-2. Checkpoints within SA-2 were

likewise placed according to the FGDC standards mentioned above. Since the land cover of SA-2 is nearly uniform, and no record of error distribution was available at the time of research, checkpoint locations were selected in an effort to best represent the geographic area of SA-2 per FGDC standards.

The number of GCPs used in SA-2 (21 total) was just as extensive as SA-1 as both survey areas share a GCP distribution of approximately 1 GCP per 0.5 acres. SA-2 possess more total GCPs simply as a result of its larger geographic size. Again, the extensive use of GCPs in both survey areas was done intentionally to optimize georectification accuracy of all sUAS derived survey data. As with SA-1, the FDGC minimum of 20 checkpoints were again used for accuracy testing of SA-2 survey data in compliance with FGDC accuracy testing standards. Again, this number of checkpoints was expected to be completely sufficient for accuracy testing across the geographic scope of SA-2. Figure 4.5 below shows an example of checkpoint(s) used in both SA-1 and SA-2, while Figure 4.6 shows all GCP and checkpoint locations collected during *in situ* field methods for SA-2.

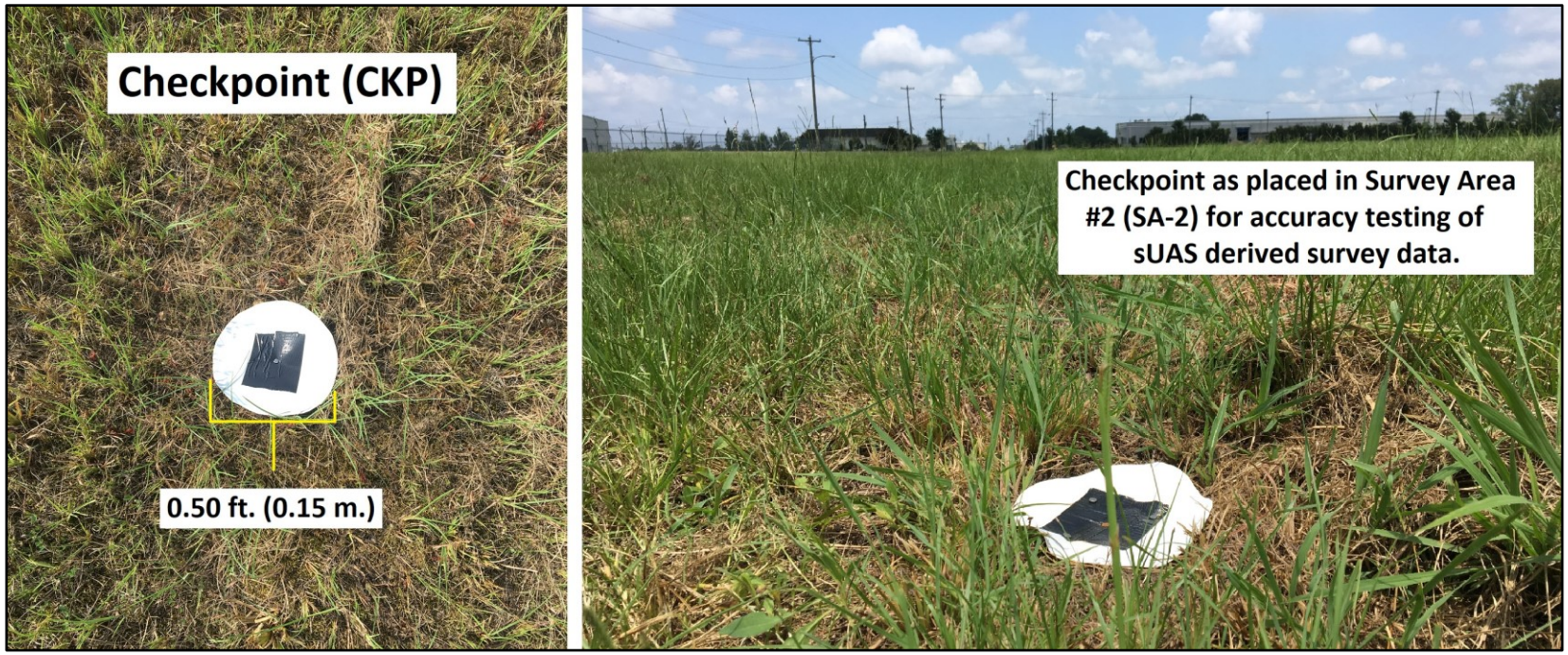

Figure 4.5 Checkpoint placement

All checkpoints placed in SA-1 and SA-2 measure 0.50 ft. (0.15 m.) in diameter with ~0.33 ft. (0.10 m) contrast square marking. *In situ* GPS measurement with Trimble R6 Rover made at the nail center-point of each checkpoint.

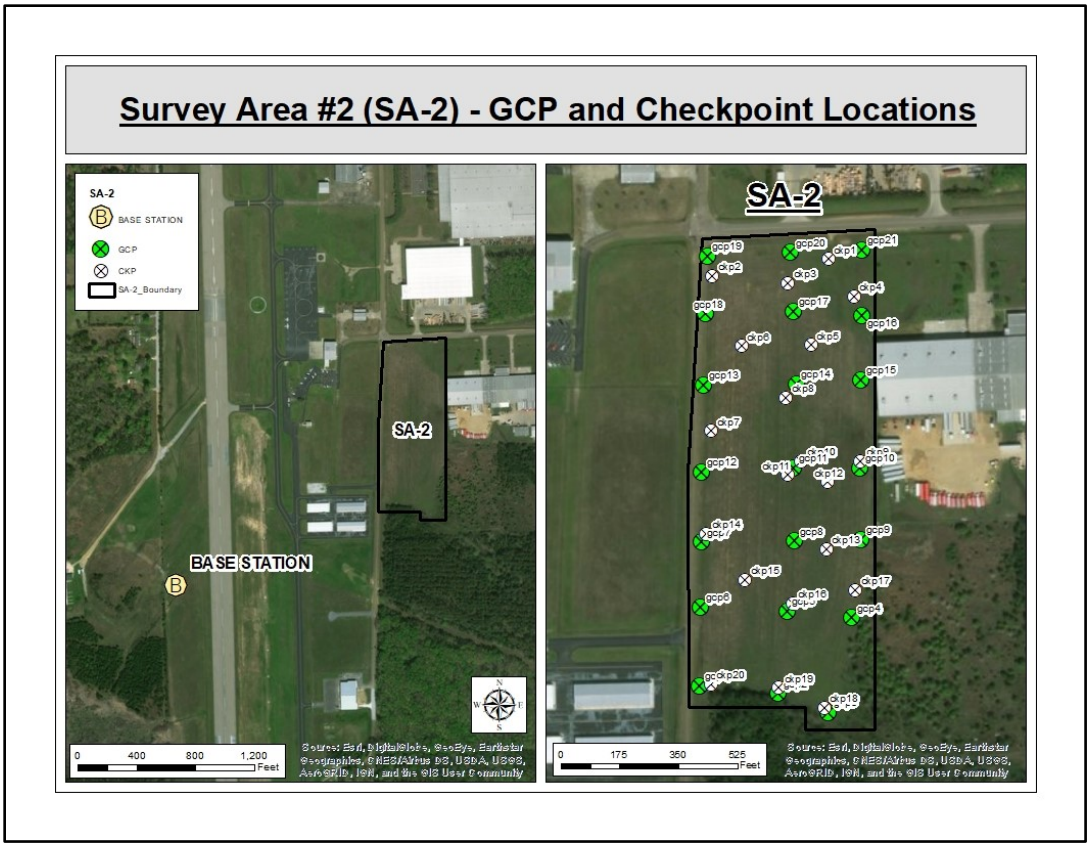

Figure 4.6 Survey Area #2 (SA-2) – GCPs and Checkpoints

SA-2 ground control points (gcp) for georectification, checkpoints (ckp) for accuracy testing, and Trimble R6 Base Station relative to SA-2 for *in situ* data collection.

Remote sensing survey equipment

Remote sensing survey equipment for this research effort includes two modern prosumer sUAS platforms. The specific make and model of these platforms includes the DJI Phantom 3 Advanced and the DJI Phantom 4 Pro, hereafter referred to as P3A and P4P respectively.

The P3A model was released in April 2015 and represents the mid-level platform between the "Standard" and "Professional" Phantom 3 models. The P3A possesses a 12-megapixel RGB camera payload powered by a 1/2.3" complementary metal-oxide semiconductor (CMOS) sensor with an electrical rolling-shutter mechanism. For the purpose of this research, the P3A may also serve as a surrogate representation of similar prosumer sUAS platforms including the Phantom 3 Pro and Phantom 4 Standard. These additional platforms deploy a nearly identical payload camera in regards to still image capture, and only possess improved payload capabilities in regards to video capture (higher resolutions and lower frame rates). Since remote sensing data collection and corresponding SfM processing in this experiment utilize only still image data, P3A survey data accuracies observed and presented in this research are expected to be representative of Phantom 3 Pro and Phantom 4 Standard derived survey data accuracies as well.

The P4P model was released in November 2016 and represents the latest modern capabilities of the DJI Phantom prosumer platform series as only cosmetic re-renderings of this platform have been released since. The P4P platform possesses a 20-megapixel RGB camera payload powered by a 1" CMOS sensor and mechanical global-shutter mechanism. Therefore, the P4P utilizes an inherently more capable camera payload than previous Phantom generations. Besides the obvious improvement in megapixel resolution and sensor size, the mechanical global-shutter mechanism is especially important in regards to geospatial applications as previous sUAS rolling-shutter camera payloads have proved troublesome in achieving high-accuracy photogrammetric results (Liang et al. 2008, Albl et al. 2015). For this reason, P4P derived survey data accuracies

were expected to exceed that of the P3A and earlier Phantom generations. Furthermore, for the purpose of this research, the P4P is assumed to represent the latest in modern prosumer sUAS capabilities and derivative survey data accuracies until the release of newer, more capable prosumer sUAS platforms in the near future.

Remote sensing field methodology

Remote sensing field methodologies began with securing the required permissions to perform sUAS operations in the vicinity of George M. Bryan Field. With proper permissions secured, remote sensing data collection flights were planned for both SA-1 and SA-2 using the proprietary Pix4D Capture mobile application installed on an iPhone 6S. The use of Pix4D Capture in planning and conducting remote sensing data collection was a intentional decision as this application allows for streamlined consistency between data collection and SfM processing of remotely sensed digital image data in Pix4D Mapper Pro (discussed further in Chapter 5 – DATA PROCESSING). Furthermore, Pix4D Capture allows for a number of specific, user-defined data collection parameters, such as flight altitude and image overlap, which are integral to resulting survey data accuracy.

Specific data collection parameters

User adjustments were made only to Pix4D Capture data collection parameters which are standard in all sUAS data collection programs and are known to influence SfM processing and resulting survey data accuracy. Adjusted parameters and their exact corresponding values are as follows: Altitude = 300 ft. AGL, Angle of the camera = 90˚, Front overlap = 85%, and Side overlap = 85%. Remaining Pix4D Capture data collection

parameters (those being mostly unique to the Pix4D Capture application) were left at default settings. These parameters and their exact default values are as follows: Look at grid's center = Yes, Picture trigger mode = Fast mode, Drone speed: Normal, White Balance = Auto, and Ignore homepoint = No. All final Pix4D Capture parameters as listed here are shown in the Pix4D Capture interface below in Figure 4.7.

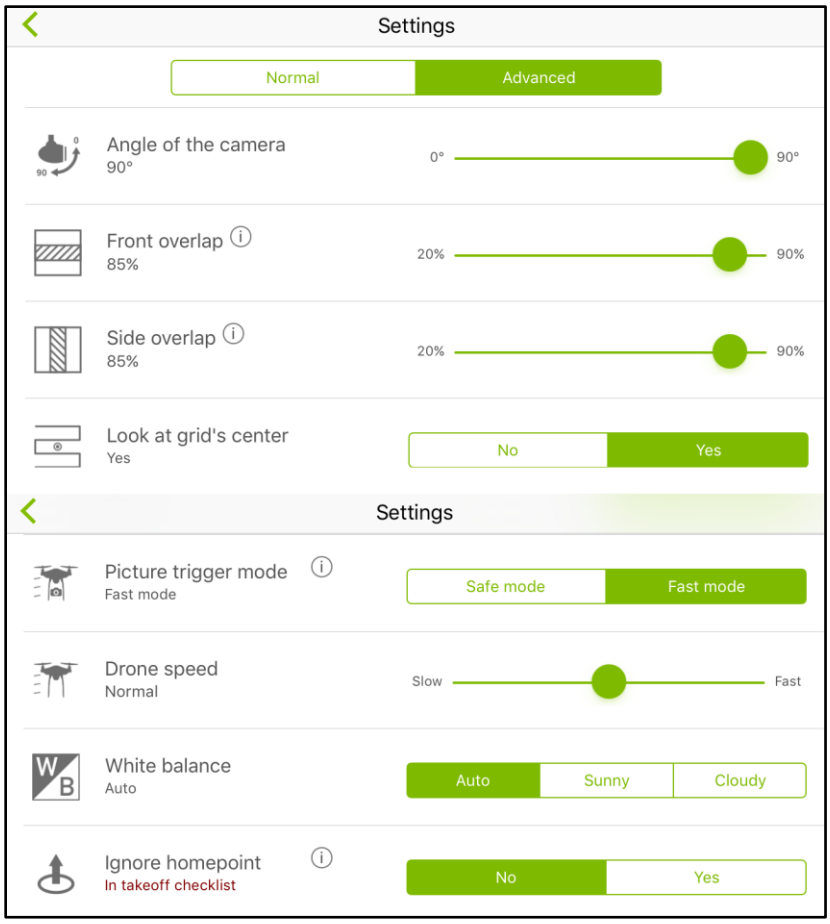

Figure 4.7 Pix4D Capture – Remote sensing data collection parameters

Remote sensing data collection parameters as shown in Pix4D Capture mobile application. All parameters were held constant throughout sUAS remote sensing data collection with both the P3A and P4P, at both SA-1 and SA-2. Not pictured are Altitude = 300 ft. Above Ground Level (AGL). Resulting Ground Sample Distance (GSD) for P3A ~ 4.0 cm. or 0.13 ft. per pixel. Resulting GSD for P4P ~ 2.5 cm. or 0.08 ft. per pixel.

The above Pix4D Capture parameters were held constant for all remote sensing data collection flights with both the P3A and P4P, at both SA-1 and SA-2. The choice to adjust these parameters, or have them remain at default values, was made consciously in an effort to achieve optimal survey data accuracy using only those parameters which are commonly available across all sUAS remote sensing platforms. In doing so, experimental results were intended to be more widely applicable and not specific to the Pix4D Capture application itself. Additionally, the consistent use of these parameters by both sUAS platforms, and at both survey areas, was also intentional as this was meant to reduce the possibility of introducing methodological variables which may have unintentionally affected resulting survey data accuracies. Finally, it is important to again note remote sensing data collection with both sUAS platforms was conducted at 300' AGL. However, as a result of camera payload variations (i.e. improved payload in P4P), resulting Ground Sample Distances (GSD) varied between the two platforms (P3A GSD ~ 4.0 cm. or 0.13 ft. per pixel, P4P GSD ~ 2.5 cm. or 0.08 ft. per pixel).

Remote sensing field methods for survey area #1 (SA-1)

Remote sensing data collection at SA-1 began on July 26, 2017 at approximately 12:21 p.m. to allow for optimal, evenly distributed incident lighting across the built-up landscape. Remote sensing data collection was conducted with all 12 GCPs and 20 checkpoints in place and easily visible. A total of 4 data collection flights were planned, whereby each sUAS platform would perform 2 data collection flights of SA-1. The first flight would perform data collection at a North/South orientation flight path, while the second flight plan would take an East/West orientation. Data collection at these opposing orientations has been shown to benefit SfM processing as the cumulative image dataset

provides additional perspective for SfM feature matching and surface reconstruction (Westoby et al. 2012, Franesco & Remondino 2014, Ishiguro et al. 2016) – especially for built-up surface features like those in SA-1.

P3A data collection was conducted first with the North/South orientation flight taking place from 12:21 p.m. – 12:28 p.m. and yielding 91 JPG digital images. In preparation for launch of the East/West flight plan, the P3A returned a "motors overheated" error. After attempting to cool the P3A for approximately 10 minutes and still receiving this error, the East/West flight plan was scrapped in the interest of safety. Therefore, only the 91 JPG images collected during the first flight were utilized in later SfM processing and survey data generation for the P3A at SA-1. Fortunately, this represents the only instance of instrumentation error during all remote sensing data collection efforts.

P4P remote sensing data collection at SA-1 commenced with the North/South orientation flight from 12:40 p.m. – 12:50 p.m. yielding 120 JPG digital images. This flight was immediately followed by the East/West orientation flight from 12:55 p.m. – 1:06 p.m. yielding 121 JPG digital images. Therefore, between the two flights, a cumulative remote sensing dataset of 241 JPG digital images was achieved for later SfM processing and survey data generation for the P4P at SA-1. Figure 4.8 below shows both P4P flights in the Pix4D Capture user interface as conducted at SA-1.

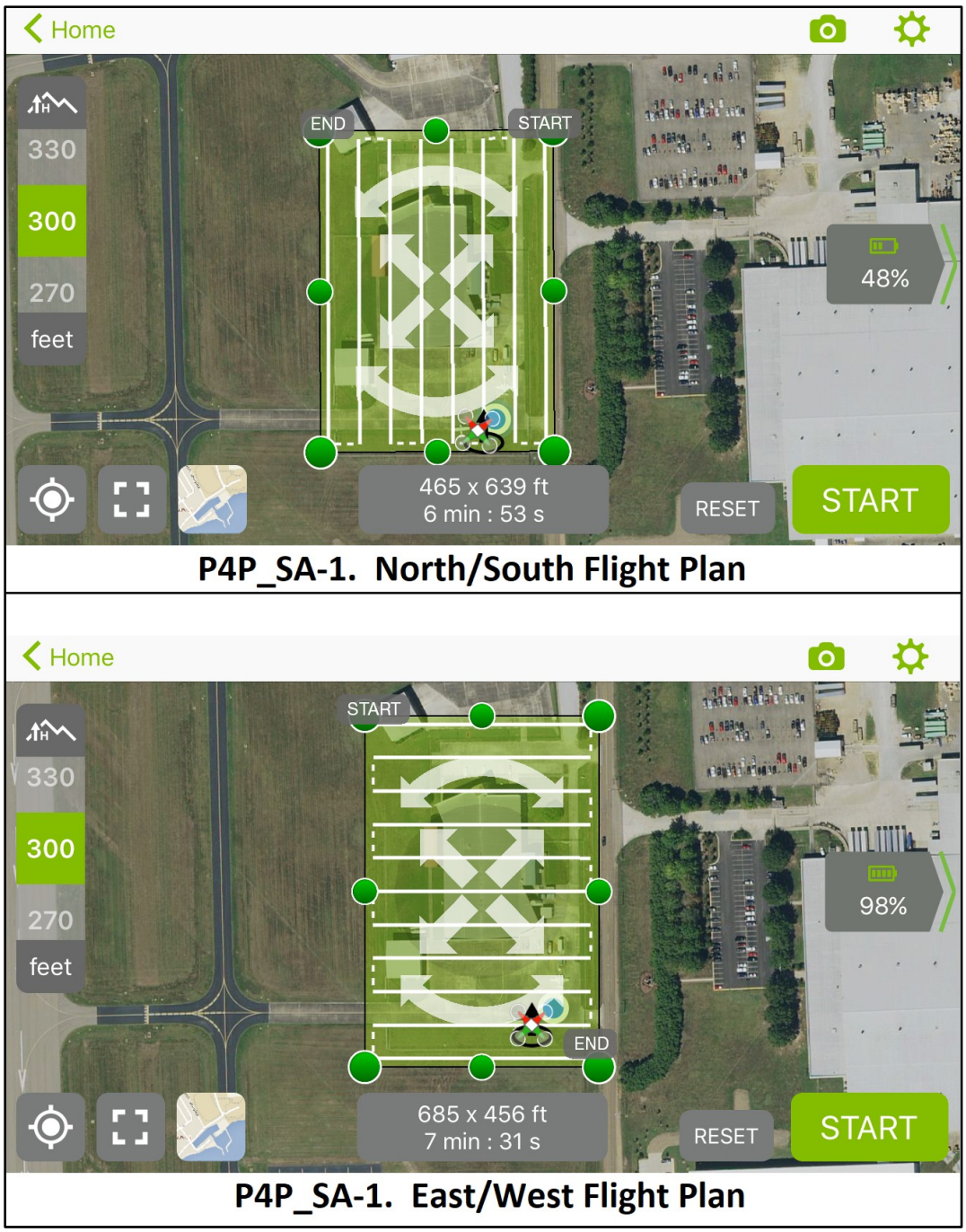

Figure 4.8 Flight Plans – P4P at Survey Area #1 (SA-1)

P4P flight plans (North/South and East/West) as conducted during remote sensing data collection at SA-1 on July 26, 2017. Perpendicular flight plans were intended to aid later Structure-from-Motion (SfM) processing and reconstruction of SA-1 survey data.

Remote sensing field methods for survey area #2 (SA-2)

Remote sensing data collection for SA-2 was conducted in the late morning hours of July 26, 2017 prior to remote sensing data collection at SA-1. The choice to start remote sensing data collection at SA-2 was intentional as the land-cover of this survey area was far less subject to uneven incident lighting and shadowing than SA-1. A total of 4 data collection flights were conducted, again with each sUAS platform performing 2 data collection flights utilizing the North/South and East/West flight paths.

P4P remote sensing data collection commenced first with the North/South data collection flight at approximately 10:35 a.m. – 10:49 a.m. and yielding 279 JPG digital images. Immediately following this flight, the P4P East/West flight was conducted from approximately 11:03 a.m. – 11:17 a.m. and yielded 240 JPG digital images. Therefore, between the two flights, a cumulative remote sensing dataset of 519 JPG digital images was achieved for SfM processing and survey data generation for the P4P at SA-2. Figure 4.9 below shows both P4P flights in the Pix4D Capture user interface as conducted at SA-2.

Figure 4.9 Flight Plans – P4P at Survey Area #2 (SA-2)

P4P flight plans (North/South and East/West) as conducted during remote sensing data collection at SA-2 on July 26, 2017. Again, perpendicular flight plans meant to aid later Structure-from-Motion (SfM) processing and reconstruction of SA-2 survey data.

Immediately following the P4P flights, P3A remote sensing data collection commenced at SA-2 beginning with the East/West flight at approximately 11:24 a.m. – 11:36 a.m. and yielding 153 JPG digital images. Next, P3A remote sensing data collection continued with the North/South flight at approximately 11:46 a.m. – 11:57 a.m. which yielded 161 JPG digital images. Therefore, between the two flights, a cumulative remote sensing dataset of 314 JPG digital images was achieved for SfM processing and survey data generation for the P3A at SA-2.

Meteorological considerations

Given the known implications of meteorological conditions on sUAS operations and derivative data accuracies (Remondino et al. 2011, Colomina & Molina 2014), this research aimed to assess sUAS derived survey data collected in favorable meteorological conditions. For the purpose of this research, favorable meteorological conditions were considered to be 1) minimal wind speed, ideally < 5 mph, and 2) minimal cloud cover, ideally < 1/8 opaque cloud sky cover. Favorable meteorological conditions were scouted using National Weather Service (NWS) forecasts and eventually led to remote sensing data collection on July 26, 2017. Meteorological conditions were recorded in the field during remote sensing data collection and later verified via NWS weather observations as shown in Appendix B.

Based on these official NWS meteorological observations, wind speeds during all remote sensing data collection flights were indicated as “Calm”, which is defined by the NWS as “A weather condition when no air motion (wind) is detected”. Therefore, all sUAS remote sensing data collection was indeed conducted in favorable meteorological conditions in regards to wind. Similarly, NWS meteorological observations also

demonstrate favorable Weather and Sky Conditions as “Clear” and “SKC” (skies clear), respectively, for most remote sensing data collection operations. However, these favorable conditions ceased sometime around 12:45 p.m. as this specific NWS observation reports weather conditions of “Mostly Cloudy”, which is defined by the NWS as up to 5/8 sky coverage by opaque clouds. The timing of this specific NWS observation and corresponding meteorological conditions coincides with the timing of P4P remote sensing data collection at SA-1 at approximately 12:40 p.m. – 1:06 p.m. Examination of the P4P digital image data collected at SA-1 during this time corroborates the NWS observation as regions of cloud-obstructed, uneven incident lighting are visible as shown in Figure 4.10 below. Therefore, it must be noted that P4P derived survey data at SA-1 was collected in less-than-favorable meteorological conditions in regards to cloud cover.

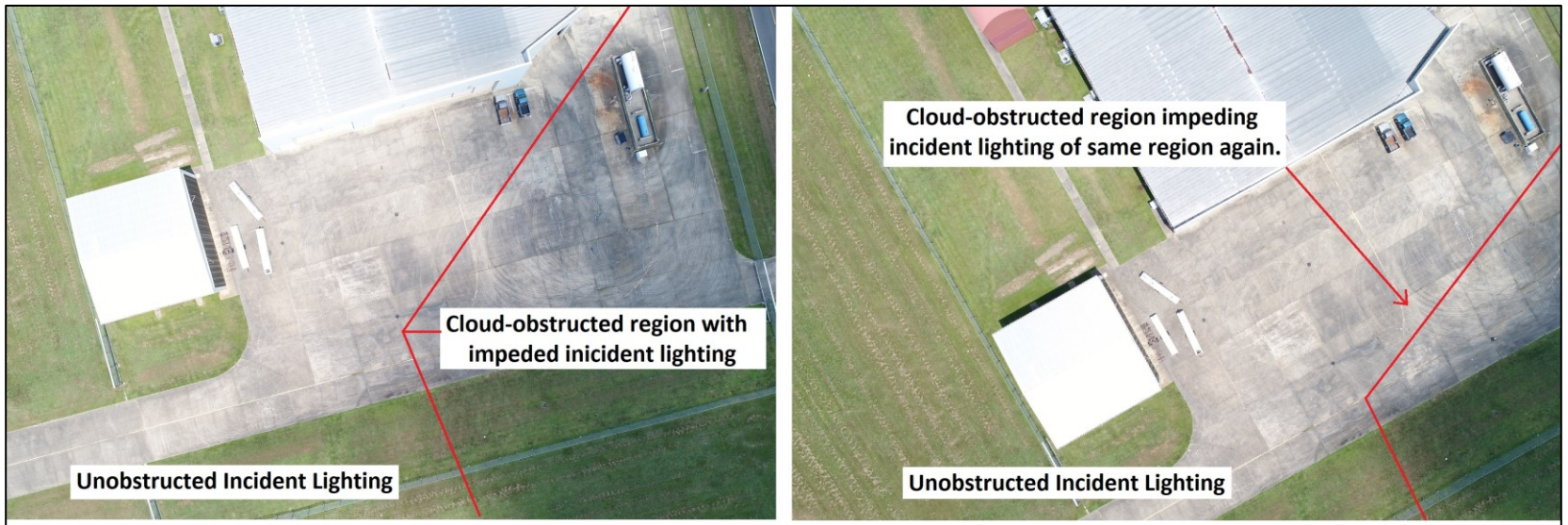

Figure 4.10 Cloud-obstructed incident lighting - P4P remote sensing data at SA-1

Sporadic cloud cover represents an unfavorable condition for sUAS remote sensing as uneven lighting can contribute to erroneous SfM reconstructions. Cloud cover during P4P remote sensing data collection of SA-1 cannot be ruled out as a potential source of error in later geospatial analysis and results discussion for this dataset.

CHAPTER V

DATA PROCESSING METHODS

With field data collection complete, research efforts immediately shifted to processing of *in situ* and remote sensing data and resulting survey data generation. Trimble R6 *in situ* data included x, y, and z coordinates (NAD 1983 State Plane Mississippi East FIPS 2301 Feet) in comma-separated value format (.csv) for all GCP and checkpoint positions in both survey areas. Additionally, Trimble R6 *in situ* data also included base station receiver files (.T02) which were used to verify base station positional accuracy on NGS Monument DJ1746 through the NGS Online Positioning User Service (NGS.OPUS 2018). All sUAS remotely sensed JPG image data were transferred to a field laptop post-flight, and later transferred from the field laptop to the primary data processing laptop. Image data was then organized according to sUAS platform and survey area (e.g. P3A_SA-1, P4P_SA-2) for processing. Lastly, SfM processing and survey data generation was then carried out for each image dataset using Pix4D Mapper Pro.

Pix4D mapper pro

Pix4D Mapper Pro, a proprietary SfM photogrammetry software, was used exclusively for all SfM processing of sUAS remote sensing data (Pix4D Mapper Pro – Version 3.3.29). Pix4D Mapper Pro performs all the fundamental processes of SfM photogrammetry including feature matching, bundle-block adjustment, surface

reconstruction, and geometric transformation, and also has numerous platform-specific processing capabilities as well. Also, as previously mentioned, Pix4D Mapper Pro is strategically compatible with the Pix4D Capture mobile application used during sUAS remote sensing data collection. This compatibility allows for the automation of vital remote sensing processes including camera payload calibration and metadata collection in exchangeable image file format (.EXIF). Therefore, Pix4D Mapper Pro was intentionally selected for SfM processing and survey data generation as it allows for strategic compatibility across data collection and processing methodologies. Furthermore, Pix4D Mapper Pro was also intentionally selected for its broad applicability as one of the most common, professionally-used SfM photogrammetry software solutions.

Specific processing parameters

Initial processing

Once an image dataset and its corresponding metadata are defined, "Initial Processing" represents the first SfM processing step of Pix4D Mapper Pro. During Initial Processing Pix4D Mapper Pro first computes keypoints (i.e. matching points) within stereoscopic image subject matter. These keypoints are then utilized in conjunction with proprietary feature matching algorithms to identify additional feature matches throughout the image dataset. From these matches, Pix4D Mapper Pro can conduct fundamental SfM processes including Automatic Aerial Triangulation (AAT) and Bundle Block Adjustment (BBA). At the conclusion of Initial Processing a sparse point cloud reconstruction, composed of initial "Tie Points", is generated and stored within the Pix4D Mapper Pro project (.p4d). These initial tie points can be analyzed within Pix4D Mapper Pro, or manually exported for use in other programs. While the density of initial tie

points is recognizably sparse compared to fully-processed SfM point clouds, they succeed in providing useful 3D point data in much smaller files, which are more easily manageable in non-SfM software solutions such as ESRI's ArcGIS software suite. Specific data processing parameters for Initial Processing are provided below in Figure 5.1.

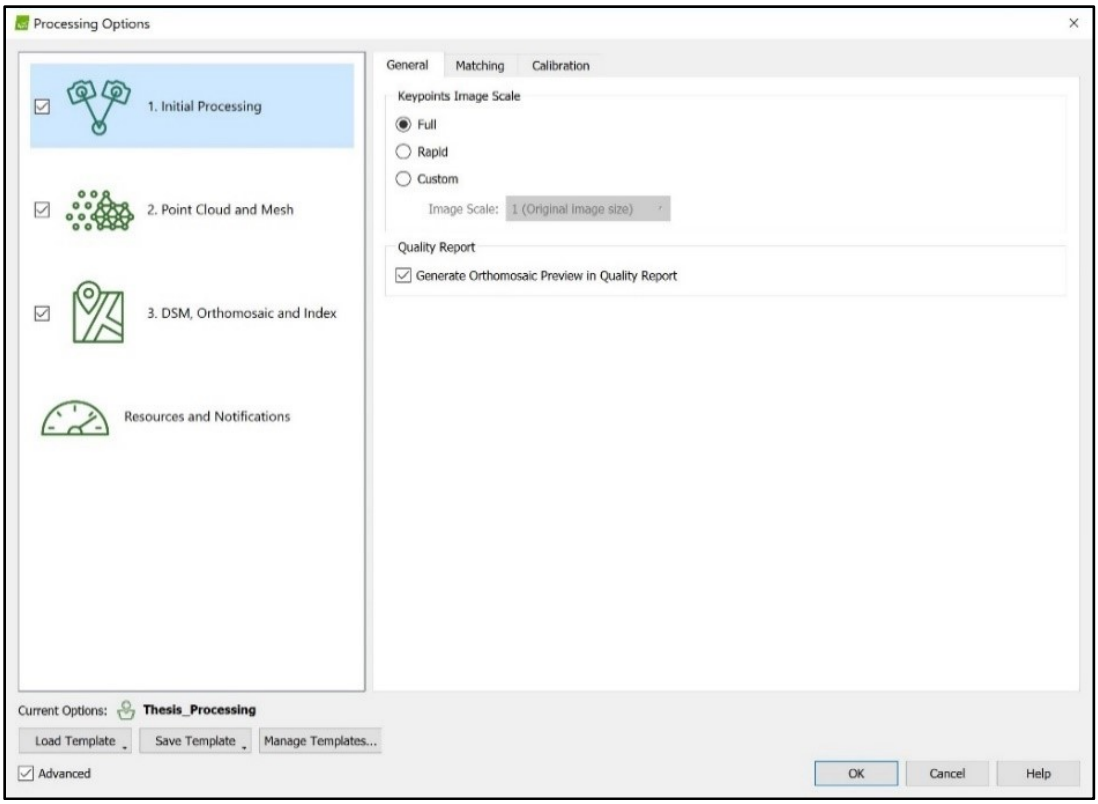

Figure 5.1 Pix4D "Initial Processing" Parameters

Initial Processing – General tab and associated settings.

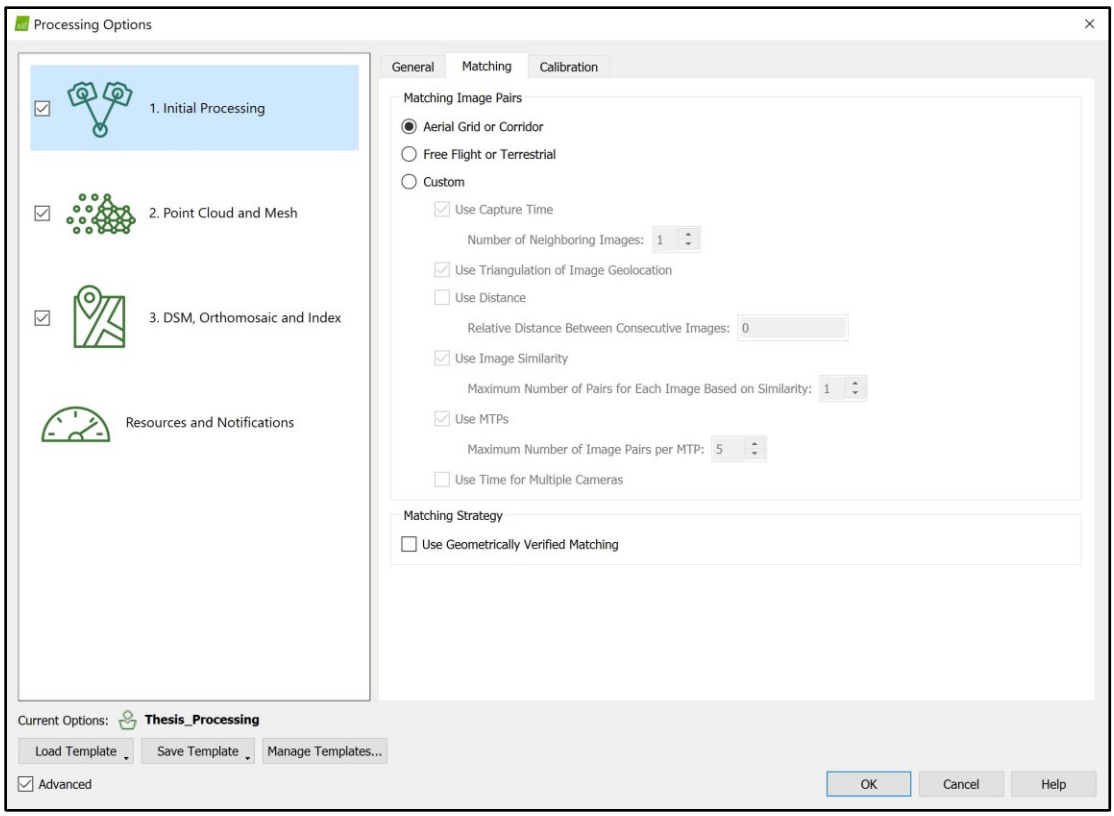

Figure 5.1 (continued)

Initial Processing – Matching tab and associated settings.

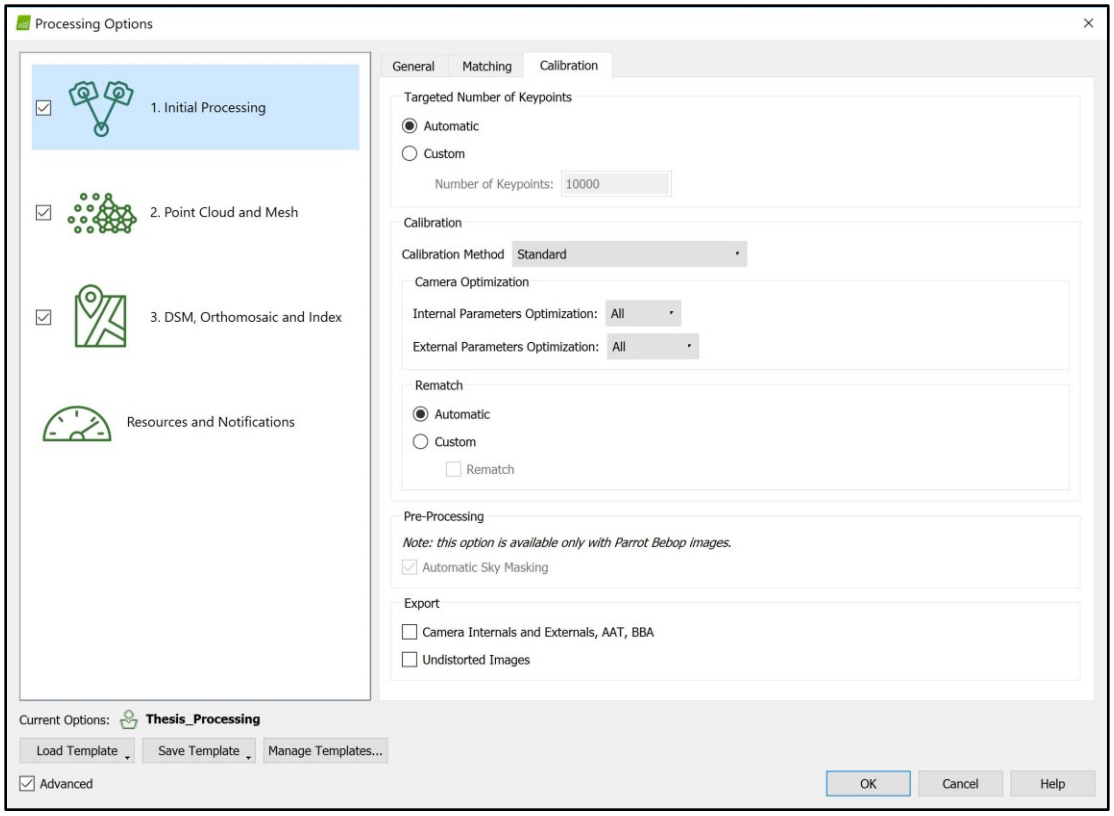

Figure 5.1 (continued)

Initial Processing – Calibration tab and associated settings.

Point cloud generation

After Initial Processing, "Point Cloud and Mesh" represents the second SfM processing step of Pix4D Mapper Pro. The name of this step refers to the derivative survey data which is generated and exported at the end of processing. For this step, survey data include the full density point cloud and 3D textured mesh model. Thesis research focused more-so on the full density point cloud survey data generated in this step as these data are more commonly suited for professional surveying applications than the 3D textured mesh data.

During Point Cloud and Mesh processing, Pix4D Mapper Pro builds upon the completed Initial Processing step to generate a fully-processed point cloud dataset with significantly higher point density. Pix4D's online support documentation provides a simple explanation that Point Cloud and Mesh processing "increases the density of 3D points of the 3D model computed in step 1. Initial Processing". After processing, resulting point cloud data are automatically exported to a pre-designated file location, and stored within the Pix4D Mapper Pro project. This differs slightly from the initial tie points data which must be manually exported if desired. Additionally, full density point cloud data are also stored in a separate Table of Contents layer within Pix4D Mapper Pro from the initial tie points data. These differences are likely due, in part, to the notion that full density point cloud data are more comprehensive (and thereby more valuable) than sparse point data such as the initial tie points. Specific data processing parameters used for step two, Point Cloud and Mesh, are provided in Figure 5.2 below.

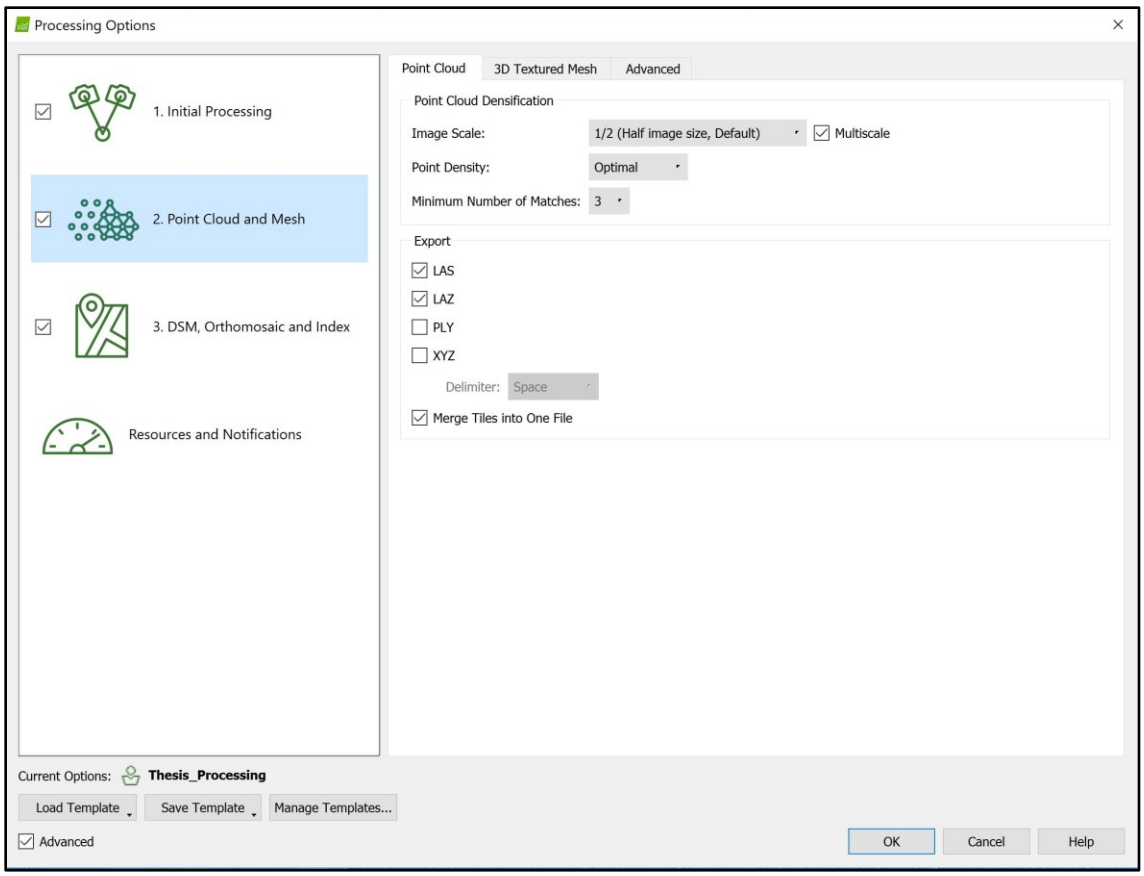

Figure 5.2 Pix4D “Point Cloud and Mesh” Parameters

Point Cloud and Mesh – Point Cloud tab and associated settings.

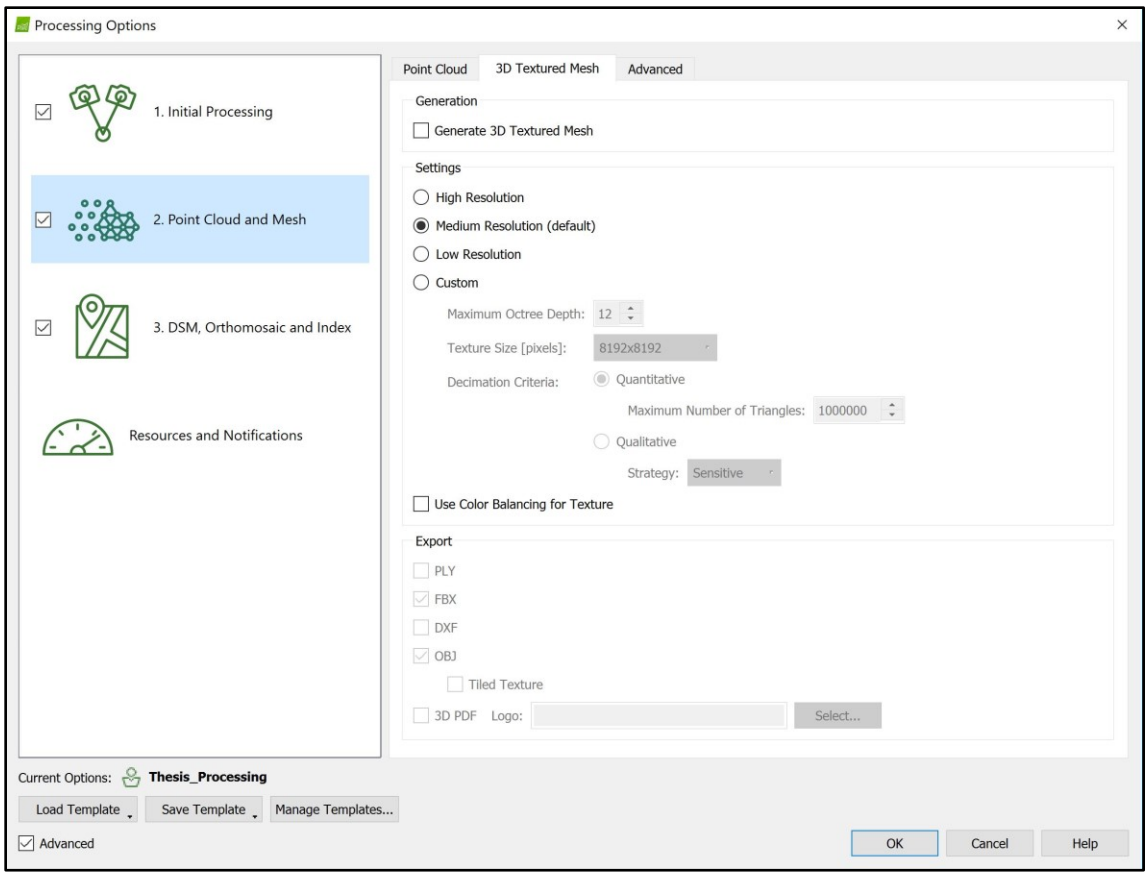

Figure 5.2 (continued)

Point Cloud and Mesh – 3D Textured Mesh tab and associated settings.

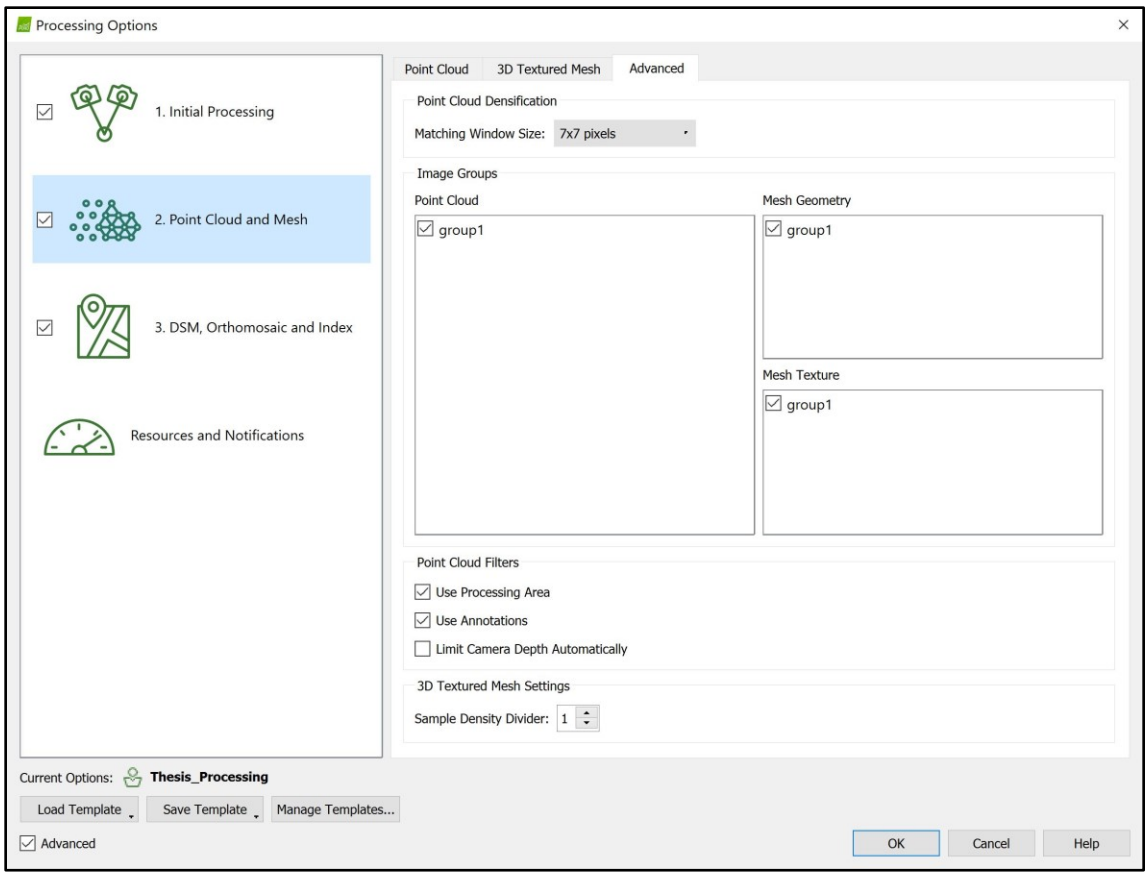

Figure 5.2 (continued)

Point Cloud and Mesh – Advanced tab and associated settings.

Raster data generation

"DSM, Orthomosaic and Index" represents the third and final SfM processing step of Pix4D Mapper Pro. The name is once again indicative of the step's resulting survey data generated at the end of processing. For this step, survey data includes two raster datasets (DSM and aerial imagery orthomosaic) and an index of associated values. Thesis research focused more-so on the DSM raster generated in this processing step as it

contains elevation values (z coordinates) for accuracy testing. However, aerial imagery orthomosaics were still generated in this step for visual aid in Appendices C – F.

During DSM, Orthomosaic and Index processing, Pix4D Mapper Pro now interpolates between the 3D points of the dense point cloud from the previous step to generate resulting DSM raster data. Two methods of interpolation, Inverse Distance Weighting (IDW) and Triangulation (Delauney), are available for this processing step. The IDW interpolation method was utilized for DSM data generation because 1) IDW is the default interpolation option within Pix4D Mapper Pro, 2) IDW was expected to achieve higher accuracy in DSM data than the Triangulation method, and 3) Triangulation interpolation method is intended to offer faster processing times for reconstruction of simple, flat survey areas per Pix4D technical support.

It is important to acknowledge the specific weighting of the IDW interpolation used in Pix4D Mapper Pro is unknown. This is because Pix4D uses a proprietary interpolation algorithm specialized to interpolate between the millions of sampled point locations provided by the point cloud survey data. Without the exact weight values, very little can be speculated about the IDW interpolation method. Nonetheless, Pix4D technical support documentation shows IDW to be the preferred interpolation method when processing time is a non-factor. Full processing parameters for this step, including interpolation method as discussed here, are shown in Figure 5.3 below.

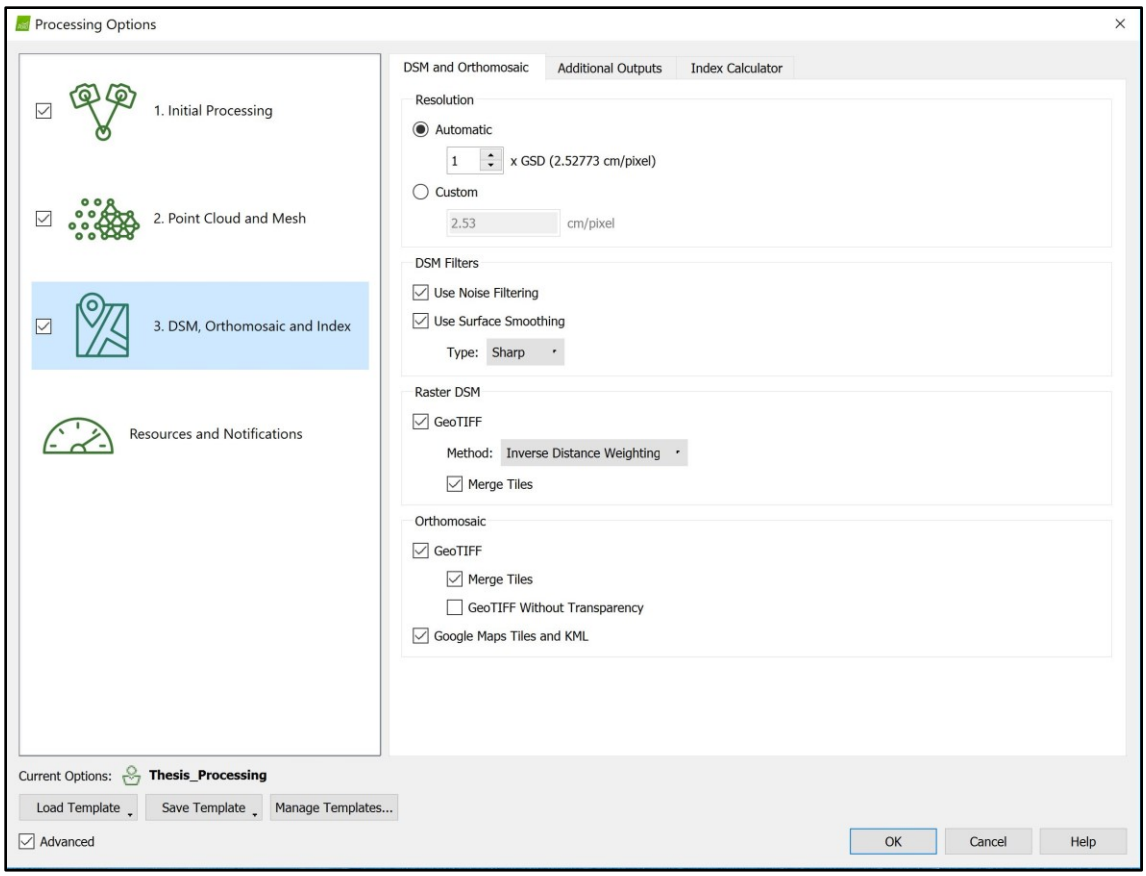

Figure 5.3 Pix4D "DSM, Orthomosaic and Index" Parameters

DSM, Orthomosaic, and Index – DSM and Orthomosaic tab and associated settings.

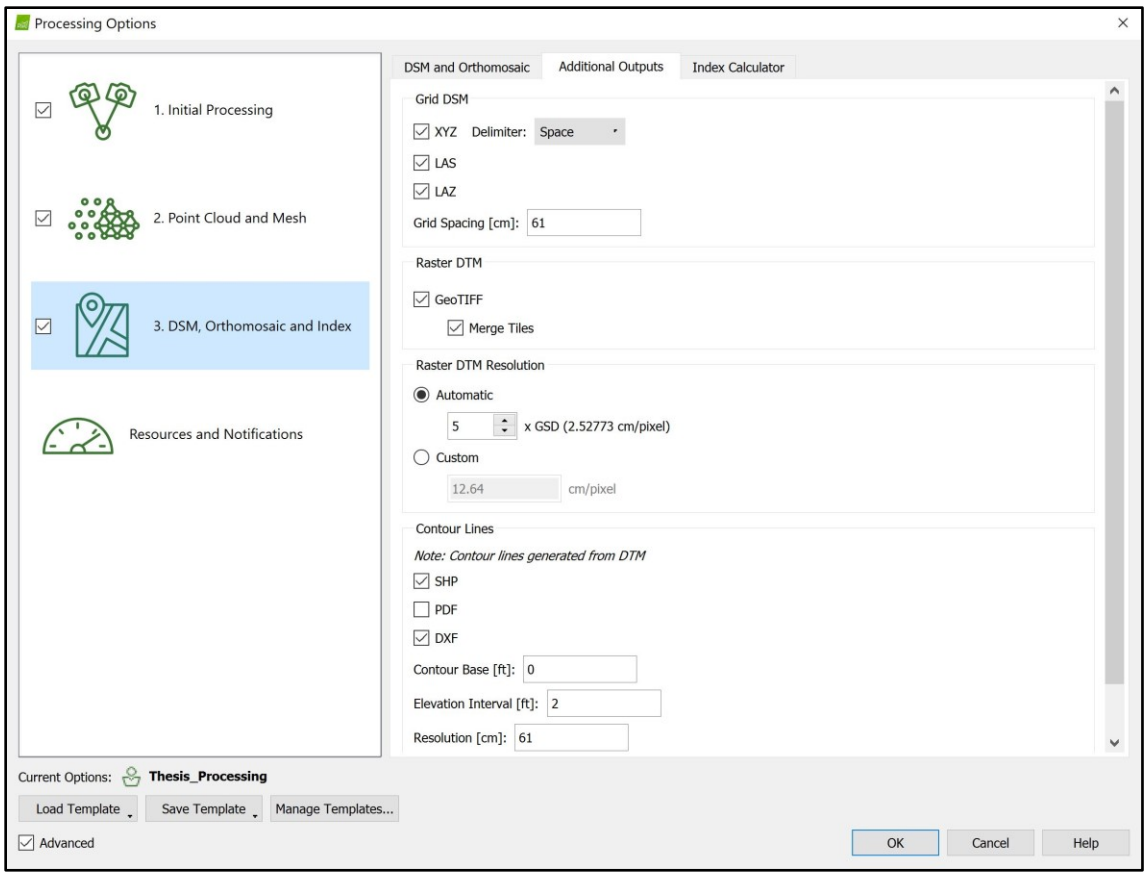

Figure 5.3 (continued)

DSM, Orthomosaic and Index – Additional Outputs tab and associated settings.

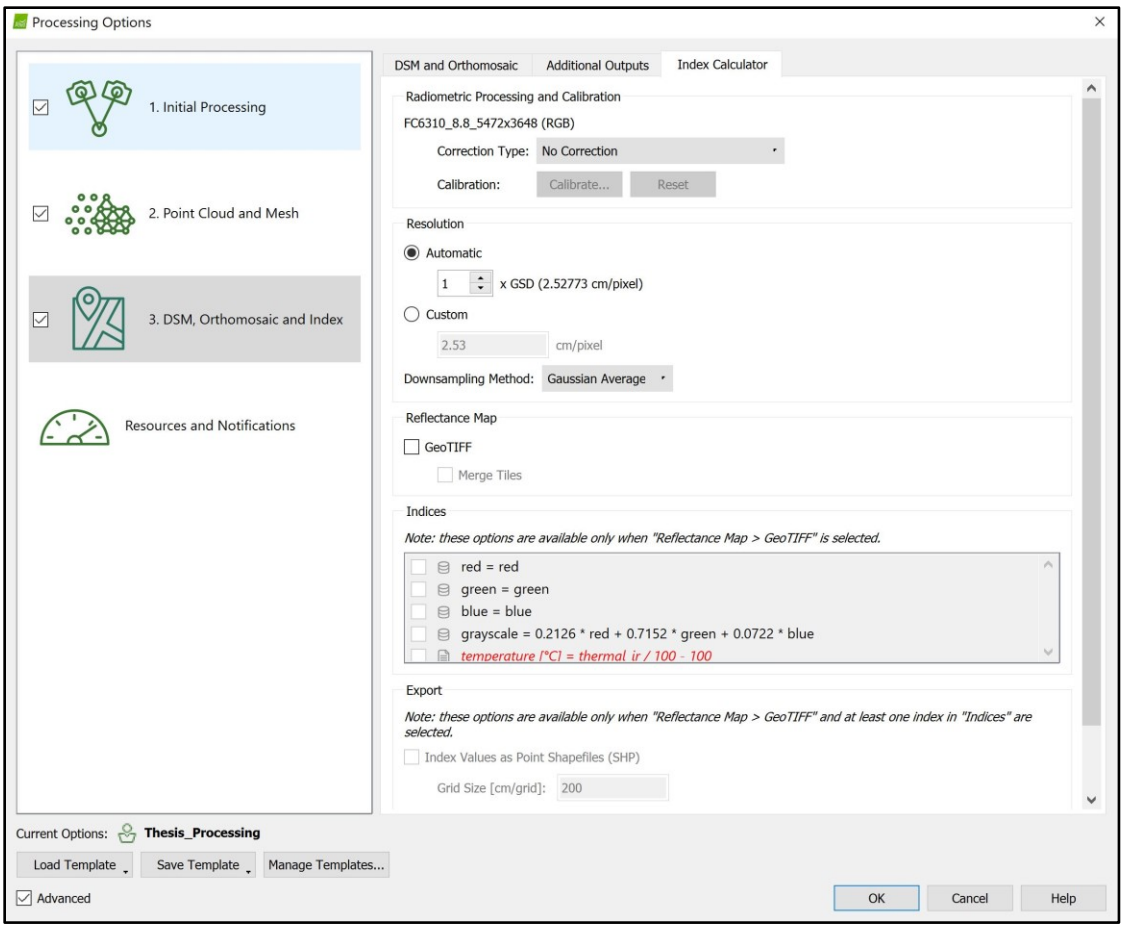

Figure 5.3 (continued)

DSM, Orthomosaic and Index – Index Calculator tab and associated settings.

In situ data incorporation

As previously mentioned, *in situ* data incorporation represents a pivotal consideration of SfM processing. This is especially true of SfM processing and data generation for high-accuracy geospatial applications. *In situ* data for these applications must accurately, effectively georectify SfM derived datasets and assess their resulting accuracy.

GCP position *in situ* data plays an active role in SfM processing by serving as points of known location for data georectification. Without GCPs, SfM reconstruction data can still be processed into a projected coordinate system, however, resulting geospatial accuracy is known to be exceptionally poor when doing so. Furthermore, research has shown that data accuracy in SfM derived datasets can be improved through optimal GCP incorporation (Agüera-Vega et al. 2017, James et al. 2017, Molina et al. 2017). Therefore, the GCP methodology used in this research was intended to be optimal for achieving the highest accuracy in SfM derived survey data.

Alternatively, checkpoint position *in situ* data plays a passive role and are not directly utilized during SfM processing. Instead, these points are used as benchmark ground-truth positions for accuracy assessment of sUAS + SfM derived survey data. Since GCPs are utilized for georectification, SfM reconstruction accuracy is generally biased in regions of near proximity to GCPs (e.g. Tonkin et al. 2014, Tonkin & Midgley 2016). Therefore, checkpoints are required (minimum of 20 by FGDC Standards) to serve as unbiased benchmark positions for accuracy testing (FGDC 1998). The details of GCP and checkpoint implementation in Pix4D Mapper Pro are discussed in the following sections.

Ground control point (GCP) implementation

In Pix4D Mapper Pro there are two methods for GCP implementation. For this research, the Pix4D recommended method was used as described here. First, Initial Processing (first SfM processing step) was completed. Next, GCP *in situ* data and all associated coordinate positions were loaded to the Pix4D project through the "GCP/MTP Manager" tool. Next, the "rayCloud Editor…" function within the GCP/MTP Manger

was launched to identify and manually "tag" GCP locations in each project's image dataset. Manual GCP tagging here is similarly found in the georectification tools of varying geospatial software solutions, such as ESRI's Georeferencing Toolbar.

For Pix4D Mapper Pro, a minimum of 3 GCPs are required for data georectificaiton, and each GCP must be manually tagged in at least 2 images. For the purpose of this research, all GCPs were manually tagged 3-7 times as research has shown additional tagging, when done properly, improves resulting accuracy of the georectification. Once GCPs were tagged, the "Reoptimize" process was selected and run within Pix4D Mapper Pro. This Reoptimize process now takes GCP positions into account to georectify the project's initial reconstruction data (tie points). At this point, any additional datasets resulting from further processing (point cloud, DSM, etc.) will be georectified as well. An example of manual GCP tagging for georectification in Pix4D Mapper Pro is provided in Figure 5.4 below.

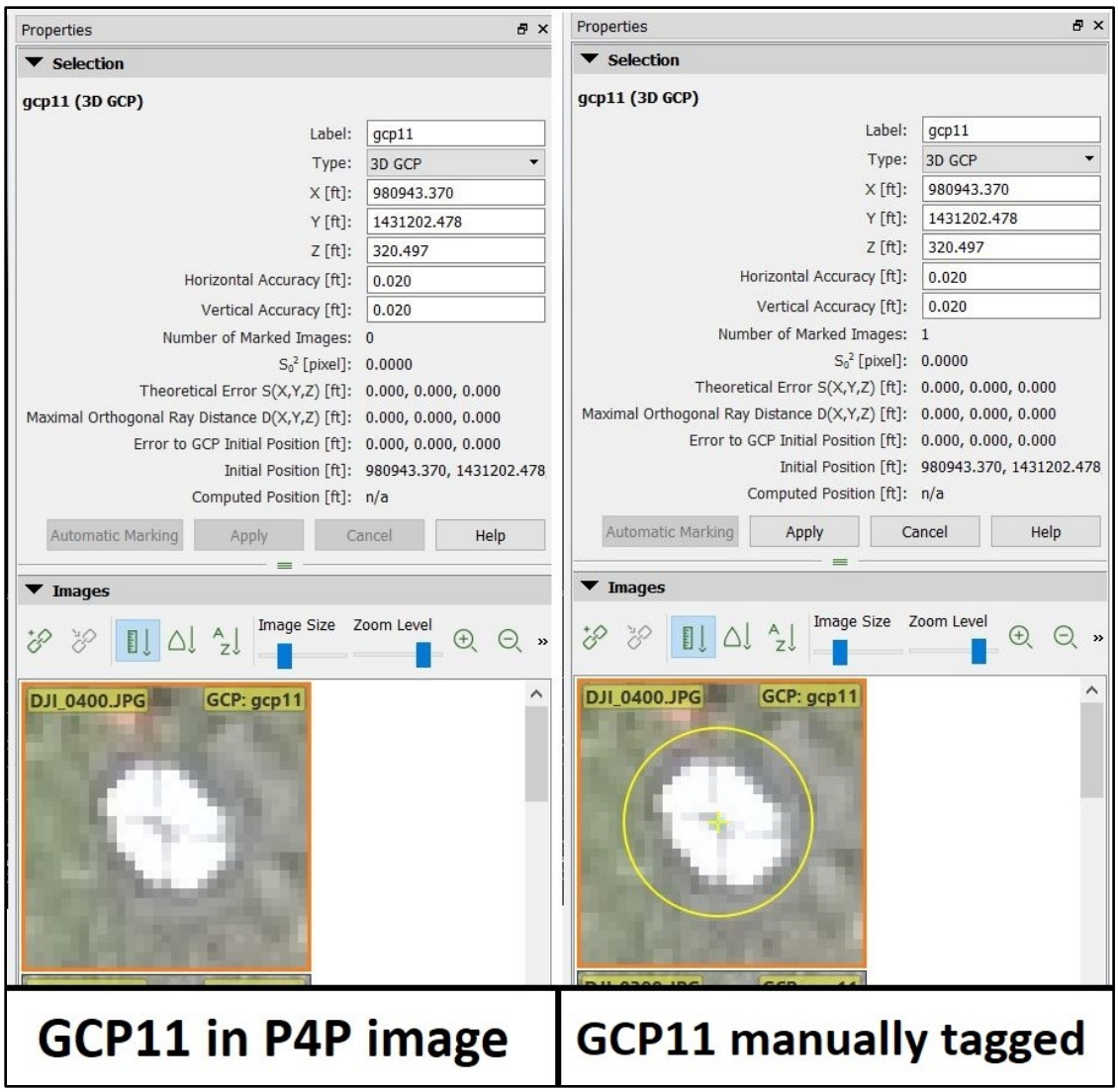

Figure 5.4 Ground Control Point (GCP) Implementation

Manual tagging of GCP11 in P4P remote sensing data at SA-2. With the contrasting X mark of GCP11 clearly visible, the GCP was tagged to best represent the center nail position where Trimble R6 *in situ* measurement was collected for accurate georectification. Once the GCP has been tagged, the "Apply" button becomes active as seen in the image on the right. Once the GCP is appropriately tagged in the required number of images, the "Apply" button is clicked to finalize the GCP position for georectification in Pix4D Mapper Pro.

Checkpoint implementation

Once the Reoptimize process was completed and project data georectified (tie points only at this point), checkpoints were added in a nearly identical fashion as the GCPs. First the GCP/MTP Manager tool is again utilized, this time to load checkpoint *in situ* data and all corresponding coordinate positions (still in .csv format). These points must then be officially designated as "Check Points" using a drop-down menu within the GCP/MTP Manager. This represents an additional, important step from the GCP workflow as the GCP/MTP Manager loads all points as "3D GCP" by default – meaning the points would be used during processing for georectification. Since this is not the purpose of these points, designating them as "Check Points" within the GCP/MTP Manager ensures they are not used in data georectification and can therefore be used as checkpoints for accuracy testing.

Per FGDC standards, a minimum of 20 checkpoints must be used for official accuracy testing (FGDC 1998). Additionally, Pix4D Mapper Pro requires that these checkpoints be manually identified (i.e. tagged) in at least 2 images each as with the GCPs. Therefore, all 20 checkpoints were implemented at each survey area (40 checkpoints total) and were tagged between 3-7 times each to maintain methodological consistency with GCP tagging. Once manual tagging is complete, deviation from the *in situ* benchmark checkpoint position is calculated. This deviation is represented in Pix4D Mapper Pro as "Error to GCP Initial Position" in the units of the GCP/checkpoint coordinates (feet in this case). It's important to note the "Error to GCP Initial Position" title is synonymous with error to checkpoint initial position, this is simply a static title

within Pix4D Mapper Pro. An example of checkpoint tagging and resulting Error to GCP Initial Position is provided in Figure 5.5 below.

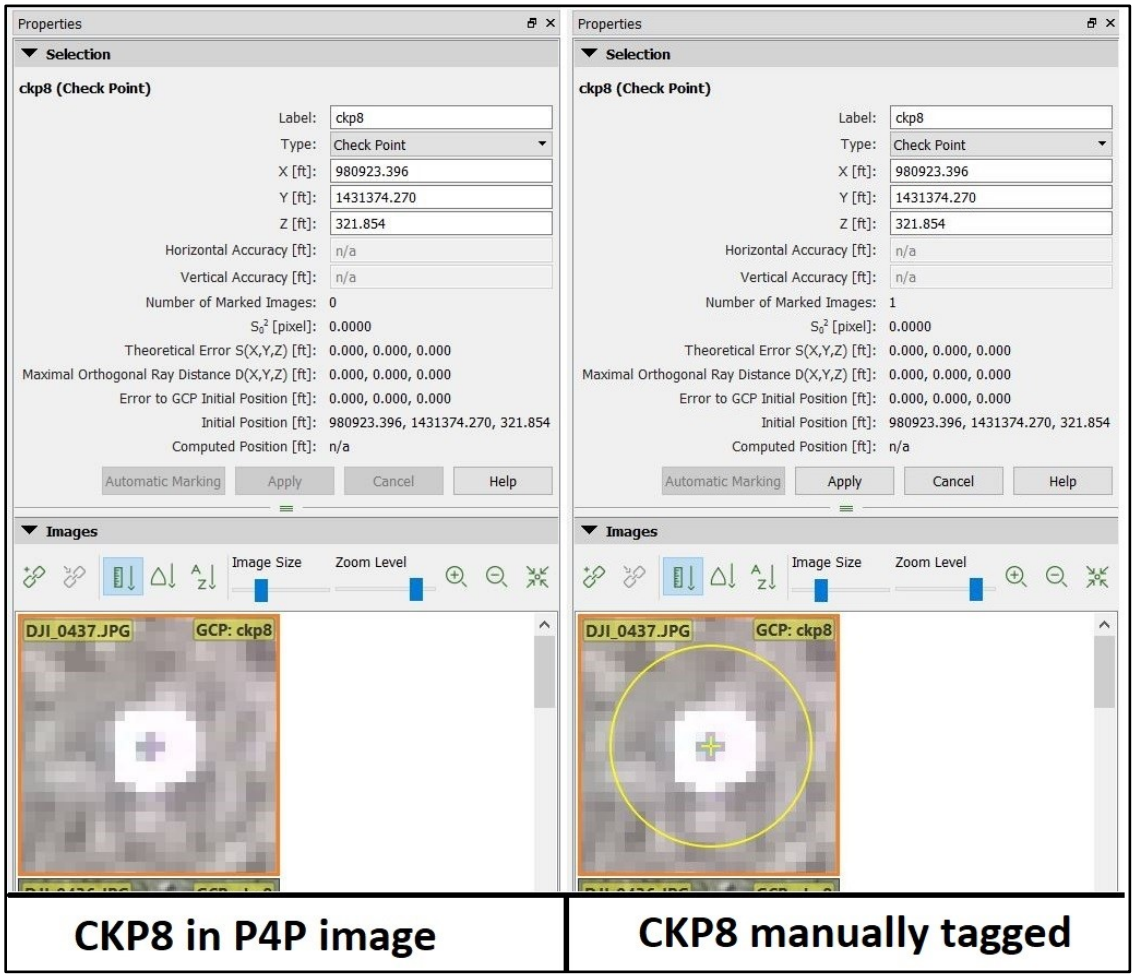

Figure 5.5 Checkpoint Implementation

Manual tagging of CKP8 in P4P remote sensing data at SA-2. With the contrasting square mark of CKP8 clearly visible, the point was tagged to best represent the center nail position where Trimble R6 *in situ* measurement was collected. Again, once the checkpoint has been tagged, the "Apply" button becomes active and is used to finalize the checkpoint position in Pix4D Mapper Pro.

Since checkpoints are not used for data georectification, the Reoptimize process is not required after checkpoint implementation has been completed. At this point, with all GCP and checkpoints properly designated in the GCP/MTP Manager and implemented in the Pix4D Mapper Pro, remaining SfM processing of full density point cloud data (second SfM processing step) and raster data (third step) can be completed with all the necessary point data for effective georectification and accuracy testing.

Processing iterations and resulting survey datasets

While all 20 checkpoints were required in each SfM datatset for official accuracy testing, the number of GCPs used for georectification was intentionally varied for each dataset, which resulted in multiple processing iterations for each remote sensing dataset and corresponding Pix4D project. For example, P3A remote sensing data for SA-1 (already stored as P3A_SA-1), when processed without GCPs, resulted in the P3A_SA-1_0GCP dataset. Similarly, the same P3A data for SA-1, when processed with 5, 8, and 12 GCPs, resulted in the P3A_SA-1_5GCP, P3A_SA-1_8GCP, and P3A_SA-1_12GCP datasets, respectively.

The first processing iteration for all datasets included no GCPs at all (0GCP) to provide baseline accuracies values for reference. Again, SfM processing and georectification is known to result in poor geospatial accuracy. Therefore, accuracies calculated for all 0GCP datasets will represent known outliers based on this methodology. However, these accuracies still valuably demonstrate the typical baseline accuracies of sUAS + SfM derived data in the absence of GCPs. In all subsequent processing iterations, the number and location of GCPs used for georeferencing were selected intentionally based on optimal GCP implementation practices for achieving

geospatial accuracy (Tonkin & Midgley 2016, James et al. 2017). At the conclusion of data processing, a total of 18 survey datasets were generated, each including initial tie points, full density point cloud, and DSM survey data for accuracy testing. All processing iterations and resulting survey datasets are represented below in Figure 5.6.

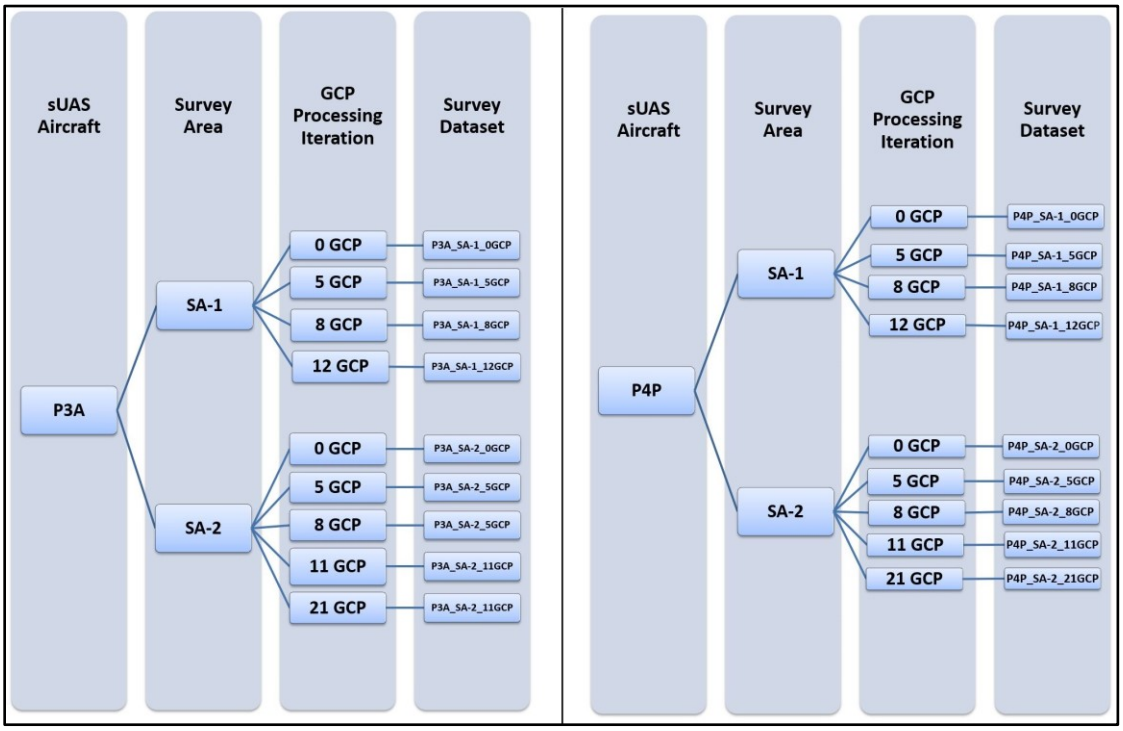

Figure 5.6 Resulting Survey Datasets

All resulting survey datasets at the completion of data processing. For each survey dataset three forms of sUAS + SfM derived survey data (initial tie points, full density point cloud, and DSM) were generated and used for accuracy testing.

CHAPTER VI

GEOSPATIAL AND STATISTICAL ANALYSIS

Geospatial analysis

FGDC Geospatial Positioning Accuracy Standards, *Part 3: National Standard for Spatial Data Accuracy* provides comprehensive guidelines and requirements for statistical analysis of, and accuracy calculation for geospatial data (FGDC 1998). For this research, geospatial analysis was first required to observe and calculate the error measurements required for full statistical analysis. Error measurements were calculated as positional deviation (Δ_x, Δ_y, Δ_z) in feet (ft.) of sUAS + SfM survey data (initial tie points, point cloud, DSM) from benchmark in-situ checkpoint positions.

Error calculation

Error calculation represented a vital step for this research effort. All observed error values would be used in statistical analysis for latter error and accuracy calculations which represent the very premise of this thesis. Additionally, error calculation was required for each of the three survey data types (initial tie points, point cloud, DSM) in each sUAS + SfM survey dataset. Given the differences in survey data types, each required a unique method of geospatial analysis for error calculation. These methods are described in the following sections before proceeding to statistical analysis discussion.

Initial tie points

Error calculation was simplest for initial tie points data generated in the first "Initial Processing" step of Pix4D Mapper Pro. During *in situ* data incorporation (discussed in previous chapter – DATA PROCESSING METHODS), error is calculated for all checkpoints within Pix4D Mapper Pro and reported as "Error to GCP Initial Position". This calculation occurs at the conclusion of manual checkpoint tagging (e.g. Figure 5.5) as shown in Figure 6.1 below.

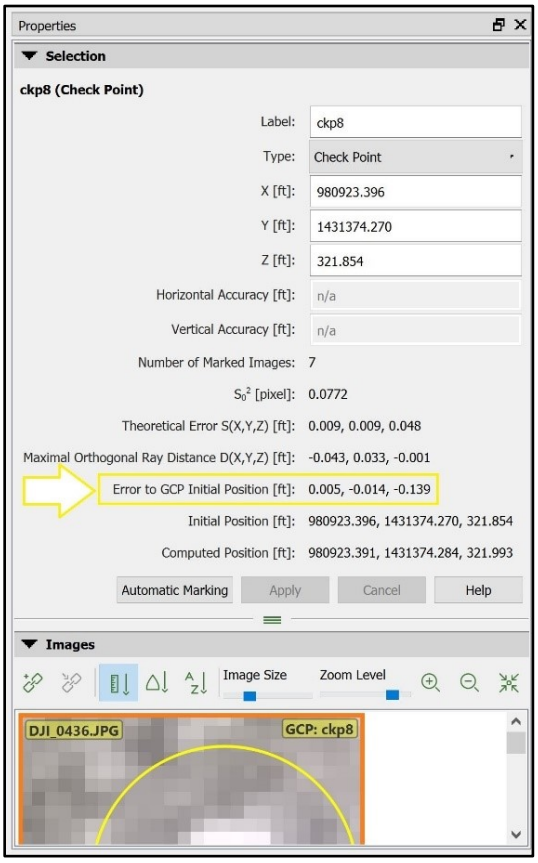

Figure 6.1 Error calculation for initial tie points.

Once manual checkpoint tagging is complete, the active "Apply" button is clicked and the "Computed Position" of the checkpoint is finalized (Apply button becomes inactive). "Error to GCP Initial Position" then represents the positional deviation (Δ_x, Δ_y, Δ_z) between the "Initial Position" and the "Computed Position" of the checkpoint.

"Error to GCP Initial Position" values were copied to Microsoft Excel spreadsheet format for all checkpoint locations in all 18 survey datasets. The excel format, as shown in Table 1.1 below, organizes all error values for further statistical analysis when calculating RMSE and accuracy later in the research effort. As you can see, the "Error to GCP Initial Position" values identified for checkpoint 8 (ckp_8) in Figure 6.1 above, are likewise listed for ckp_8 in Table 6.1 below.

Table 6.1 "Error to GCP Initial Position" for P4P_SA-2_21GCP checkpoints

P4P_SA-2_21GCP			
Error to GCP Initial Position			
	X	Y	Z
ckp_1	0.021	0.043	-0.212
ckp_2	0.016	0.002	-0.044
ckp_3	-0.138	0.002	-0.247
ckp_4	-0.036	0.057	-0.011
ckp_5	0.038	0.023	-0.115
ckp_6	0.003	0.053	-0.079
ckp_7	0.043	0.1	0.057
ckp_8	0.005	-0.014	-0.139
ckp_9	-0.025	0.053	-0.156
ckp_10	-0.032	-0.044	-0.015
ckp_11	-0.001	0.038	0.162
ckp_12	-0.112	0.003	0.04
ckp_13	0.035	0.039	-0.131
ckp_14	-0.077	0.013	-0.006
ckp_15	-0.074	0.007	-0.081
ckp_16	0.014	-0.029	-0.206
ckp_17	-0.036	-0.054	-0.205
ckp_18	-0.078	-0.078	0.108
ckp_19	0.04	-0.041	-0.472
ckp_20	-0.087	-0.021	-0.157

"Error to GCP Initial Position" values copied to Microsoft Excel for all 20 checkpoints (Δ_x, Δ_y, Δ_z) in P4P_SA-2_21GCP. Error values are organized for statistical analysis (RMSE, accuracy at 95% confidence) later in the research effort.

Point cloud

Error calculation in the fully processed point cloud survey data generated in the "Point Cloud and Mesh" step of Pix4D Mapper Pro was very similar to that for the initial tie points. However, for error calculation in this data, specific 3D points and their corresponding computed positions were used. This differs from error calculation in initial tie point as the error values were computed from the checkpoints themselves. Interestingly, the dense point cloud often provided multiple 3D points on any single checkpoint due to high reconstruction point density. Therefore, a specific 3D point within the point cloud was selected at each checkpoint location, and the point's "Computed Position" was used for error calculation. Specific points were selected to best corresponded to the central checkpoint position where the *in situ* checkpoint measurements were taken as shown in Figure 6.2 below.

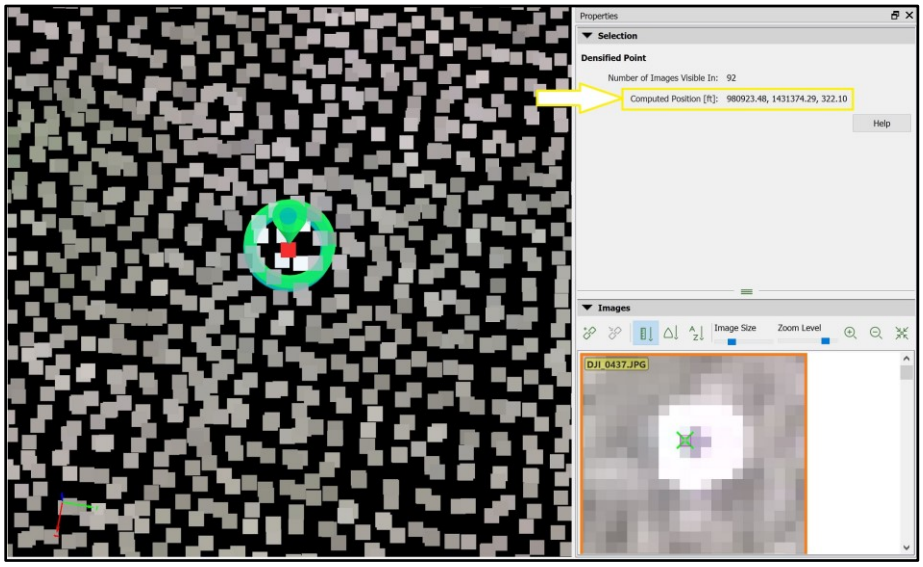

Figure 6.2 3D point selection for point cloud error calculation

The 3D point best representing the central checkpoint location was selected. The corresponding "Computed Position" for this 3D point was then used for error calculation.

As Figure 6.2 demonstrates, the dense point cloud does not guarantee point reconstruction in the exact checkpoint location. It is important to note this method provides the best option for error calculation according to FGDC requirements. However, it must be acknowledged that resulting error values for point cloud datasets may be higher than true geospatial error since 3D points rarely coincide with exact checkpoint positions.

Once a specific 3D point was selected, its "Computed Position" was copied into Microsoft Excel. Next, the "Initial Position" of the corresponding checkpoint copied into the same excel document. With the 3D point computed position and the checkpoint initial position both in excel, error values were calculated as positional deviation (Δ_x, Δ_y, Δ_z) between the points as shown in Figure 6.3 below. These error values were then copied into a separate excel document for statistical analysis as shown in Table 6.2 below.

Point_Cloud_Initial_Error_Calculations									
	3D Point Computed Position			Checkpoint Initial Position			Error_Value		
	X	Y	Z	X	Y	Z	X	Y	Z
ckp_1	981029.01	1431716.82	325.33	981029.171	1431716.837	325.107	-0.16	-0.02	0.22
ckp_2	980740.07	1431674.52	324.39	980740.262	1431674.53	323.982	-0.19	-0.01	0.41
ckp_3	980928.23	1431657.4	324.83	980928.116	1431657.341	324.537	0.11	0.06	0.29
ckp_4	981092.36	1431624.89	324.87	981092.35	1431624.78	324.542	0.01	0.11	0.33
ckp_5	980986.07	1431504.68	323.75	980985.997	1431504.671	323.547	0.07	0.01	0.20
ckp_6	980812.63	1431501.67	323.29	980812.731	1431501.722	323.056	-0.10	-0.05	0.23
ckp_7	980737.57	1431291.71	321.32	980737.615	1431291.827	321.045	-0.05	-0.12	0.27
ckp_8	980923.34	1431374.21	322.1	980923.396	1431374.27	321.854	-0.06	-0.06	0.25
ckp_9	981109.36	1431217.51	321.42	981109.29	1431217.623	321.175	0.07	-0.11	0.25
ckp_10	980961.49	1431217.02	320.74	980961.458	1431217.113	320.688	0.03	-0.09	0.05
ckp_11	980927.75	1431183.29	320.74	980927.635	1431183.29	320.358	0.11	0.00	0.38
ckp_12	981028.78	1431165.42	320.65	981028.627	1431165.486	320.239	0.15	-0.07	0.41
ckp_13	981024.52	1430999.8	318.73	981024.509	1430999.81	318.591	0.01	-0.01	0.14
ckp_14	980725.2	1431038.54	319.05	980725.2	1431038.508	318.823	0.00	0.03	0.23
ckp_15	980822.36	1430923.87	317.45	980822.273	1430923.849	317.264	0.09	0.02	0.19
ckp_16	980940.19	1430866.27	317.2	980940.212	1430866.231	316.776	-0.02	0.04	0.42
ckp_17	981096.63	1430898.05	318.08	981096.501	1430898.096	317.741	0.13	-0.05	0.34
ckp_18	981019.59	1430607.12	313.93	981019.368	1430607.022	313.645	0.22	0.10	0.29
ckp_19	980906.59	1430657.24	314.7	980906.473	1430657.127	314.421	0.12	0.11	0.28
ckp_20	980737.16	1430666.02	315.33	980737.188	1430665.997	315.189	-0.03	0.02	0.14

Figure 6.3 Error calculation for point cloud survey data.

Computed positions of 3D points and initial positions of corresponding checkpoints are used to calculate error values representing positional deviation (Δ_x, Δ_y, Δ_z) between sUAS + SfM derived point cloud survey data and benchmark checkpoint positions.

Table 6.2 Error values for P4P_SA-2_21GCP point cloud survey data

	P3A_SA-1_5GCP		
	Error to Initial GCP Position (Point Cloud)		
	X	Y	Z
ckp_1	-0.161	-0.017	0.223
ckp_2	-0.192	-0.01	0.408
ckp_3	0.114	0.059	0.293
ckp_4	0.01	0.11	0.328
ckp_5	0.073	0.009	0.203
ckp_6	-0.101	-0.052	0.234
ckp_7	-0.045	-0.117	0.275
ckp_8	-0.056	-0.06	0.246
ckp_9	0.07	-0.113	0.245
ckp_10	0.032	-0.093	0.052
ckp_11	0.115	0	0.382
ckp_12	0.153	-0.066	0.411
ckp_13	0.011	-0.01	0.139
ckp_14	0	0.032	0.227
ckp_15	0.087	0.021	0.186
ckp_16	-0.022	0.039	0.424
ckp_17	0.129	-0.046	0.339
ckp_18	0.222	0.098	0.285
ckp_19	0.117	0.113	0.279
ckp_20	-0.028	0.023	0.141

Error values copied to Microsoft Excel for all 20 checkpoints (Δ_x, Δ_y, Δ_z) in P4P_SA-2_21GCP point cloud survey data. Error values are organized for statistical analysis (RMSE, accuracy at 95% confidence) later in the research effort.

Digital surface model (DSM)

Error calculation in DSM raster data required a different approach for geospatial analysis. First, DSM raster data generated by Pix4D Mapper Pro for each survey dataset was imported to ESRI's ArcMap software program. Once in ArcMap, DSM raster data

was organized according to dataset and overlaid with *in situ* checkpoint positions using the "Add XY Data" tool. With checkpoints in place, ArcMap was zoomed to a 1:1 scale at each checkpoint location and the "Identify" tool was used to show DSM raster data elevations (i.e. "Pixel value") at each checkpoint location as shown in Figure 6.4 below.

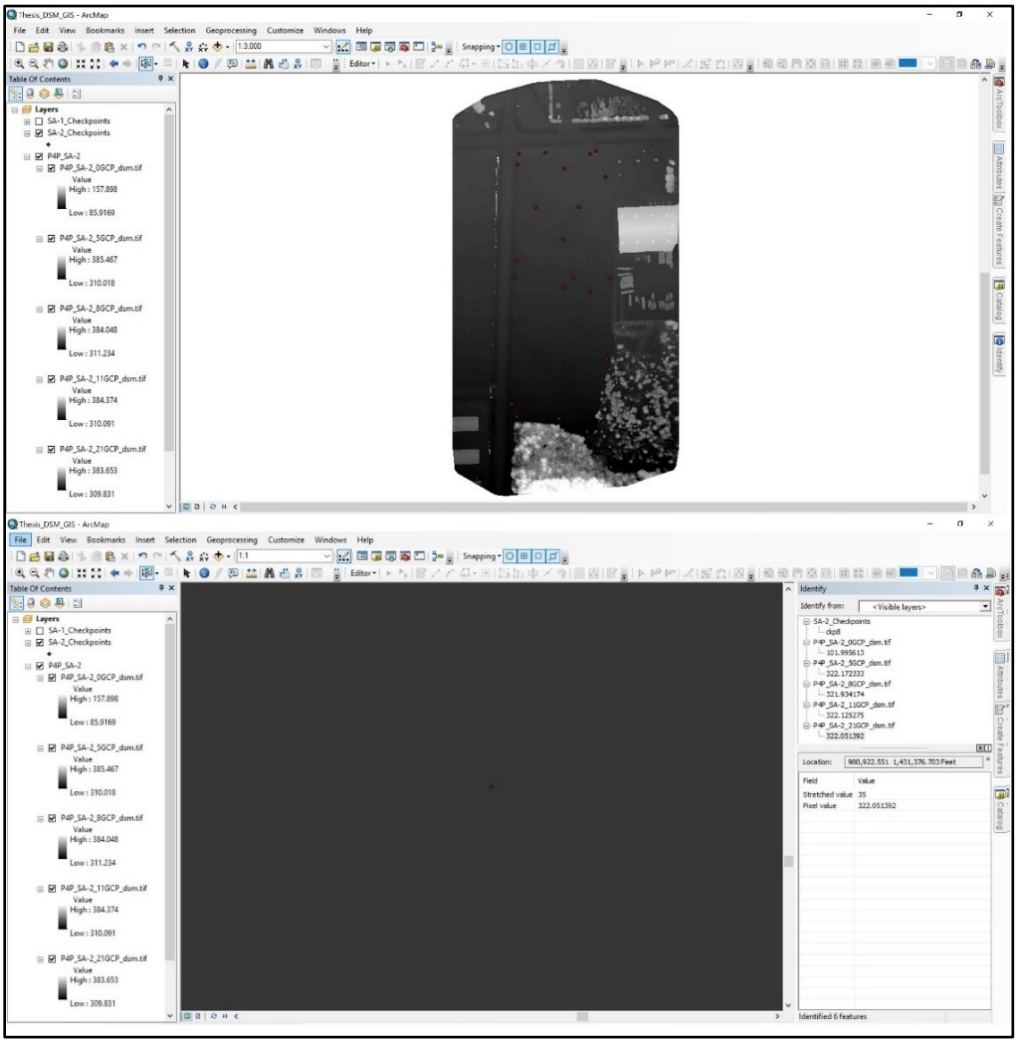

Figure 6.4 Raster pixel identification for digital surface model (DSM) error calculation.

With the "Identify" tool set to <Visible Layers> in ArcMap, DSM pixel values (elevations in ft.) were identified for all DSM survey data, at all checkpoint locations. Once identified, these pixel values were copied into Microsoft Excel for error calculation.

One prominent difference in DSM survey data, as opposed to the initial and full density point clouds, is that this raster data only possesses vertical coordinate (z) elevations values. For the purpose of this research, vertical error calculation and accuracy testing were still conducted on all DSM survey data – however, it is worth noting FGDC standards require accuracy to be reported both horizontally and vertically, which could not be done with these data without extensive additional effort to extract horizontal coordinate values manually from ArcMap. Since vertical accuracy is often more variable (and more debated) than horizontal accuracy in SfM derived survey data, vertical accuracy calculations made for DSM survey data were still considered valuable for this research effort – even though these accuracies could not be formally reported by FGDC standards (FGDC 1998).

Once DSM raster elevations were identified, the error calculation procedure matched that of the point cloud data done previously, but exclusively on vertical coordinates. All elevation pixel values were copied into Microsoft Excel along with corresponding "Initial Position" checkpoint elevations for vertical error calculation as shown in Figure 6.5 below. Resulting vertical error values were then copied to a separate excel document for statistical analysis in the same manner as Tables 1.2 and 1.3, though again with vertical coordinates only.

DSM_Initial_Error_Calculations									
	Raster Pixel Elevation			Checkpoint Initial Position			Vertical_Error_Value		
	X	Y	Z	X	Y	Z	X	Y	Z
ckp_1			325.3783			325.107			0.27
ckp_2			324.2601			323.982			0.28
ckp_3			324.8123			324.537			0.28
ckp_4			324.8308			324.542			0.29
ckp_5			323.7032			323.547			0.16
ckp_6			323.2158			323.056			0.16
ckp_7			321.3149			321.045			0.27
ckp_8			322.0632			321.854			0.21
ckp_9			321.4629			321.175			0.89
ckp_10			320.8346			320.688			0.15
ckp_11			320.7624			320.358			0.40
ckp_12			320.6844			320.239			0.45
ckp_13			319.0517			318.591			0.46
ckp_14			319.0034			318.823			0.18
ckp_15			317.5455			317.264			0.28
ckp_16			317.1905			316.776			0.41
ckp_17			318.1242			317.741			0.38
ckp_18			313.8886			313.645			0.24
ckp_19			314.8294			314.421			0.41
ckp_20			315.3147			315.189			0.13

Figure 6.5 Vertical error calculation for digital surface model (DSM) survey data.

Raster pixel elevations and initial position elevations of corresponding checkpoints are used to calculate vertical error values (Δ_z) between sUAS + SfM derived DSM survey data and benchmark checkpoint elevations.

Statistical analysis

Statistical analysis was required to calculate comprehensive error and accuracy statistics for all three survey data types (initial tie points, point cloud, DSM) in each sUAS + SfM survey dataset. Specifically, FGDC Geospatial Positioning Accuracy Standards – *Part 3: National Standard for Spatial Data Accuracy* (FGDC), Section 3.2.1 Spatial Accuracy uses RMSE "to estimate positional accuracy", while actual Accuracy is "reported in ground distances at the 95% confidence level." (FGDC 1998). The upcoming sections detail the specific statistical analysis procedures conducted per FGDC standards to calculate RMSE and Accuracy statistics for all sUAS + SfM survey datasets.

Root mean square error (RMSE) calculation

The FGDC defines RMSE for geospatial data as "the square root of the average of the set of squared differences between dataset coordinate values and coordinate values from an independent source of higher accuracy for identical points" (FGDC 1998). Therefore, "differences between dataset coordinate values" were calculated as error (positional deviation - Δ_x, Δ_y, Δ_z) during geospatial analysis and copied to Microsoft Excel as described in the previous section. Using these error values, RMSE was calculated in all coordinate directions ($RMSE_x$, $RMSE_y$, $RMSE_z$) by squaring the error, calculating the average square error, and then calculating the square root of the average square error as shown in the formulas of Figure 6.6 below taken from FGDC Appendix 3-A. Accuracy Statistics (normative).

Let:

$RMSE_x = sqrt[\sum(x_{data,i} - x_{check,i})^2/n]$
$RMSE_y = sqrt[\sum(y_{data,i} - y_{check,i})^2/n]$

where:
$x_{data,i}$, $y_{data,i}$ are the coordinates of the i th check point in the dataset
$x_{check,i}$, $y_{check,i}$ are the coordinates of the i th check point in the independent source of higher accuracy
n is the number of check points tested
i is an integer ranging from 1 to n

$RMSE_z = sqrt[\sum(z_{data\,i} - z_{check\,i})^2/n]$

where

$z_{data\,i}$ is the vertical coordinate of the i th check point in the dataset.
$z_{check\,i}$ is the vertical coordinate of the i th check point in the independent source of higher accuracy
n = the number of points being checked
i is an integer from 1 to n

Figure 6.6 RMSE formulas

Formulas used for RMSE calculation ($RMSE_x$, $RMSE_y$, $RMSE_z$) per FGDC Appendix 3-A. Accuracy Statistics (normative).

Vertical RMSE ($RMSE_z$) calculation is complete after this calculation, but further statistical analysis is required on $RMSE_x$ and $RMSE_y$ to calculate overall horizontal RMSE ($RMSE_r$). To calculate $RMSE_r$, the sum of squared $RMSE_x$ and $RMSE_y$ values was calculated first, then the square root of this sum of squares was taken as shown in the formula of Figure 6.7 below taken from FGDC Appendix 3-A, Accuracy Statistics (FGDC 1998).

Horizontal error at point i is defined as $sqrt[(x_{data,i} - x_{check,i})^2 + (y_{data,i} - y_{check,i})^2]$. Horizontal RMSE is:

$RMSE_r = sqrt[\sum((x_{data,i} - x_{check,i})^2 + (y_{data,i} - y_{check,i})^2)/n]$
$= sqrt[RMSE_x^2 + RMSE_y^2]$

Figure 6.7 Horizontal RMSE ($RMSE_r$) formula

With vertical RMSE ($RMSE_z$) already calculated, horizontal RMSE ($RMSE_r$) was calculated using the RMSE values calculated in both horizontal directions ($RMSE_x$, $RMSE_y$).

At the conclusion of RMSE calculation, resulting $RMSE_r$ and $RMSE_z$ values were organized within the existing excel document alongside initial error values. These values were then subject to further statistical analysis for accuracy calculation at the 95% confidence level per FGDC standards.

Accuracy (95% confidence) calculation

The FGDC reports accuracy "in ground distances at the 95% confidence level". Additionally, the FGDC elaborates on accuracy values in the following excerpt from FGDC Section 3.2.1 Spatial Accuracy – "Accuracy reported at the 95% confidence level means that 95% of the positions in the datasets will have an error with respect to true ground position that is equal to or smaller than the reported accuracy value. The reported accuracy value reflects all uncertainties, including those introduced by geodetic control coordinates, compilation, and final computation of ground coordinate values in the product" (FGDC 1998). Therefore, for this experiment, accuracy at the 95% confidence level means that positional deviation error (Δ_x, Δ_y, Δ_z) at only one of the 20 checkpoints (5%) for either survey area may exceed the reported accuracy.

For horizontal accuracy ($Accuracy_r$), the FGDC provides two methods or "cases" for calculation. The first case is used when RMSE is equivalent in both horizontal directions ($RMSE_x = RMSE_y$). The second case is used when RMSE is "independent in the x- and y- component and error" ($RMSE_x \neq RMSE_y$) and resulting horizontal error values are approximated. Therefore, since RSME values calculated in the previous step were observed to be independent in both horizontal directions ($RMSE_x \neq RMSE_y$), the second case and its associated formula were used to approximate $Accuracy_r$ in compliance with FGDC standards.

For vertical accuracy ($Accuracy_z$), the FGDC provides a single calculation method. Therefore, this method and its associated formula was used to calculate $Accuracy_z$ in compliance with FGDC standards. The formulas used for $Accuracy_r$ and $Accuracy_z$ calculation are shown in Figure 6.8 below as taken from FGDC Appendix 3-A, Accuracy Statistics (FGDC 1998). At the conclusion of geospatial and statistical analysis, resulting $Accuracy_r$ and $Accuracy_z$ values were organized within existing Microsoft Excel documents alongside initial error values and RMSE values for each sUAS + SfM survey dataset.

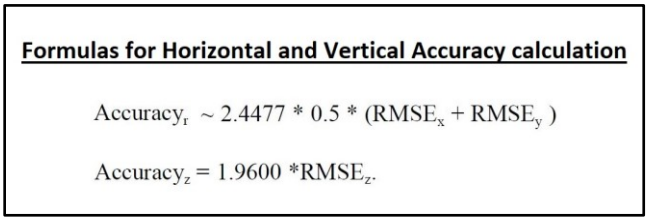

Figure 6.8 Horizontal Accuracy ($Accuracy_r$) and Vertical Accuracy ($Accuracy_z$) formulas.

With RMSE values calculated, Horizontal Accuracy ($Accuracy_r$) and Vertical Accuracy ($Accuracy_z$) were calculated using accuracy formulas from FGDC Appendix 3-A. Accuracy Statistics (normative).

CHAPTER VII

RESULTS

Accuracy results overview

The accuracy values calculated during geospatial and statistical analysis embody the fundamental research results of this thesis. As previously quoted from the FGDC, these accuracy values represent ground distances at the 95% confidence level which reflect all geospatial uncertainties in the final survey data product. To recap, resulting accuracies were calculated for two modern prosumer sUAS platforms (P3A, P4P) at two differing survey areas (SA-1, SA-2). Additionally, multiple processing iterations and resulting survey data were generated for each dataset by varying the number of GCPs used for georectification. This includes four processing iterations for SA-1 (0GCP, 5GCP, 8GCP, and 12GCP) and 5 processing iterations for SA-2 (0GCP, 5GCP, 8GCP, 11GCP, and 21GCP). In this manner, a total of 18 sUAS + SfM survey datasets were generated during the experiment as previously shown in Figure 5.6. For each survey dataset, three survey data types (initial tie points, point cloud, and DSM) were subjected to accuracy testing and calculation. For initial tie points and point cloud survey data, both horizontal and vertical accuracies ($Accuracy_r$, $Accuracy_z$) were calculated. For DSM data, only vertical accuracy was calculated ($Accuracy_z$). Resulting accuracies for all sUAS + SfM derived survey datasets are provided in Figure 7.1 below.

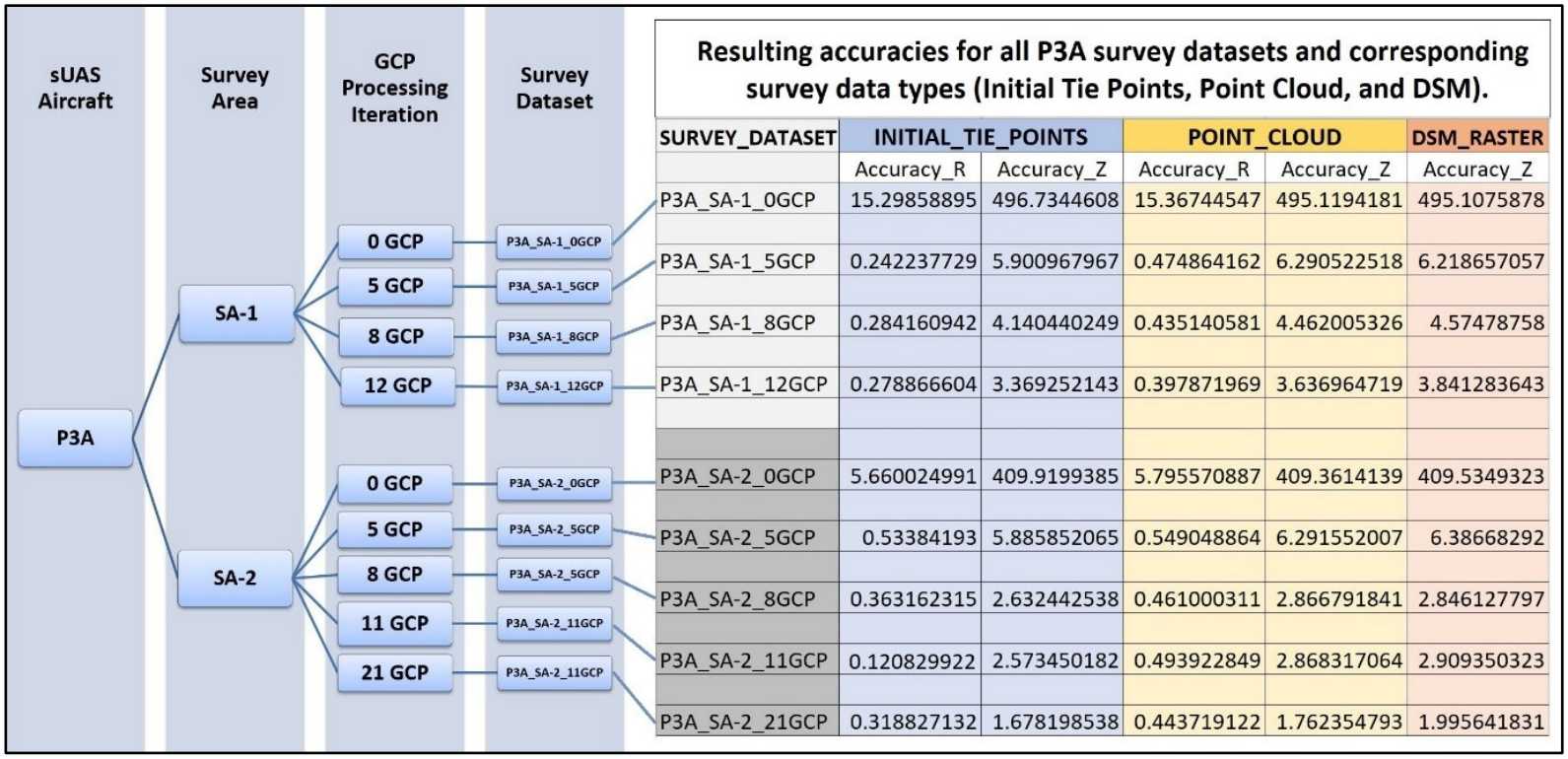

Resulting accuracies for all P3A survey datasets and corresponding survey data types (Initial Tie Points, Point Cloud, and DSM).

SURVEY_DATASET	INITIAL_TIE_POINTS		POINT_CLOUD		DSM_RASTER
	Accuracy_R	Accuracy_Z	Accuracy_R	Accuracy_Z	Accuracy_Z
P3A_SA-1_0GCP	15.29858895	496.7344608	15.36744547	495.1194181	495.1075878
P3A_SA-1_5GCP	0.242237729	5.900967967	0.474864162	6.290522518	6.218657057
P3A_SA-1_8GCP	0.284160942	4.140440249	0.435140581	4.462005326	4.57478758
P3A_SA-1_12GCP	0.278866604	3.369252143	0.397871969	3.636964719	3.841283643
P3A_SA-2_0GCP	5.660024991	409.9199385	5.795570887	409.3614139	409.5349323
P3A_SA-2_5GCP	0.53384193	5.885852065	0.549048864	6.291552007	6.38668292
P3A_SA-2_8GCP	0.363162315	2.632442538	0.461000311	2.866791841	2.846127797
P3A_SA-2_11GCP	0.120829922	2.573450182	0.493922849	2.868317064	2.909350323
P3A_SA-2_21GCP	0.318827132	1.678198538	0.443719122	1.762354793	1.995641831

Figure 7.1 Accuracy results (ft.) for sUAS + SfM derived survey data

$Accuracy_r$ and $Accuracy_z$ values as calculated for all P3A derived survey datasets and corresponding data types (initial tie points, point cloud, and DSM).

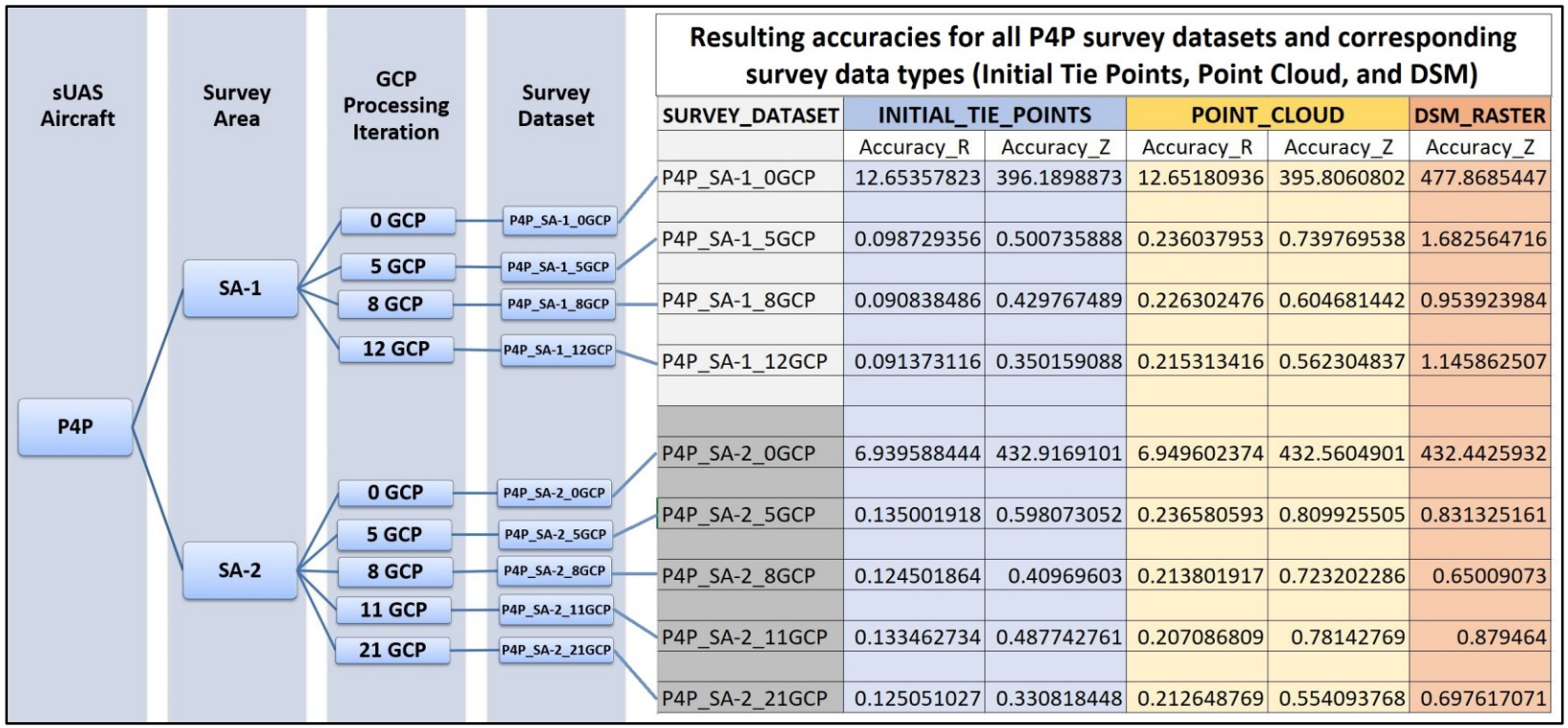

Resulting accuracies for all P4P survey datasets and corresponding survey data types (Initial Tie Points, Point Cloud, and DSM)

SURVEY_DATASET	INITIAL_TIE_POINTS		POINT_CLOUD		DSM_RASTER
	Accuracy_R	Accuracy_Z	Accuracy_R	Accuracy_Z	Accuracy_Z
P4P_SA-1_0GCP	12.65357823	396.1898873	12.65180936	395.8060802	477.8685447
P4P_SA-1_5GCP	0.098729356	0.500735888	0.236037953	0.739769538	1.682564716
P4P_SA-1_8GCP	0.090838486	0.429767489	0.226302476	0.604681442	0.953923984
P4P_SA-1_12GCP	0.091373116	0.350159088	0.215313416	0.562304837	1.145862507
P4P_SA-2_0GCP	6.939588444	432.9169101	6.949602374	432.5604901	432.4425932
P4P_SA-2_5GCP	0.135001918	0.598073052	0.236580593	0.809925505	0.831325161
P4P_SA-2_8GCP	0.124501864	0.40969603	0.213801917	0.723202286	0.65009073
P4P_SA-2_11GCP	0.133462734	0.487742761	0.207086809	0.78142769	0.879464
P4P_SA-2_21GCP	0.125051027	0.330818448	0.212648769	0.554093768	0.697617071

Figure 7.1 (continued)

$Accuracy_r$ and $Accuracy_z$ values as calculated for all P4P derived survey datasets and corresponding data types (initial tie points, point cloud, and DSM).

In reviewing the resulting accuracies presented in Figure 7.1, all 0GCP datasets were found to be statistical outliers. Since the use of GCPs has been demonstrated to improve sUAS derived accuracies in existing research, it can be assumed that any sUAS survey applications intending to achieve geospatial accuracy should indeed utilize GCPs. Therefore, by removing these 0GCP datasets and their outlier accuracy values, resulting sUAS + SfM derived accuracies can be better understood. This is demonstrated by Figures 7.2 – 7.5 below.

Figure 7.2 compares resulting horizontal accuracies ($Accuracy_r$) and vertical accuracies ($Accuracy_z$) in all remaining sUAS + SfM datasets after removing 0GCP outliers. Figure 7.3 compares resulting P3A-derived vs. P4P-derived accuracies in all datasets with 0GCP outliers removed. Figure 7.4 shows cumulative accuracies for SA-1 and compares P3A vs. P4P derived accuracies at SA-1 with 0GCP outliers removed. Finally, Figure 7.5 shows cumulative accuracies for SA-2 and compares P3A vs. P4P derived accuracies at SA-2 with 0GCP dataset outliers removed.

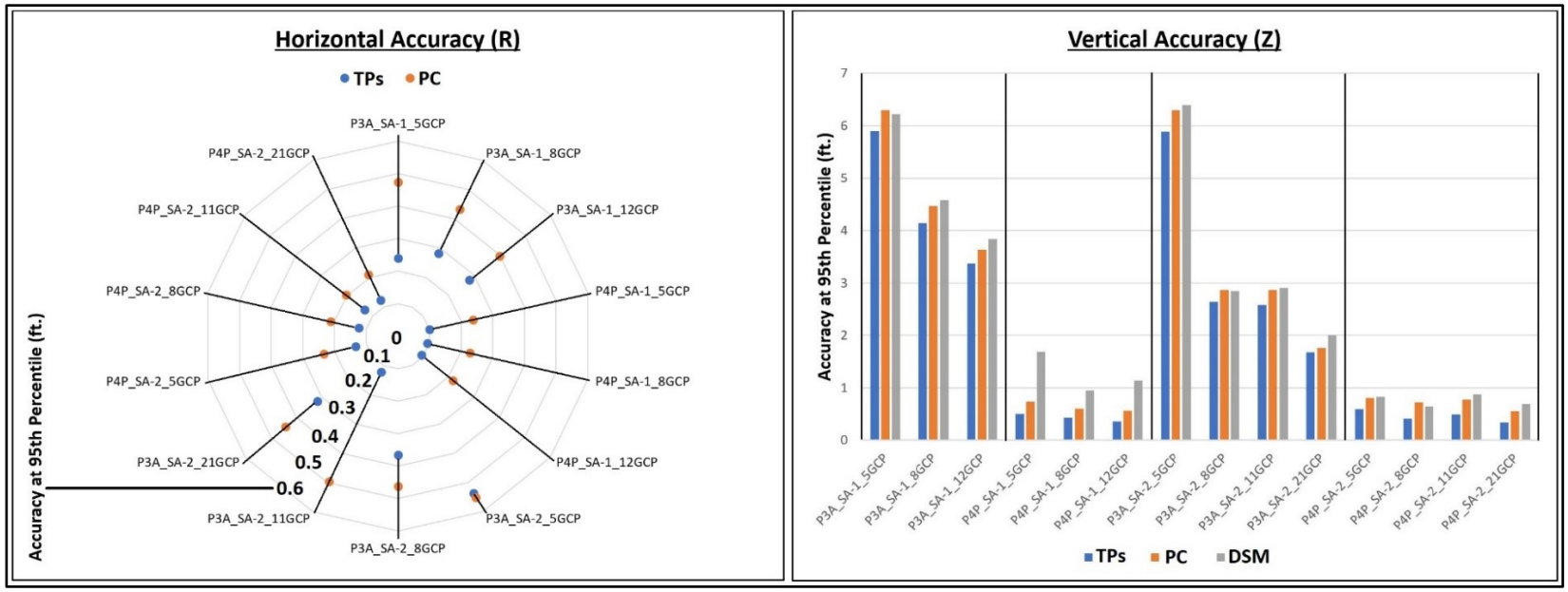

Figure 7.2 Horizontal vs. vertical accuracy comparison (0GCP outliers removed)

On the left, horizontal accuracy ($Accuracy_r$) is shown for all remaining sUAS + SfM derived survey datasets after removing 0GCP outlier datasets. Horizontal accuracy is shown as blue dots for initial tie points (TPs) survey data and orange dots for point cloud (PC) survey data. On the right, vertical accuracy ($Accuracy_z$) is shown for all remaining sUAS + SfM derived survey datasets after removing 0GCP outlier datasets. Vertical accuracy is shown as blue bars for initial tie points (TPs), orange bars for point clouds (PC), and gray bars for digital surface model (DSM) survey data.

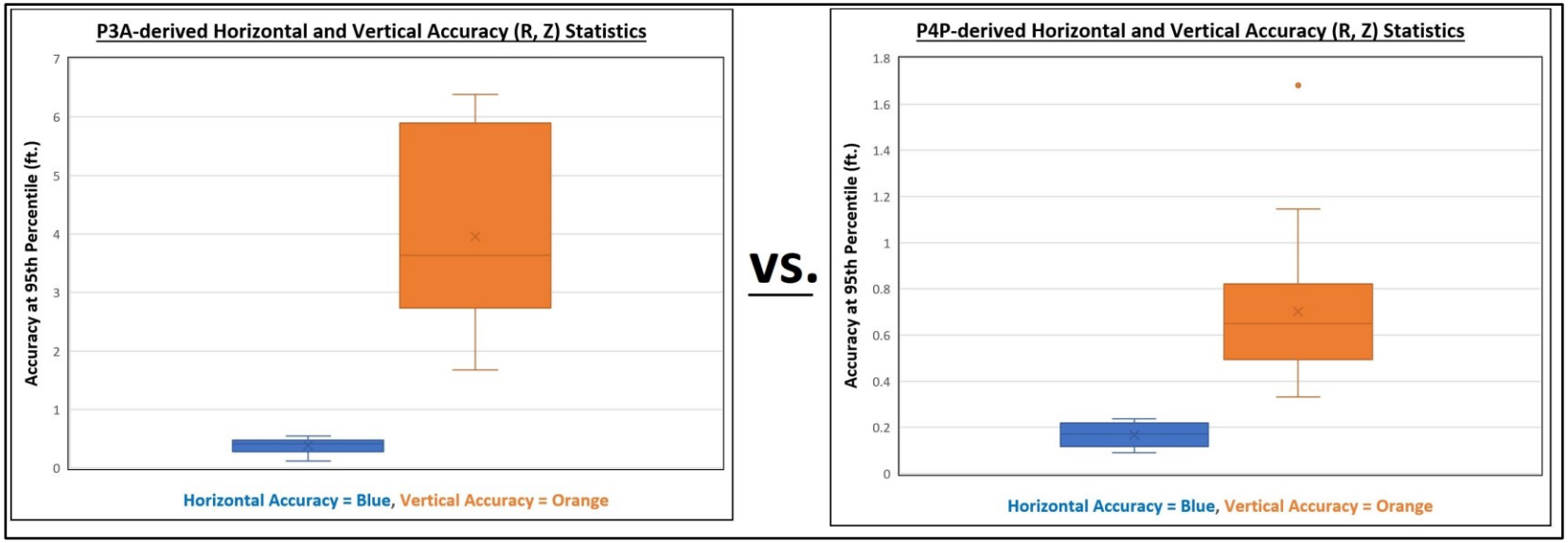

Figure 7.3 P3A vs. P4P accuracy comparison (0GCP outliers removed)

On the left, resulting P3A derived accuracies are plotted using a box and whisker diagram after removing all 0GCP outliers. On the right, resulting P4P derived accuracies are also plotted using a box and whisker diagram – again with 0GCP outliers removed. For both diagrams, horizontal accuracy ($Accuracy_r$) is shown in blue and vertical accuracy ($Accuracy_z$) is shown in orange. Additional data statistics shown on the diagram include the interquartile range (IQR, box), mean (X mark within IQR), median (line across IQR), minimum and maximum values (whiskers), and any statistical outliers (dots).

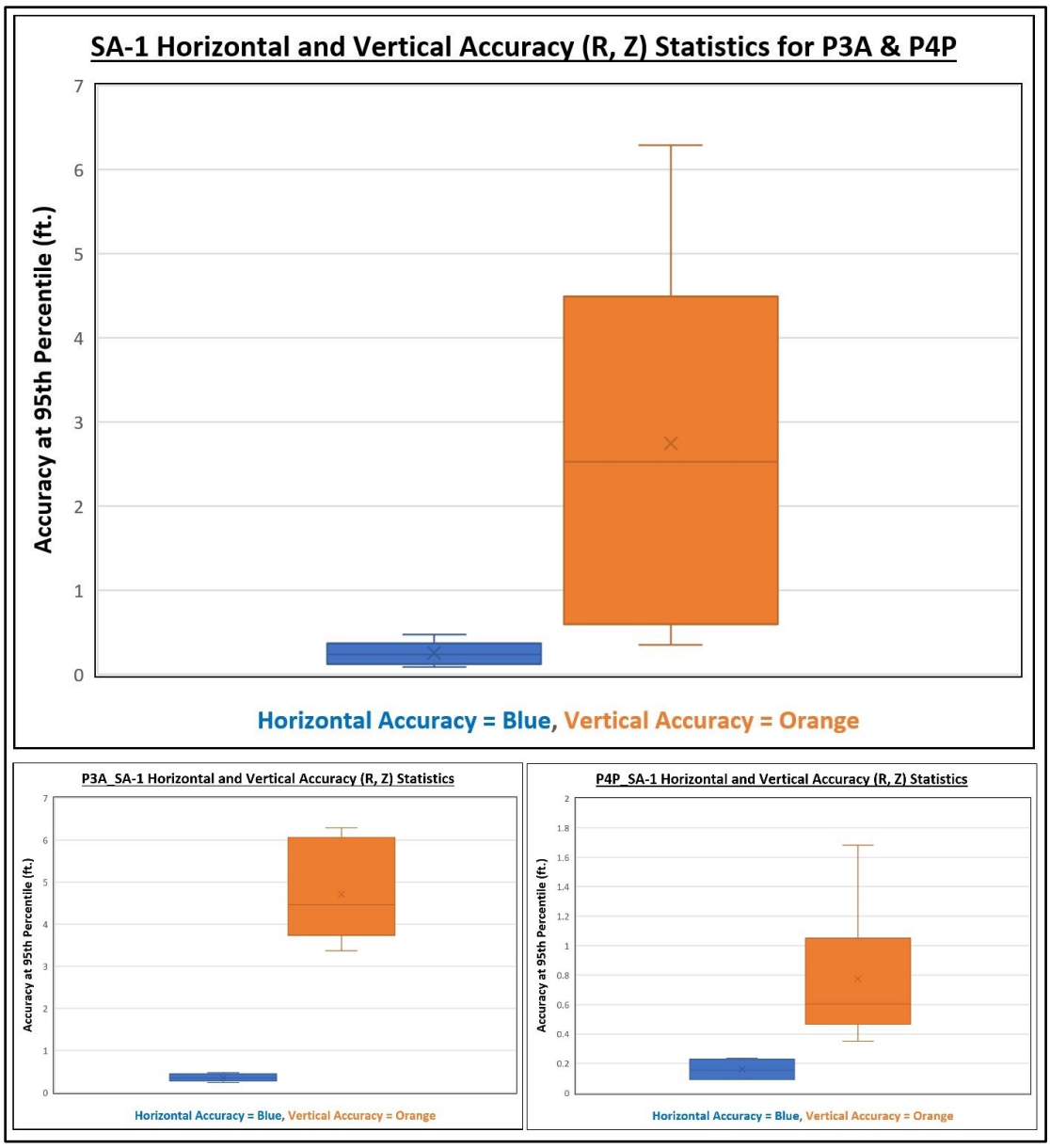

Figure 7.4 Resulting accuracies at SA-1 (0GCP outliers removed)

Cumulative accuracies from both P3A and P4P at Survey Area #1 (SA-1) are plotted in the top box and whisker diagram. Alternatively, P3A and P4P derived accuracies at SA-1 are isolated for comparison in the bottom box and whisker diagrams. For all diagrams, horizontal accuracy ($Accuracy_r$) is shown in blue and vertical accuracy ($Accuracy_z$) is shown in orange. Additional data statistics shown on the diagram include the interquartile range (IQR, box), mean (X mark within IQR), median (line across IQR), minimum and maximum values (whiskers), and any statistical outliers (dots).

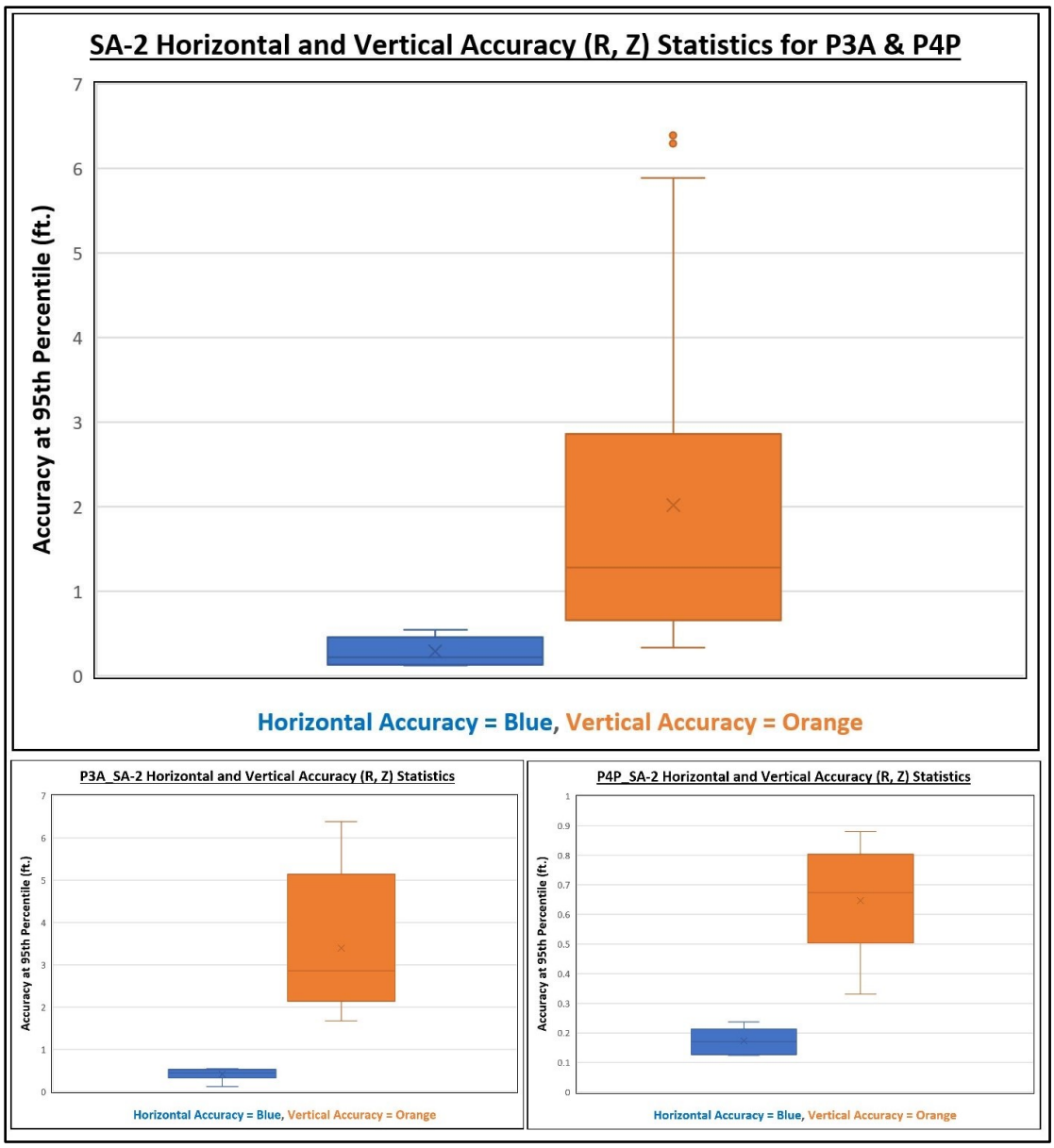

Figure 7.5 Resulting accuracies at SA-2 (0GCP outliers removed)

Cumulative accuracies from both P3A and P4P at Survey Area #2 (SA-2) are plotted in the top box and whisker diagram. Alternatively, P3A and P4P derived accuracies at SA-2 are isolated for comparison in the bottom box and whisker diagrams. For all diagrams, horizontal accuracy ($Accuracy_r$) is shown in blue and vertical accuracy ($Accuracy_z$) is shown in orange. Additional data statistics shown on the diagram include the interquartile range (IQR, box), mean (X mark within IQR), median (line across IQR), minimum and maximum values (whiskers), and any statistical outliers (dots).

Accuracy reporting and classification results

It was necessary to report these accuracies according to FGDC standards and identify their corresponding accuracy classification(s) (FGDC 1998). First, resulting horizontal and vertical accuracies were reported per FGDC standards for each survey data type (vertical accuracy only for DSM data). For example, P4P_SA-2_21GCP accuracies were reported as 0.125 ft. horizontally and 0.330 ft. vertically for initial tie points survey data, and 0.212 ft. horizontally and 0.554 vertically for point cloud survey data. Overall, reported accuracies ranged from 15.367 ft. – 0.09 ft. horizontally and 496.734 ft. – 0.330 ft. vertically for all initial tie point and point cloud survey data. Vertical accuracies for DSM raster survey data ranged from 495.107 ft. – 0.65 ft. consistent with vertical accuracies reported in the initial tie points and point cloud survey data types.

Next, reported accuracies were classified according to established FGDC accuracy classifications shown in Figure 7.6 below as taken from the FGDC Geospatial Positioning Accuracy Standards – *Part 2: Standards for Geodetic Networks*, Section 2.21 Accuracy Standards, Table 2.1.

Table 2.1 -- Accuracy Standards
Horizontal, Ellipsoid Height, and Orthometric Height

Accuracy Classification	95-Percent Confidence Less Than or Equal to:
1-Millimeter	0.001 meters
2-Millimeter	0.002 "
5-Millimeter	0.005 "
1-Centimeter	0.010 "
2-Centimeter	0.020 "
5-Centimeter	0.050 "
1-Decimeter	0.100 "
2-Decimeter	0.200 "
5-Decimeter	0.500 "
1-Meter	1.000 "
2-Meter	2.000 "
5-Meter	5.000 "
10-Meter	10.000 "

Figure 7.6 FGDC accuracy classifications

For geodetic control networks, the FGDC utilizes these accepted accuracy classifications to effectively group and communicate survey data geospatial accuracy. Given their federal use for this purpose, these classifications are likewise commonly used to communicate survey data accuracy outside of geodetic control networks – such as the accuracy results of this research effort.

Since accuracies can be reported at similar or near identical values, FGDC classifications provide a consistent means of grouping and communicating geospatial accuracy through specific accuracy thresholds in metric values. For example, horizontal accuracy reported at 0.212 ft. for P4P_SA-2_21GCP point cloud survey data would fall under the 1-Decimeter (0.328 ft.) accuracy classification, as it does not achieve the

threshold accuracy value of the next classification (5-Centimeter, 0.164 ft.). Likewise, vertical accuracy reported at 0.554 ft. for P4P_SA-2_21GCP point cloud survey data would fall under the 2-Decimeter (0.656 ft.) accuracy classification.

These FGDC accuracy classifications represent established and commonly used accuracy threshold values by which geospatial accuracies are effectively communicated. For this research, the 5-Centimeter (0.164 ft. equivalent) accuracy classification served as the threshold for "survey-grade" accuracy. Overall, sUAS + SfM derived survey datasets achieved accuracy classifications between the 5-Meter and 2-Centimeter (16.504 – 0.065 ft. equivalent) classifications horizontally, and no better than the 1-Decimeter (0.328 ft. equivalent) classification vertically.

Among all sUAS + SfM survey datasets, 8.8% of derivative survey data achieved "survey-grade" accuracy at the 5-Centimeter (0.164 ft.) accuracy classification or better (8 of 90 calculated accuracies). However, those survey data which achieved "survey-grade" accuracy were found to do so in horizontal accuracy ($Accuracy_r$) only. Additionally, this "survey-grade" horizontal accuracy was observed only in initial tie points survey data, and not in subsequent survey data types (point cloud, DSM). Specifically, these sUAS + SfM survey datasets which exhibited "survey-grade" horizontal accuracy ≤ 0.164 in initial tie points data included: P4P_SA-1_5GCP, P4P_SA-1_8GCP, P4P_SA-1_12GCP, P3A_SA-2_11GCP, P4P_SA-2_5GCP, P4P_SA-2_8GCP, P4P_SA-2_11GCP, and P4P_SA-2_21GCP. Finally, no sUAS + SfM survey datasets were found to achieve "survey-grade" vertical accuracy ($Accuracy_z$), even those which did so horizontally.

Resulting geospatial accuracies as calculated, reported, and classified here for sUAS + SfM derived survey datasets again represent the very premise of this thesis research. However, additional results and insight were made possible through descriptive analysis of these accuracy values.

Descriptive analysis of resulting accuracies

All survey datasets (18 total)

Combined_Accuracy_R		
Range	15.276602 [15.36744547, 0.0908384858]	
Mean	2.473900933	
Median	0.301494037	
Standard Deviation (SD)	4.58212086	

Combined_Accuracy_Z			
Range	496.4036424	[496.7344608 , 0.33081844]	
Mean	99.65587308		
Median	2.856459819		
Standard Deviation (SD)	184.6962599		

	INITIAL_TIE_POINTS		POINT_CLOUD		DSM_RASTER
Survey Dataset	Accuracy_R	Accuracy_Z	Accuracy_R	Accuracy_Z	Accuracy_Z
P3A_SA-1_0GCP	15.29858895	496.7344608	15.36744547	495.1194181	495.1075878
P3A_SA-1_5GCP	0.242237729	5.900967967	0.474864162	6.290522518	6.218657057
P3A_SA-1_8GCP	0.284160942	4.140440249	0.435140581	4.462005326	4.57478758
P3A_SA-1_12GCP	0.278866604	3.369252143	0.397871969	3.636964719	3.841283643
P4P_SA-1_0GCP	12.65357823	396.1898873	12.65180936	395.8060802	477.8685447
P4P_SA-1_5GCP	0.098729356	0.500735888	0.236037953	0.739769538	1.682564716
P4P_SA-1_8GCP	0.090838486	0.429767489	0.226302476	0.604681442	0.953923984
P4P_SA-1_12GCP	0.091373116	0.350159088	0.215313416	0.562304837	1.145862507
P3A_SA-2_0GCP	5.660024991	409.9199385	5.795570887	409.3614139	409.5349323
P3A_SA-2_5GCP	0.53384193	5.885852065	0.549048864	6.291552007	6.38668292
P3A_SA-2_8GCP	0.363162315	2.632442538	0.461000311	2.866791841	2.846127797
P3A_SA-2_11GCP	0.120829922	2.573450182	0.493922849	2.868317064	2.909350323
P3A_SA-2_21GCP	0.318827132	1.678198538	0.443719122	1.762354793	1.995641831
P4P_SA-2_0GCP	6.939588444	432.9169101	6.949602374	432.5604901	432.4425932
P4P_SA-2_5GCP	0.135001918	0.598073052	0.236580593	0.809925505	0.831325161
P4P_SA-2_8GCP	0.124501864	0.40969603	0.213801917	0.723202286	0.65009073
P4P_SA-2_11GCP	0.133462734	0.487742761	0.207086809	0.78142769	0.879464
P4P_SA-2_21GCP	0.125051027	0.330818448	0.212648769	0.554093768	0.697617071

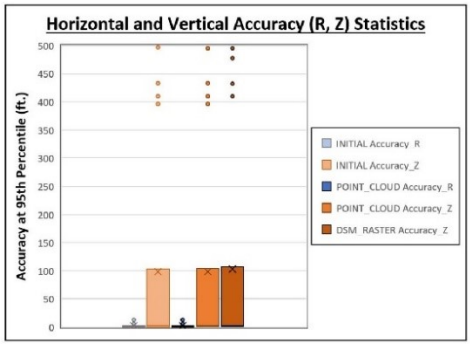

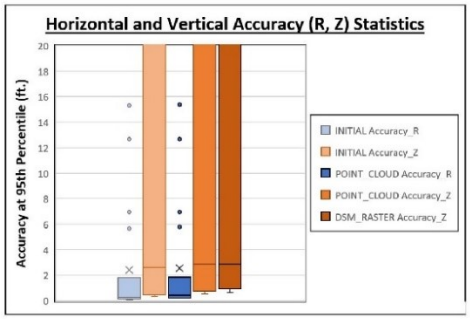

Figure 7.7 Descriptive statistics for all survey datasets

Descriptive statistics for resulting geospatial accuracies in all 18 sUAS + SfM derived survey datasets show accuracy values to be wide-ranging and skewed as a result of statistical outlier values from 0GCP datasets with poor geospatial accuracy.

Descriptive statistics for all 18 survey datasets as shown in Figure 7.7 above provide additional insight into resulting survey data accuracies. First, $Accuracy_r$

consistently outperformed $Accuracy_z$ in all survey data types and datasets. This outcome is consistent with the results of similar recent studies and supports the notion that vertical accuracy is challenging to achieve with the sUAS + SfM methodology (more-so than horizontal accuracy; e.g. Clapuyt et al. 2016, Agüera-Vega et al. 2017, Cook 2017). Additionally, the range of accuracy values (both $Accuracy_r$ and $Accuracy_z$) observed for all survey datasets is relatively broad and skewed. These characteristics are demonstrated in both the large range statistics and the difference in mean and median statistics for all accuracy values in Figure 7.7.

The wide-ranging and skewed nature of resulting accuracy values was expected for this research as 0GCP datasets are known to demonstrate less geospatial accuracy than datasets which possess optimal GCPs for georectification in SfM processing (Tonkin & Midgley 2016, Agüera-Vega et al. 2017, James et al. 2017). Again, statistical analysis determined these 0GCP accuracies to be statistical outliers which are represented in Figure 7.7 as blue and orange dots 1.5x beyond the highest inter-quartile range (IQR) of other accuracy results. Removing 0GCP outliers provides a more accurate representation of sUAS + SfM derivative accuracies as shown the various charts of Figure 7.8 below.

0GCP outliers removed, ≥ 5GCP datasets only (14 total)

Combined_Accuracy_R_Outlier_0GCP_Values_Removed		
Range	0.458202	[0.549048864 , 0.0908384]
Mean	0.276579459	
Median	0.236309273	
SD	0.145677118	

Combined_Accuracy_Z_Outlier_0GCP_Values_Removed		
Range	5.95970406	[6.2905225 , 0.33081844]
Mean	2.329878312	
Median	1.680381627	
SD	2.012515062	

	INITIAL_TIE_POINTS		POINT_CLOUD		DSM_RASTER
Survey Dataset	Accuracy_R	Accuracy_Z	Accuracy_R	Accuracy_Z	Accuracy_Z
~~*P3A_SA-1_0GCP*~~	~~*15.2985889*~~	~~*496.734461*~~	~~*15.3674455*~~	~~*495.119418*~~	~~*495.107588*~~
P3A_SA-1_5GCP	0.242237729	5.900967967	0.474864162	6.290522518	6.218657057
P3A_SA-1_8GCP	0.284160942	4.140440249	0.435140581	4.462005326	4.57478758
P3A_SA-1_12GCP	0.278866604	3.369252143	0.397871969	3.636964719	3.841283643
~~P4P_SA-1_0GCP~~	~~12.65357823~~	~~396.1898873~~	~~12.65180936~~	~~395.8060802~~	~~477.8685447~~
P4P_SA-1_5GCP	0.098729356	0.500735888	0.236037953	0.739769538	1.682564716
P4P_SA-1_8GCP	0.090838486	0.429767489	0.226302476	0.604681442	0.953923984
P4P_SA-1_12GCP	0.091373116	0.350159088	0.215313416	0.562304837	1.145862507
~~P3A_SA-2_0GCP~~	~~5.660024991~~	~~409.9199385~~	~~5.795570887~~	~~409.3614139~~	~~409.5349323~~
P3A_SA-2_5GCP	0.53384193	5.885852065	0.549048864	6.291552007	6.38668292
P3A_SA-2_8GCP	0.363162315	2.632442538	0.461000311	2.866791841	2.846127797
P3A_SA-2_11GCP	0.120829922	2.573450182	0.493922849	2.868317064	2.909350323
P3A_SA-2_21GCP	0.318827132	1.678198538	0.443719122	1.762354793	1.995641831
~~P4P_SA-2_0GCP~~	~~6.939588444~~	~~432.9169101~~	~~6.949602374~~	~~432.5604901~~	~~432.4425932~~
P4P_SA-2_5GCP	0.135001918	0.598073052	0.236580593	0.809925505	0.831325161
P4P_SA-2_8GCP	0.124501864	0.40969603	0.213801917	0.723202286	0.65009073
P4P_SA-2_11GCP	0.133462734	0.487742761	0.207086809	0.78142769	0.879464
P4P_SA-2_21GCP	0.125051027	0.330818448	0.212648769	0.554093768	0.697617071

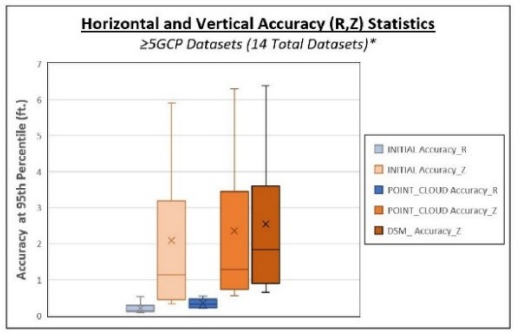

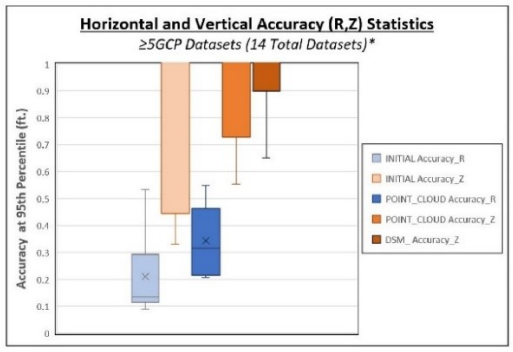

Figure 7.8 Descriptive statistics for ≥ 5GCP survey datasets

After removing the 0GCP outlier accuracy values, accuracy statistics for the remaining 14 sUAS + SfM derived survey datasets demonstrate a reduction in overall range, center measures (mean and median), and standard deviation values.

By comparing Figure 7.7 with Figure 7.8, the influence of 0GCP outliers on cumulative descriptive statistics is apparent. Removing these outliers reduced all calculated statistics for the remaining 14 sUAS + SfM survey datasets with ≥ 5 GCPs. First, the range of $Accuracy_r$ values was reduced from 15.276 ft. to 0.458 ft. (3,235% change) and $Accuracy_z$ values from 496.403 ft. to 5.959 ft. (8,230% change). Additionally, remaining accuracy values are less skewed after removing 0GCP outliers.

This is shown in Figure 7.8 with mean statistics becoming a more accurate measure of center for resulting accuracies than previously in Figure 7.7.

Therefore, based on these results, the value of GCP placement and collection for achieving geospatial accuracy in sUAS + SfM derived survey data must be echoed here as it has in previous studies (Colomina & Molina 2014, Cryderman et al. 2014). However, in addition to GCPs, this research must also consider accuracy variations observed between the two sUAS platforms used for remote sensing data collection.

While P3A derived accuracies in this research were not found to be statistical outliers (excluding 0GCP P3A datasets), they were consistently observed to be less accurate both horizontally and vertically in comparison to P4P derived accuracies at both survey areas. For example, P3A_SA-2_5GCP point cloud survey data exhibited $Accuracy_r$ = 0.594 ft. and $Accuracy_z$ = 6.291 ft., while P4P_SA-2_5GCP point cloud survey data (same survey data type, same survey area, same GCPs used) was found to be $Accuracy_r$ = 0.236 ft. and $Accuracy_z$ = 0.809 ft. Likewise, when georeferencing is optimized with all GCPs available, P3A_SA-2_21GCP point cloud survey data exhibits $Accuracy_r$ = 0.443 ft. and $Accuracy_z$ = 1.762 ft., while P4P_SA-2_21GCP point cloud data (again, same survey data type, area, and GCPs used) was found to be $Accuracy_r$ = 0.212 ft. and $Accuracy_z$ = 0.554 ft.

The most likely reason for accuracy improvement in P4P derived data is the improved quality and capability of the P4P camera payload – especially in regards to shutter mechanism. Again, the P3A camera payload utilizes a digital rolling-shutter mechanism which has already been found detrimental to geospatial accuracy in sUAS + SfM derived survey data (Liang et al. 2008, Albl et al. 2015). In contrast, the P4P utilizes

a mechanical-shutter which eliminates the geospatial issues resulting from rolling-shutter image capture. Additionally, the P4P camera payload also possesses a larger sensor size and megapixel resolution than the P3A camera payload. Therefore, since the P4P represents the latest modern sUAS platform and corresponding capabilities used in this research effort, further insight into resulting survey data accuracies can be achieved by isolating the P4P datasets, again with 0GCP outliers excluded.

P4P ≥ 5GCP datasets only (7 total)

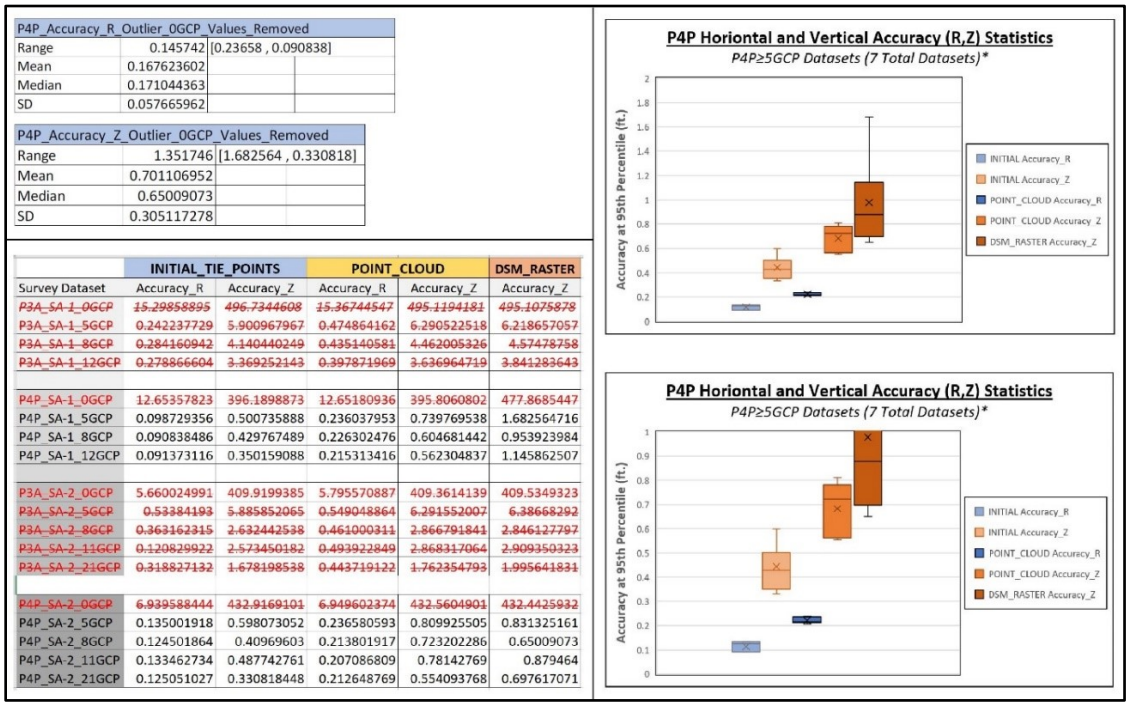

P4P_Accuracy_R_Outlier_0GCP_Values_Removed		
Range	0.145742	[0.23658 , 0.090838]
Mean	0.167623602	
Median	0.171044363	
SD	0.057665962	

P4P_Accuracy_Z_Outlier_0GCP_Values_Removed		
Range	1.351746	[1.682564 , 0.330818]
Mean	0.701106952	
Median	0.65009073	
SD	0.305117278	

	INITIAL_TIE_POINTS		POINT_CLOUD		DSM_RASTER
Survey Dataset	Accuracy_R	Accuracy_Z	Accuracy_R	Accuracy_Z	Accuracy_Z
~~P3A_SA-1_0GCP~~	~~15.29858895~~	~~496.7344608~~	~~15.36744547~~	~~495.1194181~~	~~495.1075878~~
~~P3A_SA-1_5GCP~~	~~0.242237729~~	~~5.900967967~~	~~0.474864162~~	~~6.290522518~~	~~6.218657057~~
~~P3A_SA-1_8GCP~~	~~0.284160942~~	~~4.140440249~~	~~0.435140581~~	~~4.462005326~~	~~4.57478758~~
~~P3A_SA-1_12GCP~~	~~0.278866604~~	~~3.369252143~~	~~0.397871969~~	~~3.636964719~~	~~3.841283643~~
P4P_SA-1_0GCP	12.65357823	396.1898873	12.65180936	395.8060802	477.8685447
P4P_SA-1_5GCP	0.098729356	0.500735888	0.236037953	0.739769538	1.682564716
P4P_SA-1_8GCP	0.090838486	0.429767489	0.226302476	0.604681442	0.953923984
P4P_SA-1_12GCP	0.091373116	0.350159088	0.215313416	0.562304837	1.145862507
P3A_SA-2_0GCP	5.660024991	409.9199385	5.795570887	409.3614139	409.5349323
~~P3A_SA-2_5GCP~~	~~0.53384193~~	~~5.885852065~~	~~0.549048864~~	~~6.291552007~~	~~6.38668292~~
~~P3A_SA-2_8GCP~~	~~0.363162315~~	~~2.632442538~~	~~0.461000311~~	~~2.866791841~~	~~2.846127797~~
~~P3A_SA-2_11GCP~~	~~0.120829922~~	~~2.573450182~~	~~0.493922849~~	~~2.868317064~~	~~2.909350323~~
~~P3A_SA-2_21GCP~~	~~0.318827132~~	~~1.678198538~~	~~0.443719122~~	~~1.762354793~~	~~1.995641831~~
~~P4P_SA-2_0GCP~~	~~6.939588444~~	~~432.9169101~~	~~6.949602374~~	~~432.5604901~~	~~432.4425932~~
P4P_SA-2_5GCP	0.135001918	0.598073052	0.236580593	0.809925505	0.831325161
P4P_SA-2_8GCP	0.124501864	0.40969603	0.213801917	0.723202286	0.65009073
P4P_SA-2_11GCP	0.133462734	0.487742761	0.207086809	0.78142769	0.879464
P4P_SA-2_21GCP	0.125051027	0.330818448	0.212648769	0.554093768	0.697617071

Figure 7.9 Descriptive statistics for P4P ≥ 5GCP survey datasets

With only P4P ≥ 5GCP datasets remaining (7 total), descriptive statistics show resulting accuracies from these specific datasets are higher accuracy, and more consistently and evenly distributed than the cumulative accuracy statistics for all sUAS + SfM survey datasets (18 total).

Figure 7.9 above shows the descriptive statistics as calculated for P4P ≥ 5GCP survey datasets only (7 total datasets). After removing all 0GCP outlier datasets and all P3A derived datasets, descriptive statistics show the remaining accuracies are significantly smaller ranging and more evenly distributed than previous statistics for all survey datasets. First, the range of $Accuracy_r$ values was improved from 15.276 ft. for all survey datasets, to 0.458 ft. with 0GCP outliers removed, now to 0.145 ft. in P4P ≥ 5GCP derived accuracies. Likewise, the range of $Accuracy_z$ values was improved from 496.403 ft. for all survey datasets, to 5.959 ft. with 0GCP outliers removed, now to 1.351 ft. in P4P ≥ 5GCP derived accuracies. Additionally, statistical skew in the remaining accuracy values is practically negligible as the difference in mean and median measures of center for P4P ≥ 5GCP datasets differ by only ~0.01 ft. for $Accuracy_r$ and ~ 0.05 ft. for $Accuracy_z$.

Frequency distribution for resulting accuracies

While the P4P ≥ 5GCP survey datasets clearly achieved greater geospatial accuracy than other datasets in the experiment, it must be noted that descriptive statistics for these datasets used only a limited sample of the available sUAS + SfM survey datasets for calculation (7 of 18 total datasets). Likewise, descriptive statistics calculated for all ≥ 5GCP survey dataset accuracy values (0GCP outliers excluded) also used a limited sample (14 of 18 total datasets). With this consideration in mind, the descriptive statistics for these survey datasets provide additional insight into resulting sUAS + SfM derived accuracies as intended – especially regarding GCP and sUAS camera payload variables and their influence on derivative geospatial accuracy.

Therefore, for this thesis research, geospatial accuracies derived from ≥ 5GCP datasets and P4P ≥ 5GCP datasets are expected to provide the most relevant results. In addition to the descriptive statistics provided above, the frequency distribution of resulting accuracies for these survey datasets are shown in the histograms of Figure 7.10 below. Likewise, Figures 7.11 and 7.12 provide accuracy distribution comparisons between survey areas (SA-1, SA-2) and sUAS platforms (P3A, P4P) with 0GCP outliers removed (coincides with Figures 1.27 – 1.30).

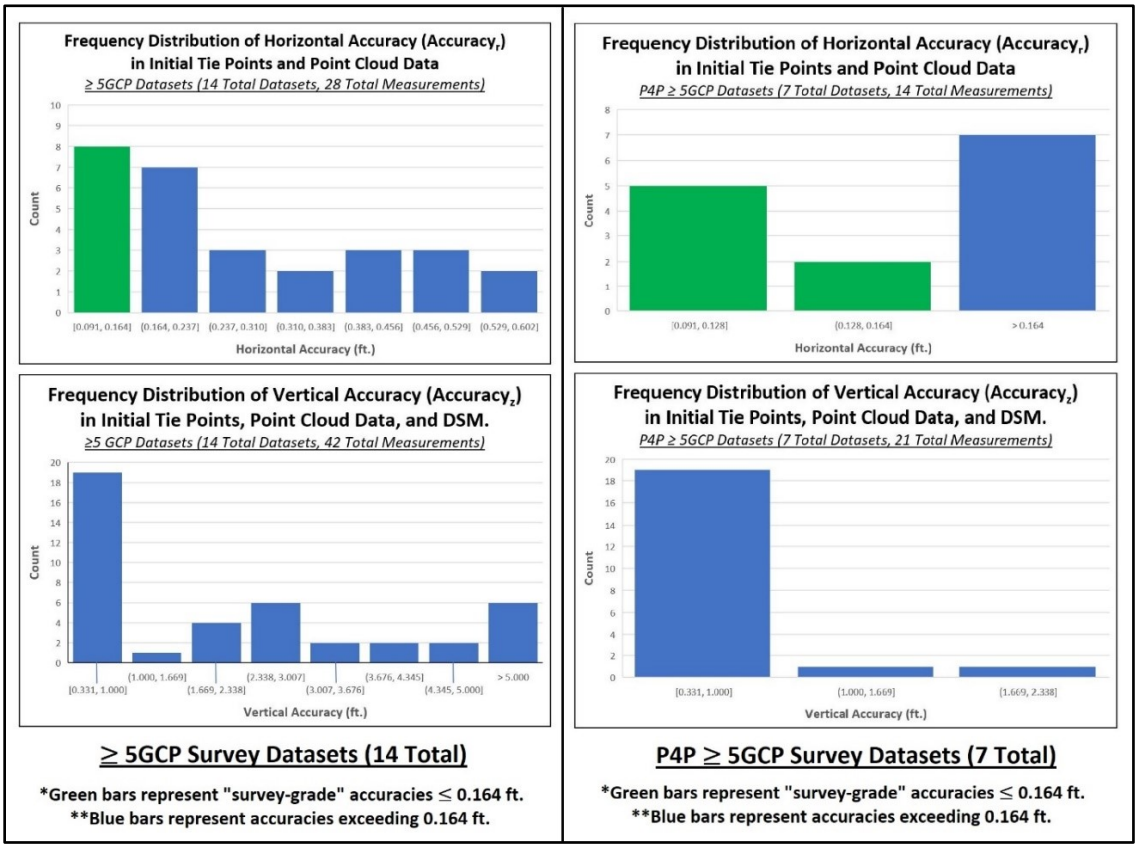

Figure 7.10 Frequency distribution of accuracy in ≥ 5GCP and P4P ≥ 5GCP datasets

Frequency distributions of resulting accuracies in ≥ 5GCP and P4P ≥ 5GCP survey datasets. Distributions show "survey-grade" accuracies numbered fewer than non-survey grade accuracies in sUAS + SfM derived survey data. Additionally, no survey data types or datasets were found to achieve "survey-grade" vertical accuracy.

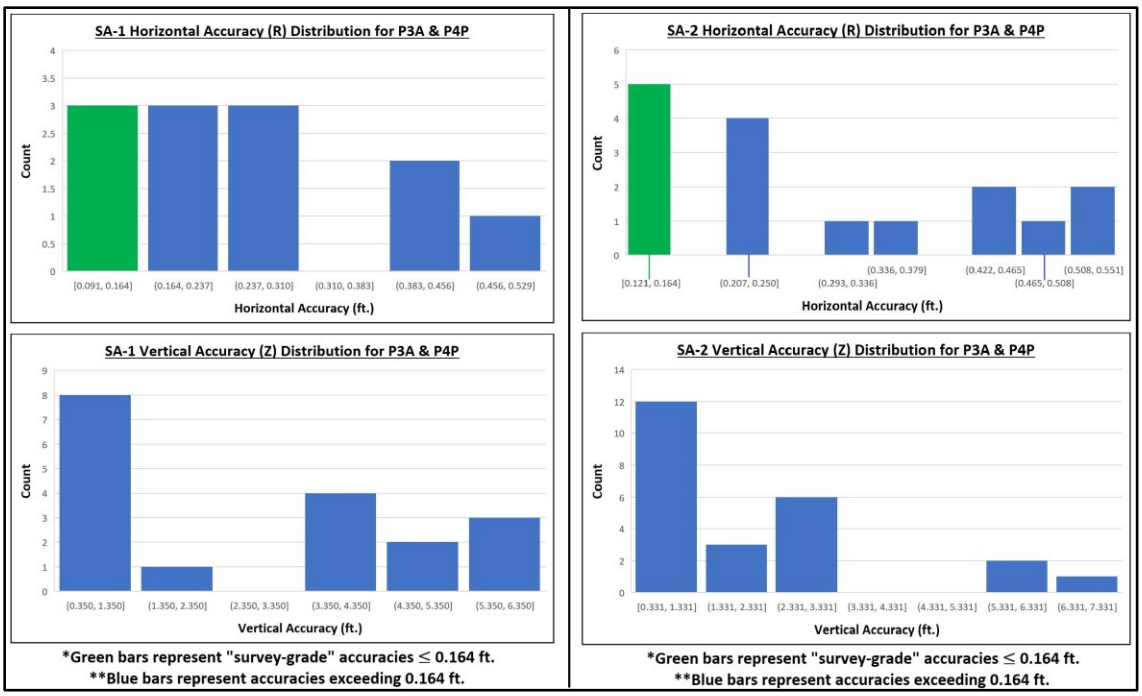

Figure 7.11 SA-1 and SA-2 accuracy distributions (0GCP outliers removed)

On the left, distribution of SA-1 derived accuracies for both P3A and P4P are shown. On the right, distribution of SA-2 derived accuracies for both P3A and P4P are shown. For both sides, green bars indicate "survey-grade" accuracies ≤ 0.164 ft. and blue bars indicate accuracies exceeding the 0.164 ft. threshold.

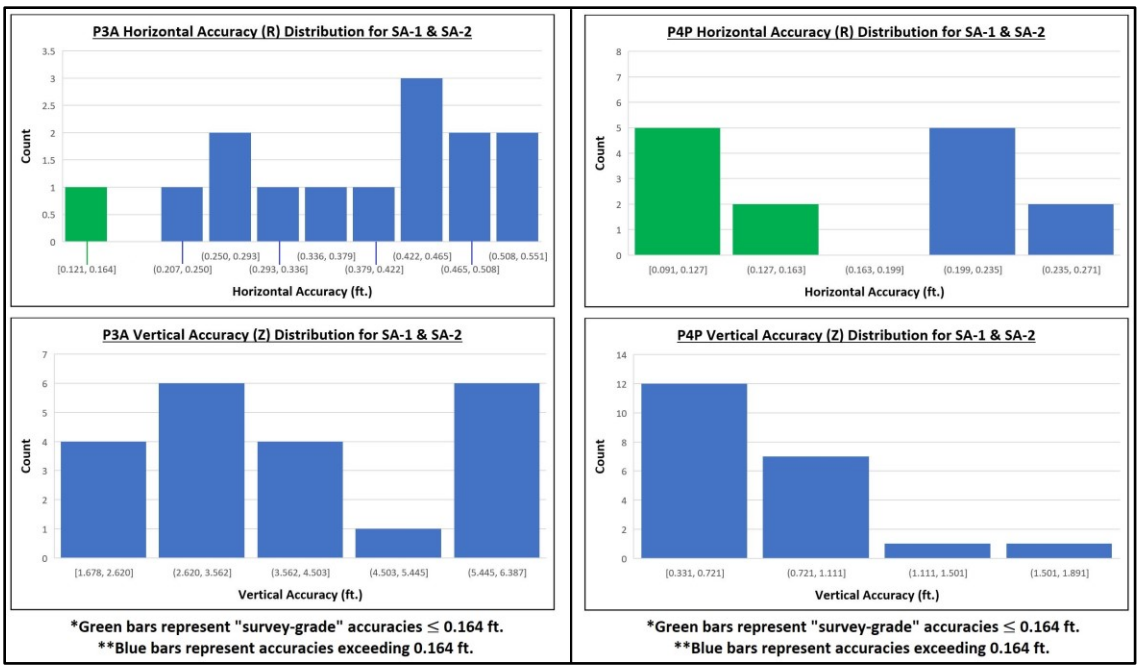

Figure 7.12 P3A and P4P accuracy distributions (0GCP outliers removed)

On the left, distribution of P3A derived accuracies at both SA-1 and SA-2 are shown. On the right, distribution of P4P derived accuracies for both SA-1 and SA-2 are shown. For both sides, green bars indicate "survey-grade" accuracies ≤ 0.164 ft. and blue bars indicate accuracies exceeding the 0.164 ft. threshold.

CHAPTER VIII

DISCUSSION

Research objective evaluation

All research efforts were conducted to address a specific research objective as presented in Chapter I – INTRODUCTION. Specifically, the research objective posed three questions relating to geospatial accuracy in sUAS + SfM derived survey data. Having conducted the experiment and calculated accuracy results and associated statistics, it was necessary to evaluate final results against the questions posed in the research objective.

Question 1. What geospatial accuracies were observed?

The first question specifically asked, "What geospatial accuracies are observed in survey data derived from modern prosumer sUAS platforms and SfM photogrammetry?". Referring back to Figures 1.26 – 1.31, horizontal accuracies ($Accuracy_r$) were observed from 15.37 ft. – 0.09 ft. and vertical accuracies ($Accuracy_z$) observed from 496.73 ft. – 0.33 ft. Greatest geospatial accuracies were most frequently observed in survey datasets which utilized all available GCPs for georectification. This includes 12 GCPs at SA-1, and 21 GCPs at SA-2, distributed systematically throughout the extent of each survey area at approximately 1 GCP per 0.5 acres. Poorest geospatial accuracies were exclusively observed in 0GCP survey datasets, consistent with existing research (e.g. Tonkin & Midgley 2016, Agüera-Vega et al. 2017, Cook 2017, James et al. 2017). For

example, P4P_SA-2_0GCP vertical accuracies were only accurate within ~432 ft., which holds very little value for any high accuracy geospatial application. Alternatively, P4P_SA-2_21GCP vertical accuracies were reported as high as 0.33 ft. – the highest observed vertical accuracy of the experiment.

After removing 0GCP derived accuracy values as statistical outliers, remaining ≥ 5GCP derived horizontal accuracies ($Accuracy_r$) were observed between 0.549 ft. – 0.09 ft. and vertical accuracies ($Accuracy_z$) between 6.290 ft. – 0.33 ft, again with accuracies improving as additional GCPs are incorporated. These resulting accuracies are shown sUAS + SfM survey dataset in Figure 8.1 below.

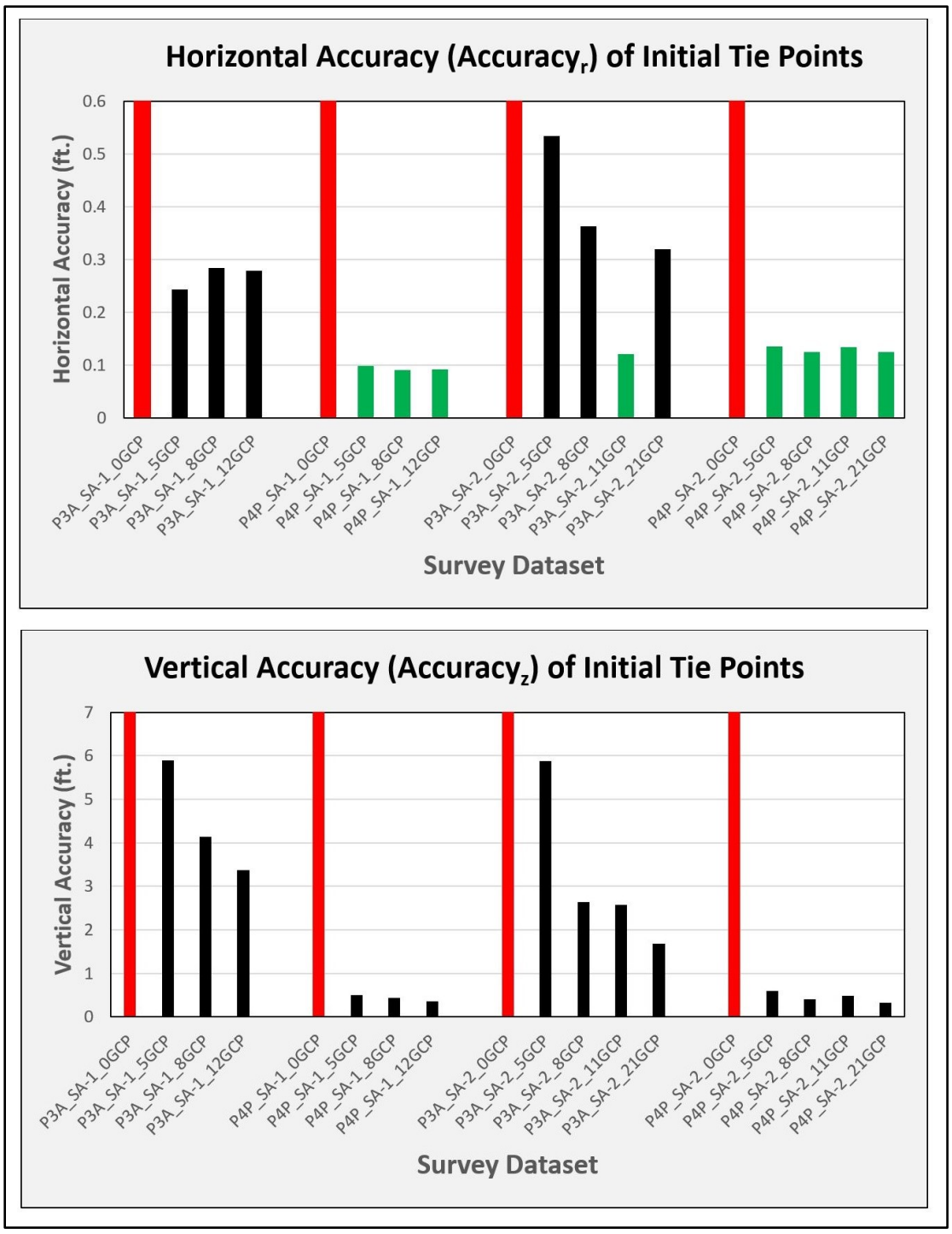

Figure 8.1 Resulting accuracy by sUAS + SfM dataset

Resulting accuracies in initial tie points survey data for all sUAS + SfM survey datasets. Red bars represent statistical outliers extending beyond the scope of the graph. Green bars represent "survey-grade" accuracies at ≥ 0.164 ft.

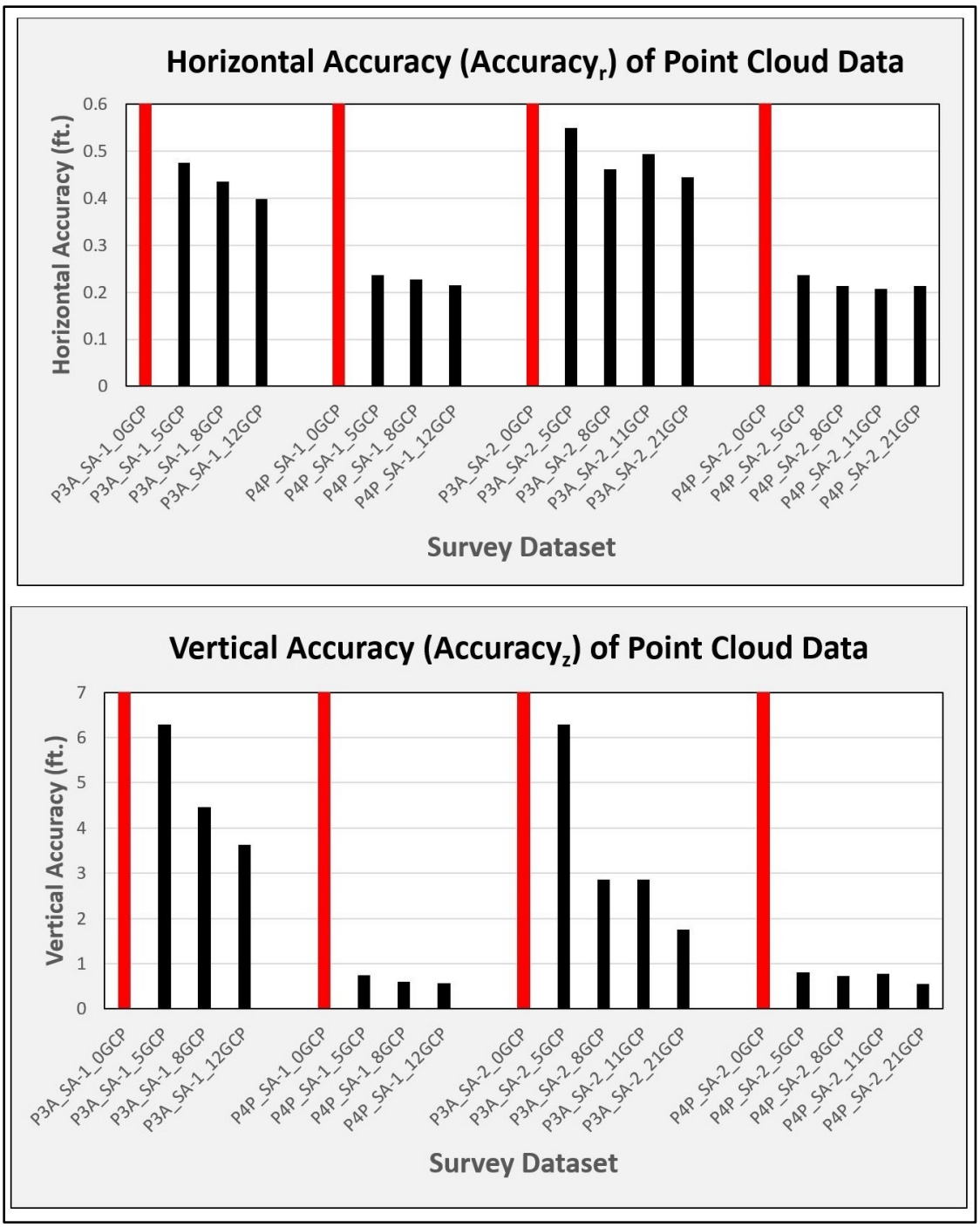

Figure 8.1 (continued)

Resulting accuracy in point cloud survey data for all sUAS + SfM survey datasets. Red bars represent statistical outliers extending beyond the scope of the graph. No datasets were found to achieve "survey-grade" accuracy ≥ 0.164 ft.

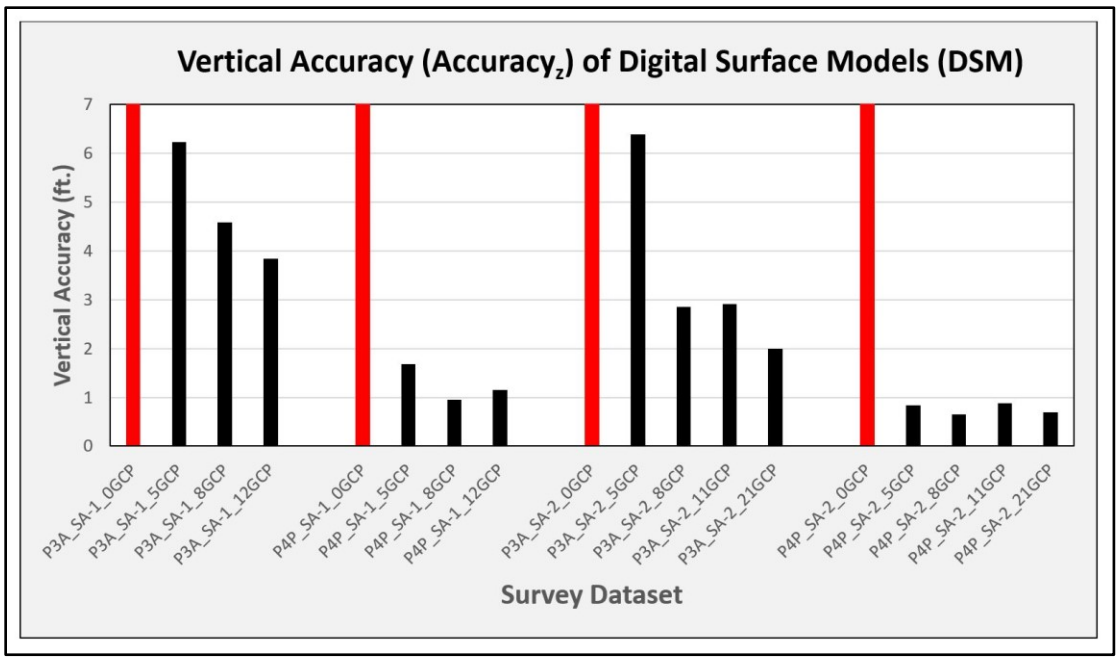

Figure 8.1 (continued)

Resulting vertical accuracy in digital surface model (DSM) survey data for all sUAS + SfM survey datasets. Red bars represent statistical outliers extending beyond the scope of the graph. No datasets were found to achieve "survey-grade" accuracy ≥ 0.164 ft.

Among these accuracy results, a clear distinction existed between datasets derived from the two different sUAS platforms used (P3A, P4P). Geospatial accuracies derived from the older P3A platform were consistently observed to be 2-3 times poorer horizontally, and up to 5-6 times poorer vertically, than accuracies derived from the newer P4P platform. For example, P3A_SA-1_5GCP initial tie point survey data exhibited horizontal accuracy of 0.533 ft., while P4P_SA-1_5GCP initial tie points achieved a horizontal accuracy of 0.135 ft. at the same survey area and using the same GCPs. Again, the most likely reason for higher observed accuracies in P4P derived survey data is the improved camera payload of the P4P as previously described. Since,

the P4P represents the latest of the two sUAS platforms used in this research, P4P derivative survey accuracies are expected to be a more accurate representation of current and near-term modern sUAS capabilities.

Question 2. What accuracy classifications (FGDC) were achieved?

As previously stated in Chapter VII - RESULTS, sUAS + SfM derived survey datasets achieved accuracy classifications between 5-Meter and 2-Centimeter (16.504 – 0.065 ft. equivalent) horizontally, and no better than 1-Decimeter (0.328 ft. equivalent) vertically. These classifications are consistent with established FGDC accuracy classifications previously shown in Figure 7.6. Again, since FGDC accuracy classifications are provided in metric unit values only, equivalent imperial values have been cited alongside metric accuracy classifications throughout this thesis for unit consistency.

In practice, FGDC accuracy classifications serve to provide a consistent means of communicating geospatial accuracy in survey data. Specifically, these FGDC classifications are used in communicating the accuracy (again at the 95% confidence level) of geodetic control networks (FGDC 1998). However, given their established use for this practice, FGDC standards are also often used to communicate accuracy for other geospatial data beyond geodetic control networks – such as the sUAS + SfM derived survey data of this research. Therefore, while resulting FGDC accuracies classifications do not provide a great deal of additional insight into resulting accuracy values, these classifications serve two important roles for the purpose of this research.

First, resulting FGDC accuracy classifications provide the established means of communicating geospatial accuracy, versus simply reporting $Accuracy_r$ and $Accuracy_z$ as

calculated (done for Question 1 above). In professional surveying practice it is much more common to hear geospatial accuracy communicated as 1-Meter, 1-Centimeter, 1-Millimeter, etc., than 0.068 meter, 6.8 centimeter, or 68 millimeter. This is because FGDC classifications are based on threshold accuracy values where resulting accuracies greater than or equal to the stated accuracy threshold at 95% confidence are grouped. For example, observed accuracies of 0.011 meters and 0.019 meters would both be classified as 2-Centimeter accuracy using the FGDC classifications. Therefore, for the purpose of this research, resulting FGDC accuracy classifications as described here in response to Question 2 serve to provide an established, broadly-applicable means of communicating resulting accuracies observed in this research.

Second, and most importantly for the purpose of this research, the 5-Centimeter FGDC accuracy classification has served as the qualifying accuracy classification for "survey-grade" accuracy. As previously mentioned, "survey-grade" accuracy refers to geospatial accuracy which is considered adequate for professional surveying and engineering practice. Generally, "survey-grade" accuracy is required where geospatial accuracy directly translates to the safety and/or structural integrity of a project or application. Some industry debate exists as to whether "survey-grade" accuracy should refer to sub-centimeter accuracy only (FGDC Millimeter accuracy classifications), or if "survey-grade" accuracy includes centimeter accuracies as well. To be clear, this research has assumed the latter and again used the 5-Centimeter (0.164 ft.) accuracy classification to designate "survey-grade" accuracy in resulting sUAS + SfM survey data.

At this point, it must be noted that FGDC classifications are provided in metric units only (again demonstrated in Figure 7.6). This differs from FGDC accuracy

reporting guidelines which allow accuracies to be reported in either metric or imperial units (whichever unit used in the dataset) per FGDC Geospatial Positioning Accuracy Standards – *Part 3: National Standard for Spatial Data Accuracy* (FGDC). The reason for this difference is again based on the fact that FGDC classifications are designed to communicate accuracy for geodetic control networks per FGDC Geospatial Positioning Accuracy Standards, *Part 2: Standards for Geodetic Networks*. Therefore, since imperial unit accuracy classifications are not established by the FGDC, equivalent imperial units (feet in this case) have been provided for all resulting FGDC accuracy classifications in order to utilize consistent units for the purpose of this thesis.

Question 3. Is "survey-grade" accuracy achieved, both horizontally and vertically?

No, resulting accuracies as observed and classified in Questions 1 and 2 demonstrate that no sUAS + SfM derived data achieved survey-grade accuracy both horizontally and vertically at the 5-Centimeter (0.164 ft.) FGDC classification or greater. As previously discussed, FGDC accuracy classifications are reported in ground distances at the 95% confidence level. This means that 95% of positional error within the dataset must be ≤ the reported accuracy. With 20 checkpoints collected by independent source of higher accuracy for use in accuracy testing, sUAS + SfM survey data error values at 19 checkpoints (95%) must be observed within the reported accuracy. Likewise, sUAS + SfM survey data error at only one checkpoint (5%) may fall beyond the reported accuracy. Therefore, to achieve survey-grade accuracy at the 5-Centimeter (0.164) FGDC classification, sUAS + SfM survey data error values at 19 of the 20 checkpoints must be ≤ 0.164 ft.

To further examine this point, the sUAS + SfM survey datasets with the highest reported accuracies from each sUAS platform at each survey area were isolated so that positional errors could be evaluated against the ≤ 0.164 ft. survey-grade threshold. Specifically, these datasets included P3A_SA-1_12GCP, P3A_SA-2_21GCP, P4P_SA-1_12GCP, and P4P_SA-2_21GCP. Reported accuracies for these selected datasets are shown in Figure 8.2 below.

	INITIAL_TIE_POINTS		POINT_CLOUD		DSM_RASTER
Survey Dataset	Accuracy_R	Accuracy_Z	Accuracy_R	Accuracy_Z	Accuracy_Z
P3A_SA-1_12GCP	0.278866604	3.369252143	0.397871969	3.636964719	3.841283643
P3A_SA-2_21GCP	0.318827132	1.678198538	0.443719122	1.762354793	1.995641831
P4P_SA-1_12GCP	0.091373116	0.350159088	0.215313416	0.562304837	1.145862507
P4P_SA-2_21GCP	0.125051027	0.330818448	0.212648769	0.554093768	0.697617071

Figure 8.2 Highest reported accuracies (ft.) by sUAS platform and survey area

Highest reported accuracies in sUAS + SfM derived survey by sUAS platform and survey area were observed between 0.443 ft. – 0.091 ft. horizontally and 3.841 ft. – 0.330 ft. vertically. Of these accuracies, only 2 reported "survey-grade" accuracy at ≤ 0.164 ft. were observed as outlined in blue. Remaining accuracies outlined in red exceed the ≤ 0.164 ft. "survey-grade" accuracy threshold.

As shown by the blue outlined values in Figure 7.4, only 2 of the remaining survey datasets/types achieved survey-grade horizontal accuracy at ≤ 0.164 ft. (P4P_SA-1_12GCP, P4P_SA-2_21_GCP). By reverting to all 18 sUAS + SfM survey datasets, a total of 8 datasets (including the 2 above) achieved similar survey-grade horizontal accuracy in initial tie points data with seven being P4P derived and one being P3A

derived. However, neither these datasets nor any other resulting sUAS + SfM derived survey data of the experiment were found to achieve survey-grade horizontal accuracy in subsequent survey data types (point cloud, DSM). Additionally, no resulting sUAS + SfM survey data in the experiment was found to achieve survey-grade vertical accuracy at ≤ 0.164 ft. To further examine this point a comprehensive error analysis was performed on each of the 4 highest accuracy sUAS + SfM derived datasets (P3A_SA-1_12GCP, P3A_SA-2_21GCP, P4P_SA-1_12GCP, and P4P_SA-2_21GCP). The results of each analysis are provided in Appendices C – F. Figure 8.3 below provides an excerpt from each of these appendices to demonstrate the results of survey-grade accuracy evaluation for the purpose of answering research question 3.

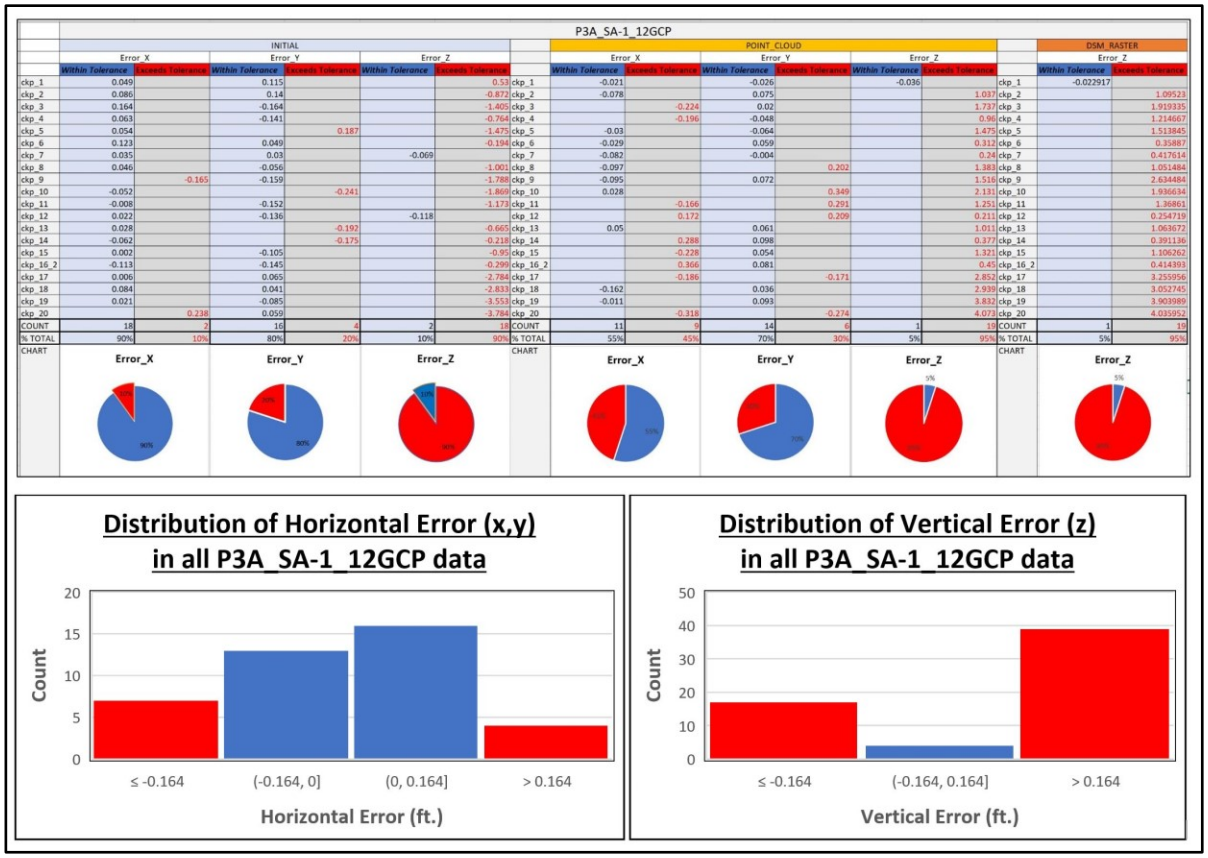

Figure 8.3 Survey-grade accuracy evaluation of sUAS + SfM error values

Positional error as recorded in P3A_SA-1_12GCP derived survey data. Red error values and corresponding red sections in the associated charts represent error values exceeding the ≤ 0.164 ft. survey-grade threshold tolerance. Blue error values and corresponding blue sections in the associated charts represent error values within the ≤ 0.164 ft. tolerance.

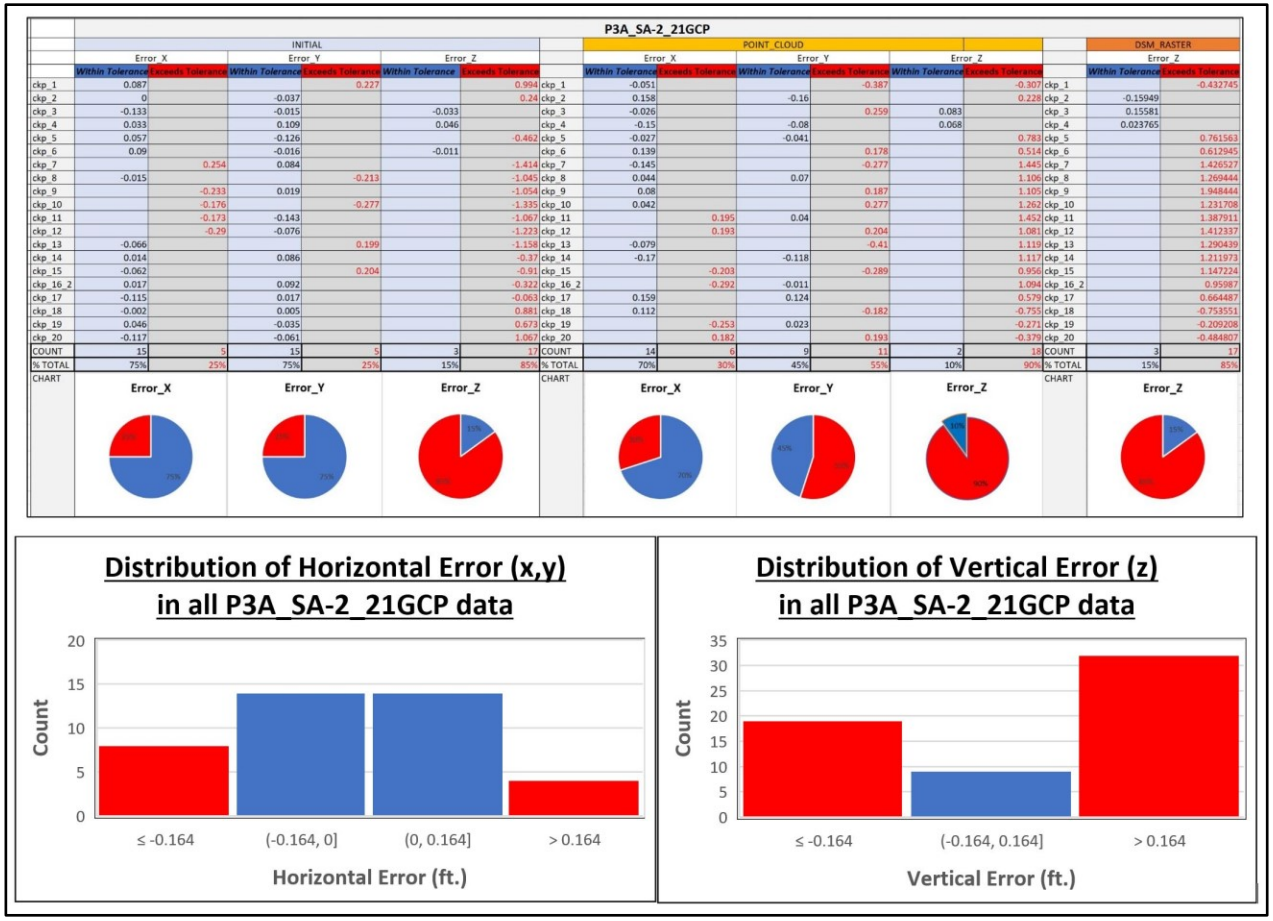

Figure 8.3 (continued)

Positional error as recorded in P3A_SA-2_21GCP derived survey data. Red error values and corresponding red sections in the associated charts represent error values exceeding the ≤ 0.164 ft. survey-grade threshold tolerance. Blue error values and corresponding blue sections in the associated charts represent error values within the ≤ 0.164 ft. tolerance.

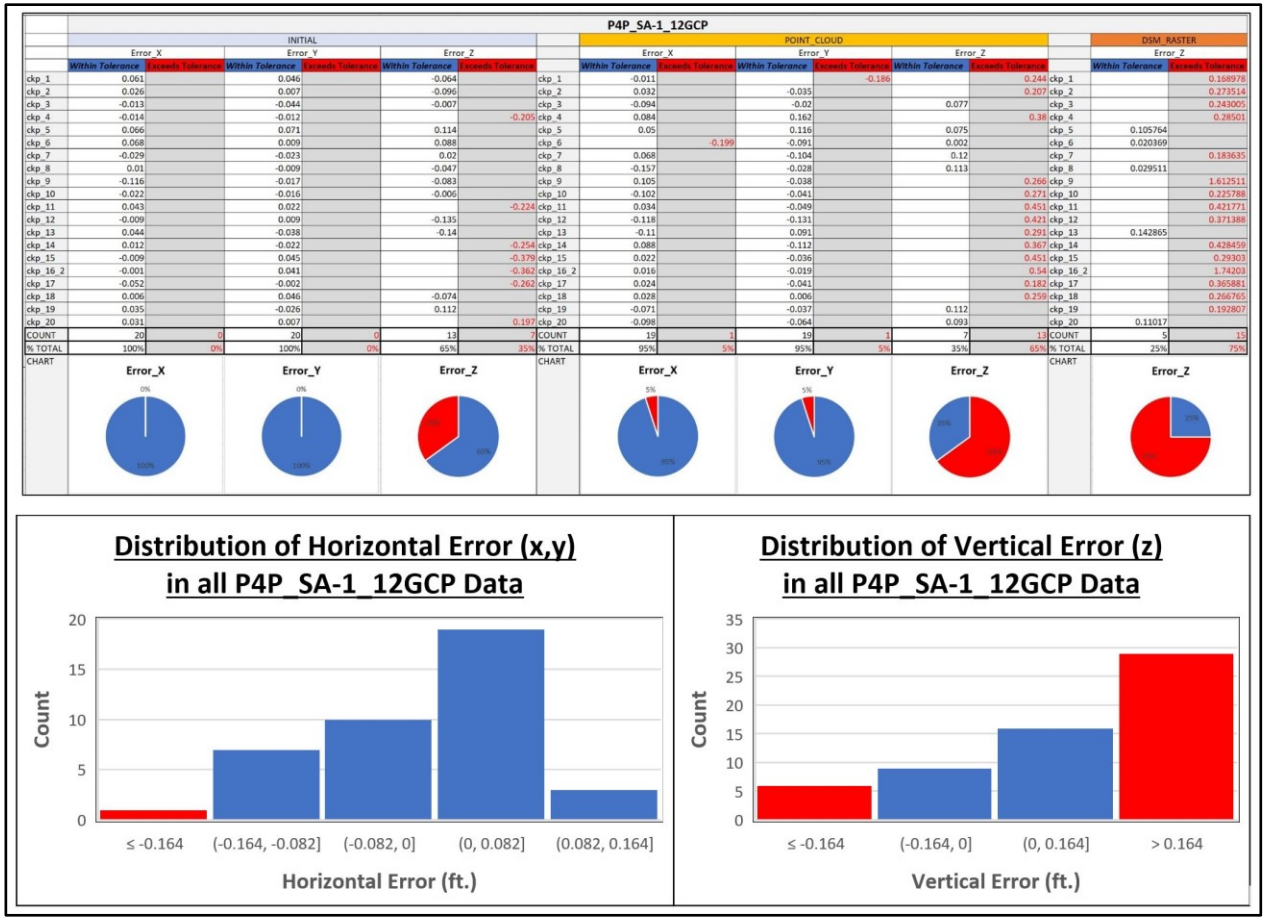

Figure 8.3 (continued)

Positional error as recorded in P4P_SA-1_12GCP derived survey data. Red error values and corresponding red sections in the associated charts represent error values exceeding the ≤ 0.164 ft. survey-grade threshold tolerance. Blue error values and corresponding blue sections in the associated charts represent error values within the ≤ 0.164 ft. tolerance.

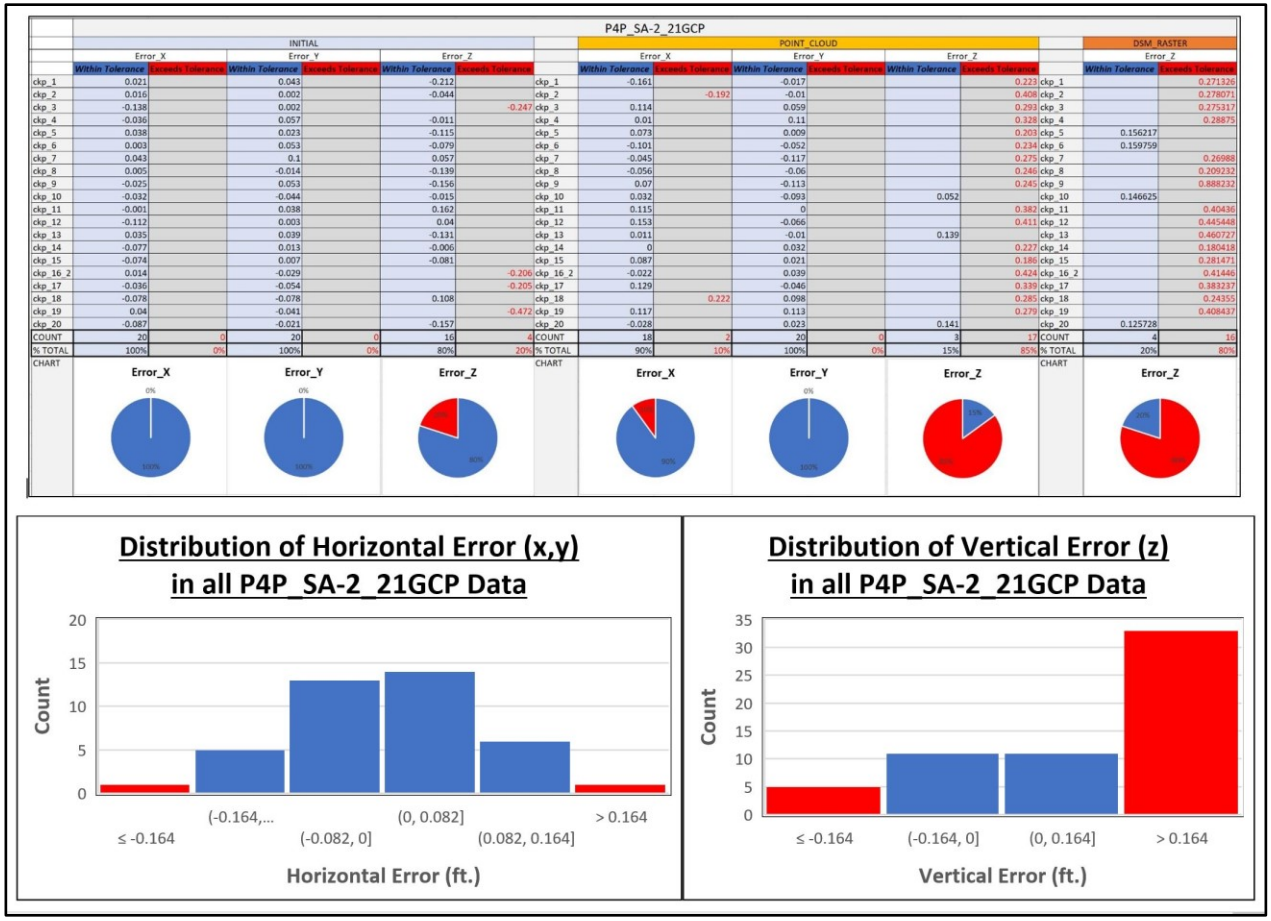

Figure 8.3 (continued)

Positional error as recorded in P4P_SA-2_21GCP derived survey data. Red error values and corresponding red sections in the associated charts represent error values exceeding the ≤ 0.164 ft. survey-grade threshold tolerance. Blue error values and corresponding blue sections in the associated charts represent error values within the ≤ 0.164 ft. tolerance.

As shown in Figure 7.5, positional error values observed for the sUAS + SfM datasets with the highest reported accuracies clearly fall short of achieving survey-grade accuracy at ≤ 0.164 ft. in most cases. The only exemptions which did achieve survey grade accuracy among these datasets were found to do so in horizontal accuracy only, and not in vertical accuracy. These exemptions include P4P_SA-1_12GCP and P4P_SA-2_21GCP initial tie points survey data – 2 of the 8 datasets reporting "survey-grade" horizontal accuracy initial tie points data as shown in Figure 7.4.

Interestingly, the full density point cloud survey data from each of these survey datasets (P4P_SA-1_12GCP and P4P_SA-2_21GCP) also tested relatively well in regards to positional error at checkpoint locations. In fact, positional error values at 18 of 20 checkpoint locations in both datasets were observed to be within the ≤ 0.164 ft. survey-grade threshold. However, since FGDC accuracies are reported at the 95% confidence level, these datasets fall short of survey-grade accuracy with only 90% of observed error (18 of 20 checkpoints) being ≤ 0.164 ft. survey-grade threshold. This corroborates the calculated horizontal accuracies for both P4P_SA-1_12GCP and P4P_SA-2_21GCP point cloud data which were reported as 0.215 ft and 0.212 ft., respectively, as previously shown in Figure 7.4.

Figure 8.4 below as taken from Appendix E further demonstrates how positional error in P4P_SA-2_21GCP initial tie point survey data achieved survey-grade horizontal accuracy (reported at 0.125 ft.) with regards to horizontal error, and how point cloud survey data from the same dataset did not (horizontal accuracy reported at 0.212 ft.). Additionally, Figure 8.5 below, also taken from Appendix E, demonstrates how vertical error in both the initial tie points and the point cloud data of these same datasets failed to

achieve survey-grade vertical accuracy. Similar evaluations and graphics are provided for each of the 4 highest accuracy sUAS + SfM survey datasets in the comprehensive error evaluations of Appendices C-F.

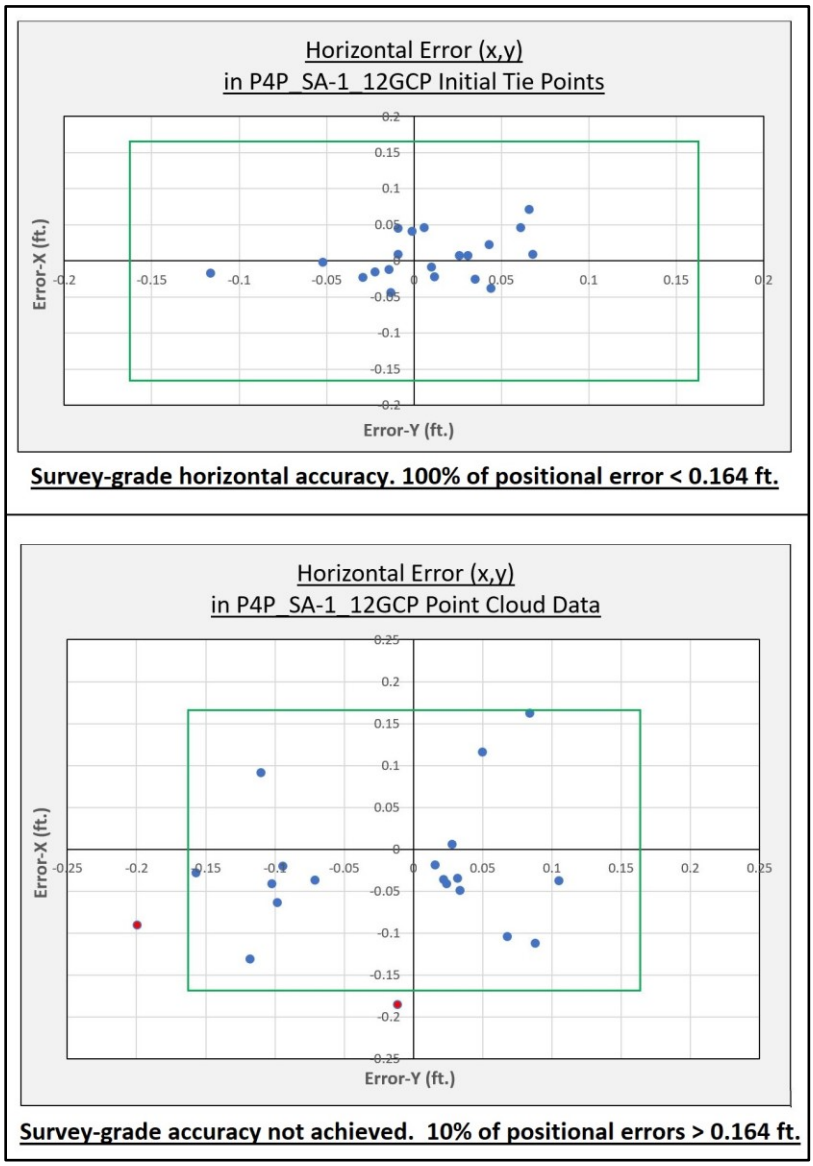

Figure 8.4 Horizontal error in relation to survey-grade accuracy at P4P_SA-1_12GCP

Survey-grade horizontal accuracy at ≤ 0.164 ft. is represented by the green outline. Checkpoint locations with horizontal error ≤ 0.164 ft. are represented in blue, while checkpoint locations with horizontal error > 0.164 ft. are represented in red.

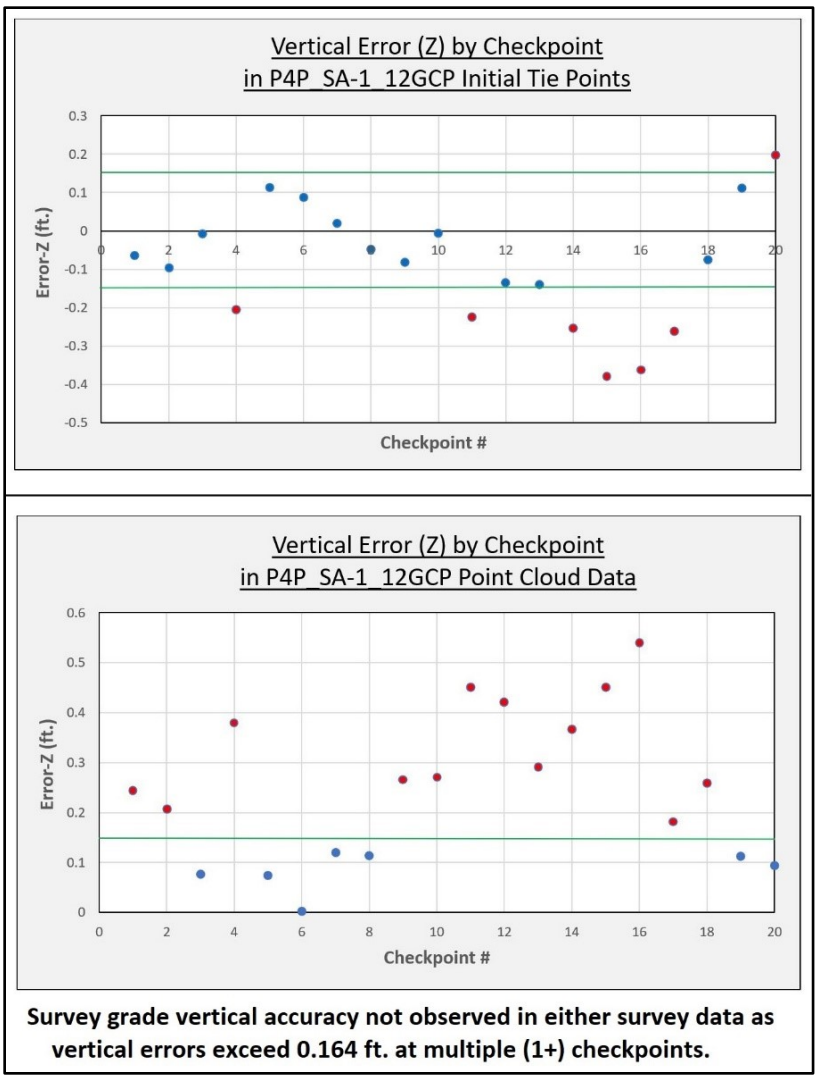

Figure 8.5 Vertical error in relation to survey-grade accuracy at P4P_SA-1_12GCP

Survey-grade vertical accuracy at 0.164 ft. is represented by the green lines. Checkpoint locations with vertical error < 0.164 ft. are represented in blue, while checkpoint locations with vertical error > 0.164 ft. are represented in red.

Therefore, after examining the resulting sUAS + SfM survey data accuracies from this experiment, and analyzing the positional error observed in the four highest accuracy datasets as shown here and in APPENDICES C-F, it can be confirmed that survey-grade

accuracy was not achieved both horizontally and vertically at the 5-Centimeter (0.164 ft.) FGDC classification for any sUAS + SfM derived survey data in the experiment.

Additional discussion

Having addressed the research objective questions of this thesis, some additional topics of discussion remain noteworthy. These topics are discussed in detail below.

Error calculation considerations for various survey data types

Datasets which achieved "survey-grade" horizontal accuracy were observed to do so in initial tie points survey data only (P4P_SA-1_12GCP, P4P_SA-2_21GCP). Upon further analysis, it is clear reported accuracies for initial tie points survey data were consistently greater (more accurate) than reported accuracies for subsequent survey data types (point cloud and DSM). It is expected these higher accuracies were the result of using Pix4D Mapper Pro calculated error ("Error to GCP Initial Position") at checkpoint positions for initial tie points data, as opposed to using actual 3D point positions and raster cells for error calculation as done for point cloud and DSM survey data. The use of checkpoint "Error to GCP Initial Position" values for initial tie points error calculation was done intentionally, however, resulting accuracies for initial tie points data are expected to have benefited from this methodology.

For sUAS + SfM derived point cloud survey data, it is important to note that multiple 3D points were reconstructed at all checkpoint locations given the high point density of these data. Even with multiple 3D points available, rarely does a single 3D point coincide perfectly with the central checkpoint position where *in situ* collection of the checkpoint was made. Even though error calculation was made from 3D points

selected to best represent central checkpoint positions within the point cloud, it must be acknowledged this method is imperfect as selected 3D points again rarely coincide with the exact checkpoint position from which error calculations were made. Therefore, while error calculation and accuracy reporting for point cloud data was conducted consistent with FGDC accuracy testing requirements, resulting error and accuracy values for all point cloud data were undoubtably influenced by the proximity of selected 3D points to the true checkpoint location were *in situ* checkpoint collection was made.

Alternatively, sUAS + SfM derived DSM survey data was not subject to the same error evaluation short comings of point cloud data. For DSM survey data, raster pixels which coincided with exact checkpoint positions were used for error calculation in ArcMap. Unfortunately, since only vertical coordinate values (z) were available for DSM data, only vertical error and vertical accuracy could be calculated for this data. Nonetheless, these vertical error and vertical accuracy values for DSM data are expected to be highly accurate as the error calculation method for these data was more consistent than error calculation for point cloud survey data.

P4P accuracy considerations

As previously discussed, P4P derived survey data consistently outperformed P3A derived survey data in regard to geospatial accuracy. This result was expected given the improved camera payload of the newer P4P platform. However, upon further examination, P4P derived survey data accuracy was also found to be remarkably consistent with regards to the number and frequency of GCPs used in SfM processing. For example, P4P_SA-1_5GCP point cloud data achieved a horizontal accuracy of 0.236 ft. and a vertical accuracy of 0.739 ft., while P4P_SA-2_5GCP point cloud data achieved

a horizontal accuracy of 0.236 ft. and a vertical accuracy of 0.809 ft. In this case, with both datasets using an equivalent number of GCPs (5), P4P derived accuracies differ by only 0.0004 ft. horizontally and 0.07 ft. vertically. Once optimized with all available GCPs, P4P_SA-1_12GCP point cloud data reports a horizontal accuracy of 0.215 ft. and a vertical accuracy of 0.562 ft., while P4P_SA-2_21GCP point cloud data reports horizontal accuracy of 0.212 ft. and vertical accuracy of 0.554. In this case, with both datasets using an equivalent frequency of GCPs (1 GCP per 0.5 acre), P4P derived accuracies are again very consistent with differences of only 0.003 ft. horizontally and 0.008 ft. vertically. Therefore, it must be noted that P4P derived survey data not only consistently outperformed the older P3A platform with regards to geospatial accuracy, but that P4P derived survey data also generated consistent accuracies across SA-1 and SA-2 with regard to the number and frequency of GCPs used in SfM processing.

Revisiting field method considerations

Two previously acknowledged variables relating to geospatial accuracy in sUAS + SfM derived survey data in this research must be revisited. First, as stated in Chapter IV – FIELD METHODS, P3A remote sensing data collection at SA-1 was cut short due to a hardware error (motors overheated). As a result, only 91 JPG digital images were available for SfM processing of all P3A_SA-1 survey datasets. This number of images was significantly fewer for SfM processing than that of all other sUAS + SfM datasets of the experiment. Therefore, error values and resulting accuracies as reported for all P3A_SA-1 survey datasets may have been negatively affected by the limited number of JPG images available for SfM processing. Second, and also previously stated in Chapter IV – FIELD METHODS, P4P remote sensing data collection at SA-1 was conducted in

sky cover conditions which were less than ideal in regards to incident lighting. It was confirmed that cloud cover during this time did result in uneven incident lighting across SA-1 as previously shown in Figure 4.10. Therefore, error values and resulting accuracies reported for all P4P-SA-1 survey data may have been negatively affected by this uneven lighting as demonstrated in similar research (Cryderman et al 2014, Clapuyt et al. 2016).

Opportunities for additional research

Having addressed the research objective questions for this thesis, numerous opportunities for additional research remain plausible for sUAS derived survey data. First, the scope of this thesis research was limited to only 2 modern prosumer sUAS platforms and their derived survey data accuracy. One opportunity for additional research comes in extending the accuracy test experiment of this thesis to include "professional" sUAS platforms. An accuracy test of these professional platforms would not only provide equivalent insight into the geospatial accuracy of survey data derived from professional sUAS, but also how those accuracies compare to resulting accuracies derived from prosumer sUAS as presented here.

Additionally, the scope of this research was also limited to only 2 survey area test sites where accuracy testing was conducted. These survey area test sites both exhibited certain land use characteristics which are known to challenge SfM processing practices (steep elevations changes in SA-1, vegetation in SA-2). Another opportunity for additional research comes by expanding the survey areas used for accuracy testing. Ideally, future research efforts would not only expand the number of survey areas used for accuracy testing, but also the geographic size and land use characteristics of the

survey areas themselves. For example, no bare-earth survey areas were available for accuracy testing during this thesis research. However, existing scientific research currently shows that bare-earth survey environments can be ideal subjects for SfM photogrammetry under the right conditions (e.g. Hugenholtz et al. 2013, Cryderman et al. 2014, Siebert & Teizer 2014, Ishiguro et al. 2016). Therefore, additional research which evaluates sUAS + SfM derived survey data accuracies at bare-earth survey environments, as opposed to those used in this research, would certainly provide further results and insight on the topic of sUAS + SfM derived accuracies.

Furthermore, the scope of this research was also limited to only a single sUAS data collection application and SfM processing software – Pix4D Capture and Pix4D Mapper Pro, respectively. While both of these solutions are commonly used for surveying applications with sUAS, they represent only 2 of the many sUAS data collection and SfM processing solutions currently on the market. Additionally, the specific parameters used for data collection and SfM processing in this thesis represent only a fraction of the many parameters available for performing both tasks. Therefore, additional research opportunities can be readily found in the examination of multiple sUAS data collection and SfM processing solutions not utilized within this thesis research (e.g. Jaud et al. 2016). Furthermore, additional research opportunities are also available for examination of specific data collection and/or SfM processing parameters and their resulting influence on sUAS + SfM derived survey data accuracy (e.g. Udin & Ahmad, 2014, Mesas-Carrascosa et al. 2016).

Also, while many factors known to influence geospatial accuracy have been acknowledged and discussed in this thesis research, additional research opportunities

abound for quantifying the influence of these factors on geospatial accuracy. To do so, more advanced statistical analytics would likely be required. For example, the use of regression analysis to evaluate and quantify the influence of factors such as wind speed, incident lighting variations, GCP distribution, etc. as independent variables on the dependent variable of geospatial accuracy would be especially valuable. Ideally, additional research efforts in this area would provide more detailed insight on the influence of these factors, and thereby allow geospatial professionals and academics to more effectively plan and conduct successful sUAS surveying operations.

Finally, research efforts studying the sources of systematic error from which geospatial accuracy suffers when using the sUAS + SfM methodology represents a most pivotal opportunity for additional research. The purpose of this thesis research has been to observe and report geospatial accuracies achieved using the sUAS + SfM methodology. Having now done so, if only to a very small extent, the geospatial community would now benefit most from additional research which provides insight for improving geospatial accuracy when using this methodology. Additional research into systematic errors, such as those arising from spatial projection, resampling, and interpolation methods, and potential solutions to address these errors seems the most logical approach to do so.

CHAPTER IX

SUMMARY AND CONCLUSIONS

Summary

Modern prosumer sUAS platforms have significantly reduced the long-standing cost and expertise barriers associated with aerial remote sensing. Additionally, modern sUAS platforms now allow for aerial remote sensing at lower altitudes and higher spatial and temporal resolutions than ever before. As a result, geospatial professionals and academics which utilize aerial remote sensing data have rapidly adopted sUAS platforms for a number of applications. This thesis research has focused exclusively on the application of surveying and mapping by sUAS. More specifically, thesis research has been conducted to strategically evaluate geospatial accuracy in sUAS derived survey data. Research in this specific area was necessary as a current debate exists among geospatial professionals and scientists as to whether modern prosumer sUAS platforms are capable of achieving "survey-grade" accuracy. Additionally, since sUAS platforms and components continue to develop rapidly, continued research is and will remain necessary to understand the capabilities of increasingly modernized sUAS.

In order to address the geospatial accuracy debate surrounding sUAS derived survey data and contribute scientifically to the existing body of geospatial research on sUAS, a controlled accuracy test experiment was conducted for this thesis research. The accuracy test was conducted in accordance with FGDC testing requirements and

guidelines to ensure consistency with established geospatial standards. Additionally, the accuracy test experiment was conducted to address a thesis research objective which posed 3 specific questions relating to geospatial accuracy in sUAS derived survey data. In essence, these questions were 1) What geospatial accuracies is observed, 2) What corresponding FGDC accuracy classifications are met, and 3) Is "survey-grade" accuracy achieved both horizontally and vertically.

The experiment began with *in situ* and remote sensing data collection during the experiment's field methods stage (Chapter IV). At this stage, GCPs and checkpoints were placed throughout 2 differing survey areas (SA-1, SA-2) and collected by means of higher accuracy (Trimble R6) for georectification and error calculation. With GCPs and checkpoints in place, remote sensing data collection was conducted with 2 modern prosumer sUAS platforms (P3A, P4P) at each survey area using the Pix4D Capture mobile application. Remote sensing data collection was conducted in 2 flights per sUAS platform at each survey area utilizing perpendicular flight paths (North/South flight, and East/West flight). Once field methods were completed, all *in situ* GCP and checkpoint positions (.csv), remote sensing digital image data (JPGs), and flight log notes/meteorological observations were stored and later transferred to a primary processing laptop.

With field methods completed, experiment focus shifted towards the data processing stage where all sUAS digital image data was subject to SfM photogrammetric processing (Chapter V). At this stage, Pix4D Mapper Pro was used to conduct all SfM processing and survey data generation. This processing also included *in situ* data incorporation of GCP positions for data georectification, and checkpoint positions for

error calculation, all within Pix4D Mapper Pro. Additionally, numerous processing iterations of each sUAS digital image dataset were generated by systematically increasing (i.e. optimizing) the number of GCPs used for georectification during SfM processing. As a result, 18 total sUAS + SfM survey datasets were generated during SfM processing and stored according to sUAS platform, survey area, and GCP iteration (e.g. P3A_SA-1_5GCP, P4P_SA-2_21GCP).

After SfM processing was completed, both geospatial and statistical analysis were required to evaluate the 18 resulting sUAS + SfM survey datasets and their corresponding survey data types (Chapter VI – GEOSPATIAL AND STATISTICAL ANALYSIS). At this stage, error (positional deviation in x,y,z) was calculated by comparing sUAS + SfM derived survey data to 20 checkpoints serving as benchmark ground-truth positions at each survey area. Pix4D Mapper Pro was used at this stage for geospatial analysis of all initial tie points and point cloud survey data types, while ESRI's ArcMap was used for geospatial analysis of DSM survey data. At the conclusion of geospatial analysis, sUAS + SfM derived point cloud and DSM survey data positions (x,y,z) were copied into Microsoft Excel along with checkpoint positions (x,y,z) for error calculation. This was not required for initial tie points survey data as Pix4D error calculations were held as the error values for these data and also copied into Microsoft Excel. With positional deviation error values calculated for all sUAS + SfM survey datasets, further statistical analysis was performed to calculate RMSE and Accuracy at the 95% confidence level ($Accuracy_r$, $Accuracy_z$).

At the conclusion of geospatial and statistical analysis, resulting accuracies at the 95% confidence level were presented as the fundamental results of the accuracy test

experiment for this thesis (Chapter VII – RESULTS AND DISCUSSION). At this stage, descriptive analysis was conducted on resulting accuracy figures to further evaluate and discuss experimental results. During descriptive analysis, resulting accuracies from all 0GCP survey datasets were shown to be statistical outliers which heavily skewed the descriptive statistics for all survey datasets (18 total). After removing all 0GCP datasets, descriptive statistics for the remaining survey datasets (14 total) were less skewed and provided greater insight into sUAS + SfM derived accuracies assuming the use of ≥ 5 GCPs. Additionally, P4P derived survey datasets were found to exhibit consistent accuracies with regard to GCP number/frequency, and also consistently surpassed P3A derived survey data accuracies at both survey areas. Since this research was specifically targeted at "modern" sUAS platforms, and the P4P represents the latest modern sUAS platform used during the experiment, all P4P derived datasets with ≥ 5 GCPs were isolated for further analysis (7 total). These P4P ≥ 5 GCP survey datasets were observed to achieve the highest reported accuracies and most consistent descriptive statistics of the experiment.

Lastly, an evaluation was conducted of all resulting sUAS + SfM derived accuracies against the specific questions of the research objective. Specifically, accuracies were reported from 15.367 ft. – 0.09 ft. horizontally and 496.734 ft. – 0.330 ft. vertically for all resulting sUAS + SfM survey data. These accuracies were found to achieve FGDC accuracy classifications between 5-Meter and 2-Centimeter (16.504 – 0.065 ft. equivalent) horizontally, and no better than 1-Decimeter (0.328 ft. equivalent) vertically. No sUAS + SfM derived survey data was found to achieve survey grade

accuracy both horizontally and vertically at the 5-Centimeter (0.164 ft.) FGDC classification as demonstrated in Appendices C – F.

Conclusions

In consideration of existing research and the results of this experiment, it is clear the debate surrounding prosumer sUAS + SfM survey data accuracy is justifiable. The latest generation sUAS platform tested in this experiment (P4P) derived survey data with accuracies bordering on, and sometimes achieving, survey-grade accuracy at the 5-Centimeter (0.164 ft.) FGDC accuracy classification. However, the results of this thesis research clearly demonstrate that no sUAS + SfM survey data of the experiment achieved survey-grade accuracy both horizontally and vertically. Therefore, in regards to the hypothesis of this thesis, it can be concluded that modern prosumer sUAS derived survey data did not achieve survey grade accuracy in this experiment. Given the relatively limited scope of this thesis research, this conclusion cannot be definitively made for all sUAS + SfM derived survey data – especially where sUAS platform, data collection, data processing, and other relevant variables are present. Nonetheless, some valuable conclusions can be drawn from the results of this research.

First, the optimal placement, collection, and incorporation of GCPs can be concluded as proportional to resulting geospatial accuracy in sUAS + SfM survey data. This is clearly demonstrated by the increasing accuracy of sUAS + SfM survey datasets when increasing the frequency of GCPs in each processing iteration. This conclusion also supports several instances of existing research which found similar research results (e.g. Tonkin & Midgley 2016, Agüera-Vega et al. 2017, James et al. 2017). Most importantly, this conclusion also demonstrates that sUAS + SfM derived survey data

which does not utilize any GCPs for georectification will achieve poor geospatial accuracies which are unfit for most geospatial applications. This conclusion can be rendered moot in the case of RTK capable sUAS platforms which do not require GCPs for georectification. Since modern prosumer sUAS platforms do not currently possess RTK capabilities in most cases, this capability is generally associated with professional sUAS platforms only. As prosumer sUAS continue to advance, it is certainly possible that RTK capabilities will become available in future prosumer sUAS platforms. However, given the historical use and demonstrated value of GCPs for accurate georectification, it is expected the use of GCPs would continue even for RTK capable sUAS platforms as an additional means of georectification and/or accuracy assessment (James et al. 2017, Molina et al. 2017).

Second, it can be concluded that P4P derived survey data was consistently more accurate than P3A derived survey data. This conclusion is demonstrated by the accuracy values in Figure 7.1 and the many subsequent figures which show P4P derived accuracies exceeding that of the P3A at both survey areas using identical GCPs. This conclusion is further demonstrated by the seven P4P derived survey datasets which achieved survey-grade horizontal accuracy in initial tie points data, versus only one dataset for the P3A. Again, it must be noted that sUAS data collection and SfM processing methods were held constant for all P4P and P3A survey datasets. For the purpose of this research, the only known variable between these sUAS platforms (excluding meteorological conditions at the time of remote sensing data collection) was their camera payload. As previously discussed, the P4P possesses a superior camera payload to the P3A in terms of both sensor size and image resolution. Furthermore, the documented shortcomings of the P3A

camera payload's rolling-shutter mechanism are assumed to have influenced P3A derivative accuracies as shown in similar research efforts (e.g. Liang et al. 2008, Albl et al. 2015). Additional statistical analysis beyond the scope of this thesis would be required to confirm the P4P camera payload was indeed the variable which influenced greater geospatial accuracy on behalf of the P4P. However, this point is speculated here for the purpose of this research as P4P survey data was concluded to be of consistently higher accuracy than P3A survey data.

Lastly, and most importantly, it can be concluded that horizontal and vertical accuracies at the 95% confidence level provide a more statistically accurate measure of geospatial accuracy than RMSE. As previously discussed, FGDC standards recognize RMSE as an accepted estimate of geospatial accuracy. Alternatively, FGDC standards explicitly state that reported accuracies at the 95% confidence level reflect all uncertainties "including those introduced by geodetic control coordinates, compilation, and final computation of ground coordinate values in the product". This final conclusion, while not scientifically ground-breaking, plays directly to the heart of the geospatial accuracy debate surrounding sUAS derived survey data. Much of the existing research on sUAS derived accuracy uses only RMSE values to represent geospatial accuracy (e.g. Niethammer et al. 2012, Mancini et al. 2013, Bemis et al. 2014, Ruzgiene et al. 2015). Additionally, even Pix4D Mapper Pro uses RMSE to communicate geospatial accuracy of resulting survey data. However, the statistical nature of RMSE ensures these values are nearly always lower (lower error = higher accuracy) than calculated accuracy at the 95% confidence level.

Final thoughts

The results of this thesis research show that achieving "survey-grade" accuracy both horizontally and vertically with modern prosumer sUAS is somewhat unlikely, but not completely implausible. To this point, it must be acknowledged that all conditions of the accuracy test experiment including sUAS platforms used, survey area characteristics, flight setting and environmental conditions, and data collection and processing methodologies are all assumed to have contributed to the final geospatial accuracy results. Therefore, it cannot be definitively stated that prosumer sUAS are unable to achieve "survey-grade" accuracy.

Variations in any of the above experimental conditions could have potentially improved or worsened the resulting accuracies reported herein. For example, conducting sUAS remote sensing data collection at a lower altitude (< 300 ft. AGL) would have resulted in smaller ground sample distances (GSD) for both sUAS platforms. This altitude adjustment could certainly improve resulting accuracy values in the proper conditions. However, sUAS data collection altitude has a proportional relationship to sUAS survey coverage capability. Thus, reducing sUAS data collection altitude also effectively reduces the geographic scope which the sUAS can survey. Likewise, a higher GCP frequency may have benefitted resulting accuracy through improved sUAS data georectification. However, this requires much additional time and effort to place and collect said GCPs. Essentially, a significant trade-off exists between achieving geospatial accuracy with modern prosumer sUAS and the additional time, effort, and cost required to do so (i.e. low altitude data collection, extensive GCP placement, additional hardware/software requirements, etc.). For this reason, traditional surveying instruments

and methods should not be relinquished in favor of prosumer sUAS for complex applications requiring "survey-grade" accuracy at this time.

Also, it can be speculated that use of RMSE to communicate geospatial accuracy may be a contributor to the greater debate surrounding sUAS derived survey data. Had RMSE been used to communicate geospatial accuracy for this thesis research, nine additional survey datasets could have been inaccurately or inadvertently interpreted as exhibiting survey-grade accuracy (more than doubling the "survey-grade" accuracy results). While these datasets exhibit RMSE values ≤ 0.164 ft., their calculated accuracies at the 95% confidence level exceeded the survey-grade accuracy threshold by almost five times in some cases. Therefore, while the impact of RMSE misinterpretation as geospatial accuracy can only be speculated, accuracy at the 95% confidence level is expected to be a more effective measure of geospatial accuracy based on the results this research.

Finally, it must be acknowledged that sUAS derived accuracies observed in this research may certainly be sufficient for applications requiring moderate "mapping-grade" geospatial accuracy. Geospatial data of "mapping-grade" accuracy still possess significant value – especially when compiled alongside additional data in a GIS or other data repository. Furthermore, the geospatial accuracies achieved with modern prosumer sUAS and sufficient ground control in this research are very impressive given the relatively low cost and operational ease of these platforms. Therefore, the capabilities and benefits offered by modern prosumer sUAS should not be disregarded for current and future geospatial applications.

REFERENCES

Agüera-Vega, F., Carvaljal-Ramírez, F., Martínez-Carricondo, P., 2017. Assessment of photogrammetric mapping accuracy based on variation ground control points using unmanned aerial vehicle. *Measurement: Journal of the International Measurement Confederation*. **98**, 221-227.

Albl, C., Kukelova, Z., Pajdla, T., 2015. R6P – Rolling shutter absolute pose problem. *Proceedings of the IEEE Computer Society*. Conference on Computer Vision and Pattern Recognition. **07**, 12-June-2015. 2292-2300.

Bemis, S., et al., 2014. Ground-based and UAV-Based photogrammetry: A multi-scale, high-resolution mapping tool for structural geology and paleoseismology. *Journal of Structural Geology*. **69**, 163-178.

Birdseye, C.H., 1940. Stereoscopic Photographic mapping. *Annals of the Association of American Geographers*. **30**, 1-24. DOI: 10.1080/00045604009357193.

Chao, H., Cao, Y., Chen, Y., 2010. Autopilots for Small Unmanned Aerial Vehicles: A Survey. *International Journal of Control, Automation, and Systems*. **8**, 1, 36-44.

Clapuyt, F., Vanacker, V., Van Oost, K., 2016. Reproducibility of UAV-based earth topography reconstructions based on Structure-from-Motion algorithms. *Geomorphology*. **260**, 4-15.

Colomina, I., Molina, P., 2014. Unmanned aerial systems for photogrammetry and remote sensing: A review. *ISPRS Journal of Photogrammetry and Remote Sensing*. **92**, 79-97.

Cook, K., 2017. An evaluation of the effectiveness of low-cost UAVs and structure from motion for geomorphic change detection. *Applied Geomatics*. **278**, 195-208.

Cooper, A., Redman, C., Stoneham, D., Gonzalez, L., Etse, V., 2015. A Dynamic Navigation Model for Unmanned Aircraft Systems and an Application to Autonomous Front-On Environmental Sensing and Photography Using Low-Cost Sensor Systems. *Sensors*. **15**, e21537-e21553.

Cryderman, C., Mah, B., Shufletoski, A., 2014. Evaluation of UAV Photogrammetric Accuracy for Mapping and Earthworks Computations. *GEOMATICA*, Vol. **68**, No. 4, 2014, pp. 259- 271.

Federal Aviation Administration (FAA), Office of Aviation Policy and Plans, Forecasts and Performance Analysis Division (APO-100), 2017. *FAA Aerospace Forecast: Fiscal Years 2017 – 2037*.

Federal Aviation Administration (FAA), 2018. *Title 14, Chapter I, Subchapter F, Part 107*. Electronic Code of Federal Regulations (e-CFR). https://www.ecfr.gov/cgi-bin/text- idx?SID=e331c2fe611df1717386d29eee38b000&mc=true&node=pt14.2.107&rgn=div5.

Federal Geographic Data Committee (FGDC), 1998. Geospatial Positioning Accuracy Standards, *Part 2: Standards for Geodetic Networks*. National Spatial Data Infrastructure (NSDI). FGDC-STD-007.2-1998.

Federal Geographic Data Committee (FGDC): Sub-Committee for Base Cartographic Data., 1998. Geospatial Positioning Accuracy Standards, *Part 3: National Standard for Spatial Data Accuracy*. National Spatial Data Infrastructure (NSDI). FGDC-STD-007.3-1998.

Fladeland, M., Schoenung, S., Lord, M., 2017. UAS Platforms. NCAR/EOL Workshop – Unmanned Aircraft Systems for Atmospheric Research – February 2017.

Förstner, W., 1986. A feature-based correspondence algorithm for image matching. *International Archives of Photogrammetry and Remote Sensing*. **26**, 150–166.

Franesco, N., Remondino, F., 2014. UAV for 3D mapping applications: A review. *Applied Geomatics*. **6**, 1-15.

Harris, C., Stephens, M., 1988. A combined corner and edge detector. Proceedings of the Fourth Alvey Vision Conference, Manchester, pp. 147–151.

Hirai, T., 1962. On the results of the examiniation for the aerial photograph on the large scale basic mapping. *Journal of the Japan society of photogrammetry*. **1**(2): 78-84.

Holland, D., Pook, C., Capstick, D., Hemmings, A., 2016. The Topographic Data Deluge – Collecting and Maintaining Data in a 21st Century Mapping Agency. *The International Archives of the Photogrammetry, Remote Sensing and Spatial Information Sciences*. **41**, 727-731.

Hugenholtz, C., et al., 2013. Geomorphological mapping with a small unmanned aircraft system (sUAS): Feature detection and accuracy assessment of a photogrammetrically-derived digital terrain model. *Geomorphology*. **194**, 16-24.

Ishiguro, S., Yamano, H., Oguma, H., 2016. Evaluation of DSMs generated from multi-temporal aerial photographs using emerging structure from motion-multi-view stereo technology. *Geomorphology*. **268**, 64-71.

James, M., Robson, S., D'oleire-Oltmanns, S., et al., 2017. Optimising UAV topographic surveys processed with structure-from-motion: Ground control quality, quantity and bundle adjustment. *Geomorphology*. **280**, 51-66.

Jaud, M., Passot, S., Le Bevic, R., et al., 2016. Assessing the accuracy of high resolution digital surface models computed by PhotoScan© and MicMac© in sub-optimal survey conditions. *Remote Sensing*. Vol. **8**, Issue 6, 465.

Jensen, J., 2007. *Remote Sensing of the Environment – An Earth Resource Perspective*. Pearson Prentice Hall. ISBN 0-13-188950-8. 1-592.

Jensen, J., 2015. *Introductory Digital Image Processing – A Remote Sensing Perspective, 4th Edition*. Pearson Series in Geographic Information Science. Pearson. ISBN-10 013405816X. 1-544.

Konstantinos, G. N., Konstantina, S., Ioannis, K.K., Nikolaos, G. A., 2016. UAV vs. classical aerial photogrammetry for archaeological studies. *Journal of Archaeological Science*: Reports (2016).

Liang, C., Chang, L., Chen, H., 2008. Analysis and compensation of rolling shutter effect. *IEEE Transactions on Image Processing*. **17**. Issue 8. 1323-1330.

Mah, S., Cryderman, C., 2015. Implementation of an Unmanned Aerial Vehicle System for Large Scale Mapping. *The International Archives of the Photogrammetry, Remote Sensing and Spatial Information Sciences*. **40**, 47-54.

Mancini, F. et. al., 2013. Using Unmanned Aerial Vehicles (UAV) for High-Resolution Reconstruction of Topography: The Structure from Motion Approach on Coastal Environments. *Remote Sensing*. **5**, 6880-6898. DOI: 10.3390/rs5126880.

Marshall, D., Barnhart, R., Shappee, E., Most, M., 2016. *Introduction to Unmanned Aircraft Systems, Second Edition*. CRC Press; 2 edition. ISBN-10: 1482263939. 1-395.

McCaffrey, K., Jones, R., Holdsworth, R., et al., 2005. Unlocking the spatial dimension: digital technologies and the future of geoscience fieldwork. *Journal of the Geological Society*. **162**, 6, 927. DOI: 10.1144/0016-764905-017.

Mesas-Carrascosa, F., Garcia, M., Larriva, J., Garcia-Ferrer, J., 2016. An Analysis of the Influence of Flight Parameters in the Generation of Unmanned Aerial Vehicle (UAV) Orthomosaics to Survey Archaeological Areas. *Sensors*. **16**, 1838.

Molina, P., Blazquez, M., Cucci, D., Colomina, I., 2017. First Results of a Tandem Terrestrial-Unmanned Aerial mapKITE System with Kinematic Ground Control Points for Corridor Mapping. *Remote Sensing*. **9**, 60.

NGS.OPUS, 2018. https://www.ngs.noaa.gov/OPUS/. National Geodetic Survey (NGS).

Niethammer, U., James, M., Rosthmund, S., Travelletti, J., Joswig, M., 2012. UAV-based remote sensing of the Super-Sauze landslide: Evaluation and results. *Engineering Geology*. **128**. 2-11.

Nikolakopoulos, K., Soura, K., Koukouvelas, I., et al., 2017. UAV vs classical aerial photogrammetry for archaeological studies. *Journal of Archaeological Science: Reports*. **14**, 758-773.

Oshima, T., Usami, Y., 1964. On the vertical accuracy of aerial photograph. *Journal of the Japan society of photogrammetry*. **3**(1): 21-27.

Pineux, N., Lisein, J., Swerts, G., et al., 2017. Can DEM time series produced by UAV be used to quantify diffuse erosion in an agricultural watershed? *Geomorphology*. **280**, 122-136.

Remondino, F., et al., 2011. UAV Photogrammetry for Mapping and 3D Modeling – Current Status and Future Perspectives. *ISPRS – International Archives of the Photogrammetry, Remote Sensing, and Spatial Information Sciences*. XXXVII-1/C22, 25-31.

Ruzgiene, B., Berteška, T., Gečyte, S., et al., 2015. The surface modelling based on UAV Photogrammetry and qualitative estimation. *Measurement: Journal of the International Measurement Confederation*. **73**, 619-627.

Siebert, S., Teizer, J., 2014. Mobile 3D mapping for surveying earthwork projects using an Unmanned Aerial Vehicle (UAV) system. *Automation in Construction*. **41**, 1-14.

Spetsakis, M.E., Aloimonos, Y., 1991. A multi-frame approach to visual motion perception. *International Journal of Computer Vision*. **6**, 245–255.

Sushchenko, O., Goncharenko, A., 2016. Design of Robust Systems for Stabilization of Unmanned Aerial Vehicle Equipment. *International Journal of Aerospace Engineering*. 2016, Article ID 6054081.

United States Geological Survey (USGS), 2017. *USGS Global Positioning Application and Practice*. U.S. Department of the Interior. https:// water.usgs.gov /osw/gps/.

Tonkin, T., Midgley, N., Graham, D., Labadz, J., 2014. The potential of small unmanned aircraft systems and structure-from-motion for topographic surveys: A test of emerging integrate approaches at Cwn Idwal, North Wales. *Geomorphology*. **226**, 35-43.

Tonkin, T., Midgley, N., 2016. Ground-control networks for image based surface reconstruction: An investigation of optimum survey designs using UAV derived imagery and structure-from-motion photogrammetry. *Remote Sensing*. Vol. **8**, Issue 9, 16-19.

Udin, W., Ahmad, A., 2014. Assessment of photogrammetric mapping accuracy based on variation flying altitude using unmanned aerial vehicle. *IOP Conference Series: Earth and Environmental Science*. **18**, 1-7.

Uysal, M., Toprak, A., Polat, N., 2015. DEM generation with UAV Photogrammetry and accuracy analysis in Sahitler hill. *Measurement: Journal of the International Measurement Confederation*. **73**, 539-543.

Vasuki, Y., Holden, E., Kovesi, P., Micklethwaite, S., 2014. Semi-automatic mapping of geological Structures using UAV-based photogrammetric data: An image analysis approach. *Computers & Geosciences*. **69**, 22-32.

Wallace, L., Lucieer, A., Malenovskỳ Z., et al., 2016. Assessment of forest structure using two UAV techniques: A comparison of airborne laser scanning and structure from motion (SfM) point clouds. *Forests*. Vol. **7**, Issue 3, 1-16.

Watanabe, Y., Kawahara, Y., 2016. UAV Photogrammetry for Monitoring Changes in River Topography and Vegetation. *Procedia Engineering*. **154**, 317-325.

Wester-Ebbinghaus, W., 1980. Aerial Photography by radio controlled model helicopter, *The Photogrammetric Record*, **10**, 55, 85-92.

Westoby, J., Brasington, J., Glasser, N., Hambrey, M., Reynolds, J., 2012. Structure-from-Motion photogrammetry: A low-cost, effective tool for geosciences applications. *Geomorphoogy*. *179*, 300-314.

Whittlesley, J. H., 1970. Tethered Balloon for Archaeological Photos, *Photogrammetric Engineering*, **36**, 2, 181-186.

APPENDIX A

NATIONAL GEODETIC SURVEY (NGS) MONUMENT DJ1746 DATASHEET

The NGS Data Sheet

See file dsdata.pdf for more information about the datasheet.

```
PROGRAM = datasheet95, VERSION = 8.12.4.1
1        National Geodetic Survey,   Retrieval Date = APRIL 15, 2018
 DJ1746 ***********************************************************************
 DJ1746  CBN         -  This is a Cooperative Base Network Control Station.
 DJ1746  DESIGNATION -  STARKVILLE CBL 1130
 DJ1746  PID         -  DJ1746
 DJ1746  STATE/COUNTY-  MS/OKTIBBEHA
 DJ1746  COUNTRY     -  US
 DJ1746  USGS QUAD   -  STARKVILLE (1982)
 DJ1746
 DJ1746                        *CURRENT SURVEY CONTROL
 DJ1746  ______________________________________________________________________
 DJ1746* NAD 83(2011) POSITION- 33 25 53.56377(N) 088 50 58.34171(W)   ADJUSTED
 DJ1746* NAD 83(2011) ELLIP HT-    70.356 (meters)        (06/27/12)   ADJUSTED
 DJ1746* NAD 83(2011) EPOCH   -  2010.00
 DJ1746* NAVD 88 ORTHO HEIGHT -    98.51  (meters)      323.2   (feet) LEVELING
 DJ1746  ______________________________________________________________________
 DJ1746  GEOID HEIGHT    -        -28.164 (meters)                    GEOID12B
 DJ1746  NAD 83(2011) X  -    106,981.786 (meters)                    COMP
 DJ1746  NAD 83(2011) Y  - -5,327,240.982 (meters)                    COMP
 DJ1746  NAD 83(2011) Z  -  3,494,039.287 (meters)                    COMP
 DJ1746  LAPLACE CORR    -         -1.09  (seconds)                   DEFLEC12B
 DJ1746  VERT ORDER      -  THIRD ?
 DJ1746
 DJ1746  Network accuracy estimates per FGDC Geospatial Positioning Accuracy
 DJ1746  Standards:
 DJ1746         FGDC (95% conf, cm)     Standard deviation (cm)     CorrNE
 DJ1746            Horiz  Ellip           SD_N   SD_E   SD_h      (unitless)
 DJ1746  ------------------------------------------------------------------
 DJ1746  NETWORK    1.09   3.86           0.45   0.44   1.97     -0.00050734
 DJ1746  ------------------------------------------------------------------
 DJ1746  Click here for local accuracies and other accuracy information.
 DJ1746
 DJ1746
 DJ1746.This mark is at George M Bryan Airport (STF)
 DJ1746
 DJ1746.The horizontal coordinates were established by GPS observations
 DJ1746.and adjusted by the National Geodetic Survey in June 2012.
 DJ1746
 DJ1746.NAD 83(2011) refers to NAD 83 coordinates where the reference frame has
 DJ1746.been affixed to the stable North American tectonic plate. See
 DJ1746.NA2011 for more information.
 DJ1746
 DJ1746.The horizontal coordinates are valid at the epoch date displayed above
 DJ1746.which is a decimal equivalence of Year/Month/Day.
 DJ1746
 DJ1746.The orthometric height was determined by differential leveling.
 DJ1746.The vertical network tie was performed by a horz. field party for horz.
 DJ1746.obs reductions. Reset procedures were used to establish the elevation.
 DJ1746
 DJ1746.Significant digits in the geoid height do not necessarily reflect accuracy.
 DJ1746.GEOID12B height accuracy estimate available here.
 DJ1746
 DJ1746.The X, Y, and Z were computed from the position and the ellipsoidal ht.
 DJ1746
 DJ1746.The Laplace correction was computed from DEFLEC12B derived deflections.
```


Figure A.1 National Geodetic Survey (NGS) Monument DJ1746 Datasheet

Page 1 of 4.

```
DJ1746
DJ1746.The ellipsoidal height was determined by GPS observations
DJ1746.and is referenced to NAD 83.
DJ1746
DJ1746. The following values were computed from the NAD 83(2011) position.
DJ1746
DJ1746;                    North         East     Units Scale Factor Converg.
DJ1746;SPC MS E     -   435,899.067   298,492.986   MT  0.99995003   -0 00 32.1
DJ1746;SPC MS E     - 1,430,112.19    979,305.74    sFT  0.99995003   -0 00 32.1
DJ1746;UTM  16      - 3,700,659.064   328,057.917   MT  0.99996450   -1 01 09.2
DJ1746
DJ1746!             -  Elev Factor  x  Scale Factor =   Combined Factor
DJ1746!SPC MS E     -   0.99998895  x   0.99995003  =   0.99993899
DJ1746!UTM  16      -   0.99998895  x   0.99996450  =   0.99995346
DJ1746
DJ1746:                Primary Azimuth Mark                    Grid Az
DJ1746:SPC MS E     -  STARKVILLE CBL 430                      358 34 00.0
DJ1746:UTM  16      -  STARKVILLE CBL 430                      359 34 37.1
DJ1746
DJ1746_U.S. NATIONAL GRID SPATIAL ADDRESS: 16SCC2805700659(NAD 83)
DJ1746
DJ1746|-----------------------------------------------------------------------|
DJ1746| PID    Reference Object                    Distance      Geod. Az  |
DJ1746|                                                          dddmmss.s |
DJ1746| DJ1744 STARKVILLE AIRPORT BEACON          APPROX. 1.2 KM 0174436.0 |
DJ1746| DJ1747 STARKVILLE CBL 430                 APPROX. 0.7 KM 3583327.9 |
DJ1746| DJ1745 STARKVILLE CBL 0                   APPROX. 1.1 KM 3583329.9 |
DJ1746|-----------------------------------------------------------------------|
DJ1746
DJ1746                          SUPERSEDED SURVEY CONTROL
DJ1746
DJ1746  NAD 83(2007)-  33 25 53.56366(N)    088 50 58.34208(W) AD(2002.00) 0
DJ1746  ELLIP H (02/10/07)   70.380  (m)                       GP(2002.00)
DJ1746  ELLIP H (04/15/02)   70.349  (m)                       GP(       ) 4 2
DJ1746  ELLIP H (02/15/02)   70.348  (m)                       GP(       ) 4 1
DJ1746  NAD 83(1993)-  33 25 53.56360(N)    088 50 58.34249(W) AD(       ) B
DJ1746  ELLIP H (01/12/94)   70.464  (m)                       GP(       ) 4 2
DJ1746  ELLIP H (01/12/94)   70.464  (m)                       GP(       ) 4 1
DJ1746  NAD 83(1992)-  33 25 53.57400(N)    088 50 58.34078(W) AD(       ) 2
DJ1746  NAD 83(1986)-  33 25 53.57412(N)    088 50 58.33789(W) AD(       ) 2
DJ1746  NAD 27      -  33 25 53.13645(N)    088 50 58.14219(W) AD(       ) 3
DJ1746  NGVD 29             98.47   (m)          323.1    (f) LEVELING    3
DJ1746
DJ1746.Superseded values are not recommended for survey control.
DJ1746
DJ1746.NGS no longer adjusts projects to the NAD 27 or NGVD 29 datums.
DJ1746.See file dsdata.pdf to determine how the superseded data were derived.
DJ1746
DJ1746_MARKER: DQ = CALIBRATION BASE LINE DISK
DJ1746_SETTING: 7 = SET IN TOP OF CONCRETE MONUMENT
DJ1746_STAMPING: 1130 1978
DJ1746_MARK LOGO: NGS
DJ1746_MAGNETIC: N = NO MAGNETIC MATERIAL
DJ1746_STABILITY: C = MAY HOLD, BUT OF TYPE COMMONLY SUBJECT TO
DJ1746+STABILITY: SURFACE MOTION
DJ1746_SATELLITE: THE SITE LOCATION WAS REPORTED AS SUITABLE FOR
DJ1746+SATELLITE: SATELLITE OBSERVATIONS - November 05, 2005
DJ1746
DJ1746  HISTORY     - Date     Condition        Report By
DJ1746  HISTORY     - 1978     MONUMENTED       MSSU
DJ1746  HISTORY     - 1988     GOOD             NGS
DJ1746  HISTORY     - 19910214 GOOD             NGS
DJ1746  HISTORY     - 19921008 GOOD             MSHD
DJ1746  HISTORY     - 19930511 GOOD
DJ1746  HISTORY     - 20000911 GOOD             MSHD
```


Figure A.1 (continued)

Page 2 of 4.

```
DJ1746  HISTORY     - 20051105 GOOD             MSSU
DJ1746
DJ1746                          STATION DESCRIPTION
DJ1746
DJ1746'DESCRIBED BY MISSISSIPPI STATE UNIVERSITY 1978 (RB)
DJ1746'LOCATED 3 MILES SW OF STARKVILLE, 1 MILE SOUTH OF MS HWY 12, 300 FT
DJ1746'WEST OF C/L OF STARKVILLE AIRPORT RUNWAY, 12.1 M NW OF DITCH, 21.7 M
DJ1746'SE OF EAST CORNER OF CIVIL AIR PATROL BUILDING.  A STD BASELINE DISK
DJ1746'IN CONCRETE CYLINDER.
DJ1746
DJ1746                          STATION RECOVERY (1988)
DJ1746
DJ1746'RECOVERY NOTE BY NATIONAL GEODETIC SURVEY 1988 (AJL)
DJ1746'THE STATION IS LOCATED ABOUT 4.0 KM (2.5 MI)
DJ1746'SOUTHWEST OF STARKVILLE,
DJ1746'1.4 KM (0.9 MI) SOUTH OF STATE HIGHWAY 12, ON THE WESTERN EDGE OF
DJ1746'THE PROPERTY FOR THE STARKVILLE-GEORGE M. BRYAN AIRPORT,
DJ1746'NEAR THE CENTER OF THE FIELD.
DJ1746'OWNERSHIP--CITY OF STARKVILLE, C/O CITY ENGINEER JOE WEBB, CITY
DJ1746'HALL, STARKVILLE, MS 39759.  PHONE (601) 325-8581.
DJ1746'
DJ1746'TO REACH THE STATION FROM THE JUNCTION OF STATE HIGHWAYS 12 AND 25
DJ1746'IN SOUTHWEST STARKVILLE, GO WEST FOR 2.4 KM (1.5 MI) ON HIGHWAY 12
DJ1746'TO A PAVED CROSSROAD.
DJ1746'TURN LEFT AND GO SOUTH FOR 0.5 KM (0.3 MI) ON THE PAVED ROAD TO A
DJ1746'GATE ON THE RIGHT AT THE SOUTHEAST CORNER OF THE UNIVERSITY HANGAR.
DJ1746'TURN RIGHT AND GO WEST FOR 0.3 KM (0.2 MI) ON THE PARKING PAD AND
DJ1746'RAMP TO THE RUNWAY.
DJ1746'TURN LEFT AND GO SOUTH FOR 1.0 KM (0.6 MI) ON THE RUNWAY TO THE
DJ1746'STATION ON THE RIGHT JUST EAST OF AN ABANDONED BUILDING.
DJ1746'
DJ1746'THE STATION IS A STANDARD NGS DISK
DJ1746'STAMPED---1130 1978---,
DJ1746'SET INTO THE TOP OF A ROUND CONCRETE MONUMENT
DJ1746'26 CM IN DIAMETER FLUSH WITH GROUND.  LOCATED
DJ1746'68.6 METERS (225.0 FT) WEST FROM THE WEST EDGE OF THE RUNWAY,
DJ1746'55.2 METERS (181.0 FT) EAST FROM A POWER POLE WITH A TRANSFORMER,
DJ1746'23.6 METERS (77.5 FT) EAST-SOUTHEAST FROM THE SOUTHEAST CORNER
DJ1746'OF THE ABANDONED BUILDING,
DJ1746'21.6 METERS (71.0 FT) SOUTHEAST FROM THE NORTHEAST CORNER OF THE
DJ1746'ABANDONED BUILDING, AND
DJ1746'0.6 METERS (2.0 FT) SOUTH FROM A METAL WITNESS POST.
DJ1746'THE UNDERGROUND MARK IS A STANDARD MSU DISK
DJ1746'STAMPED---1130 1978---,
DJ1746'SET INTO AN IRREGULAR MASS OF CONCRETE 1.1 METERS BELOW THE SURFACE.
DJ1746'
DJ1746'DESCRIBED BY D.D. REXRODE, TYPED BY C.L. SMITH.
DJ1746
DJ1746                          STATION RECOVERY (1991)
DJ1746
DJ1746'RECOVERY NOTE BY NATIONAL GEODETIC SURVEY 1991 (LPB)
DJ1746'MARK IS A COMPONENT OF THE STARKVILLE CALIBRATION BASE LINE, LOCATED
DJ1746'ABOUT 4.0 KM (2.49 MI) SOUTHWEST OF STARKVILLE, ALONG THE WEST
DJ1746'BOUNDARY OF THE STARKVILLE CITY AIRPORT IN SECTION 17 T 18 N R 14 E
DJ1746'(STARKVILLE 7.5 MIN QUAD).  OWNERSHIP--CITY OF STARKVILLE.
DJ1746'FOR PERMISSION TO ENTER AIRPORT PROPERTY PLEASE CONTACT MR. JOE WEBB,
DJ1746'BOX 6062, MISSISSIPPI STATE UNIVERSITY, MISSISSIPPI STATE, MS 39762.
DJ1746'TELEPHONE 601-323-8581 OR 325-3010.  TO OBTAIN THE KEYS TO THE LOCKED
DJ1746'GATES CONTACT THE CIVIL ENGINEERING DEPARTMENT OF MISSISSIPPI STATE
DJ1746'UNIVERSITY OR THE STARKVILLE POLICE DEPARTMENT.
DJ1746'
DJ1746'TO REACH FROM THE JUNCTION OF MISSISSIPPI STATE HIGHWAYS 12 AND 25, IN
DJ1746'SOUTHWEST STARKVILLE, GO WEST ON HIGHWAY 12 FOR 2.4 KM (1.49 MI) TO
DJ1746'AN INTERSECTION LEADING TO THE AIRPORT ON THE LEFT.  CONTINUE WEST
DJ1746'FOR 0.56 KM (0.35 MI) TO A GRAVEL ROAD LEFT.  TURN LEFT AND GO SOUTH
```


Figure A.1 (continued)

Page 3 of 4.

```
DJ1746'FOR 0.85 KM (0.53 MI) TO A LOCKED GATE.  PROCEED THROUGH THE GATE AND
DJ1746'FOLLOW THE FENCE LINE SOUTH FOR 0.39 KM (0.24 MI) TO THE MARK ON THE
DJ1746'LEFT, ACCESSED THROUGH A LOCKED GATE.
DJ1746'
DJ1746'MARK IS SET IN THE TOP OF A 28 CM (11 IN) DIAMETER CONCRETE POST FLUSH
DJ1746'WITH GROUND SURFACE.  IT IS 38.4 M (125.98 FT) SOUTHEAST OF A GATE
DJ1746'CENTER POST, 29.1 M (95.47 FT) EAST OF A WIRE FENCE, 22.9 M
DJ1746'(75.13 FT) NORTHWEST OF A MSU REFERENCE MARK, 0.5 M (1.64 FT)
DJ1746'NORTHWEST OF A METAL WITNESS POST, AND 0.5 M (1.64 FT) SOUTHEAST OF A
DJ1746'METAL WITNESS POST.
DJ1746'FOR MORE INFORMATION CONTACT MR. ROFFIE BURT, DEPARTMENT OF CIVIL
DJ1746'ENGINEERING, P.O. DRAWER CE, MISSISSIPPI STATE, MS 39762.  TELEPHONE
DJ1746'601-325-7188 OR 325-3050.  OR CONTACT MR. DONALD REXRODE, P.O. BOX
DJ1746'6366, JACKSON, MS 39208.  TELEPHONE 601-944-9098.
DJ1746
DJ1746                          STATION RECOVERY (1992)
DJ1746
DJ1746'RECOVERY NOTE BY MISSISSIPPI STATE HIGHWAY DEPARTMENT 1992
DJ1746'THE STATION IS LOCATED ABOUT 3.5 MI (5.6 KM) SOUTHWEST OF STARKVILLE,
DJ1746'0.9 MI (1.4 KM) SOUTH OF STATE HIGHWAY 12, ON THE WESTERN EDGE OF THE
DJ1746'PROPERTY OF THE STARKVILLE-GEORGE M. BRYAN AIRPORT, NEAR THE CENTER
DJ1746'OF THE FIELD AND IS IN SECTION 17, T 18N, R 14E. OWNERSHIP--CITY OF
DJ1746'STARKVILLE, C/O CITY ENGINEER JOE WEBB, CITY HALL, STARKVILLE, MS
DJ1746'39759. PHONE (601) 325-8581.
DJ1746'TO REACH THE STATION FROM THE JUNCTION OF STATE HIGHWAYS 12 AND 25 IN
DJ1746'SOUTHWEST STARKVILLE, GO WEST ON STATE HIGHWAY 12 FOR 1.5 MI
DJ1746'(2.4 KM) TO A CROSSROAD, TURN LEFT AND GO SOUTH ON A PAVED ROAD FOR
DJ1746'0.3 MI (0.5 KM) TO A GATE ON THE RIGHT AT THE SOUTHWEST CORNER OF THE
DJ1746'UNIVERSITY HANGAR, TURN RIGHT THROUGH THE GATE AND GO WEST ON A
DJ1746'PARKING PAD AND RAMP FOR 0.2 MI (0.3 KM) TO THE RUNWAY, TURN LEFT AND
DJ1746'GO SOUTH ON THE RUNWAY FOR 0.6 MI (1.0 KM) TO THE MARK ON THE RIGHT.
DJ1746'MARK IS A STANDARD NGS CALIBRATION BASE LINE DISK SET IN THE TOP OF A
DJ1746'ROUND CONCRETE POST, FLUSH WITH THE GROUND, 225 FT (68.6 M) WEST OF
DJ1746'THE WEST EDGE OF THE RUNWAY, 181 FT (55.2 M) EAST OF A POWER POLE
DJ1746'WITH A TRANSFORMER, 118 FT (36.0 M) EAST SOUTHEAST OF THE SOUTH POST
DJ1746'OF A DOUBLE GATE, 95.5 FT (29.1 M) EAST OF A FENCE AND 2 FT (0.6 M)
DJ1746'SOUTH OF A METAL WITNESS POST. (NOTE) THE ABANDONED BUILDING MENTIONED
DJ1746'IN THE PREVIOUS DESCRIPTION NO LONGER EXISTS.
DJ1746
DJ1746                          STATION RECOVERY (1993)
DJ1746
DJ1746'RECOVERED 1993
DJ1746'RECOVERED IN GOOD CONDITION.
DJ1746
DJ1746                          STATION RECOVERY (2000)
DJ1746
DJ1746'RECOVERY NOTE BY MISSISSIPPI STATE HIGHWAY DEPARTMENT 2000
DJ1746'RECOVERED AS DESCRIBED.
DJ1746
DJ1746                          STATION RECOVERY (2005)
DJ1746
DJ1746'RECOVERY NOTE BY MISSISSIPPI STATE UNIVERSITY 2005 (HAK)
DJ1746'RECOVERED IN GOOD CONDITION.

*** retrieval complete.
Elapsed Time = 00:00:04
```


Figure A.1 (continued)

Page 4 of 4.

APPENDIX B

NATIONAL WEATHER SERVICE (NWS) OBSERVATIONS FOR JULY 26, 2017

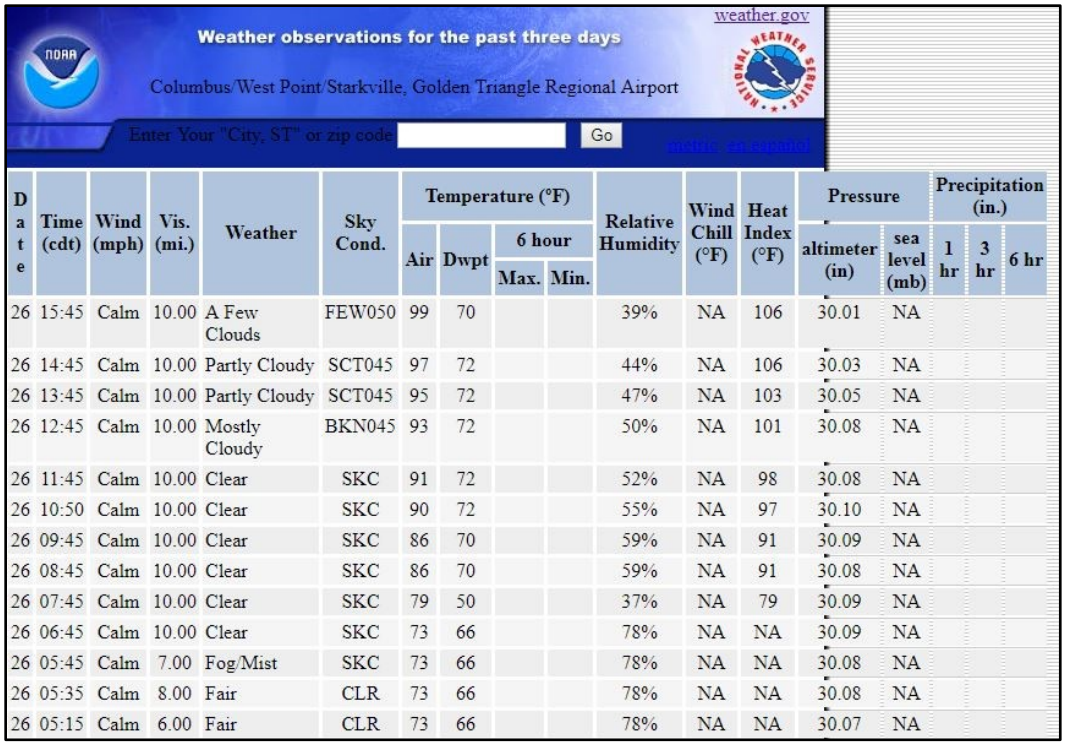

Weather observations for the past three days

weather.gov

Columbus/West Point/Starkville, Golden Triangle Regional Airport

Enter Your "City, ST" or zip code Go

Date	Time (cdt)	Wind (mph)	Vis. (mi.)	Weather	Sky Cond.	Temperature (°F)				Relative Humidity	Wind Chill (°F)	Heat Index (°F)	Pressure		Precipitation (in.)		
						Air	Dwpt	6 hour					altimeter (in)	sea level (mb)	1 hr	3 hr	6 hr
								Max.	Min.								
26	15:45	Calm	10.00	A Few Clouds	FEW050	99	70			39%	NA	106	30.01	NA			
26	14:45	Calm	10.00	Partly Cloudy	SCT045	97	72			44%	NA	106	30.03	NA			
26	13:45	Calm	10.00	Partly Cloudy	SCT045	95	72			47%	NA	103	30.05	NA			
26	12:45	Calm	10.00	Mostly Cloudy	BKN045	93	72			50%	NA	101	30.08	NA			
26	11:45	Calm	10.00	Clear	SKC	91	72			52%	NA	98	30.08	NA			
26	10:50	Calm	10.00	Clear	SKC	90	72			55%	NA	97	30.10	NA			
26	09:45	Calm	10.00	Clear	SKC	86	70			59%	NA	91	30.09	NA			
26	08:45	Calm	10.00	Clear	SKC	86	70			59%	NA	91	30.08	NA			
26	07:45	Calm	10.00	Clear	SKC	79	50			37%	NA	79	30.09	NA			
26	06:45	Calm	10.00	Clear	SKC	73	66			78%	NA	NA	30.09	NA			
26	05:45	Calm	7.00	Fog/Mist	SKC	73	66			78%	NA	NA	30.08	NA			
26	05:35	Calm	8.00	Fair	CLR	73	66			78%	NA	NA	30.08	NA			
26	05:15	Calm	6.00	Fair	CLR	73	66			78%	NA	NA	30.07	NA			

Figure B.1 National Weather Service (NWS) Observations for July 26, 2017.

Observation times of 09:45 – 13:45 coincide with all remote sensing data collection flights at Survey Area #1 (SA-1) and Survey Area #2 (SA-2).

APPENDIX C

P3A_SA-1_12GCP COMPREHENSIVE ERROR EVALUATION

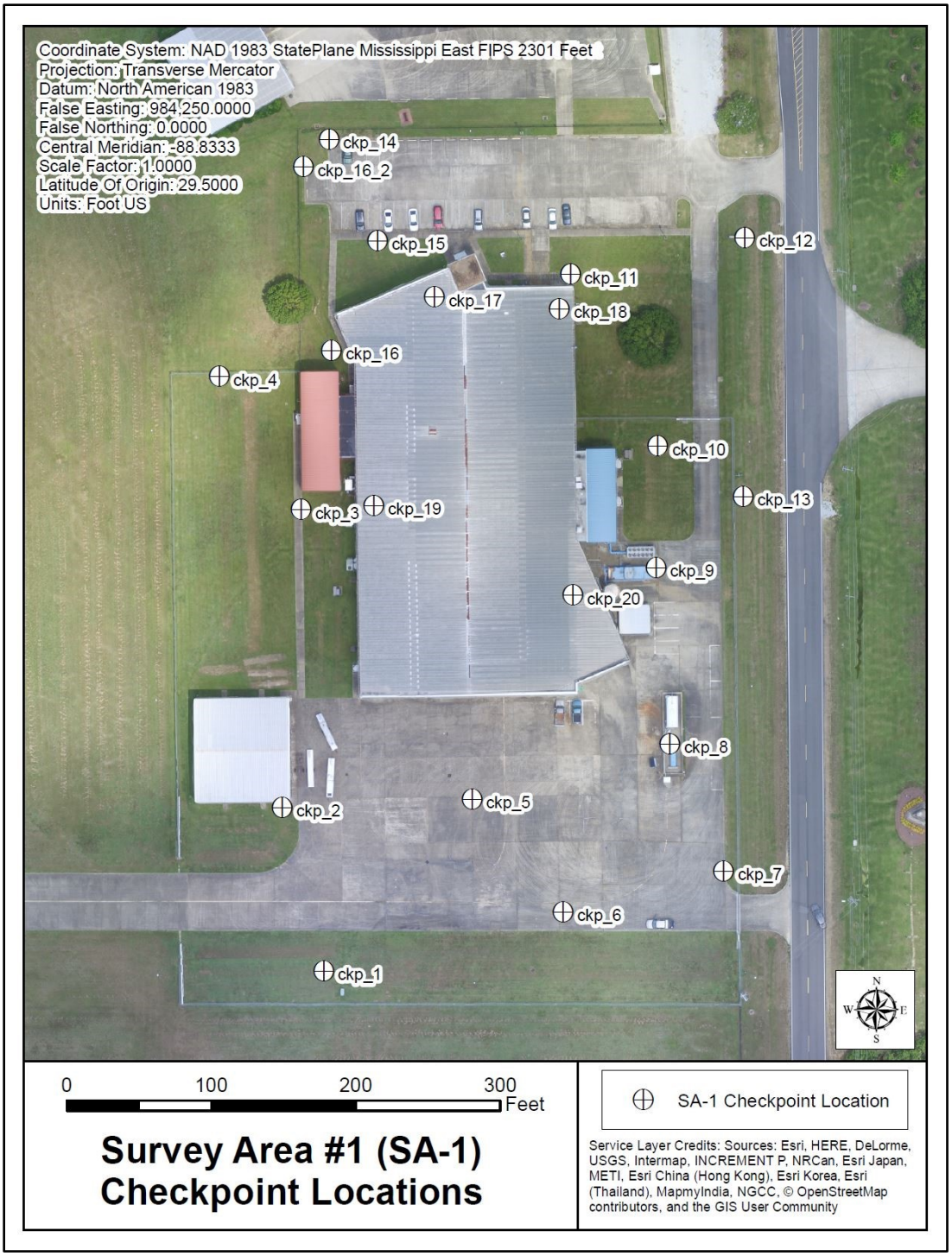

Figure C.1 Error evaluation – P3A_SA-1_12GCP checkpoint locations

Checkpoint locations collected via independent source of higher accuracy (Trimble R6) and used for positional error calculation and accuracy testing in P3A_SA-1_12GCP data.

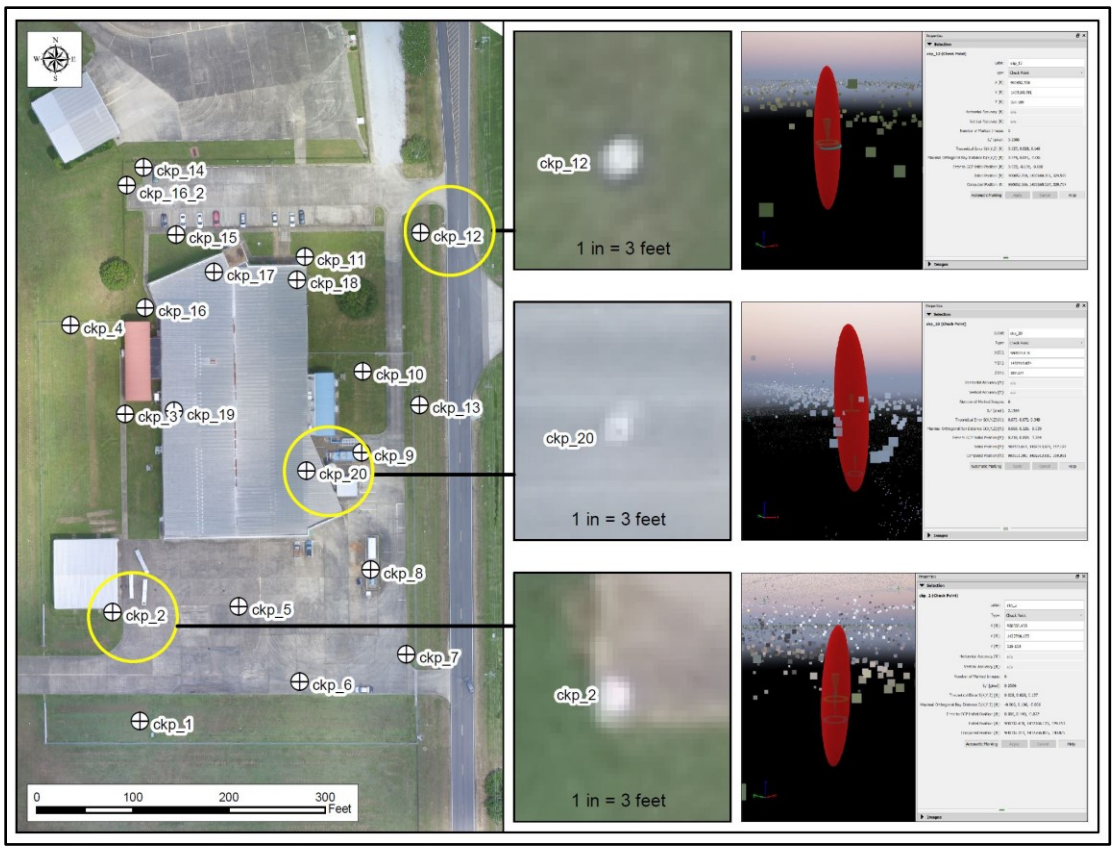

Figure C.2 Examples of error at various checkpoints in P3A_SA-1_12GCP dataset

In Pix4D Mapper Pro, positional error between initial and computed point positions can be visualized using the “Ray Cloud Editor” and corresponding “Error Ellipsoid” function.

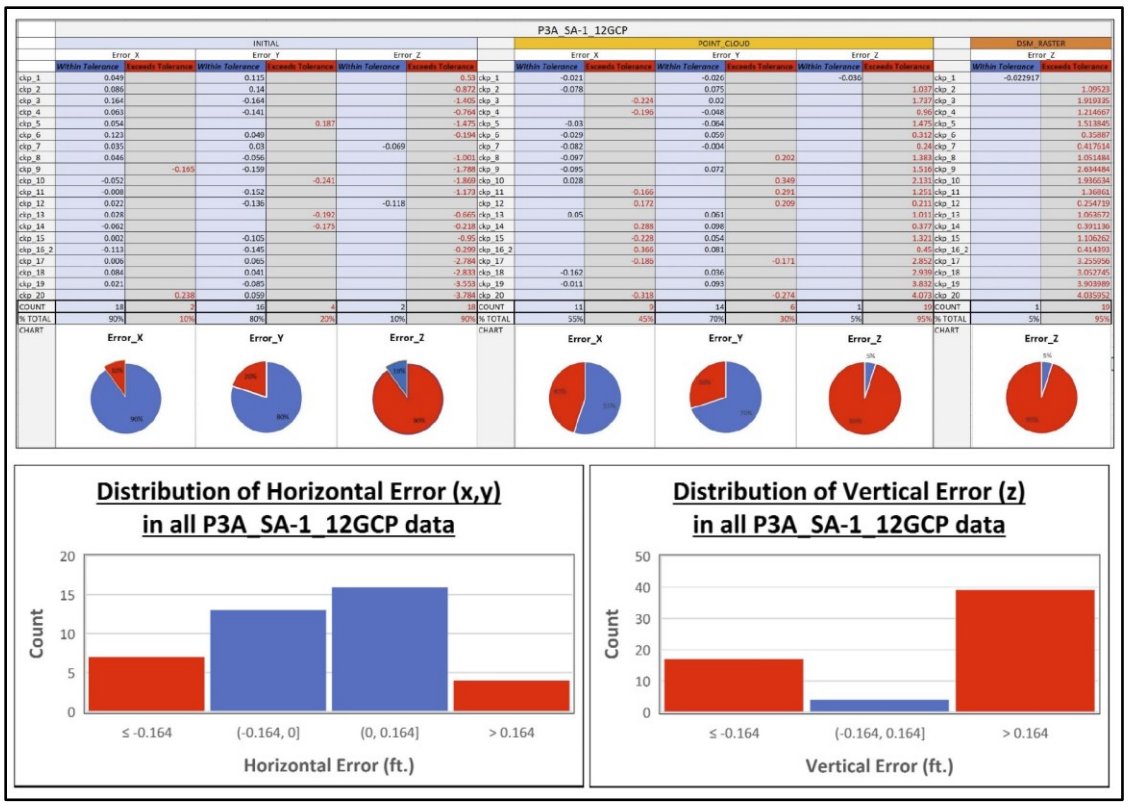

Figure C.3 Survey-grade accuracy evaluation of P3A_SA-1_12GCP error values

Positional error as recorded in P3A_SA-1_12GCP derived survey data. Red error values and corresponding red sections in the associated charts represent error values exceeding the ≤ 0.164 ft. survey-grade threshold tolerance. Blue error values and corresponding blue sections in the associated charts represent error values within the ≤ 0.164 ft. tolerance.

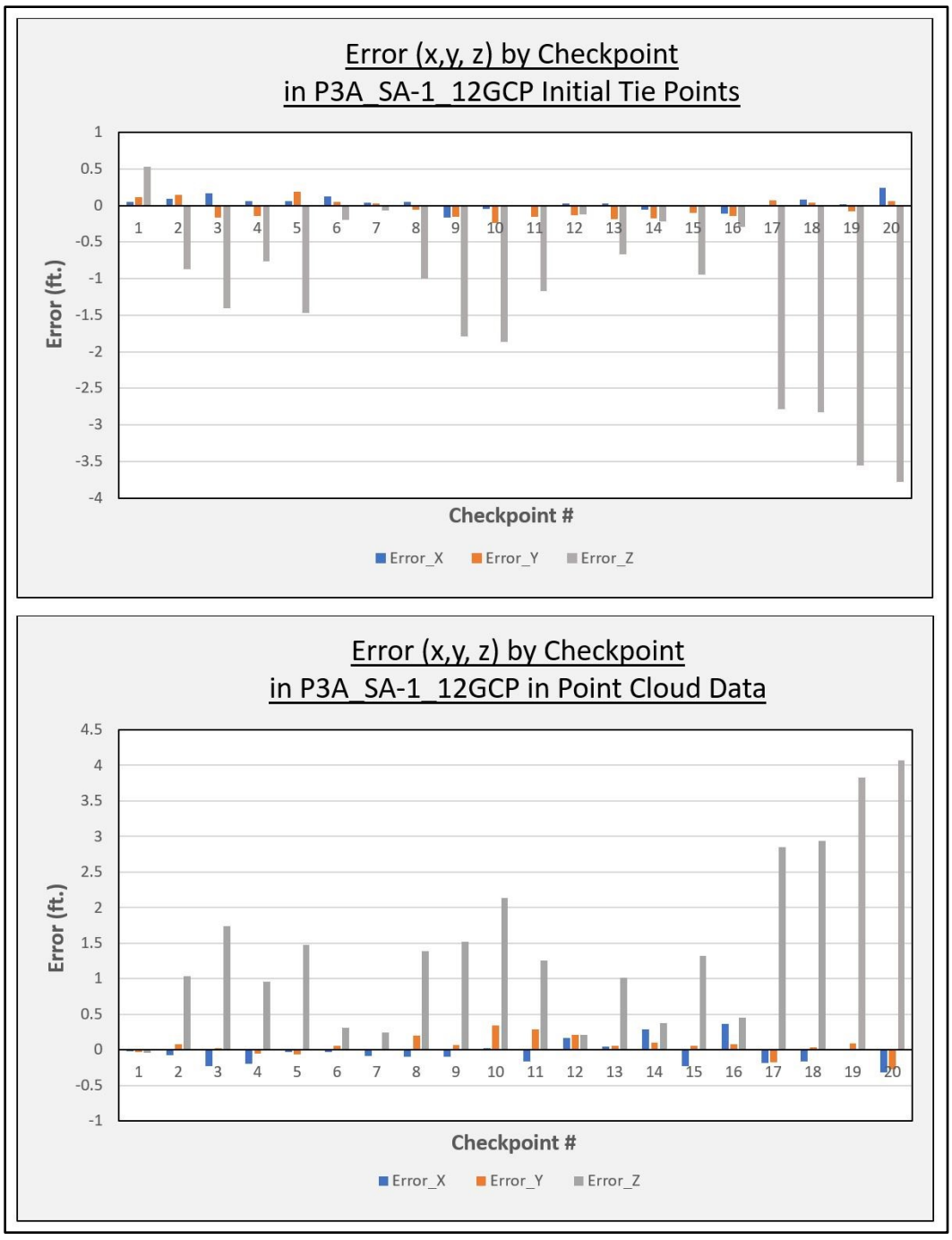

Figure C.4 Positional error by checkpoint for P3A_SA-1_12GCP dataset

Positional error (x = blue, y = orange, z = gray) at each checkpoint location in the various survey data types of the P3A_SA-1_12GCP dataset.

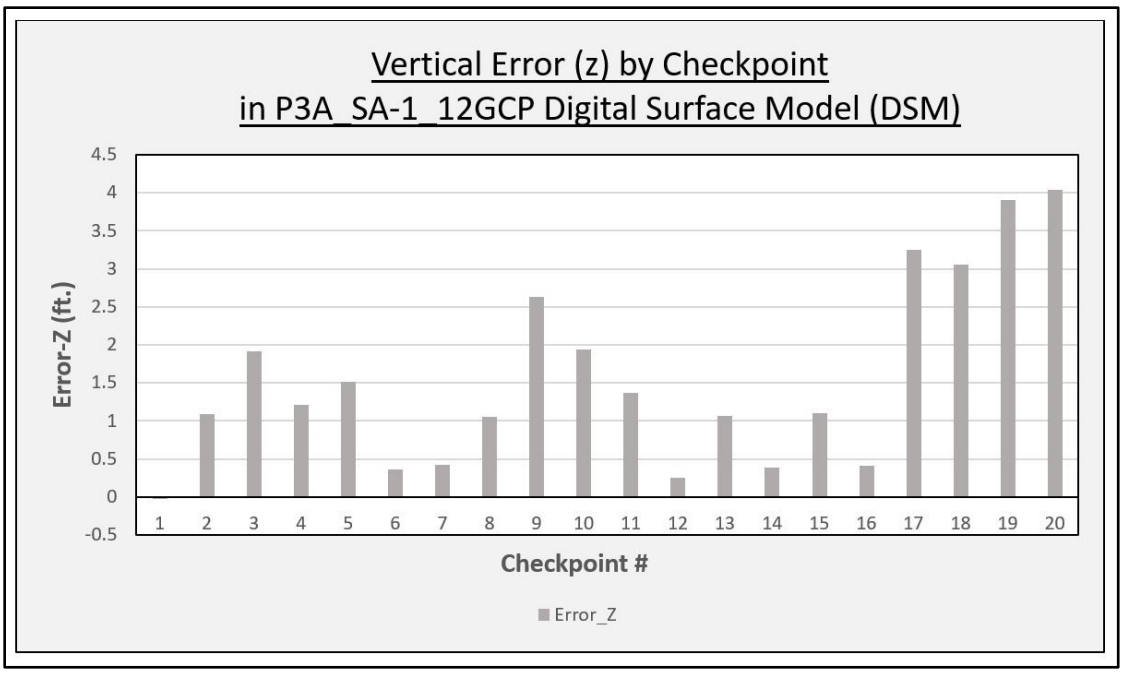

Figure C.5 Vertical error by checkpoint for P3A_SA-1_12GCP DSM

Vertical error (z = gray) at each checkpoint location in the digital surface model (DSM) raster survey data of P3A_SA-1_12GCP.

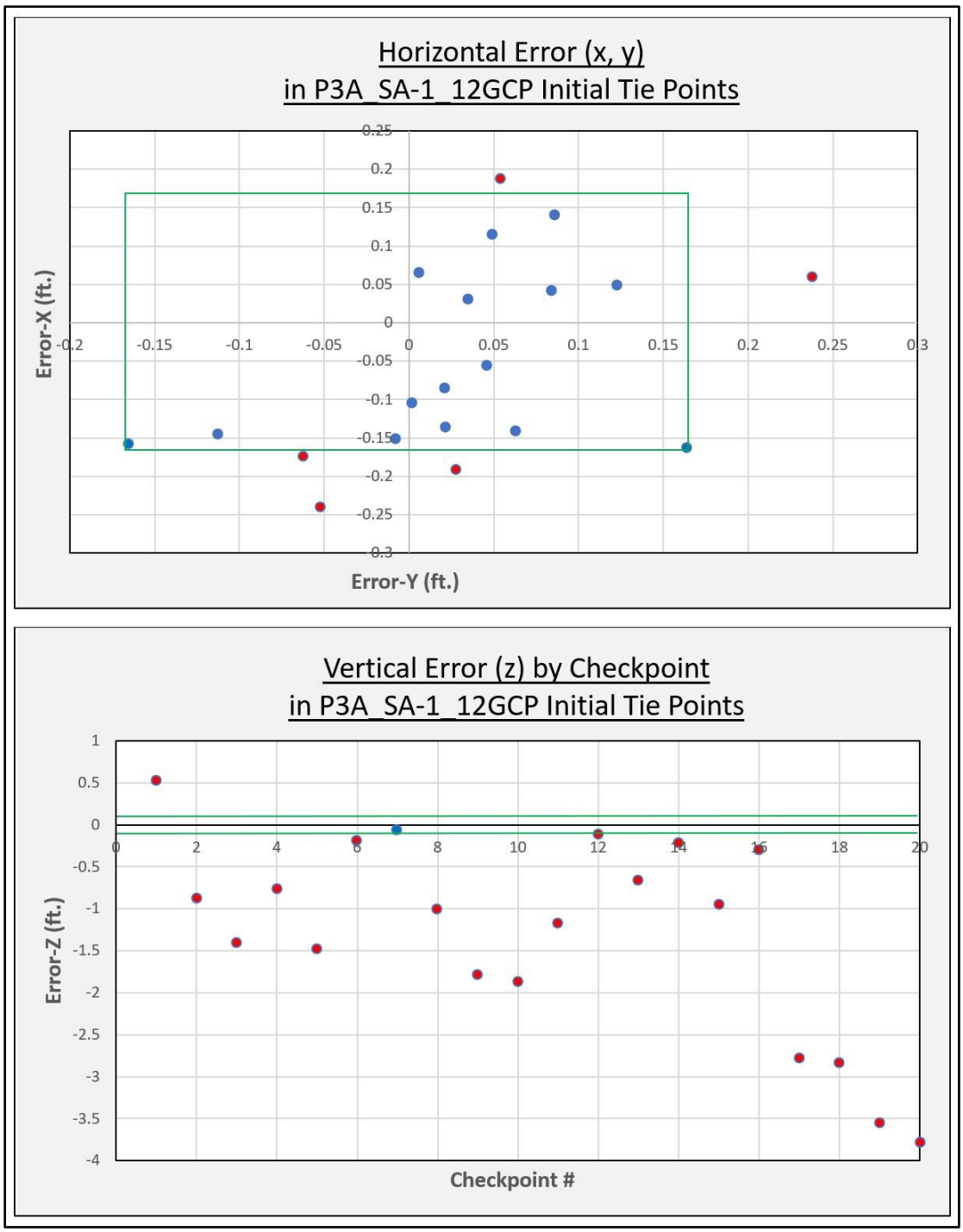

Figure C.6 Horizontal and vertical error in relation to survey-grade accuracy for P3A_SA-1_12GCP initial tie points data

Survey-grade accuracy at ≤ 0.164 ft. is represented by the green outline. Checkpoint locations with error ≤ 0.164 ft. are represented in blue, while checkpoint locations with error > 0.164 ft. are represented in red.

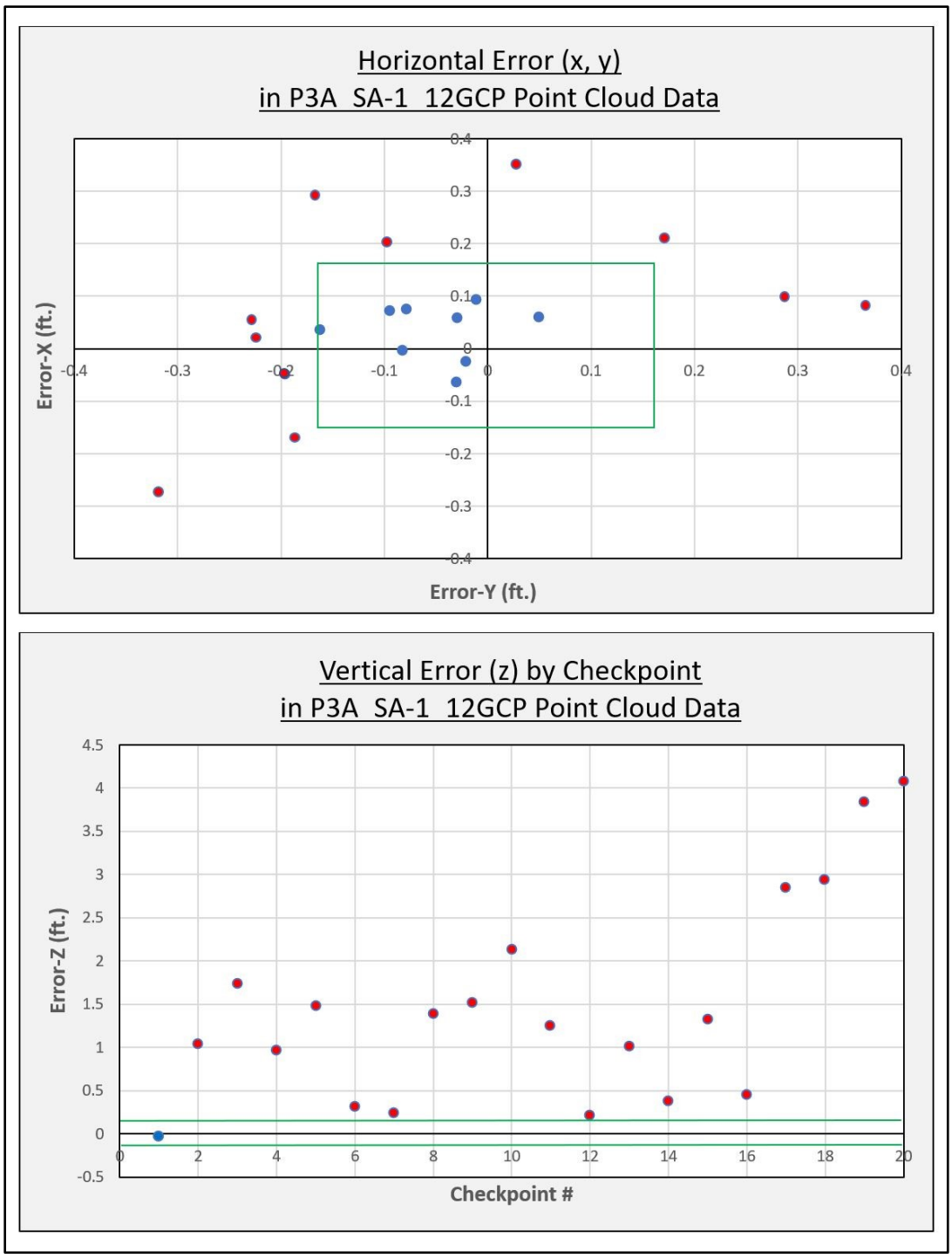

Figure C.7 Horizontal and vertical error in relation to survey-grade accuracy for P3A_SA-1_12GCP point cloud data

Survey-grade accuracy at ≤ 0.164 ft. is represented by the green outline. Checkpoint locations with error ≤ 0.164 ft. are represented in blue, while checkpoint locations with error > 0.164 ft. are represented in red.

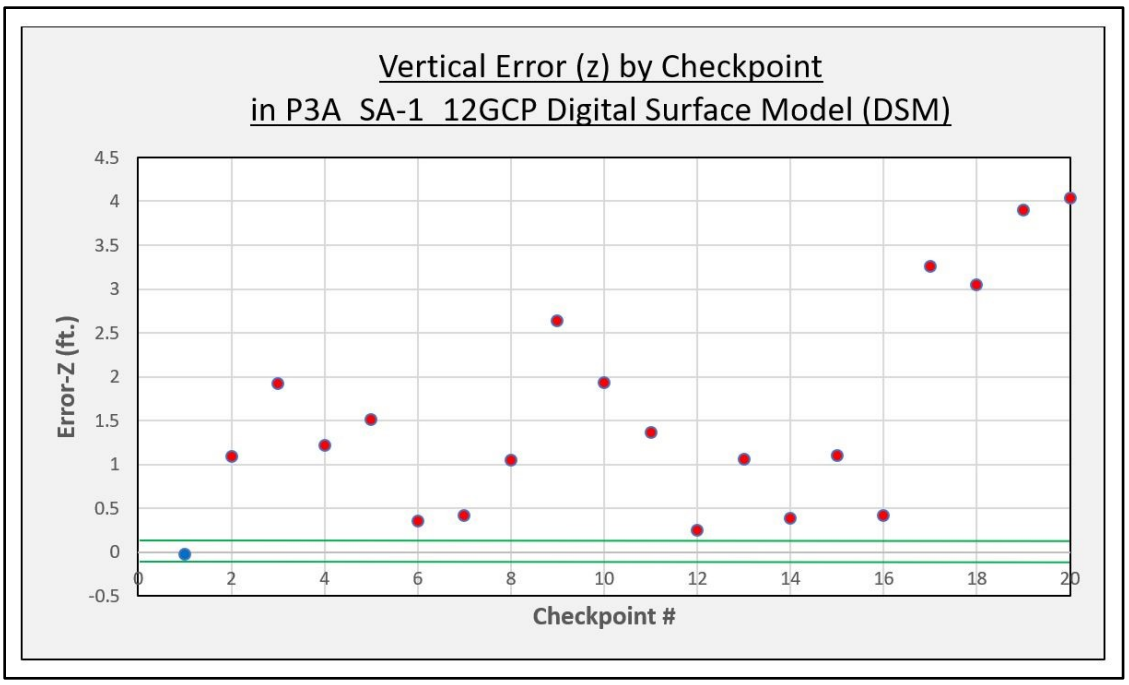

Figure C.8 Vertical error in relation to survey-grade accuracy for P3A-SA-1_12GCP DSM data

Survey-grade vertical accuracy at ≤ 0.164 ft. is represented by the green outline. Checkpoint locations with vertical error ≤ 0.164 ft. are represented in blue, while checkpoint locations with vertical error > 0.164 ft. are represented in red.

APPENDIX D

P3A_SA-2_21GCP COMPREHENSIVE ERROR EVALUATION

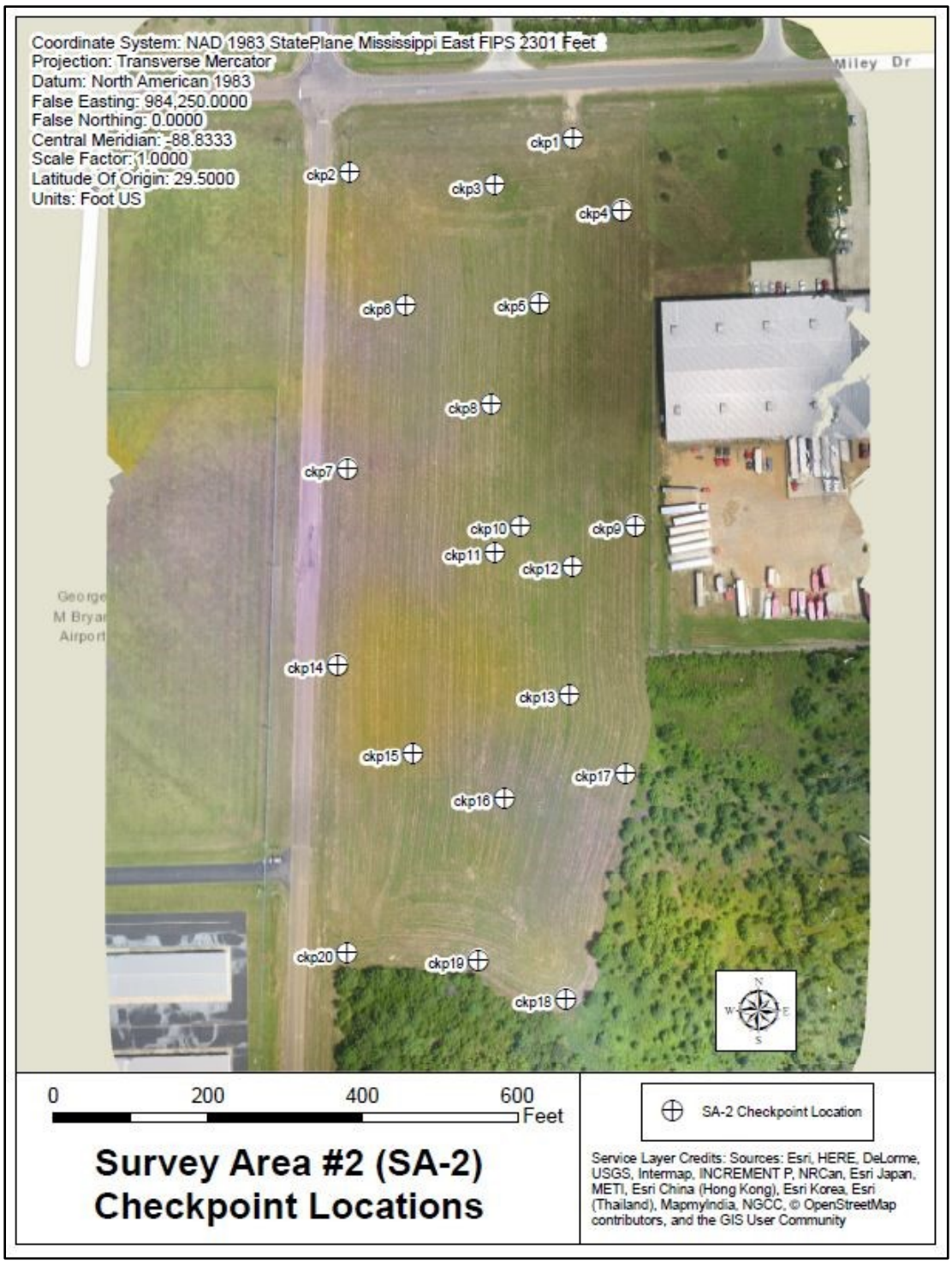

Figure D.1 Error evaluation – P3A_SA-2_21GCP checkpoint locations

Checkpoint locations collected via independent source of higher accuracy (Trimble R6) and used for positional error calculation and accuracy testing in P3A_SA-2_21GCP data.

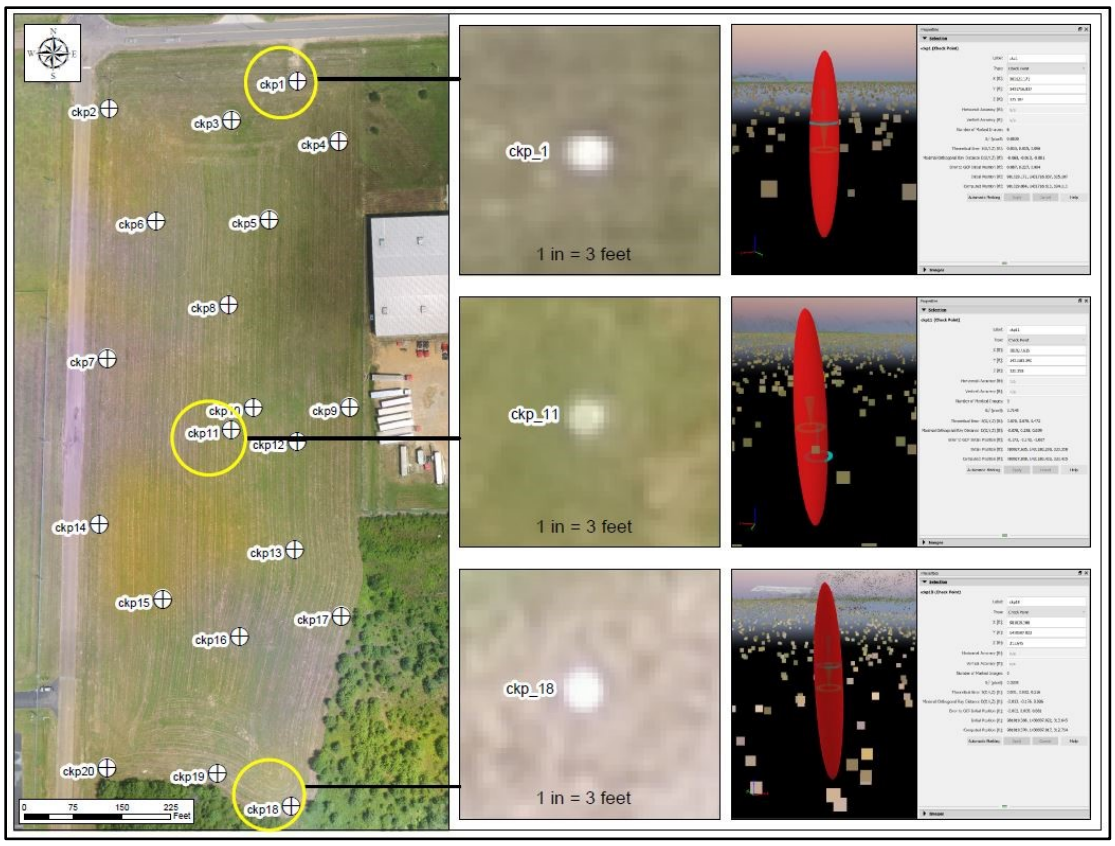

Figure D.2 Examples of error at various checkpoints in P3A_SA-2_21GCP dataset

In Pix4D Mapper Pro, positional error between initial and computed point positions can be visualized using the “Ray Cloud Editor” and corresponding “Error Ellipsoid” function.

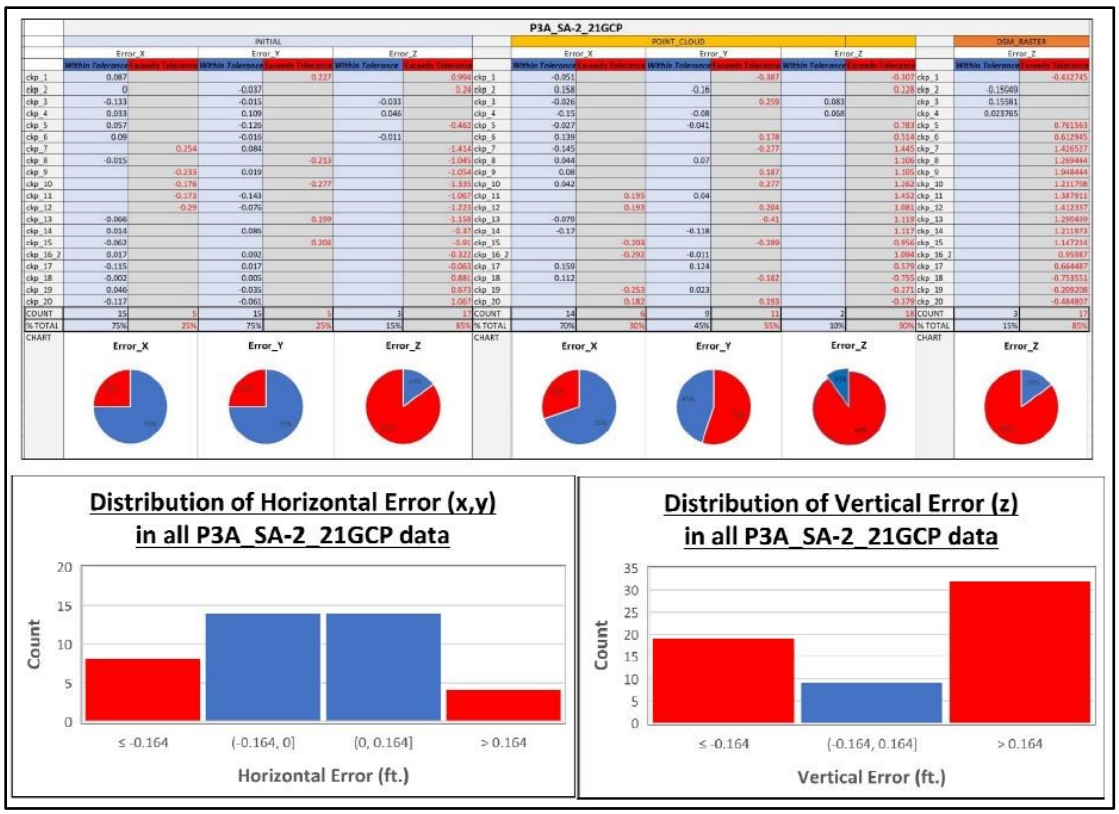

Figure D.3 Survey-grade accuracy evaluation of P3A_SA-2_21GCP error values

Positional error as recorded in P3A_SA-2_21GCP derived survey data. Red error values and corresponding red sections in the associated charts represent error values exceeding the ≤ 0.164 ft. survey-grade threshold tolerance. Blue error values and corresponding blue sections in the associated charts represent error values within the ≤ 0.164 ft. tolerance.

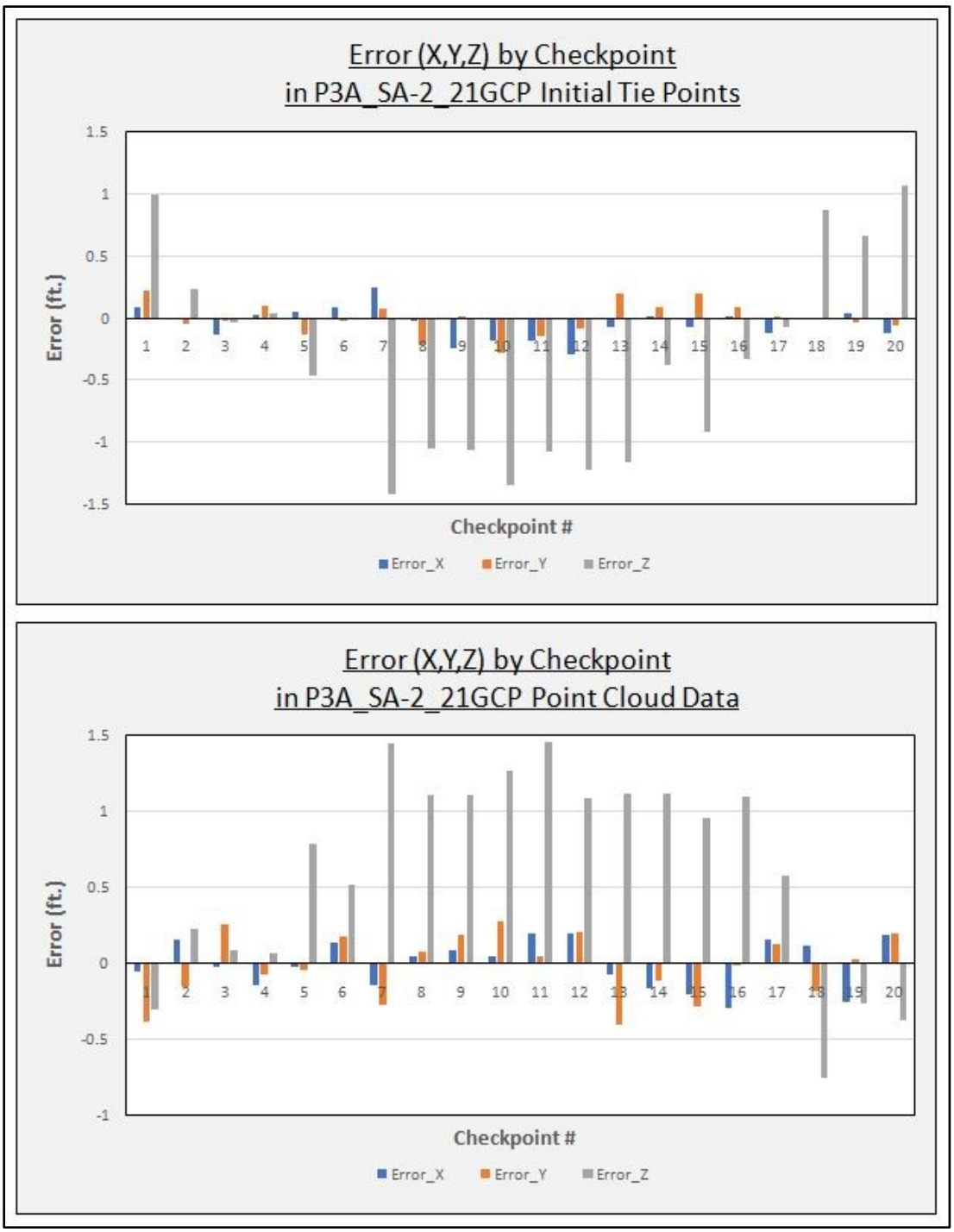

Figure D.4 Positional error by checkpoint for P3A_SA-2_21GCP dataset

Positional error (x = blue, y = orange, z = gray) at each checkpoint location in the various survey data types of the P3A_SA-2_21GCP dataset.

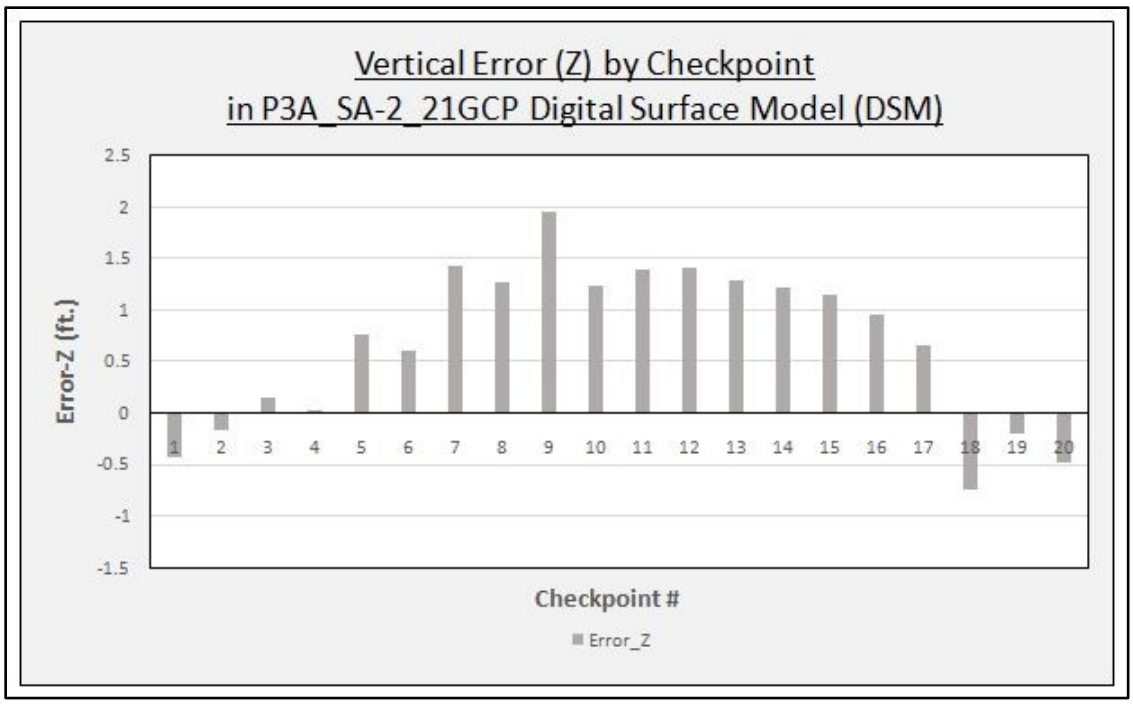

Figure D.5 Vertical error by checkpoint for P3A_SA-2_21GCP DSM

Vertical error (z = gray) at each checkpoint location in the digital surface model (DSM) raster survey data of P3A_SA-2_21GCP.

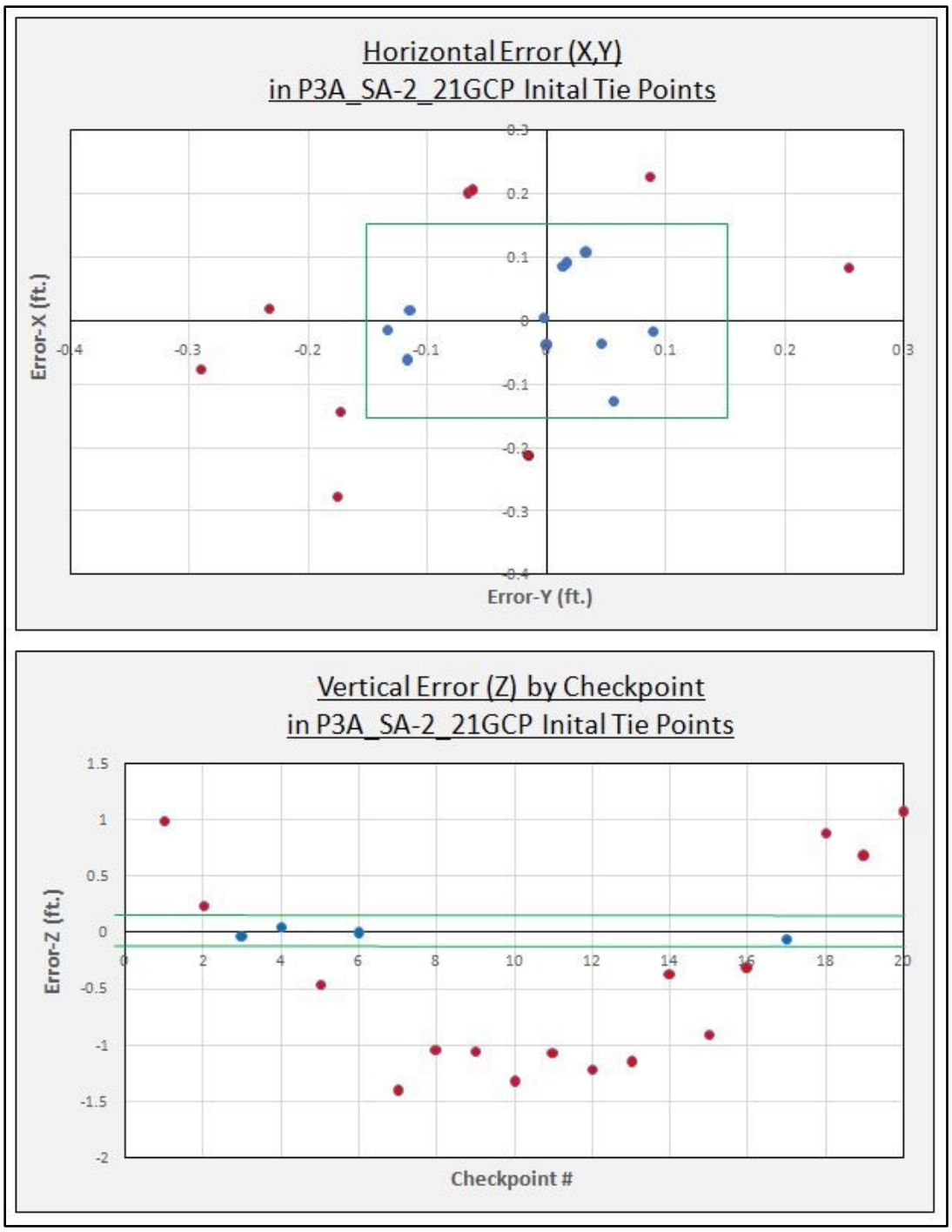

Figure D.6 Horizontal and vertical error in relation to survey-grade accuracy for P3A_SA-2_21GCP initial tie points data

Survey-grade accuracy at ≤ 0.164 ft. is represented by the green outline. Checkpoint locations with error ≤ 0.164 ft. are represented in blue, while checkpoint locations with error > 0.164 ft. are represented in red.

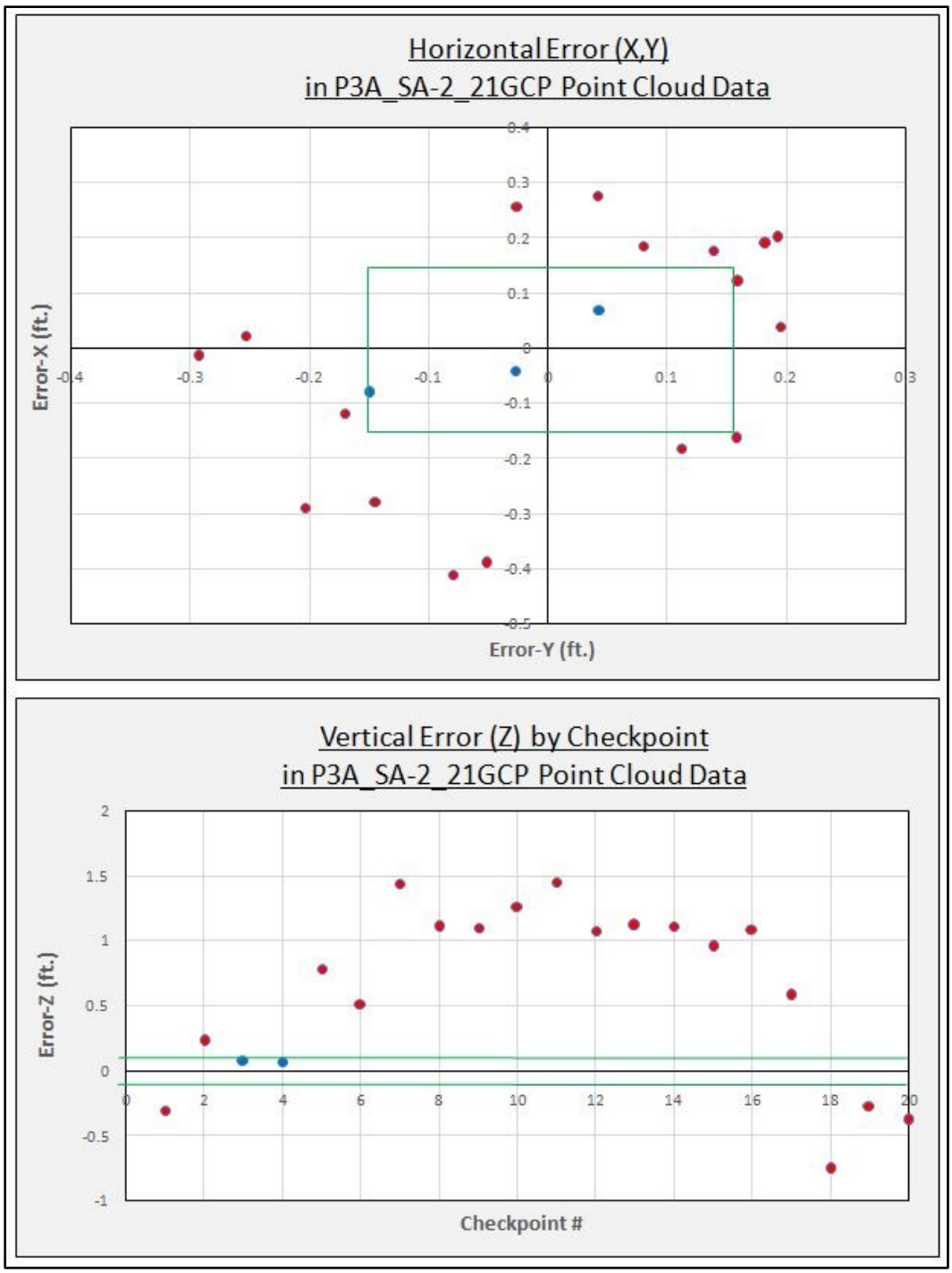

Figure D.7 Horizontal and vertical error in relation to survey-grade accuracy for P3A_SA-2_21GCP point cloud data

Survey-grade accuracy at ≤ 0.164 ft. is represented by the green outline. Checkpoint locations with error ≤ 0.164 ft. are represented in blue, while checkpoint locations with error > 0.164 ft. are represented in red.

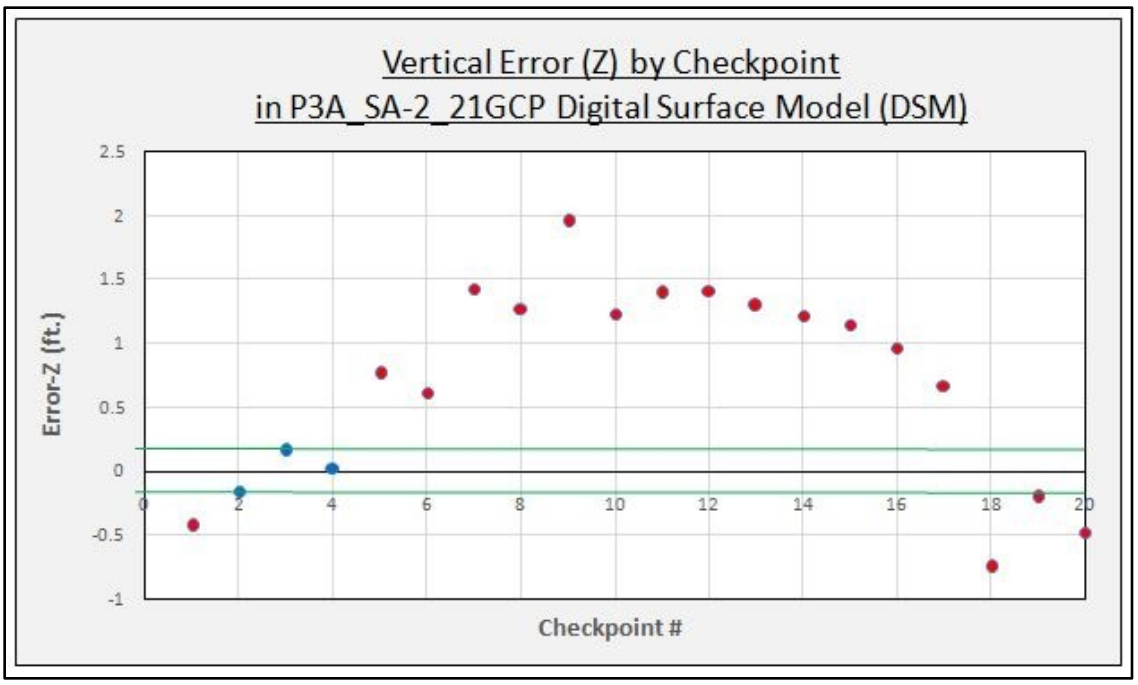

Figure D.8 Vertical error in relation to survey-grade accuracy for P3A_SA-2_21GCP DSM data

Survey-grade vertical accuracy at ≤ 0.164 ft. is represented by the green outline. Checkpoint locations with vertical error ≤ 0.164 ft. are represented in blue, while checkpoint locations with vertical error > 0.164 ft. are represented in red.

APPENDIX E

P4P_SA-1_12GCP COMPREHENSIVE ERROR EVALUATION

Figure E.1 Error evaluation – P4P_SA-1_12GCP checkpoint locations

Checkpoint locations collected via independent source of higher accuracy (Trimble R6) and used for positional error calculation and accuracy testing in P4P_SA-1_12GCP data.

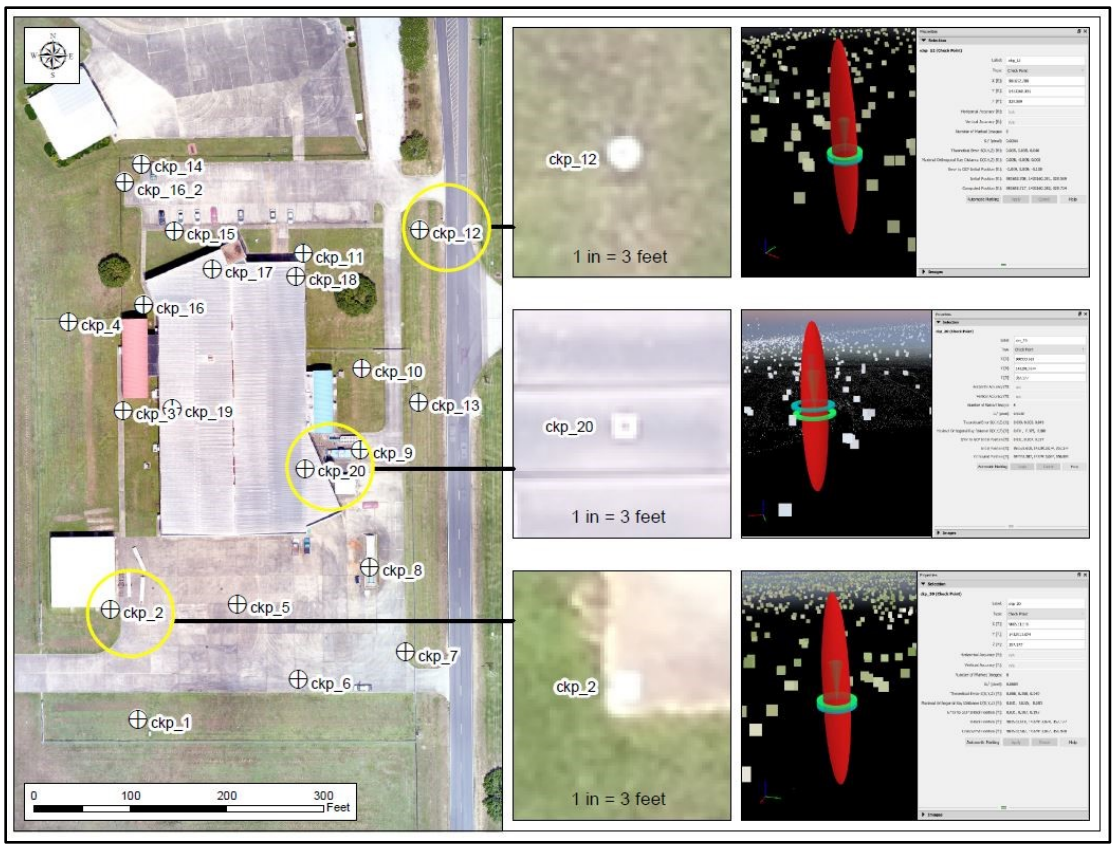

Figure E.2 Examples of error at various checkpoints in P4P_SA-1_12GCP dataset

In Pix4D Mapper Pro, positional error between initial and computed point positions can be visualized using the “Ray Cloud Editor” and corresponding “Error Ellipsoid” function.

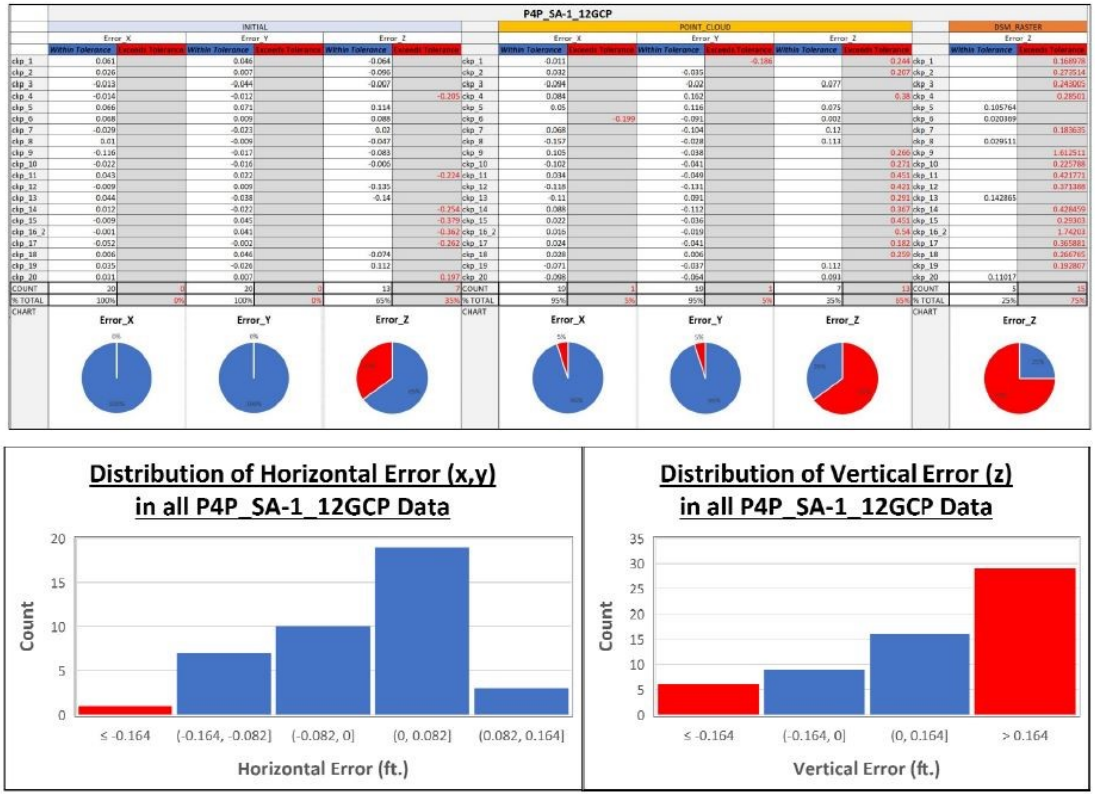

Figure E.3 Survey-grade accuracy evaluation of P4P_SA-1_12GCP error values

Positional error as recorded in P4P_SA-1_12GCP derived survey data. Red error values and corresponding red sections in the associated charts represent error values exceeding the ≤ 0.164 ft. survey-grade threshold tolerance. Blue error values and corresponding blue sections in the associated charts represent error values within the ≤ 0.164 ft. tolerance.

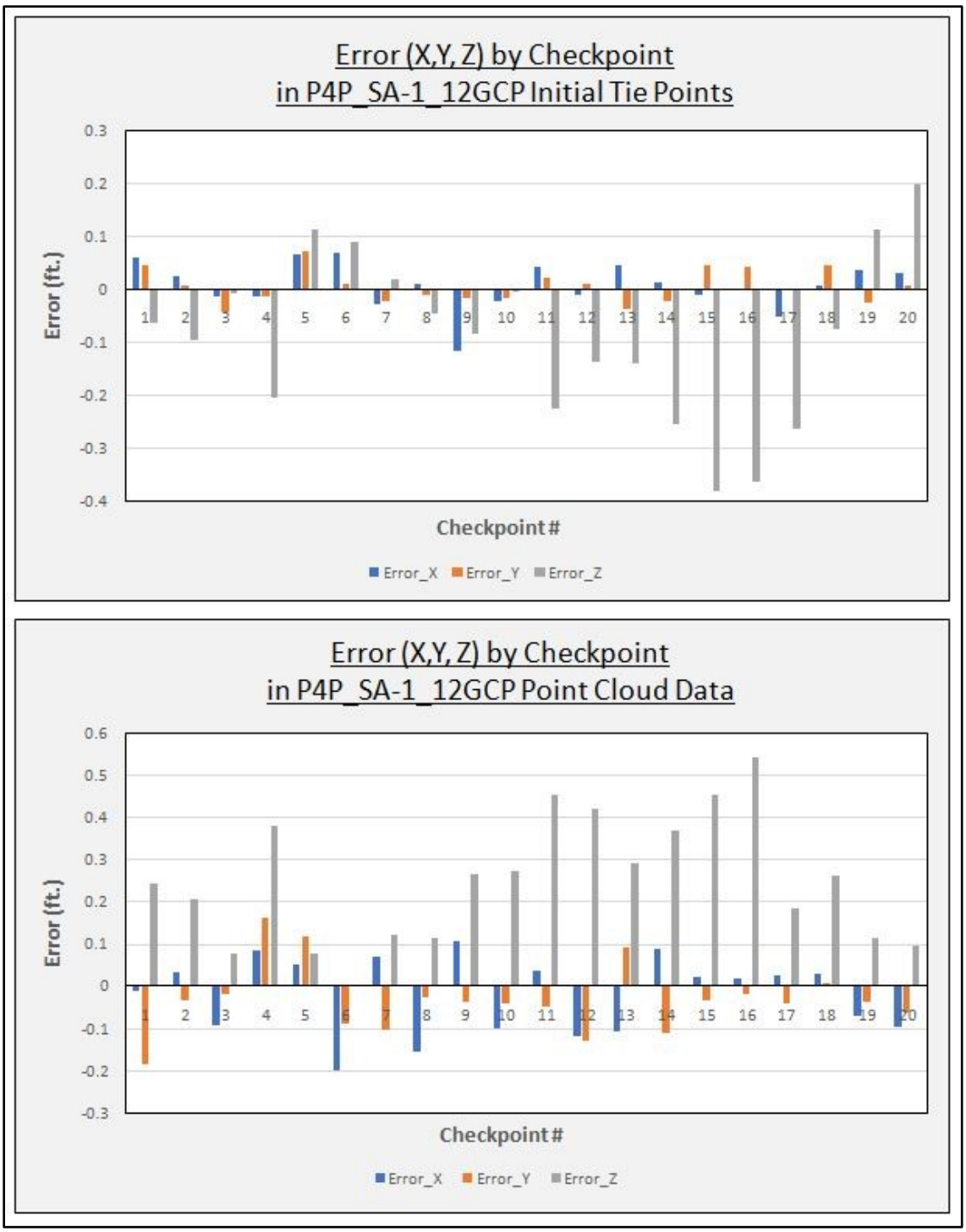

Figure E.4 Positional error by checkpoint for P4P_SA-1_12GCP dataset

Positional error (x = blue, y = orange, z = gray) at each checkpoint location in the various survey data types of the P4P_SA-1_12GCP dataset.

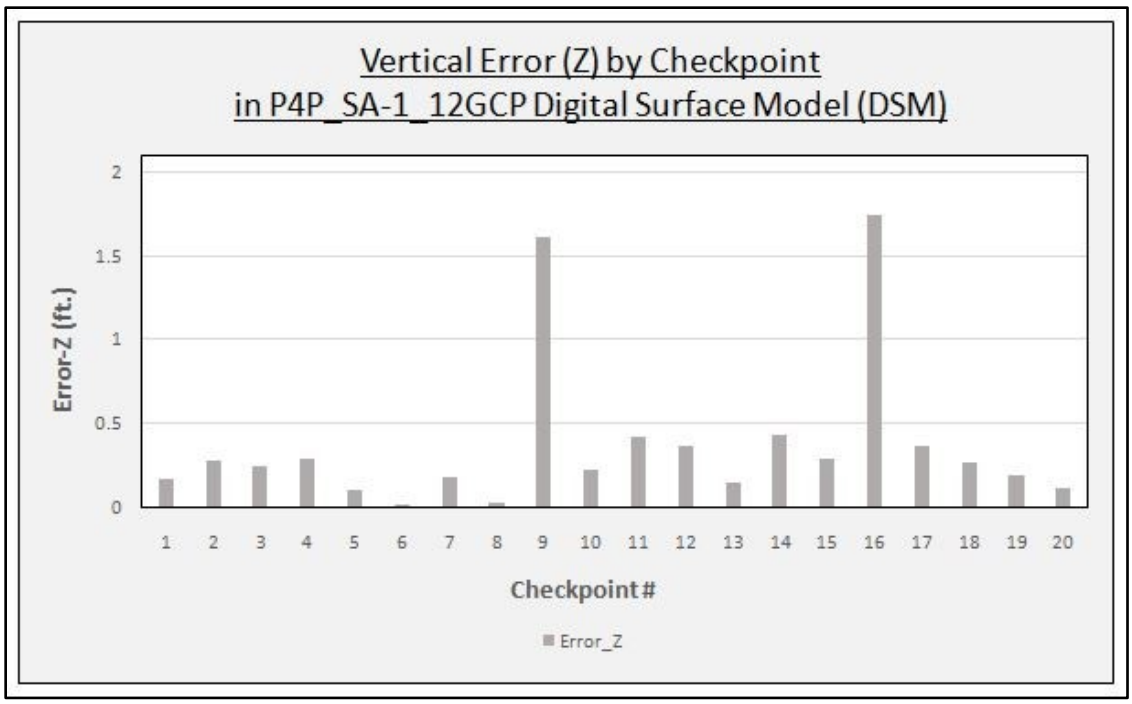

Figure E.5 Vertical error by checkpoint for P4P_SA-1_12GCP DSM

Vertical error (z = gray) at each checkpoint location in the digital surface model (DSM) raster survey data of P4P_SA-1_12GCP.

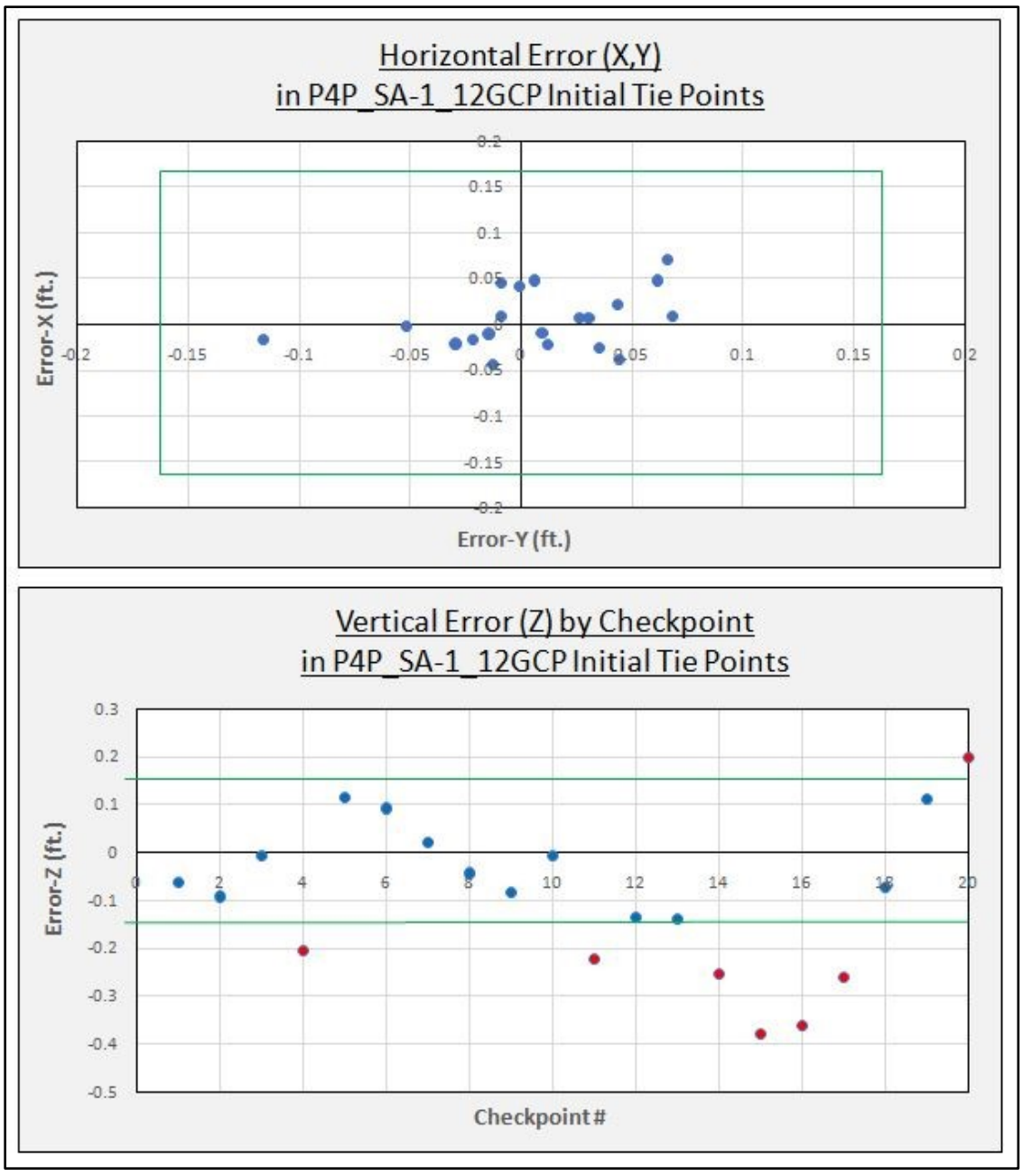

Figure E.6 Horizontal and vertical error in relation to survey-grade accuracy for P4P_SA-1_12GCP initial tie points data

Survey-grade accuracy at ≤ 0.164 ft. is represented by the green outline. Checkpoint locations with error ≤ 0.164 ft. are represented in blue, while checkpoint locations with error > 0.164 ft. are represented in red.

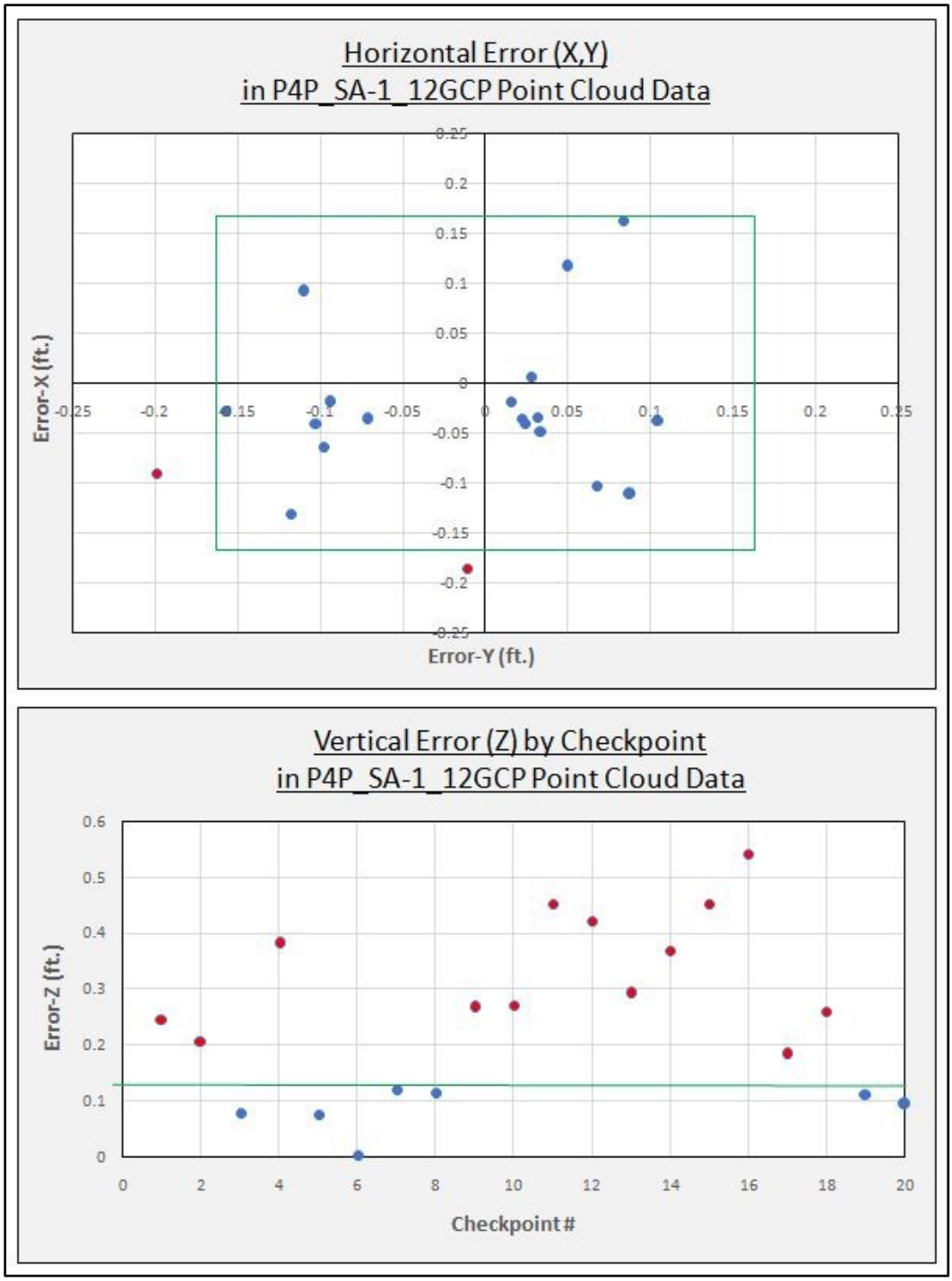

Figure E.7 Horizontal and vertical error in relation to survey-grade accuracy for P4P_SA-1_12GCP point cloud data

Survey-grade accuracy at ≤ 0.164 ft. is represented by the green outline. Checkpoint locations with error ≤ 0.164 ft. are represented in blue, while checkpoint locations with error > 0.164 ft. are represented in red.

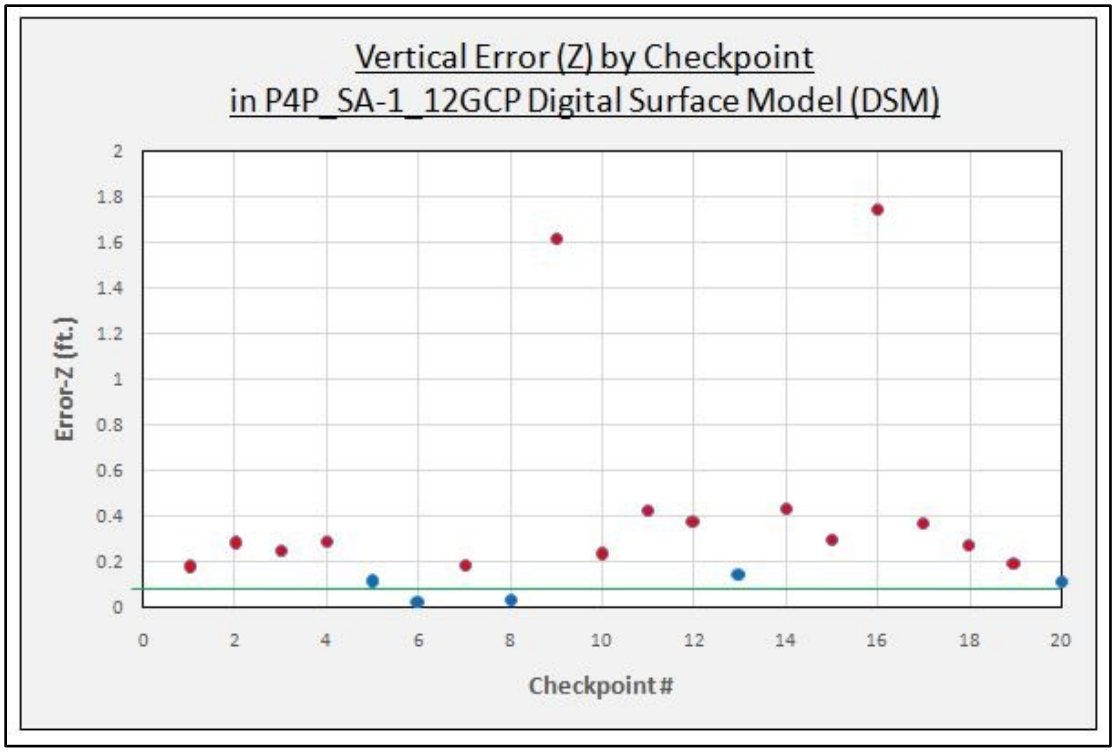

Figure E.8 Vertical error in relation to survey-grade accuracy for P3A-SA-1_12GCP DSM data

Survey-grade vertical accuracy at ≤ 0.164 ft. is represented by the green outline. Checkpoint locations with vertical error ≤ 0.164 ft. are represented in blue, while checkpoint locations with vertical error > 0.164 ft. are represented in red.

APPENDIX F

P4P_SA-2_21GCP COMPREHENSIVE ERROR EVALUATION

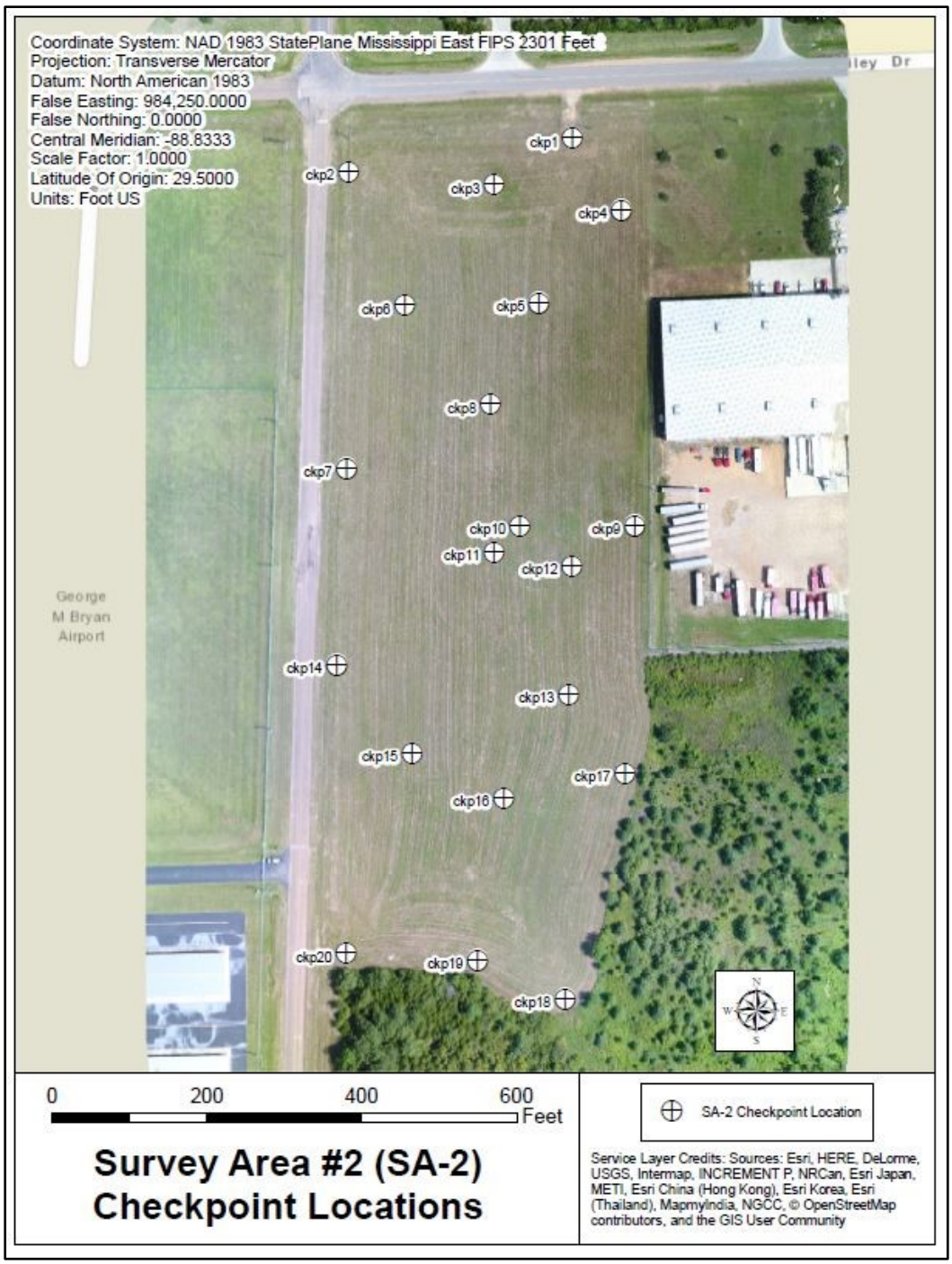

Figure F.1 Error evaluation – P4P_SA-2_21GCP checkpoint locations

Checkpoint locations collected via independent source of higher accuracy (Trimble R6) and used for positional error calculation and accuracy testing in P4P_SA-2_21GCP data.

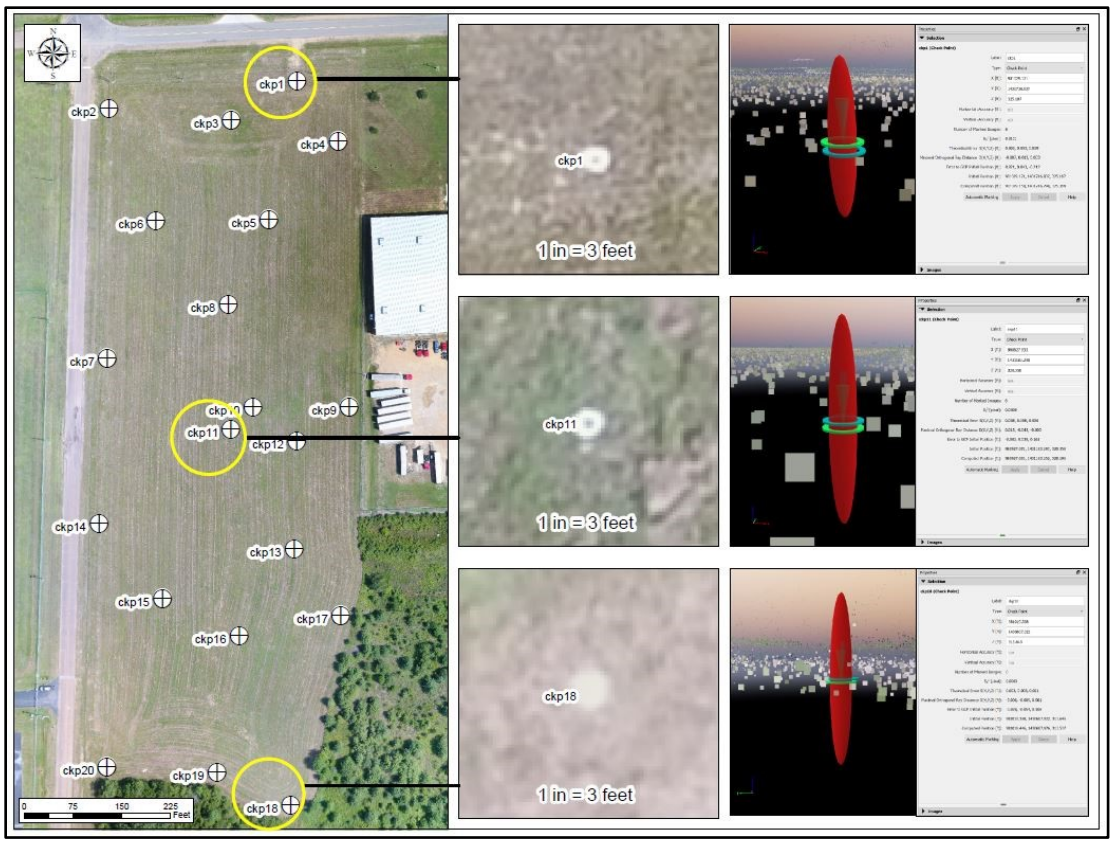

Figure F.2 Examples of error at various checkpoints in P4P_SA-2_21GCP dataset

In Pix4D Mapper Pro, positional error between initial and computed point positions can be visualized using the “Ray Cloud Editor” and corresponding “Error Ellipsoid” function.

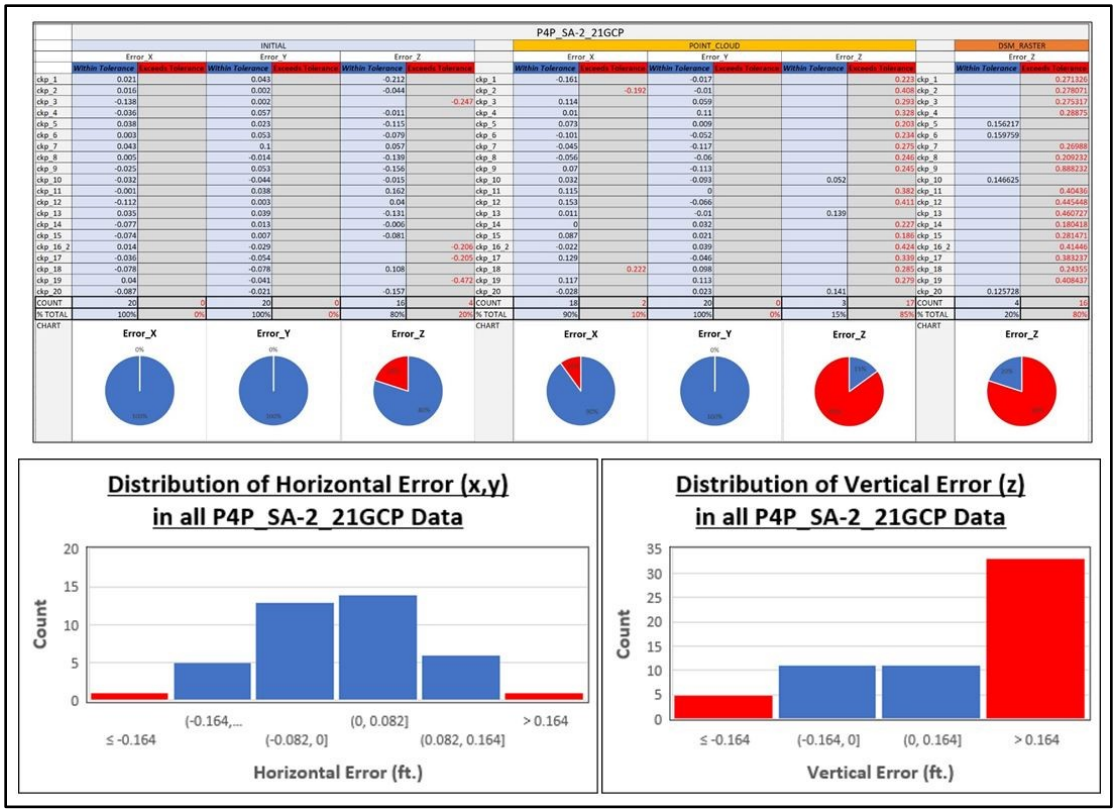

Figure F.3 Survey-grade accuracy evaluation of P4P_SA-2_21GCP error values

Positional error as recorded in P4P_SA-2_21GCP derived survey data. Red error values and corresponding red sections in the associated charts represent error values exceeding the ≤ 0.164 ft. survey-grade threshold tolerance. Blue error values and corresponding blue sections in the associated charts represent error values within the ≤ 0.164 ft. tolerance.

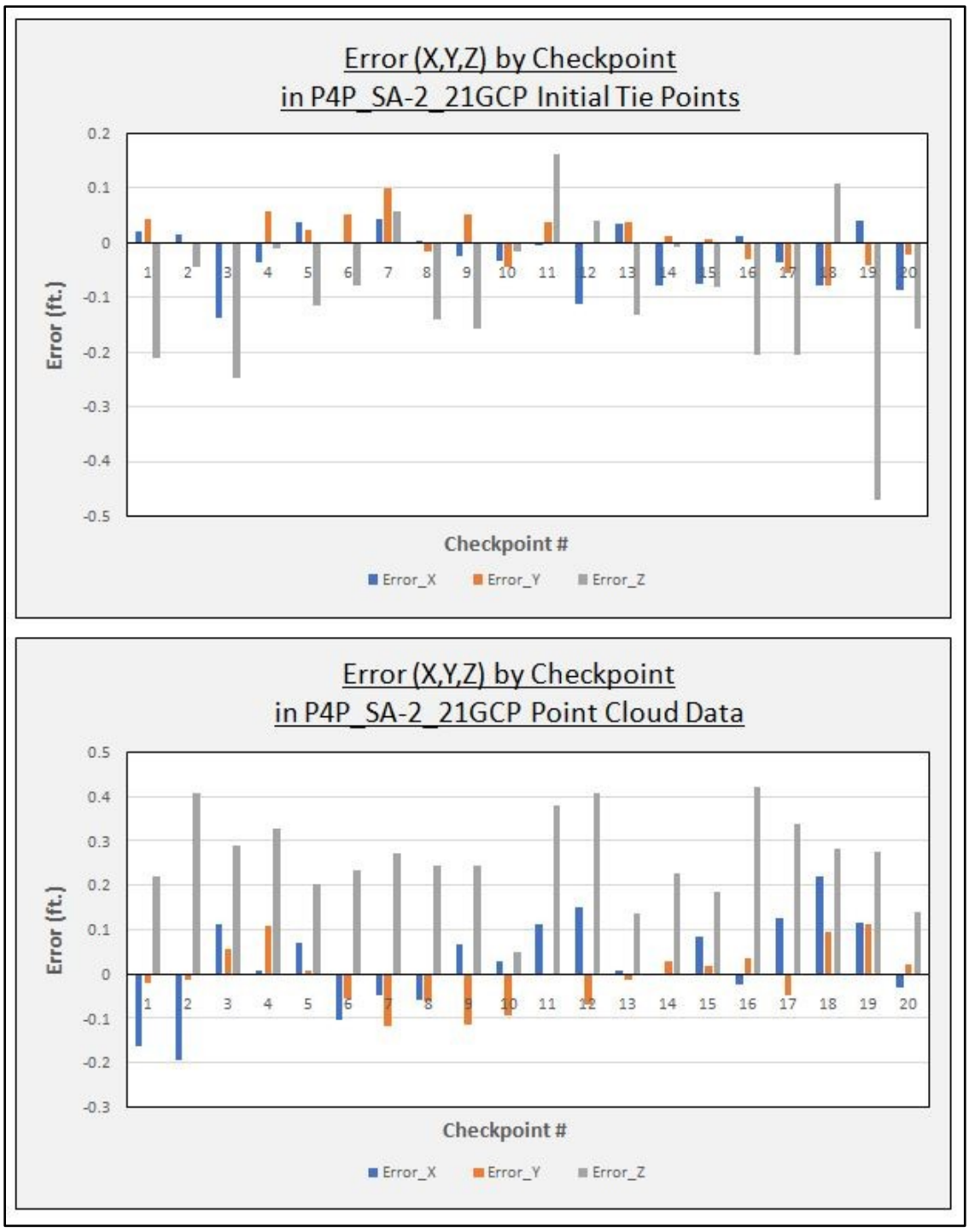

Figure F.4 Positional error by checkpoint for P3A_SA-2_21GCP dataset

Positional error (x = blue, y = orange, z = gray) at each checkpoint location in the various survey data types of the P4P_SA-2_21GCP dataset.

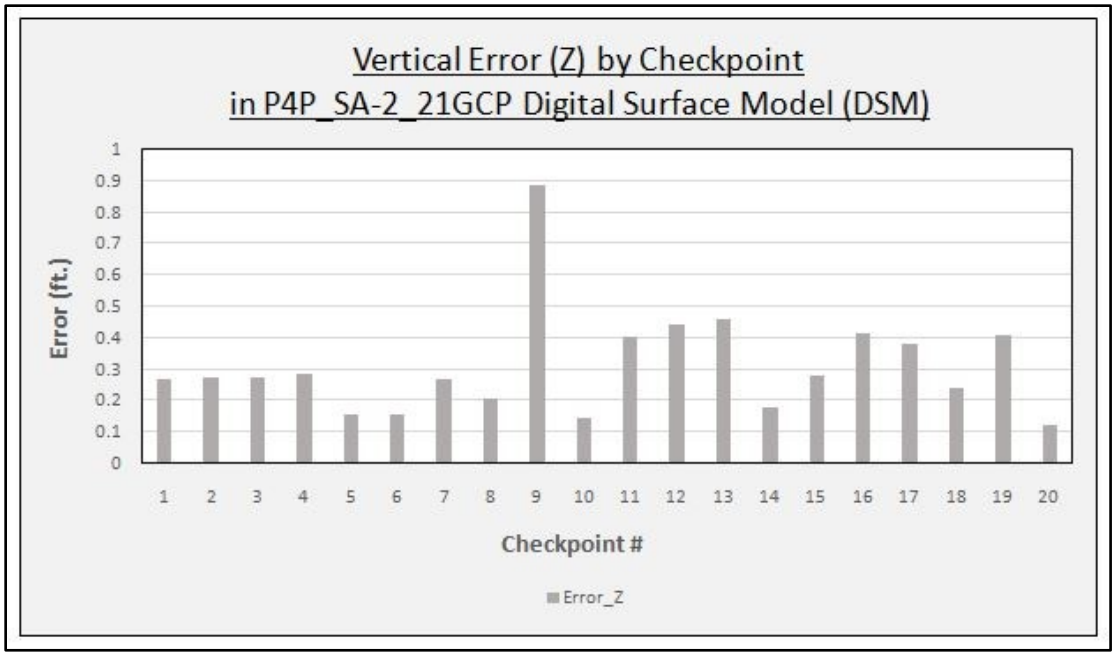

Figure F.5 Vertical error by checkpoint for P4P_SA-2_21GCP DSM

Vertical error (z = gray) at each checkpoint location in the digital surface model (DSM) raster survey data of P4P_SA-2_21GCP.

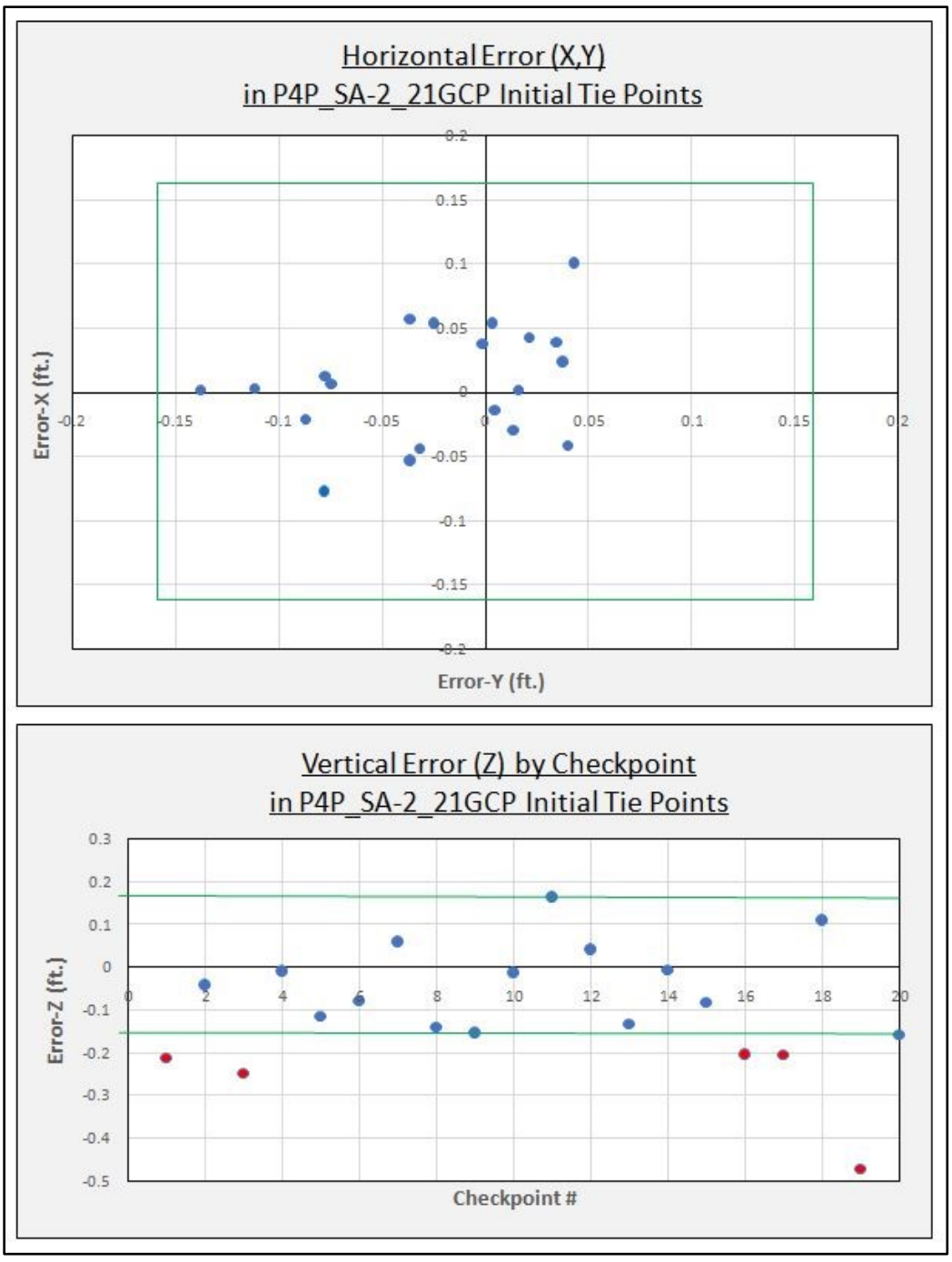

Figure F.6 Horizontal and vertical error in relation to survey-grade accuracy for P4P_SA-2_21GCP initial tie points data

Survey-grade accuracy at ≤ 0.164 ft. is represented by the green outline. Checkpoint locations with error ≤ 0.164 ft. are represented in blue, while checkpoint locations with error > 0.164 ft. are represented in red.

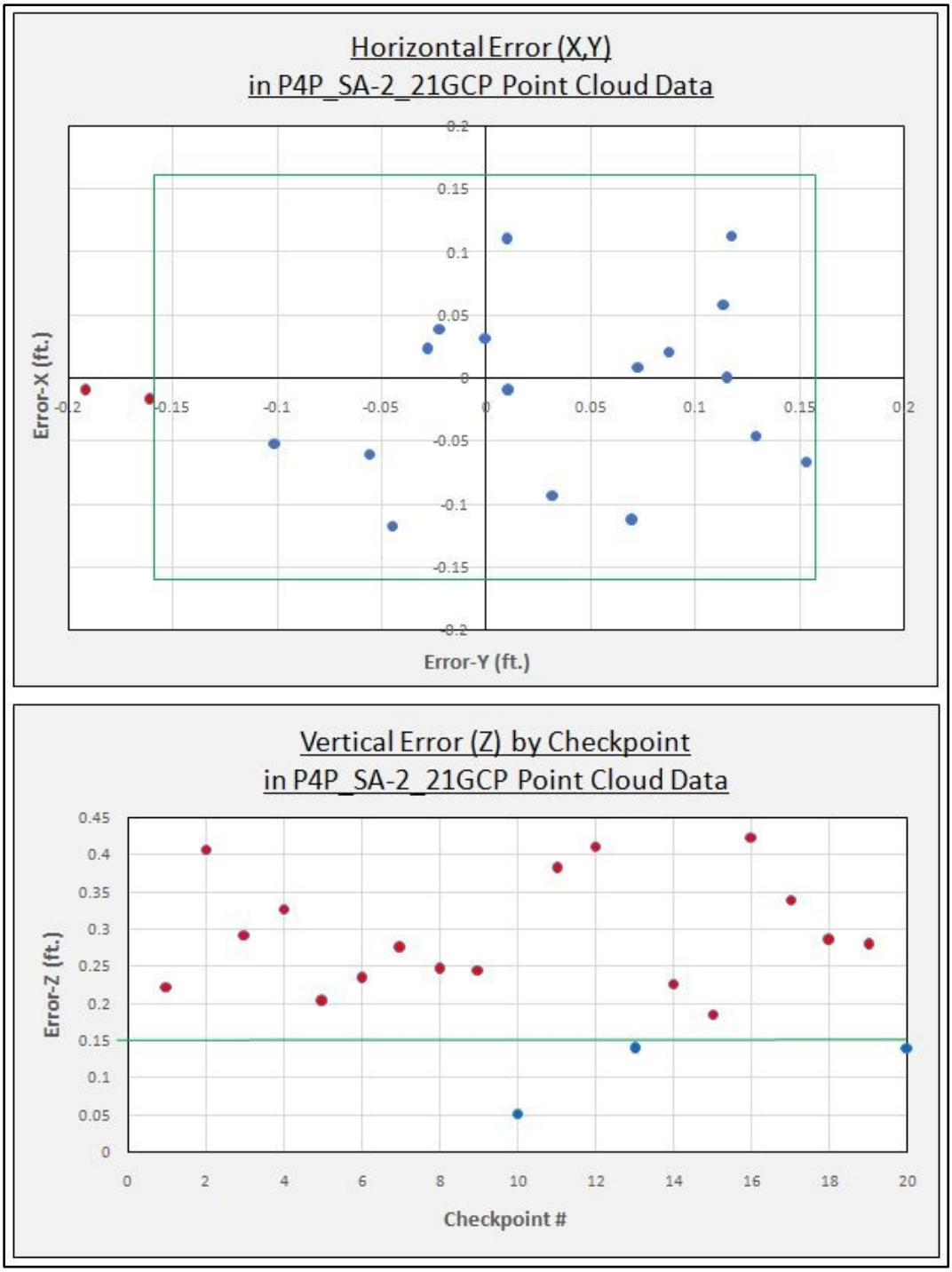

Figure F.7 Horizontal and vertical error in relation to survey-grade accuracy for P4P_SA-2_21GCP point cloud data

Survey-grade accuracy at ≤ 0.164 ft. is represented by the green outline. Checkpoint locations with error ≤ 0.164 ft. are represented in blue, while checkpoint locations with error > 0.164 ft. are represented in red.

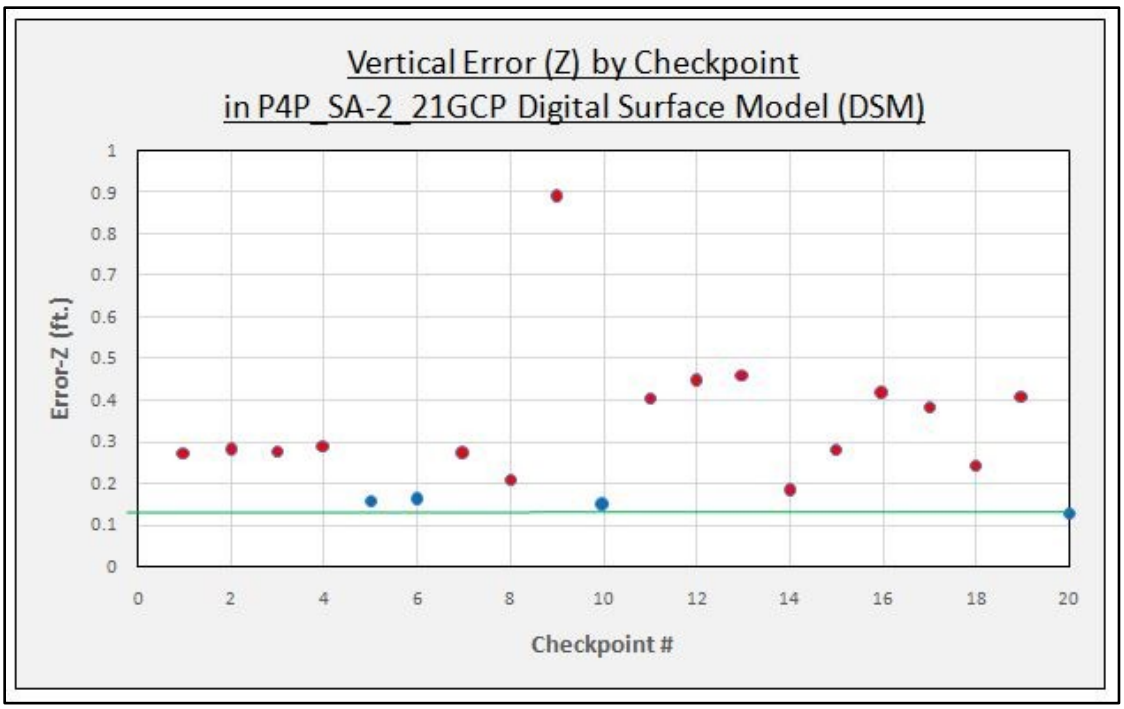

Figure F.8 Vertical error in relation to survey-grade accuracy for P4P_SA-2_21GCP DSM data

Survey-grade vertical accuracy at ≤ 0.164 ft. is represented by the green outline. Checkpoint locations with vertical error ≤ 0.164 ft. are represented in blue, while checkpoint locations with vertical error > 0.164 ft. are represented in red.